Spectroscopic Ellipsometry of Spin-Chain Cuprates and $LaNiO_3$-based Heterostructures

Von der Fakultät Mathematik und Physik
der Universität Stuttgart
zur Erlangung der Würde eines Doktors der Naturwissenschaften
(Dr. rer. nat.) genehmigte Abhandlung

vorgelegt von

Yulia Matiks
aus Frunze (Kirgistan)

Hauptberichter: Prof. Dr. Bernhard Keimer
Mitberichter: Prof. Dr. Martin Dressel

Tag der mündlichen Prüfung: 3. Juni 2011

Max-Planck-Institut für Festkörperforschung

Stuttgart 2011

for my parents

Contents

Deutsche Zusammenfassung

Der elektronische Transport in niederdimensionalen Kupferoxiden war in den vergangenen Jahrzehnten aufgrund der ungewöhnlichen supraleitenden Zustände dieser geschichteten Systeme im Fokus intensiver Forschungsbemühungen. Hierbei sind die eindimensionalen Kuprate nicht nur für analytische und numerische Rechnungen wesentlich leichter zugänglich, sondern können darüber hinaus auch Einsichten für die zweidimensionalen Systeme liefern. Einer der zentralen Punkte effektiver Theorien zu niederenergetischen Anregungen in den Kupraten ist der Zhang-Rice-Singulett-Zustand. Die energetisch niedrigsten exzitonischen Anregungen über die Mott-Hubbard-Energielücke hinweg unter Beteiligung des doppelt besetzten Kupfers und des Zhang-Rice-Singuletts sind Gegenstand vieler dieser theoretischen Untersuchungen. Um einen eindeutigen Nachweis exzitonischer Zustände zu erbringen und deren charakteristische Energien, Kopplungsstärke und Temperaturabhängigkeit zu bestimmen und mit Modellrechnungen zu vergleichen, sind detaillierte experimentelle spektroskopische Untersuchungen erforderlich.

Die vorliegende Arbeit konzentriert sich auf Verbindungen mit eindimensionalen Ketten aus CuO_4-Quadraten mit jeweils gemeinsamen Kanten, in denen langreichweitige Austauschwechselwirkungen exotische magnetische Eigenschaften hervorrufen. Aufgrund der außergewöhnlich kleinen elektronischen Bandbreite bilden diese Kuprate ein ideales System, die Bildung von Exzitonen und das Wechselspiel von Spins und Ladungen zu untersuchen.

Mittels Ellipsometrie wurden umfassende Untersuchungen der Ladungsanregungen über die Band-Lücke hinweg an $LiCuVO_4$, $NaCu_2O_2$, Li_2CuO_2, $CuGeO_3$ und α-CuV_2O_6-Einkristallen hoher Güte durchgeführt. In allen Verbindungen konnten die Exziton-Zustände, die vom Zhang-Rice-Singulett-Zustand herrühren, bestimmt werden. Es wurden schwache Strukturen bei 2.15 und 2.95 eV in $LiCuVO_4$, 2.15 und 2.65 eV in $NaCu_2O_2$, 3.05 und 3.7 eV in $CuGeO_3$, 1.75 und 2.15 eV in α-CuV_2O_6 und 3.7 eV in Li_2CuO_2 identifiziert, die die Absorptionskante entlang der CuO-Ketten bilden. Diese Bänder wurden als Exziton-Dupletts identifiziert, deren Ursprung in der langreichweitigen Wechselwirkung zwischen nächsten und übernächstbenachbarten Kupferatomen in den Ketten liegt. Des Weiteren wurde das Temperaturverhalten dieser exzitonischen Bänder untersucht. Da die Temperaturabhängigkeit den Spin-Korrelationen innerhalb der Ketten folgt, werden diese erst bei tiefen Temperaturen beobachtbar. Diese Ergebnisse zeigen nicht nur überzeugend die Bildung der Mott-Hubbard-Exzitonen, sondern quantifizieren auch die charakteristischen Energieskalen, wie lokale Hubbard U- (2.55 – 4.3 eV) und langreichweitige Coulomb V-Wechselwirkungen (0.8 – 1.6 eV).

Seit der Entdeckung der Supraleitung sind die geschichteten Kuprate die einzigen Materialien, die einen Phasenübergang oberhalb des Siedepunkts flüssigen Stickstoffs zeigen. Zwar konnte bis zum heutigen Tag in den dem Kupfer benachbarten Bulk-Nickelaten keine Supraleitung nachgewiesen werden, Heterostrukturen jedoch eröffnen neue Perspektiven, da von theoretischer Seite her in Nickel-Übergittern eine, die elektronische Struktur der Kuprat-Supraleiter nachbildende, in Bezug auf die Orbitale nichtentartete Spin-1/2-Struktur zu erwarten ist. Übergitter, in denen sich metallische $LaNiO_3$ Schichten mit band-isolierenden $LaAlO_3$ Schichten abwechseln, bilden einer kürzlich vorgeschlagenen Theorie zufolge die doppellagigen Kuprate mit ähnlichen niederenergetischen elektronischen und Spin-Anregungen nach.

In der Praxis hat sich gezeigt, dass die üblichen Methoden, die elektronischen Zustände in künstlichen Bulk-Materialien zu beobachten, oft fehlschlagen, wenn die Dicke der aus atomar dünnen Oxidschichten aufgebauten Proben unter 100 nm liegt. Die Spektralellipsometrie jedoch ist eine sehr leistungsfähige Methode, die es erlaubt die Dynamik von Ladungsträgern in künstlichen Systemen zu untersuchen. Im Gegensatz zu anderen Techniken werden die intrinsischen elektrodynamischen Eigenschaften des Materials unbeeinflusst von elektrischer Kontaktierung oder ausgedehnten Defekten ermittelt.

Ausführliche optische Untersuchungen wurden an $[LaNiO_3]_N - [LaAlO_3]_N$ ($N = 2, 4$) Übergittern durchgeführt. Als Substrate dienten $SrTiO_3$ und $LaSrAlO_4$, was im ersten Fall zu Zug- im zweiten zu Druckspannungen im aufgewachsenen Film führt. Es konnte gezeigt werden, dass Übergitter mit $LaNiO_3$ mit einer Dicke von 2 Einheitszellen ($N = 2$) bei sinkender Temperatur einen Ladungsordnungs-Phasenübergang durchlaufen. Für $N = 4$ bleibt das Material im vermessenen Temperaturbereich hingegen metallisch und paramagnetisch. Dies zeigt, dass eine volle dimensionale Kontrolle der kollektiven Instabilität gewährleistet ist. Dieses Phasenverhalten ist qualitativ ähnlich dem von Bulk-$RNiO_3$, wobei R ein Anion mit kleinem Radius bezeichnet, wo es durch die Verkleinerung der Bandbreite aufgrund der Verkippung der NiO_6-Oktaeder hervorgerufen wird. Die Übergangstemperatur jedoch ist im vorliegenden System, wohl aufgrund der reduzierten Dimensionalität, erheblich niedriger. Dieser größeren Neigung der zwei-dimensionalen Systeme zur Ladungs- und Spinordnung liegt womöglich das verstärkte Nesting der $LaNiO_3$ Fermifläche zugrunde. Es zeigt sich, dass für die $N = 2$ Übergitter unter Zugspannung die optische Leitfähigkeit im Infrarot-Bereich höher und die Übergangstemperatur niedriger ist. Dieses verstärkte metallische Verhalten im Vergleich zu den Übergittern unter Druckspannung könnte von einer Verbreiterung der Ni *3d*-Bänder und/oder einer erhöhten Besetzung der Ni $d_{x^2-y^2}$-Orbitale, die parallel zu den $LaNiO_3$-Schichten polarisiert sind, herrühren. Dies zeigt weitere Möglichkeiten auf, wie über die Orbitale das kollektive Phasenverhalten der Nickelate gesteuert werden kann, was weitere experimentelle Tests für die theoretischen Vorhersagen bezüglich Hochtemperatur-Supraleitung und Multiferroizität in diesen Systemen ermöglicht.

Summary

Electronic transport in low-dimensional copper oxides has been the focus of much activity during the past decades, because of unusual superconducting states observed in layered cuprates. The one-dimensional cuprates are more amenable to analytical and numerical calculations and may well hold lessons for the two-dimensional systems as well. One of the central issues of low-energy effective theories of the cuprates is the Zhang-Rice singlet state. The lowest energy elementary excitations of excitonic nature across the Mott-Hubbard gap, involving a doubly occupied Cu site and the Zhang-Rice singlet, have been addressed in many of these theoretical studies. In order to provide a clear evidence of exciton states, to determine their characteristic energies, strengths and temperature dependencies and compare these results with model calculations, a detailed experimental spectroscopic study is required.

In our study we focus on compounds, comprised of chains of the edge-sharing CuO_4 plaquettes, in which the long-range exchange interactions between far neighbours give rise to the exotic magnetic properties. By virtue of their exceptionally narrow electronic band-width, the edge-sharing cuprates thus provide a highly favorably platform for the investigation of exciton formation and the interplay between spin and charge correlations.

We have performed a comprehensive ellipsometric study of the charge excitations across the optical gap in high-quality $LiCuVO_4$, $NaCu_2O_2$, Li_2CuO_2, $CuGeO_3$ and α-CuV_2O_6 single crystals. In all these compounds, the exciton states associated with the Zhang-Rice singlet state were assigned. We observed weak structures centered at 2.15 and 2.95 eV in $LiCuVO_4$, 2.15 and 2.65 eV in $NaCu_2O_2$, 3.05 and 3.7 eV in $CuGeO_3$, 1.75 and 2.15 eV in α-CuV_2O_6, and 3.7 eV in Li_2CuO_2, which form the absorption edge along the CuO chains. These bands were identified as exciton doublets, originating from the long-range Coulomb interaction between the nearest- and the next-nearest-neighbour Cu sites along the chains. We also studied the temperature dependencies of the observed excitonic bands. Since their evolution with temperature follows the spin correlations within the chains, they are observable only at low temperatures. These results have not only persuasively demonstrated the formation of the Mott-Hubbard excitons, but also quantified characteristic energy scales, such as the local Hubbard U $(2.55 - 4.3$ eV) and long-range Coulomb V $(0.8 - 1.6$ eV) interactions.

Since the discovery of superconductivity, the layered cuprates remain the only materials which exhibit a transition to the superconducting state above the boiling temperature of nitrogen. It has not proved possible to extend superconductivity to the Cu-neighbouring bulk nickelates, but heterostructures may offer new possi-

bilities. From a theoretical point of view, an orbitally nondegenerate spin one-half electronic structure resembling that of cuprate superconductors may be expected in $LaNiO_3$-based superlattices, opening new perspectives for high-T_c superconductivity. According to a recent proposal, superlattices in which metallic $LaNiO_3$ layers are alternated with band-insulating $LaAlO_3$ layers imitate the double-layer cuprates with analogous low-energy electronic and spin excitations.

In practice, conventional methods to probe electronic states in bulk materials often fail for artificial structures that are typically less than 100 nm thick and comprised of atomically thin individual oxide layers. Spectral ellipsometry is a powerful tool to study the charge dynamics of such artificial systems. In contrast to other methods it exposes the intrinsic electrodynamic response, which is not influenced by contacts or extended defects.

A comprehensive optical study was performed on $[LaNiO_3]_N - [LaAlO_3]_N$ (N = 2, 4) superlattices grown on both $SrTiO_3$ and $LaSrAlO_4$ substrates, which induce tensile and compressive strain in the overlayer, respectively. We have shown that superlattices with $LaNiO_3$ layers as thin as two unit cells undergo a charge-ordering transition as a function of decreasing temperature. By showing that the $N = 4$ counterparts remain uniformly metallic and paramagnetic at all temperatures, we have demonstrated full dimensionality control of the collective instability. The phase behavior is qualitatively similar to the one observed in bulk $RNiO_3$ with small radius of the R anions, which results from bandwidth narrowing due to rotation of NiO_6 octahedra, but the transition temperature is substantially lower, probably because of the reduced dimensionality. The higher propensity towards charge and spin order in the two-dimensional systems probably reflects enhanced nesting of the $LaNiO_3$ Fermi surface. We have found, that the infrared conductivity is higher and the transition temperatures are lower in the N = 2 superlattices grown under tensile strain. The more metallic response of these superlattices, compared to those grown under compressive strain, may reflect a widening of the Ni$3d$ bandwidth and/or an enhanced occupation of the Ni $d_{x^2-y^2}$ orbital polarized parallel to the $LaNiO_3$ layers. This indicates further opportunities for orbital control of the collective phase behavior of the nickelates, which may enable experimental tests of theories predicting high temperature superconductivity or multiferroicity in these systems.

The thesis is organized as follows: The principles of spectroscopic ellipsometry and details of laboratory setups are described in Chapter 1. Chapter 2 gives an overview of the physics of the quasi one-dimensional copper oxides and a literature survey of optical spectroscopy experiments published to date. The results of our spectroscopic ellipsometry studies for $LiCuVO_4$, $NaCu_2O_2$, Li_2CuO_2, $CuGeO_3$ and α-CuV_2O_6 compounds are presented in Chapter 3. The discussion of $LiCuVO_4$, $NaCu_2O_2$ and Li_2CuO_2 is supplemented by results of theoretical calculations consistent with the details of measured optical spectra. A summary of this Chapter is given in section 3.6. The study of the charge dynamics in Ni-based heterostructures is reported in Chapter 4. This contains an overview of the charge dynamics and magnetic properties of the perovskite nickel oxides and a comprehensive optical study of $LaNiO_3$-based superlattices in a wide spectral range, followed by a summary of their magnetic properties studied by low-energy muon spin rotation.

1 Spectroscopic Ellipsometry

1.1 Basic ideas

Ellipsometry goes back to the 19th century, when Paul Drude derived the mathematical formalism of ellipsometry and performed the first experiments to study the optical properties of layered films by using polarized light in 1889 (1, 2). From this point, an ellipsometry techniques have been extensively developed. Nowadays, the spectral range used in ellipsometry covers the spectrum from ultraviolet to far-infrared, giving an opportunity to study lattice vibrations, free-carrier contributions and electronic properties of solids. The non-intrusive nature of the light-matter interaction, a variety of light sources extended to synchrotron radiation and the sensitivity to sub-nm thick layers establish spectroscopic ellipsometry as a powerful method for the determination of the optical properties of bulk solids and thin-film characterization.

The basic ellipsometric scheme is sketched in Figure 1.1. The incident light is linearly polarized, with equally large p- (parallel to the plane of incidence) and s- (perpendicular to the plane of incidence) components of the electric field, wave vector $\mathbf{k}_i$ and frequency ω_i. Light reflecting from the sample at angle ϕ is elliptically polarized, with wave vector $\mathbf{k}_r = -\mathbf{k}_i$ and frequency $\omega_r = \omega_i$. The p- and s- components of the incoming light experience reflection coefficients r_p and r_s, respectively:

$$\mathbf{E}_r = \begin{pmatrix} E_{rp} \\ E_{rs} \end{pmatrix} = \begin{pmatrix} r_{pp} & r_{ps} \\ r_{sp} & r_{ss} \end{pmatrix} \begin{pmatrix} E_{ip} \\ E_{is} \end{pmatrix}. \tag{1.1}$$

The Fresnel equations give the complex reflection coefficients $r_{pp} = \frac{E_{rp}}{E_{ip}}$, $r_{ps} = \frac{E_{rp}}{E_{is}}$, $r_{sp} = \frac{E_{rs}}{E_{ip}}$, $r_{ss} = \frac{E_{rs}}{E_{is}}$. The ratios $\frac{r_{pp}}{r_{ss}}$, $\frac{r_{ps}}{r_{pp}}$, $\frac{r_{sp}}{r_{ss}}$ define new complex quantities:

$$\rho_{pp} = \frac{r_{pp}}{r_{ss}} = \tan\Psi_{pp} \cdot e^{i\Delta_{pp}}, \tag{1.2}$$

$$\rho_{ps} = \frac{r_{ps}}{r_{pp}} = \tan\Psi_{ps} \cdot e^{i\Delta_{ps}}, \tag{1.3}$$

$$\rho_{sp} = \frac{r_{sp}}{r_{ss}} = \tan\Psi_{sp} \cdot e^{i\Delta_{sp}} \tag{1.4}$$

In the simple case of isotropic media ($r_{ps} = 0$, $r_{sp} = 0$), the light reflection is described by only two quantities. They describe the changes in polarization and introduce the two ellipsometric angles $\Psi = \Psi_{pp}$ and $\Delta = \Delta_{pp}$, defining the relative amplitude change and phase shift between two components, respectively. The ellipsometric angles are sensitive to the angle of incidence ϕ. Ψ varies from 0° to

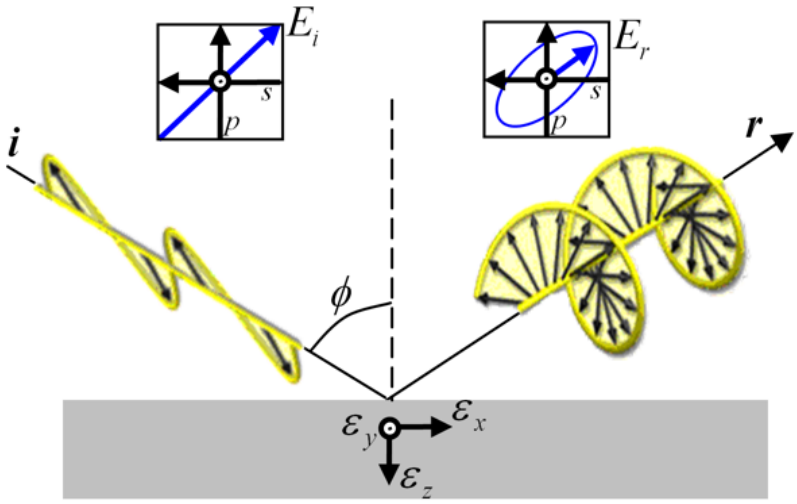

Figure 1.1: The basic geometry. Linear polarized incident light with two electrical field components E_{is} and E_{ip} is reflected by sample at angle ϕ. The polarization of the reflected light is elliptical.

45° and reaches a minimum at Brewster's angle (the angle of minimum intensity of p-polarized light). The phase shift Δ varies from $-90°$ to 90° (or from 0° to 180°) in the vicinity of Brewster's angle.

Both Ψ and Δ are directly related to the complex dielectric function of the sample under investigation $\varepsilon = \varepsilon_1 + \mathrm{i}\varepsilon_2$ and entirely determine it for a given frequency ω (3, 4):

$$\varepsilon(\omega) = \sin^2\phi + \sin^2\phi \tan^2\phi \left(\frac{1 + \tan\Psi(\omega) \cdot e^{\mathrm{i}\Delta(\omega)}}{1 - \tan\Psi(\omega) \cdot e^{\mathrm{i}\Delta(\omega)}} \right)^2 . \tag{1.5}$$

The optical conductivity $\sigma(\omega)$ is related to the complex dielectric function as $\sigma(\omega) = \frac{i\omega}{4\pi}(1 - \varepsilon(\omega))$, and the complex refractive index is $N(\omega) = n(\omega) + \mathrm{i}k(\omega) = \sqrt{\varepsilon(\omega)}$.

In contrast to regular reflection spectroscopy, where measurements are performed at normal incidence acquiring a single quantity, $R(\omega)$, ellipsometry works at oblique angles of incidence, measures the two components (Ψ, Δ), and requires neither reference measurements nor Kramers-Kronig transformations. The measurements are precise and quite sensitive to surface the conditions. This makes ellipsometry an indispensable tool to study ultra-thin films.

1.2 Ellipsometry instruments

The measurements presented in this thesis were performed mainly using the commercial ellipsometer VASE® J.A. Woollam Co. (spectral range 0.75 – 6.5 eV) and a home-built ellipsometer with Fourier-transform infrared spectrometer implemented at the ANKA synchrotron IR1-beamline, Forshungszentrum Karlsruhe (frequency range 100 – 650 cm^{-1}).

1.2.1 Experimental setup in MPI-FKF Stuttgart.

1.2.1.1 Spectrometer

The measurements in the spectral range from 0.75 to 6.5 eV were carried out on the basis of a commercial rotating analyser ellipsometer VASE® J.A. Woollam Co. The main components are:

1. A Xe arc lamp with a broad spectrum (0.62 - 6.53 eV) is used as a light source.

2. A monochromator, ensures that monochromatic light is incident on the sample. To avoid detector overload by high-intensity reflected light, the monochromator slit width is automatically adjustable during the data acquisition procedure.

3. Transmitted by a standard optical fiber, the light comes to a calcite Glan-Taylor polarizer mounted on a high-accuracy stepper-motor-driven rotational stage. The polarizer angle can be varied from measurement to measurement, but is fixed during the data acquisition procedure.

4. An auto-retarder (MgF_2 Berek waveplate) is placed behind the fixed polarizer and can be used to increase the accuracy of the measured data. Because of the optical anisotropy in the retarder, it changes the phase of an incident wave, delaying one of the two orthogonal light constituents.

5. Reflected by the sample, light passes through an analyzer system, continuously rotating with frequency f and coupled to the detector (Silicon arrays (185 - 1100 nm), InGaAs (1100 - 1700 nm)). The intensity of the detected signal is a sinusoidal function of time: $I(t) = \mathrm{DC} + a \cdot \cos(2ft) + b \cdot \sin(2ft)$. For a particular polarizer angle P, the ratios $\frac{a}{\mathrm{DC}}$ and $\frac{b}{\mathrm{DC}}$ can be expressed in terms of the ellipsometric angles Ψ and Δ:

$$\frac{a}{\mathrm{DC}} = \frac{\tan^2\Psi - \tan^2 P}{\tan^2\Psi + \tan^2 P}, \tag{1.6}$$

$$\frac{b}{\mathrm{DC}} = \frac{2\tan\Psi\cos\Delta\tan P}{\tan^2\Psi + \tan^2 P}. \tag{1.7}$$

All components are fully computer-controlled by the WVASE32 (J. A. Woollam) data acquisition software program (5). Variable angles of incidence are used for the measurements. For this, goniometers are precisely translated to a desirable angle with an accuracy within 0.010°.

1.2.1.2 Cryostat

The measurements in the temperature range from 5 to 350 K were performed using a liquid-He flow CryoVac KONTI cryostat with replaceable sample compartments. Two compartments were designed for measurements at 70° (Figure 1.2 a) and 65°, 68.5°, 72.5°, 75°, 79° (Figure 1.2 b) angles of incidence. The windows of the cryostat are made of high purity optical isotropic synthetic fused silica materials, SUPRASIL

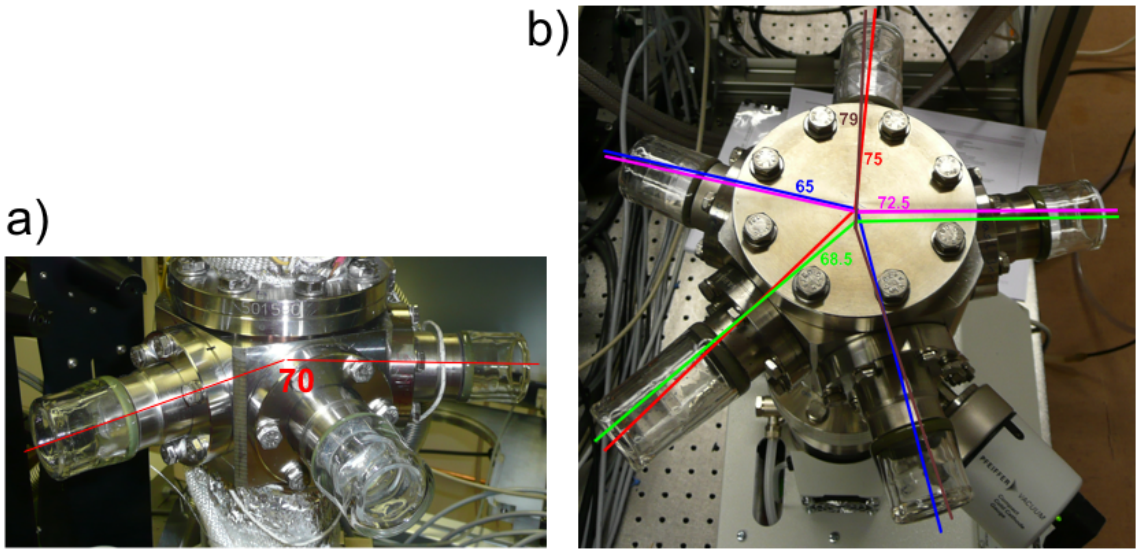

Figure 1.2: Replaceable sample compartments for KONTI cryostat CryoVac. a) Three-window compartment for measurements at 70° angle of incidence. b) Five-window compartment for measurements at 65°, 68.5°, 72.5°, 75°, 79° angles of incidence.

311, highly transparent within the spectral range from 0.5 to 7.5 eV. The SUPRASIL windows, free of bubbles and inclusions, with high degree of index homogeneity, do not affect the polarization state of incident and reflected light. A constant flow of nitrogen gas was used to blow the windows from outside to prevent water condensation.

The condition of the sample surface plays an important role and may influence the measured ellipsometric spectra. The standard procedure of sample preparation includes cleaving a bulk sample along one of the principal crystallographic axes or surface polishing to optical grade using a kit of abrasive diamond suspensions with grain-size number from 15 μm down to 0.25 μm. The diamond grains and propylene glycol of the used suspension are removed by double washing of the sample in alcohol. Then the cleaned samples are dried with pure N_2 or Ar gas. For ellipsometric measurements, the sample with a freshly prepared clean optical surface is accurately glued to the pointed tip of a copper stick by a drop of Fluka Leit-Silver 09937. The sample is placed on the sample holder of the cryostat, as shown in Figure 1.3.

In the case when the sample is sensitive to ambient conditions, the cleaving (polishing) and mounting procedures should be performed in argon atmosphere to prevent sample oxidation. The following transportation of the cleaved and mounted sample into the cryostat is carried out in an argon-flooded glove bag.

The cryostat is evacuated and baked out, until the pressure is below $< 8 \cdot 10^{-9}$ mbar, to prevent the growth of an ice layer on the sample surface at low temperatures.

Prior to the measurements, the sample surface should be placed perpendicularly to the probe beam. For this, the orientation of the cold finger of the cryostat is

Figure 1.3: The sample holder of the cryostat for ellipsometry measurements. The sample (1) and the piece of Si wafer (2) are placed in immediate proximity to the Si-diode temperature sensor (3).

adjusted on a rotational stage which also allows orthogonal translational movements. In addition, the cryostat is installed onto the sample stage by an adjustable three-points bearing. Thus, the alignment of the sample is implemented without vacuum violation.

1.2.1.3 Calibration

A calibration procedure is used to determine the exact positions of the polarizer, analyzer and auto-retarder axes relative to the sample plane of incidence. It also takes into account the AC/DC attenuation and window strain birefringence.

As a calibration sample, a silicon wafer with a thermally grown SiO_2 oxide is used, see Figure 1.3 position 2. During the calibration procedure, the Fourier coefficients of the rotating analyzer signal are measured at several wavelengths. Then the measured data are fitted to a model to determine the windows effect, polarizer and analyzer offsets and the attenuation ratio (Figure 1.4). The model incorporates the Si substrate and the SiO_2 layer with known optical constants. The calibration information is stored in the *hardware.cnf* configuration file. The procedure must be performed each time before acquiring ellipsometric data.

1.2.1.4 Temperature control and dynamic scans

In order to control the temperature in the range from 4.2 K to 350 K, the cryostat is equipped with a resistive temperature sensor, coupled to the heat-exchanger near the cold finger, and a heater. An additional Si-diode temperature sensor is placed in

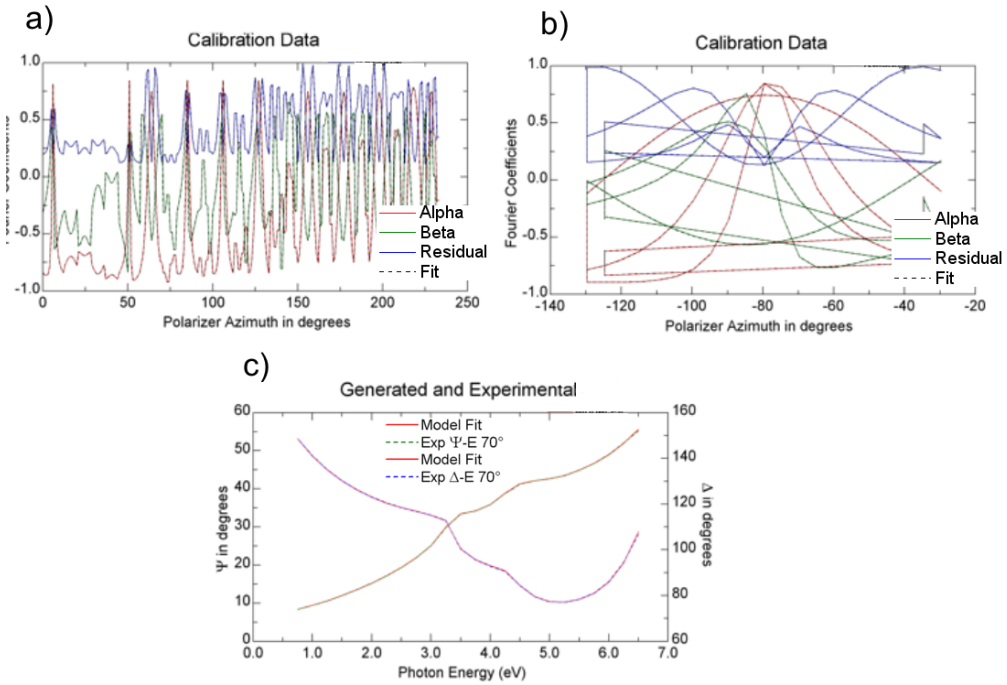

Figure 1.4: An example of calibration data returned after the calibration procedure for windows effect (a), polarizer azimuth angles (b) and measured ellipsometric angles Ψ and Δ for the Si wafer and a model fit (c).

immediate proximity to the sample (Figure 1.3 position 3). When the temperature is stabilized, the difference between the two sensors does not exceed 3 K. The heat exchanger is controlled by the temperature controller CryoVac TIC 304-MA.

He-gas flow through the KONTI cryostat is regulated manually by coarse and fine valves, or by a magnetic proportional valve controlled with TIC 304-MA.

TIC 304-MA is connected to a PC. Full control of the heat exchanger and magnetic valve is carried out by LabVIEW scripts, allowing controlled dynamic temperature measurements. The temperature changes are recorded simultaneously with the time-dependent ellipsometric data. Matching two data arrays, one can obtain temperature-dependent ellipsometric data at any particular energy.

To control the sample position *in-situ*, a small demountable camera was installed onto the middle window of the cryostat.

1.2.2 Transmission measurements

To study the weak absorption of insulating samples below the fundamental absorption edge, the ellipsometric measurements can be complemented by polarized transmission spectroscopy.

Figure 1.5 shows a sample holder for transmission measurements. Two identical apertures for the sample (position 1) and baseline (position 2) measurements are placed above each other. For transmission measurements, the sample compartment with windows placed at 180° is used.

The measurements are performed with the light of p-, s- and/or user-defined-polarization. The polarizer is automatically moved from 0° to 90° during the measurements. The monohromator slit width is adjustable to provide optimal intensity of incident light.

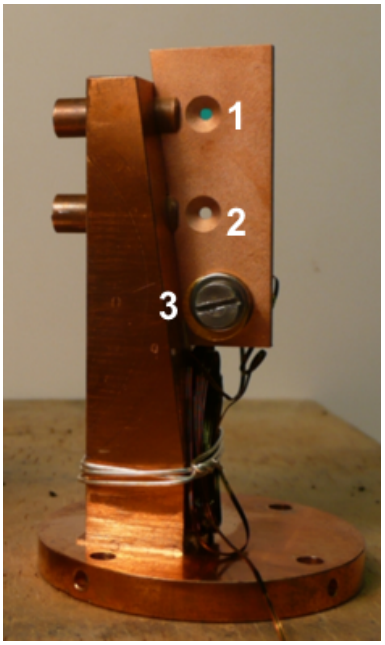

Figure 1.5: The sample holder for transmission measurements. A transparent sample is glued to cover up the aperture (1). Another aperture (2) is kept opened for the baseline measurements. A diode temperature sensor (3) is placed on the same sample holder.

Transmittance is determined as the ratio between light transmitted through the sample and baseline light intensity

$$T(\omega) = \frac{I_{trans}(\omega)}{I_{base}(\omega)}. \tag{1.8}$$

For the baseline measurements, the sample is replaced by the open aperture (Figure 1.5 position 2). Because of possible light source intensity drift, the baseline scans should be performed in close succession to the data scans.

When the sample thickness d is known, the absorption coefficient can be calculated using the relation

$$\mu(\omega) = \frac{1}{d}\ \ln\frac{[1-R(\omega)]^2}{T(\omega)}, \tag{1.9}$$

where the normal incidence reflectance $R(\omega)$ is given by (6):

$$R(\omega) = \frac{[n(\omega)-1]^2 + k(\omega)^2}{[n(\omega)+1]^2 + k(\omega)^2}. \tag{1.10}$$

Below the fundamental absorption edge, the extinction coefficient $k(\omega)$ is close to zero, whereas the index of refraction is frequency independent $[n(\omega) = n_0]$ and can be extrapolated from high-energy ellipsometric data.

The imaginary part of the dielectric function is related to the absorption coefficient $\mu(\omega)$ as (6)

$$\varepsilon_2(\omega) = \mu(\omega) n_0 \lambda / 2\pi, \tag{1.11}$$

where λ is the wavelength of the radiation in vacuum.

1.2.3 Experimental setup at FZK. Ellipsometry with synchrotron radiation

The measurements in spectral range 100 – 650 cm^{-1} were carried out at the ANKA synchrotron IR1-beamline, Forshungszentrum Karlsruhe.

Since conventional infrared light sources (mercury arc lamps or glow bars) provide very low intensity in the far-infrared range, synchrotron radiation, with brilliance of the collimated beam 100-1000 times higher, is used. A spectral ellipsometer for the far-infrared to mid-infrared range has been developed and installed, at first, at the National Synchrotron Light source at Brookhaven National Laboratory, USA (7, 8). More recently, an improved ellipsometer has been installed at the infrared beamline of the synchrotron light source ANKA at the Forschungszentrum Karlsruhe, Germany, since the edge radiation source of the ANKA synchrotron is well suited for ellipsometric measurements (9).

The setup employs the Fourier-transform infrared spectrometer Bruker IFS-66v. The basis of Fourier transform spectroscopy is an interferometer with two arms, one of which is periodically moving (Michelson interferometer), see Figure 1.6. The measured time-averaged intensity for wavelength λ depends on a movable mirror position, since constructive interference occurs only for positions $2\Delta x = n\lambda = n/\nu, n = 1, 2...$, where $2\Delta x$ (in cm) is the retardation between two light passes, ν (in cm^{-1}) is the wavenumber.

For a continuous source, the resulting intensity distribution reads

$$I'(\Delta x) = \int_{-\infty}^{\infty} I(\nu) \cos(2\pi \Delta x \nu) d\nu. \tag{1.12}$$

Then, the wavenumber-dependent spectrum $I(\nu)$ is a Fourier transform of $I(\Delta x)$:

$$I(\nu) = 2 \int_{0}^{\infty} I'(\Delta x)(1 + \cos(2\pi \Delta x \nu)) d\Delta x. \tag{1.13}$$

The integral 1.13 is limited by a finite mirror shift Δx_{max}, determining the maximal spectral resolution $\Delta\omega = 1/\Delta x_{max}$. The turning points of the movable mirror lead to artifacts in the spectrum, known as the apodization problem. The correction of the spectrum may be done through multiplication of the interferogram by an appropriate adoptisation function: Happ-Genzel, Black-Harris, Norton-Beer *etc.* The position of the movable mirror is accurately measured by a He-Ne laser beam that

passes the interferometer. An important element of the Fourier transform spectrometer is a beamsplitter. The broad band (30 – 750 cm^{-1}) far-infrared beamsplitter T222 made by Bruker is used.

By introducing several mirrors, the Bruker spectrometer is attached to the home-built ellipsometer, see Figure 1.7. The light beam, extracted from the beam-port of the IR-beamline (LS), passes through the spectrometer (FTS) to the grid-type polarizer (P). The second polarizer, which serves as an analyzer (A), is placed behind the sample (S). Both polarizers are mounted onto software-controlled rotational stages to maintain an accuracy of rotation within 0.1°. The synchrotron radiation is partially polarized. This affects the choice of the polarizer angle.

For temperature measurements, the sample is mounted on the cold finger of the He-flow CryoVac Elli cryostat. The cryostat windows are made of 3μm-thick mylar. Pumping of the cryostat is necessary to reach the pressure $\backsim 2 \cdot 10^{-6}$ mbar. Cold

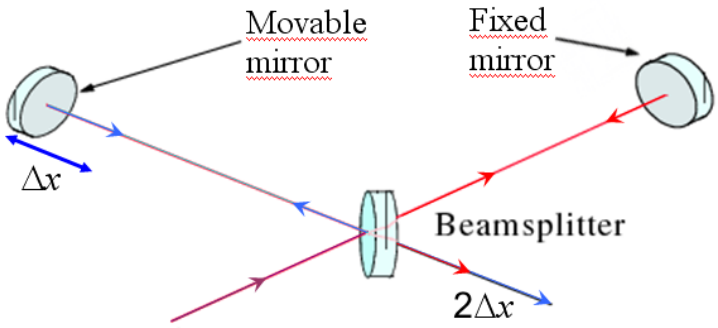

Figure 1.6: The sketch of a Michelson interferometer.

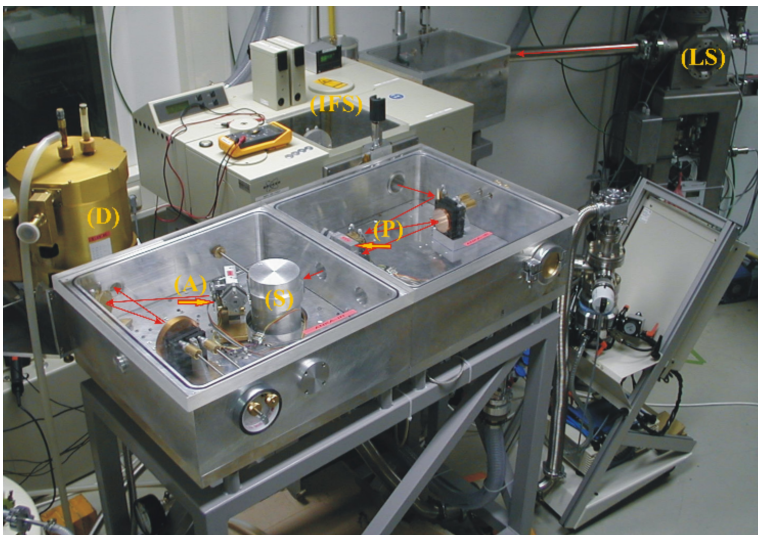

Figure 1.7: The overview of experimental setup at the ANKA synchrotron. LS - light source, FTS - Bruker spectrometer, P - polarizer, S - sample installed into cryostat, A - analyser, D - bolometer.

traps are introduced to capture the rest gas escaping from the cold finger, resulting in a vacuum around the sample of the order of 10^{-8} mbar, to avoid ice layer formation on the sample surface. The temperature control is carried out by unit TIC 304-MA.

The angle of incidence can be chosen in the range from 65° to 90°. The alignment procedure of both spectrometer and ellipsometer is performed using the visible component of synchrotron radiation. The detector (D) is a Si bolometer from Infrared Laboratories Inc. working at 1.8 K.

A detailed description of the ellipsometer setup at the IR1-beamline at the ANKA synchrotron light source can be found in Ref. (9).

After the sample is set to any of the available angles of incidence, test measurements are performed with and without cryostat lids in order to ensure that the cryostat windows do not affect the polarization state of light. To determine the exact zero positions of the polarizers, we follow the calibration procedure measuring spectra at several angles of the polarizer. The resulting spectra should not depend on the polarizer angle. Then, mathematical problem of function minimization is solved by computer program, resulting in corrections of zero positions of the polarizer and analyzer.

1.3 Generalized ellipsometry. *Ex-situ* data analysis

Spectroscopic ellipsometry is a powerful tool in measuring the optical properties of bulk samples and in characterization of thin film systems. However, the measured data are directly physically significant only in the case of bulk isotropic samples. Our study was focused on the compounds with strong bi-axial anisotropy and multilayers deposited onto substrates. The particular components of the dielectric tensor in this case can be determined *ex-situ* by modeling the near-surface region of the sample and then fitting the measured data to a model function using the desired parameters as variables.

1.3.1 Anisotropy correction

For anisotropic materials, the ellipsometric angles (Ψ, Δ) depend on the diagonal terms (the principal-axis dielectric functions ε_{xx}, ε_{yy} and ε_{zz}) of the dielectric tensor $\hat{\varepsilon}$, the orientation of the crystal's principal axes with respect to the plane of incidence and the polarization state of the incident light.

In the most general description, the dielectric tensor $\hat{\varepsilon}$ is a complex-valued second rank tensor:

$$\hat{\varepsilon} = \begin{pmatrix} \varepsilon_{xx} & \varepsilon_{xy} & \varepsilon_{xz} \\ \varepsilon_{yx} & \varepsilon_{yy} & \varepsilon_{yz} \\ \varepsilon_{zx} & \varepsilon_{zy} & \varepsilon_{zz} \end{pmatrix}. \tag{1.14}$$

For orthorhombic, tetragonal, hexagonal, and trigonal crystal systems, the off-diagonal elements of the dielectric tensor are zero. For the simplest case of an isotropic medium, the diagonal terms of the dielectric tensor ε_{xx}, ε_{yy} and ε_{zz} are

equal, and an analytic relation between the dielectric function and the ellipsometric parameters Ψ and Δ has the form:

$$\varepsilon_{xx} = \varepsilon_{yy} = \varepsilon_{zz} = \sin^2\phi \left(1 + \frac{\tan^2\phi(\cos^2 2\Psi - \sin^2 2\Psi \sin\Delta)}{(1 + \sin 2\Psi \cos\Delta)^2}\right). \tag{1.15}$$

For anisotropic (biaxial) materials, the diagonal terms are different $\varepsilon_{xx} \neq \varepsilon_{yy} \neq \varepsilon_{zz}$, and the relation 1.15 gives the pseudo-dielectric functions. To derive the principal components of the dielectric tensor from measured data, a numerical regression procedure, called anisotropy correction (4), needs to be applied.

The complex refractive indices are given by the formulae:

$$r_{pi} = \frac{\sqrt{\varepsilon_k \varepsilon_i}\cos\phi \; - \sqrt{\varepsilon_k - \sin^2\phi}}{\sqrt{\varepsilon_k \varepsilon_i}\cos\phi \; + \sqrt{\varepsilon_k - \sin^2\phi}}, \tag{1.16}$$

$$r_{si} = \frac{\cos\phi \; - \sqrt{\varepsilon_j - \sin^2\phi}}{\cos\phi \; + \sqrt{\varepsilon_j - \sin^2\phi}}, \tag{1.17}$$

where *i, j, k* index the *a,b,c* axes of a crystal.

The *ex-situ* data processing software WVASE32 gives the numerical solution of system of equations (1.16-17) by modeling the anisotropic material with a set of optical constants. The strategy is as follows.

The sample coordinate system relative to the ellipsometer coordinate system is described by the Euler angles (Figure 1.8). Three successive rotations by angles (α, β, γ) transform the basis axes *x, y, z* to a new system *X, Y, Z*. Ellipsometric data are measured for orientations (0°,0°,0°), (90°,0°,0°) and (90°,90°,0°), which corresponds to the orientations of the sample with its *a, b* and *c* axes in the plane of incidence,

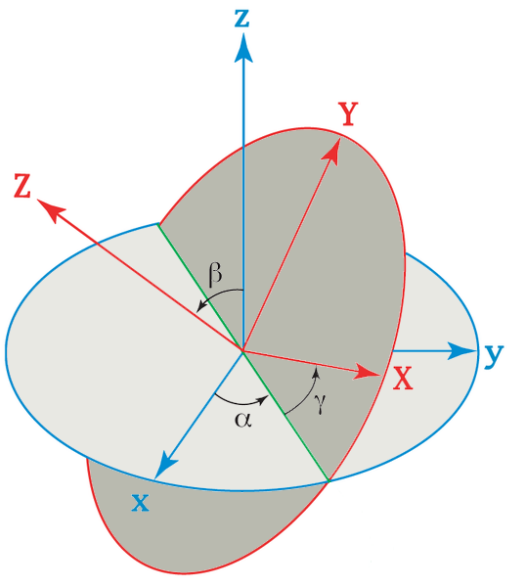

Figure 1.8: The Euler angles. The rotation of basis coordinate axes *x, y, z* by angles α, β, γ results in a new coordinate system *X, Y, Z*.

respectively. The pseudodielectric functions of all three optical axes are obtained from ellispometric data, measured for different orientations of the sample. Each of three data sets is uploaded to the WVASE32 environment into separate tabs.

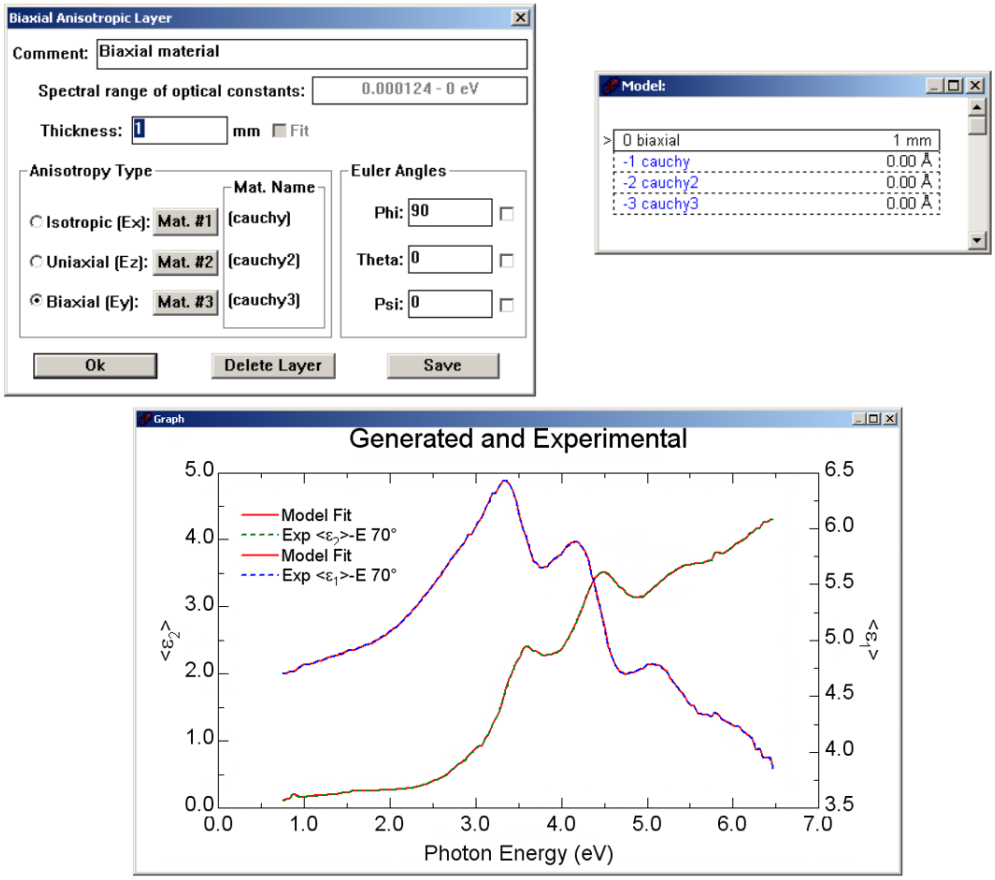

Figure 1.9: The constructed anisotropic model, parameters of the model, one of the loaded experimental data files and a model fit.

The basis of constructed model is the BIAXIAL material file, available in the WVASE32 library (5). The BIAXIAL material allows the user to specify material files representing the optical response along the principal optical axes, see Figure 1.9 upper-left panel. As material files, the dummy CAUCHY layers of zero thickness were used, for which the complex refraction index is represented by a slowly varying function of wavelength and exponential absorption tail:

$$N = A + \frac{B}{\lambda^2} + \frac{C}{\lambda^4} + i \cdot \alpha e^{\beta(\frac{1}{\lambda} - \frac{1}{\gamma})}, \tag{1.18}$$

where the A, B, C, α, β, γ parameters are variable.

The constructed model, shown in the upper-right panel in Figure 1.9, is repeated for every uploaded data set. Within every model in the dialog box of the BIAXIAL material, the orientation of the sample with respect to the plane of incidence is set by Euler angles. The resulting from the fit sets of optical constants - the dielectric functions ε_{xx}, ε_{yy} and ε_{zz} of anisotropic medium - are optical constants of

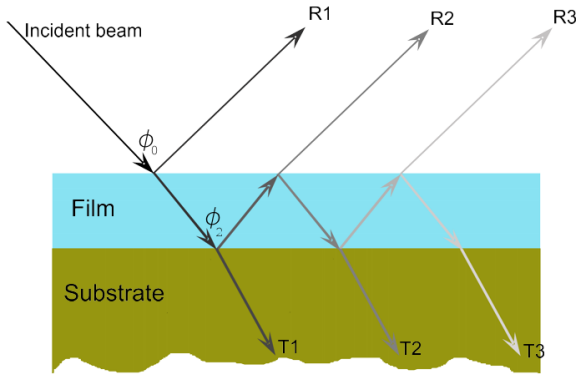

Figure 1.10: The sketch of a thin film on an optically thick substrate. The multiple reflected and transmitted beams are shown. Because of beam splitting, the reflected and transmitted beams die out.

CAUCHY layers. In the lower panel of Figure 1.9 the loaded experimental data for one orientation of the sample and the fit results to the model are presented.

1.3.2 Thin film characterization

The complex dielectric function of a thin layer deposited on a substrate can be also derived by numerical regression procedures.

Multiple reflections of the incident beam occur in a thin film on the boundary with an optically thick substrate, as shown in Figure 1.10. Therefore, measured ellipsometric data include information about the substrate, which has to be subtracted. By summing up all reflected beam components for the p- and s- polarized light, one can obtain the diagonal reflection coefficients for the ambient-film-substrate system:

$$\check{R}_p = \frac{r_{01p} - r_{12p}e^{-i\cdot 2\beta_p}}{1 + r_{01p}r_{12p}e^{-i\cdot 2\beta_p}}, \tag{1.19}$$

$$\check{R}_s = \frac{r_{01s} - r_{12s}e^{-i\cdot 2\beta_s}}{1 + r_{01s}r_{12s}e^{-i\cdot 2\beta_s}}. \tag{1.20}$$

Here, r_{01p}, r_{01s}, r_{12p} and r_{12s} denote the complex Fresnel reflection coefficients for the p- and s- polarized light at the ambient-film (01) and film-substrate (12) interfaces. For the case of an isotropic film on an isotropic substrate in an isotropic ambient (vacuum), the reflection coefficients can be obtained as follows:

$$r_{01p} = \frac{N_1^2\cos\phi_0 - (N_1^2 - \sin^2\phi_0)^{\frac{1}{2}}}{N_1^2\cos\phi_0 + (N_1^2 - \sin^2\phi_0)^{\frac{1}{2}}}, \tag{1.21}$$

$$r_{01s} = \frac{\cos\phi_0 - (N_1^2 - \sin^2\phi_0)^{\frac{1}{2}}}{\cos\phi_0 + (N_1^2 - \sin^2\phi_0)^{\frac{1}{2}}}, \tag{1.22}$$

$$r_{12p} = \frac{-N_1^2\cos\phi_2 + N_2(N_1^2 - N_2^2\sin^2\phi_2)^{\frac{1}{2}}}{N_1^2\cos\phi_2 + N_2(N_1^2 - N_2^2\sin^2\phi_2)^{\frac{1}{2}}}, \tag{1.23}$$

$$r_{12s} = \frac{-N_2 \cos\phi_2 + (N_1^2 - N_2^2 \sin^2\phi_2)^{\frac{1}{2}}}{N_2 \cos\phi_2 + (N_1^2 - N_2^2 \sin^2\phi_2)^{\frac{1}{2}}}, \tag{1.24}$$

where N_1 and N_2 are complex refractive indices of the film and substrate, ϕ_0 is the angle of incidence in the ambient and ϕ_2 is the angle of refraction at the film-substrate interface. Both angles are interrelated by Snell's law

$$\sin\phi_0 = N_2 \sin\phi_2. \tag{1.25}$$

The phase or optical thickness of the film β is given by

$$\beta = 2\pi \frac{d}{\lambda} (N_1^2 - \sin^2\phi_0)^{\frac{1}{2}}, \tag{1.26}$$

where d is a film thickness and λ is a wavelength of incident light.

The ellipsometric angles Ψ and Δ for the thin film at a given angle of incidence may be calculated, then, as

$$\check{\rho} = \tan\Psi e^{i\cdot\Delta} \equiv \frac{\check{R}_p}{\check{R}_s}. \tag{1.27}$$

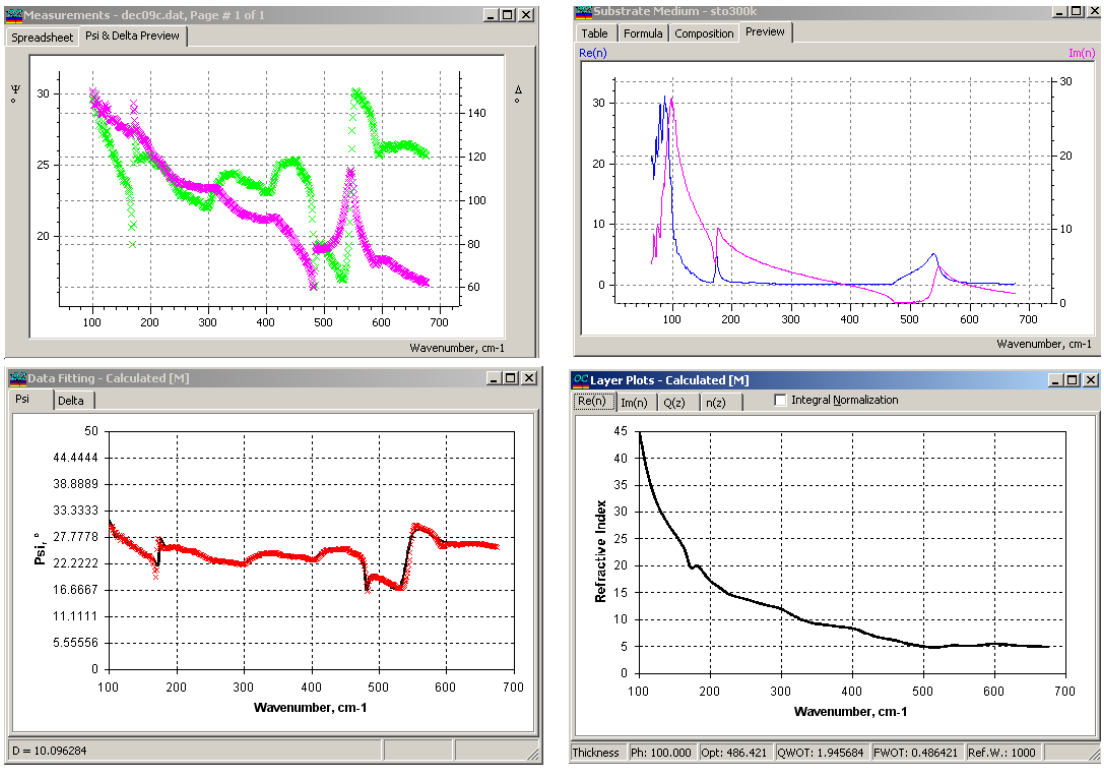

Figure 1.11: The measured Ψ and Δ angles of superlattices (upper-left panel) and refractive and extinction coefficients of a bare substrate (upper-right panel) obtained with high accuracy from Ψ and Δ angles from independent spectroscopic ellipsometry measurements. The fitting window with experimental data and model fit for Ψ (lower-left panel) and layer report with displayed refractive coefficient returned after fitting (lower-right panel).

Solution of the equations (1.21-24) is realized in the computer program *OptiChar* for the characterization of thin films and superlattices based on advanced optimization methods providing rapid convergence of the regression procedure.

For the analysis, the complex refractive indices for the substrates were obtained with high accuracy from the Ψ and Δ angles from independent spectroscopic ellipsometry measurements at different temperatures and used in the characterization procedure. The physical thickness of every superlattice is determined from X-ray diffraction measurements and hold constant in the analysis.

In Figure 1.11, as an exemplary data processing for studying the charge dynamics of $LaNiO_3$-based superlattices, the ellipsometry data obtained at the infrared beamline IR-1 at the ANKA synchrotron at frequencies ν = 10-100 meV are used. The measured Ψ and Δ angles of superlattices are loaded together with refractive and extinction coefficients of the bare substrate (Figure 1.11, upper left and right panels, respectively). The fitting window with experimental data and model fit for Ψ is shown on the left-bottom panel. The results of the fit are returned as real and imaginary parts of the complex refractive index of the overlayer (right-bottom panel).

1.3.3 Dispersion analysis: Kramers-Kronig relation. Sum rule. Drude-Lorentz model

The interaction of electromagnetic radiation with a solid is characterized by the complex dielectric function $\varepsilon = \varepsilon_1 + i\varepsilon_2$. The real and imaginary parts of ε are connected through the Kramers-Kronig relation:

$$\varepsilon_1 = \varepsilon_0 + \frac{1}{\pi} P \int_{-\infty}^{\infty} \frac{\varepsilon_2(\omega')}{\omega' - \omega} \mathrm{d}\omega', \tag{1.28}$$

$$\varepsilon_2 = -\frac{1}{\pi} P \int_{-\infty}^{\infty} \frac{\varepsilon_1(\omega') - \varepsilon_0}{\omega' - \omega} \mathrm{d}\omega', \tag{1.29}$$

where P is a principal part of the integral. Since ε_1 is an even function of ω, and ε_2 is an odd function of ω, that is $\varepsilon(-\omega) = \varepsilon(-\omega) + i \cdot \sigma(-\omega)/(-\omega) = \varepsilon_1(\omega) - i \cdot \varepsilon_2(\omega) = \varepsilon^*(\omega)$, the integrals can be transformed to the domain (0,∞):

$$\varepsilon_1 = \varepsilon_0 + \frac{2}{\pi} P \int_{0}^{\infty} \frac{\omega' \varepsilon_2(\omega')}{\omega'^2 - \omega^2} \mathrm{d}\omega', \tag{1.30}$$

$$\varepsilon_2 = -\frac{2\omega}{\pi} P \int_{0}^{\infty} \frac{\varepsilon_1(\omega') - \varepsilon_0}{\omega'^2 - \omega^2} \mathrm{d}\omega'. \tag{1.31}$$

The expressions 1.30-31 can be written in terms of the real and imaginary parts of the optical conductivity $\sigma(\omega)$.

The general sum-rule expression, proven by Kubo (10) for any system of charged particles reads as

$$\frac{2}{\pi} \int_{0}^{\infty} \mathrm{Re}\sigma(\omega) \mathrm{d}\omega = \sum \frac{n_r e_r^2}{m_r}, \tag{1.32}$$

where r specifies the type of charged particles, n_r, m_r and e_r are the respective densities, masses and charges.

For the electron system, the expression (1.32) can be written in the form based on the Drude model, when

$$\sigma(\omega) = \frac{1}{4\pi} \frac{\omega_p^2}{\gamma - i\omega}, \tag{1.33}$$

$$\int_0^\infty \mathrm{Re}\sigma(\omega)\mathrm{d}\omega = \frac{\omega_p^2}{8}, \tag{1.34}$$

where N is the density of electrons and $\omega_p^2 = \frac{4\pi N e^2}{m}$ is the frequency of collective oscillations of electrons, known as the plasma frequency.

For cases where various types of electronic excitations are well separated in frequency, a partial sum rule can be used for determination of the effective number of carriers per formula unit volume V:

$$N_{eff}(\omega) = \frac{2mV}{\pi e^2} \int_0^{\omega_c} \mathrm{Re}\sigma(\omega)\mathrm{d}\omega. \tag{1.35}$$

The simplest model describing the behavior of the complex dielectric function is the Drude-Lorentz model. It is assumed that an electron in a dielectric medium is bound to the nucleus as a harmonic oscillator. The equation of the electron movement is:

$$m\frac{\mathrm{d}^2 u}{\mathrm{d}t^2} - m\gamma\frac{\mathrm{d}u}{\mathrm{d}t} + m\omega_0 u = -eE_0 e^{i\cdot\omega t}, \tag{1.36}$$

where u is the electron's displacement, γ is a damping parameter and ω_0 is the eigenfrequency of oscillation. By solving this equation, we derive:

$$u = -\frac{eE_0}{m} \frac{e^{i\cdot\omega t}}{\omega_0^2 - \omega^2 - i\cdot\omega\gamma}. \tag{1.37}$$

In the case of multiple oscillators at frequencies ω_j and with dampings γ_j, the dielectric function is given by:

$$\varepsilon(\omega) = \varepsilon_0 + \sum_j \frac{\omega_{p,j}^2}{\omega_j^2 - \omega^2 - i\cdot\omega\gamma_j}, \tag{1.38}$$

where ε_0 is the value of the dielectric function at $\omega \to \infty$.

The frequency dependence of the complex dielectric function is shown on Figure 1.12. The variable ε_2 has a Lorentzian shape with a peak at ω_0; the halfwidth is determined by γ.

The Drude function (the dielectric function for free carriers) is obtained from the Equation 1.37 when $\omega_0 \to 0$:

$$\varepsilon(\omega) = -\frac{\omega_p^2}{\omega^2 + i\cdot\omega\gamma}. \tag{1.39}$$

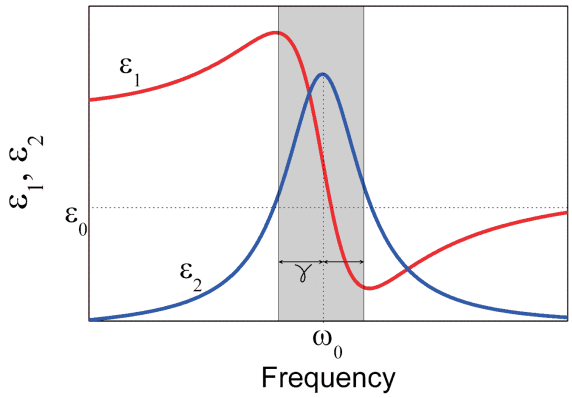

Figure 1.12: The single Lorentz oscillator: the dependence of ε_1 and ε_2 on frequency ω. The halfwidth is determined by γ.

The real part of the dielectric function ε_1 for the free-electron case is negative, because the electrons move in antiphase with electromagnetic field.

The Drude-Lorentz theory is in agreement with experimental observations. Listed formulas for fitting of raw experimental data satisfy the Kramer-Krönig relation. As in ellipsometry experiment one obtains both real and imaginary parts of the dielectric function, both spectra are loaded for fitting, and the dispersion analysis is performed by simultaneous fit of both.

2 Edge-Sharing CuO Chain Compounds

2.1 Introduction

Transition-metal oxides, and cuprates in particular, exhibit a rich variety of spin, charge and orbital phenomena within the d-shells of the transition-metal ions. In these compounds, the Coulomb interaction between d-electrons, often referred to as the correlation effect, is important and causes metal-insulator transitions (11), colossal magnetoresistance (12, 13), charge, spin and orbital ordering (14) *etc.* Among other transition-metal oxides, cuprates have been most extensively studied since the discovery of unconventional high-temperature (high-T_c) superconductivity in 1986 (15).

The formal electron configuration of Cu^{2+} ions in cuprates is $3d^9$. Three t_{2g} bands and the $d_{3z^2-r^2}$ band are fully occupied, while the $d_{x^2-y^2}$ band is half filled. Thus, the $3d$ shell of the Cu ion contains a single hole. These holes experience an on site Coulomb repulsion U_d that tends to localize them at Cu lattice sites. The value of U_d, typical for the cuprates, is of the order of $\sim 8 - 10$ eV. The excitation energy of an electron from oxygen to copper is called charge-transfer energy Δ. In the cuprates, the charge-transfer energy Δ is $\sim 2 - 3$ eV, considerably smaller than U. Thus, cuprates are classified as charge transfer insulators (16).

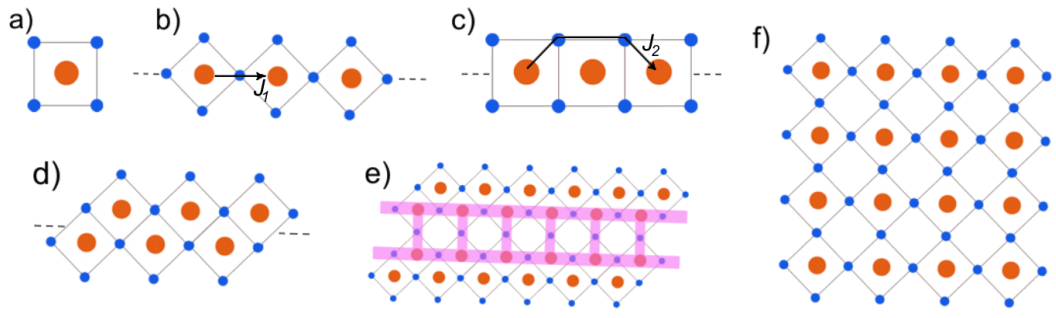

Figure 2.1: (a) The CuO_4 plaquette, basic element of cuprates. (b) A corner-sharing chain. (c) An edge-sharing chain. (e) A double chain. (e) A two-leg ladder. (f) Checkerboard-like CuO_2 plane.

The basic structural unit of any cuprate compound is a CuO_4 plaquette, shown in

Figure 2.1 (a). By using with such plaquettes as architectural units, linking them by oxigen ions, one can construct a variety of topological networks with different dimensionalities. Stacks of isolated CuO_4 plaquettes are the structural unit of the Bi_2CuO_4 compound (17). One-dimensional (1D) chains are built, when CuO_4 plaquettes share their corners (corner-sharing chains, Figure 2.1 (b)) or edges (edge-sharing chains, Figure 2.1 (c)). Well-known examples of chain compounds are Sr_2CuO_3 (18) and $CuGeO_3$ (19). Then, the chains can be combined in different ways, leading to double-chains (Figure 2.1 (d)), realized in $SrCuO_2$ (20), and to two- or multi-leg ladders (Figure 2.2 (e)), realized in $Sr_{n-1}Cu_{n+1}O_{2n}$ materials (21). Finally, a two-dimensional (2D) network can be built by joining together the corner-sharing chains (Figure 2.1 (f)). This cuprate plane, if doped with holes, becomes superconducting at relatively high temperatures (22).

Being the most studied topic for decades, the high-T_c superconductivity of cuprates has not revealed all its secrets yet. The central remaining problem is the identification of the electron-electron pairing mechanism. Despite abundant ideas, there is no universal theory explaining all the experimental findings. Thus, the so-called pseudogap observed in underdoped hole-type cuprates, the topology of the Fermi surface in the normal state of underdoped cuprates and the nature of low-lying excitations have been a matter of intensive debates for many years (23, 24, 25, 26, 27).

In view of the complexity of the CuO_2 planes as the main substructure of high-T_c cuprates, compounds with reduced dimensionality, such as the quasi-1D chain compounds, can provide better understanding of both normal and superconducting states. The 1D systems are more amenable to analytical and numerical calculations and may well hold lessons for the two-dimensional systems as well.

The edge-sharing and corner-sharing systems are realizations of the 1D spin-$\frac{1}{2}$ Heisenberg model and exhibit interesting physical properties resulting from the interplay between spin, charge and lattice degrees of freedom (28, 29, 30). To name some: $CuGeO_3$ has attracted research interest as the first inorganic spin-Peierls compound (31). Recently, multiferroic properties (ferroelectricity associated with the helical magnetic order) were evidenced in 1D chain compounds $LiCu_2O_2$ and $LiCuVO_4$ (32, 33). The spinon with spin 1/2 and the holon with charge e – the low-energy uncoupled collective spin and charge excitations in 1D system (spin-charge separation (34)) – were observed by angle-resolved photoemission spectroscopy (ARPES) in $SrCuO_2$ (35). Recent experimental studies of the thermal conductivity have accumulated evidence for heat transport via magnetic excitations in 1D spin arrays (36), consistent with theoretical predictions (37, 38).

Both electronic and magnetic properties of the cuprates are dependent on the linkage type of CuO_4 plaquettes. The Cu-O-Cu pathway angle between the nearest-neighbour Cu ions changes from 180°, corner-sharing type, to 90°, edge-sharing type. According to the Goodenough-Kanamori-Anderson rule (39, 40, 41), the nearest-neighbor (NN) Cu-Cu exchange interaction J_1 across 180° Cu-O-Cu bond, see Figure 2.1 (b), is strong and positive (antiferromagnetic) while a 90° Cu-O-Cu bond results in weak and negative (ferromagnetic) exchange. Thus, in the edge-sharing complexes the antiferromagnetic superexchange interaction is reduced by the orthogonality of Cu $3d_{x^2-y^2}$ and O $2p_\sigma$ orbitals. At the same time, the effective exchange interaction with considerable magnitude is possible through the Cu-O-O-Cu path between the

next-nearest neighbour (NNN) Cu ions, see Figure 2.1 (c). The contribution of the NNN exchange interaction J_2 is antiferromagnetic and strongly influences on the magnetic properties of edge-sharing systems, leading to magnetic frustration (42). Depending on the relative magnitudes of the spin-lattice coupling, the sign and magnitude of the ratio J_1 /J_2 and the interchain exchange interactions, a variety of ground states has been observed (31, 43, 44, 45).

The edge-sharing compounds are of particular interest as the role of long-range Coulomb interaction between far neighbours can be studied in a quantitative fashion. It may provide a detailed description of the interplay between magnetism and charge order. During the past two decades a large amount of theoretical research has been focused on the low-energy elementary excitations across the Mott-Hubbard gap, involving either doubly occupied or empty electronic sites (46, 47, 48, 49). These excitations of excitonic nature are responsible for the linear and non-linear optical properties. Although some experimental work has been published (50, 51), an accurate evidence of exciton states, a determination of their spectral weight and a quantitative comparison with model calculations have thus far not been reported.

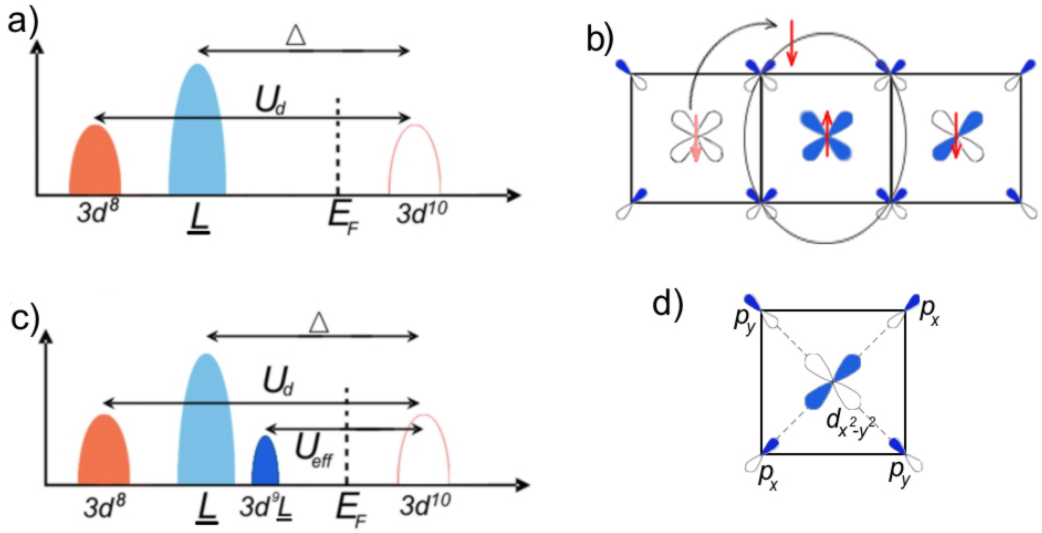

Figure 2.2: (a) Schematic density of states of the charge-transfer insulator. (b) Bright arrows denote the spins of holes. The empty site on the left is the electron, and the large complex containing four oxygen sites and two opposite spins holes is the Zhang-Rice singlet (hole). (c) Schematic density of states of the narrow-band Mott-Hubbard insulator with the introduced ZRS state ($3d^9\underline{L}$). (d) Schematic diagram of the Cu $3d_{x^2-y^2}$ and O $2p_\sigma$ Wannier orbitals. Filling represents the phase of the orbitals. Because of the phase symmetry, one $2p$ orbital can hybridize with the $3d_{x^2-y^2}$ orbital, while the other can not.

2.2 Electronic structure

The insulating cuprates can be described, as minimum, by the three-band Hubbard model (the $p-d$ model or the Emery model) (54) with following parameters: the Coulomb repulsion energy of holes on the $3d_{x^2-y^2}$ (U_d) and $2p_\sigma$ (U_p) orbitals, the intersite Coulomb energy (U_{dp}), the hopping energies of holes between d and p orbitals (t_{dp}) and p and p orbitals (t_{pp}). In addition, longer-range Coulomb interaction may also be important (see below). Schematically, the density of states of the charge transfer insulator is shown in Figure 2.2 (a). The upper Hubbard ($3d^{10}$) band (UHB) is separated from the lower Hubbard ($3d^8$) band (LHB) by the Coulomb interaction energy U_d, while the occupied oxygen $2p$ ($\underline{L}$) band is separated by the charge transfer energy Δ (16).

Doped holes introduced to the system reside on the O $2p_\sigma$ antibonding combination with the Cu $3d$ band, resulting from the strong Coulomb interaction of Cu ions and hybridization of the Cu $3d_{x^2-y^2}$ orbital with the O $2p_\sigma$ orbital [Figure 2.2 (b)]. This localized nonmagnetic state with spin $S=0$, the so-called Zhang-Rice singlet (ZRS) (52), represents an empty site. In the density of states schematic [Fig. 2.2 (c)], the ZRS state is split off from the ligand band ($3d^9\underline{L}$).

Doped electrons reside in the unoccupied UHB ($3d^{10}$). Thus, the ZRS plays the role of the LHB, and the interband excitation from ZRS to UHB determines the charge-gap with the effective Hubbard interaction U_{eff} [Figure 2.2 (c)]. Since U_{eff} is less than the charge transfer energy Δ, this brings us to the notion of the narrow-band Mott-Hubbard insulator, as an effective description of the cuprates (53).

Therefore, once the ZRS state is considered, the complex three-band model can be reduced to the effective single-band Hubbard-Wigner model, with the Hamiltonian given by the sum of kinetic and Coulomb contributions (55, 47),

$$\mathcal{H}_{Hub} = \mathcal{H}_K + \mathcal{H}_{Coul}. \tag{2.1}$$

The hopping of an electron with spin σ between sites i and $i+l$ and vice versa is described by the kinetic contribution that can be written as

$$\mathcal{H}_K = -\sum_{i,l\geqslant 1,\sigma} t_l (c^\dagger_{i,\sigma} c_{i+l,\sigma} + c^\dagger_{i+l,\sigma} c_{i,\sigma}), \tag{2.2}$$

where t_l term is the hopping of ZRS between sites; $c^\dagger_{i,\sigma}$ and $c_{i,\sigma}$ are the creation and annihilation operators for electrons with spin $\sigma = \uparrow, \downarrow$ at i site. In the edge-sharing systems where the Cu-O-Cu angle is orthogonal, the hopping term t_2 between the NNN Cu sites dominates over the hopping term t_1 between NN sites.

The Coulomb contribution reads as (53)

$$\mathcal{H}_{Coul} = U_{eff} \sum_i n_{i,\uparrow} n_{i,\downarrow} + \sum_{i,l\geqslant 1} V_l n_i n_{i+l}, \tag{2.3}$$

where density operators are $n_{i,\sigma} = c^\dagger_{i,\sigma} c_{i,\sigma}$ and $n_i = n_{i,\uparrow} + n_{i,\downarrow}$; U_{eff} reflects the strongly correlated nature of the system when the $Cu^{1+}(d^{10})$ configuration is unfavorable; V_l represents the Coulomb interaction between sites, screened by the core

electrons and polarization of neighboring chains. The latter is parameterized by the NN Coulomb interaction V as $V_l = V/l$, $l = 1, 2, ...$ (53).

In the case of dominant NN exchange interaction, when the Coulomb repulsion energy strongly exceeds the NN hopping parameter (large-U limit), the Hubbard model (2.1) can be described by the Heisenberg model, where the NN interaction J is given by $\sim \frac{4t^2}{U}$. The effective Hamiltonian is called then $t - J$ model

$$\mathcal{H}_{t-J} = -\sum_{i,l\geqslant 1,\sigma} t_l(\widetilde{c}^{\dagger}_{i,\sigma}\widetilde{c}_{i+l,\sigma} + \widetilde{c}^{\dagger}_{i+l,\sigma}\widetilde{c}_{i,\sigma}) + J\sum_{i,l}\mathbf{S}_i \cdot \mathbf{S}_l, \tag{2.4}$$

where $\widetilde{c}_{i,\sigma} = c_{i,\sigma}(1 - n_{i,-\sigma})$ is the annihilation operator of an electron with spin σ at site i with the constraint of no double occupancy, and S_i is the spin operator at site i.

2.3 Exchange interactions. Frustration

When considering the 1D edge-sharing chain compounds, one should not neglect the NNN interactions, as was mentioned above. The NNN antiferromagnetic interaction J_2 is strong and competes with the ferromagnetic NN interaction J_1 (Figure 2.3), giving an effect of frustration into the chain. The frustration ratio $\alpha = -J_2/J_1$ defines the magnetic ground states of the J_1-J_2 model (29). The effective model for the undoped edge-sharing chains is the 1D Heisenberg model with a spin Hamiltonian of the form

$$\mathcal{H} = J_1\sum_i \mathbf{S}_i \cdot \mathbf{S}_{i+1} + J_2\sum_i \mathbf{S}_i \cdot \mathbf{S}_{i+2}. \tag{2.5}$$

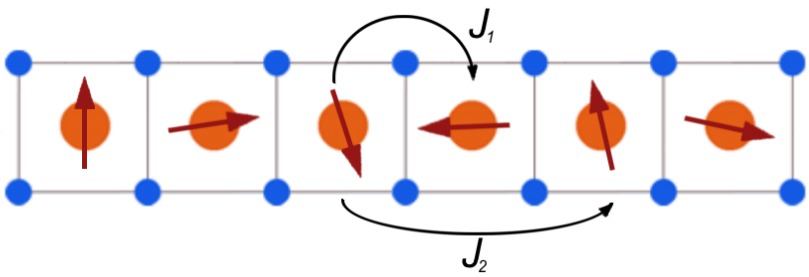

Figure 2.3: A schematic view of the exchange interactions J_1 and J_2 between NN and NNN magnetic Cu^{2+} ions in the edge-sharing chain.

In the work of Mizuno *et al.* (29), the dependencies of the exchange integrals on the Cu-O-Cu bond angle θ, the distance $d_{\text{Cu-O}}$ and the charge-transfer energy Δ were calculated and plotted on the diagram shown in Figure 2.4. While the antiferromagnetic NNN exchange J_2 depends on the bond angle moderately, the NN exchange interaction J_1 changes drastically within a 20° interval for θ with a crossing from antiferromagnetic to ferromagnetic at a critical angle 95°. The abridgement of the Cu-O distance $d_{\text{Cu-O}}$ causes the increase of hopping amplitudes and, hence, the

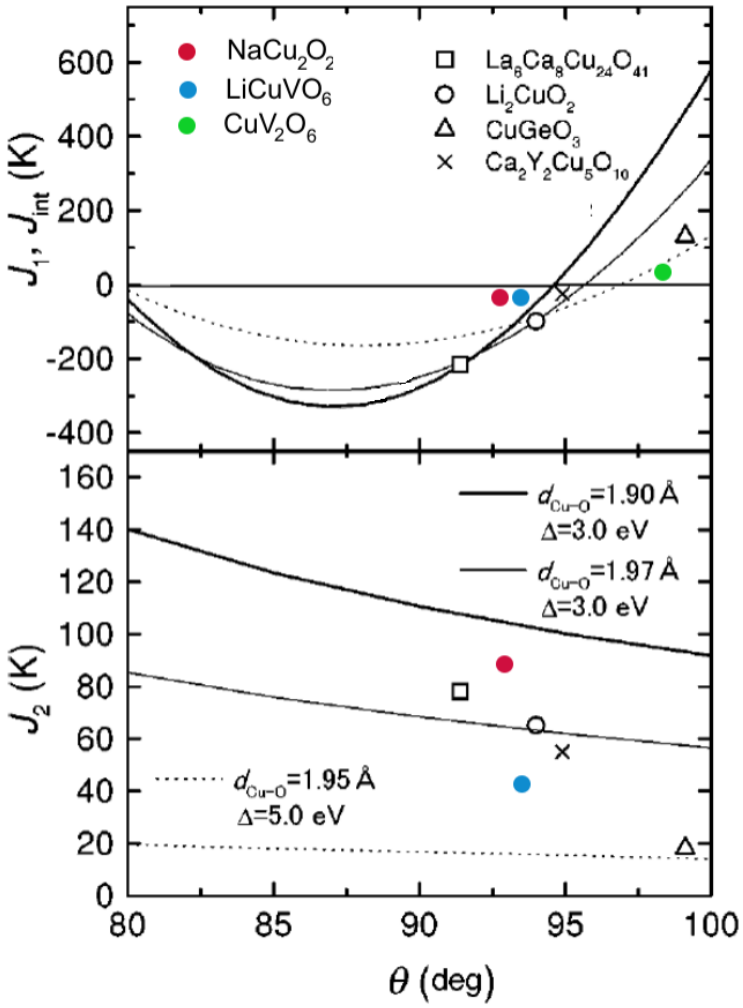

Figure 2.4: The theoretical dependencies of J_1 and J_2 exchange integrals on the Cu-O-Cu bond angle θ for different sets of $d_{\text{Cu-O}}$ and Δ. From Ref. (29). J_1 changes from ferromagnetic to antiferromagnetic at $\theta = 95°$. The blue, red and green circles are added and correspond to the J_1 and J_2 exchange integrals of $LiCuVO_4$, $NaCu_2O_2$ and CuV_2O_6 compounds; the data are taken from Refs. (43), (44), (56), respectively.

increase of exchange integrals. The larger Δ results in the reduction of exchange integrals. Figure 2.4 shows, also, experimental data for the edge-sharing compounds from Ref. (29), along with data for $LiCuVO_4$, $NaCu_2O_2$ and CuV_2O_6, taken from Refs. (43), (44), (56).

The exchange integrals can be determined from magnetic susceptibility and magnetization measurements (57). Figure 2.5 shows the susceptibility curve for $LiCuVO_4$, which is typical for this class of materials. One can mark out the high-temperature region, which obeys the Curie-Weiss law for paramagnetic media, and a broad peak at lower temperatures, corresponding to the spin-correlation effect within the chains. Such curve can be fitted within a J_1-J_2 model (29) or Bonner-Fisher model (58), which gives the exchange integrals J_1, J_2 for a simple interaction

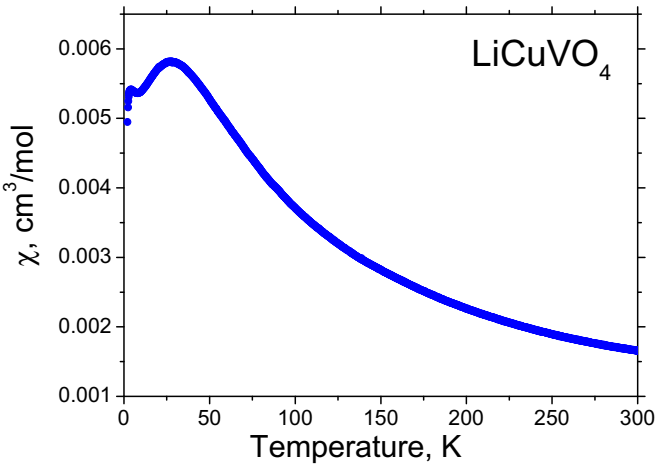

Figure 2.5: The magnetic susceptibility $\chi(T)$ of $LiCuVO_4$ single crystal in zero magnetic field measured along the chains.

scheme. However, these models do not take into account the non-zero interchain interaction, failing to reproduce the lower-temperature susceptibility data.

The exchange integrals can be determined more reliably by inelastic neutron scattering measurements of the dispersion of spin excitations, combined with low-temperature susceptibility data and magnetization (44). However, for $LiCuVO_4$ the fitting procedure includes a large number of fitting parameters, such as the intrachain NN and NNN exchanges, the two in-plane interchain exchanges and two out-of-plane interchain exchanges.

2.4 Exciton states. Charge dynamics

The nature of charge excitations across the gap in narrow-band Mott insulators such as cuprates is a challenge to current understanding of strongly correlated systems. Optical excitation across the Mott-Hubbard band in the cuprates changes two singly occupied sites to the $3d^9\underline{L}$ unoccupied site (or ZRS) in one CuO_4 unit and the d^{10} configuration (or doubly occupied UHB) in a neighbor CuO_4 unit [Figure 2.6 (a)]. Both sites are spinless, but they posses opposite charges. They form two spinless fermions called "holon" and "doublon", according to occupancy, on the magnetic background. Both fermions can move within the chains using the hopping process of electrons. Their kinetic energy, determined by the hopping integral t, may exceed the Coulomb interaction V ($V \ll t$), then a holon-doublon pair is unbound and both particles propagate independently [Figure 2.6 (b)]. In the case, when the attraction between particles exceeds their kinetic energy ($t \ll V$), the formation of a bound holon-doublon pair, or exciton, takes place [Figure 2.6 (c)], in analogy to excitons in semiconductors.

The exciton size corresponds to the interatomic Cu-Cu distance and hence a

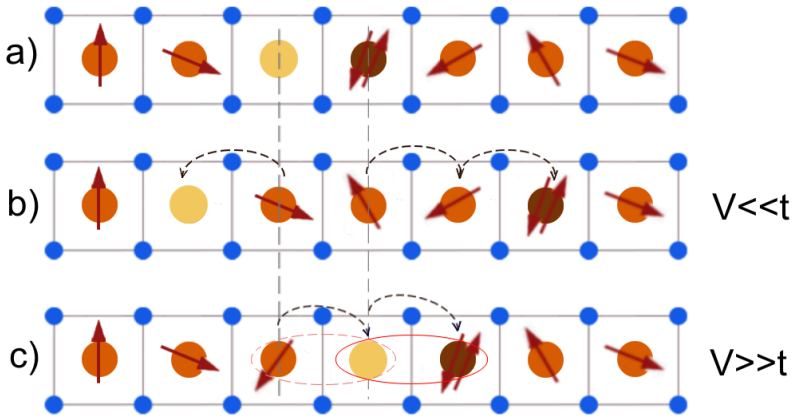

Figure 2.6: The schematic representation of (a) holon-doublon pair on the magnetic background in the edge-sharing chain, (b) an unbound holon-doublon pair in the case $V \ll t$, (c) a bound exciton in the case $V \gg t$.

large binding energy of the order of an eV is expected, which is characteristic of a tightly bound, Frenkel-type exciton. On the other hand, the two particles, holon and doublon, cannot be localized on one site at the same time because of the large on-site Coulomb interaction, U. This is in contrast to the Frenkel excitons in semiconductors, where a hole and an electron reside on the same site in the valence and conduction band, respectively.

Over the years, exciton formation of doublon-holon pairs has been considered as a possible low-energy elementary excitation in the insulating Cu-O planes (59, 60) or chains (46, 47, 48, 49). The theoretical approaches cited here are based on the nature of the spin-charge separation in 1D cuprates. The positive and negative fermions may move within the chains without disturbing the magnetic background, i.e. the effects of spin degrees of freedom are neglected. The electronic Hamiltonian for a two-particle system (2.1-2.3) includes both kinetic and Coulomb interactions, reflecting the strongly correlated nature of the system and the attraction between two carriers.

When the spin degrees of freedom are decoupled, the effective band structure can be schematically sketched, see Figure 2.7 (a). The interband transitions between holon and doublon bands are possible with no change of the total momentum $k = 0$ and with change of the total momentum k, representing the holon-doublon dispersion. Figure 2.7 (b) shows the energy range of the holon-doublon model (49), where the shaded area corresponds to the electron-hole continuum with dispersion

$$E_c(k) = U + 4t \cos\frac{k}{2} \cos p. \tag{2.6}$$

The total and relative momenta of the two particles are $k = k_1 + k_2$ and $p = (k_1 - k_2)/2$. The width of the continuum is $8t$ at $k = 0$ and decreases with increasing k.

In addition to the continuum, there is a single bound state corresponding to the exciton with dispersion (49)

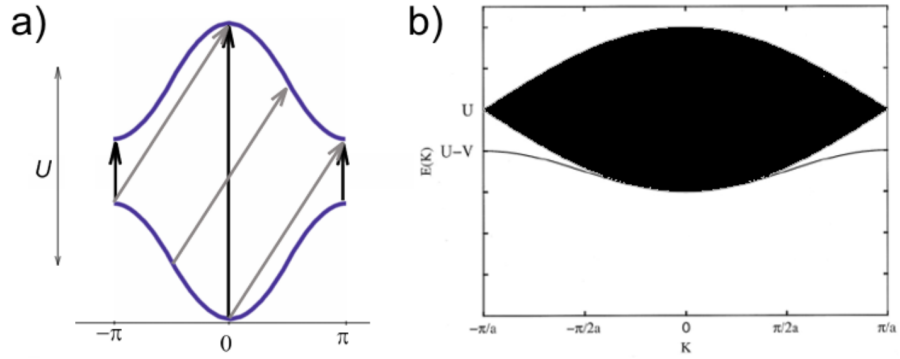

Figure 2.7: (a) The schematic representation of the band structure in the holon-doublon model. Holon (doublon) band is the lower (upper) curve. Arrows mark the possible transitions with no change of the total momentum $k = 0$ (black) and with the change of the total momentum by $k = \pi$ (gray). (b) The energy spectrum of the electron-hole continuum (shaded area) and the exciton dispersion (line) for $V = 2t$. After Gallagher *et al.* (49).

$$E_{ex}(k) = U - V - \frac{4t^2}{V}\cos^2\frac{k}{2}. \tag{2.7}$$

While at large k the bound holon-doublon state exists for any nonzero V, at $k = 0$ it emerges only for $V > 2t$.

When $V < 2t$, the holon and doublon are independent [Figure 2.6 (b)]. In the optical conductivity spectrum $\sigma_1(\omega)$ in this case, a band of width $8t$ starting at the Mott gap $E_M = U - 4t$ is formed by the pair of free charge excitations [see Figure 2.8 (a)], as calculated using the dynamical density-matrix renormalization-group (DMRG) method (47). This gap corresponds to the optical gap, since there is no other optical excitation at lower energies. In the case $V > 2t$, some spectral weight is still located within the continuous band due to independent particles, however most of it goes to the lowest energy excitation, exciton, with the energy $\omega_{ex} = U - V - \frac{4t^2}{V}$ (48). In the optical conductivity spectrum this peak becomes isolated from the band onset (47).

Above, a model incorporating only the NN hopping t is considered. However, in the case of edge-sharing chain compounds, the non-zero NNN hopping t_2 may compete with the NN hopping t_1.

An analytical study of the excitonic states extended to the case with NNN hopping term t_2 was reported by Mayr and Horsch (53). These authors consider the edge-sharing Cu-O chain compounds as a realization of the 1D Wigner crystal (61), where crystallization of the low-density electron gas takes place, and the spatial arrangement of the electrons is important, since their kinetic energy is dominated by the Coulomb interaction. In such a crystal, charge excitations can be characterized as domain-wall excitations. In particular, the authors study the excitation spectrum for the quarter-filled chain with 26 sites for the case when only NN hopping motion t_1 is considered [Figure 2.9 (a)] and when NNN hopping motion t_2 with sufficiently large value accompanies the t_1 process [Figure 2.9 (b)].

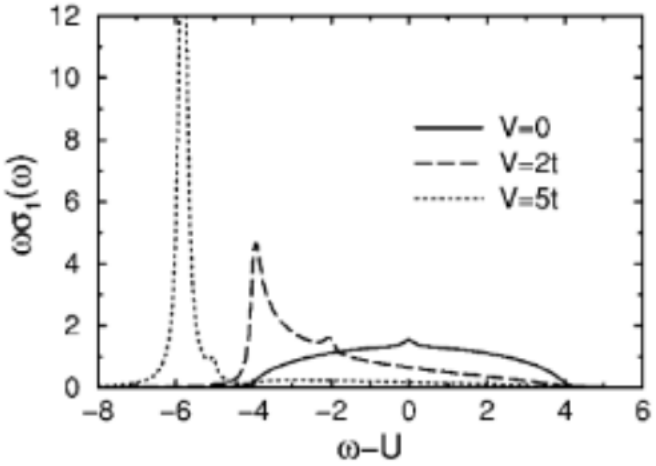

Figure 2.8: Reduced optical conductivity, $\omega\sigma_1(\omega)$, in the limit of a large Mott gap $U \gg t$, calculated for $V = 0$, $V = 2t$ and $V = 5t$ using dynamical DMRG method. After Jeckelmann (47).

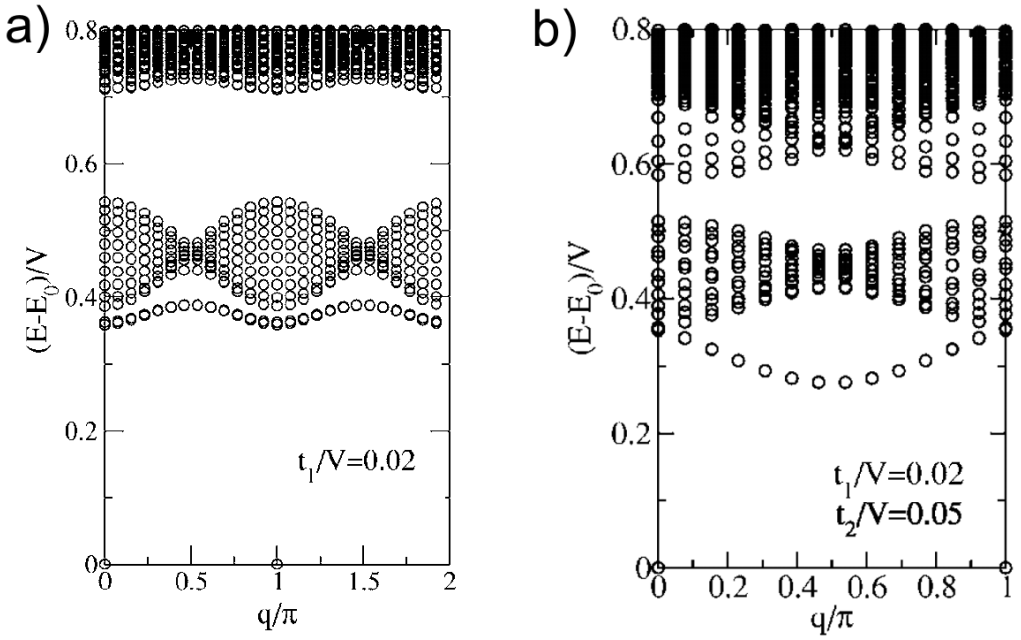

Figure 2.9: Excitation spectrum for the quarter-filled ring and Coulomb interaction for (a) the model incorporating NN hopping $t_1 = 0.02V$ and (b) the model incorporating NNN hopping $t_2 = 0.05V$, $t_2 > t_1$. After Mayr and Horsch (53).

Numerical results for the excitation spectra in the pure t_1 case displayed in Figure 2.9 (a) show a degenerate ground states at $q = 0$ and π. Domain wall continua are seen at high energies (due to excitations of four domain-walls) and centered around $E \sim 0.45V$ (due to domain-wall pairs). The bound state emerges below the

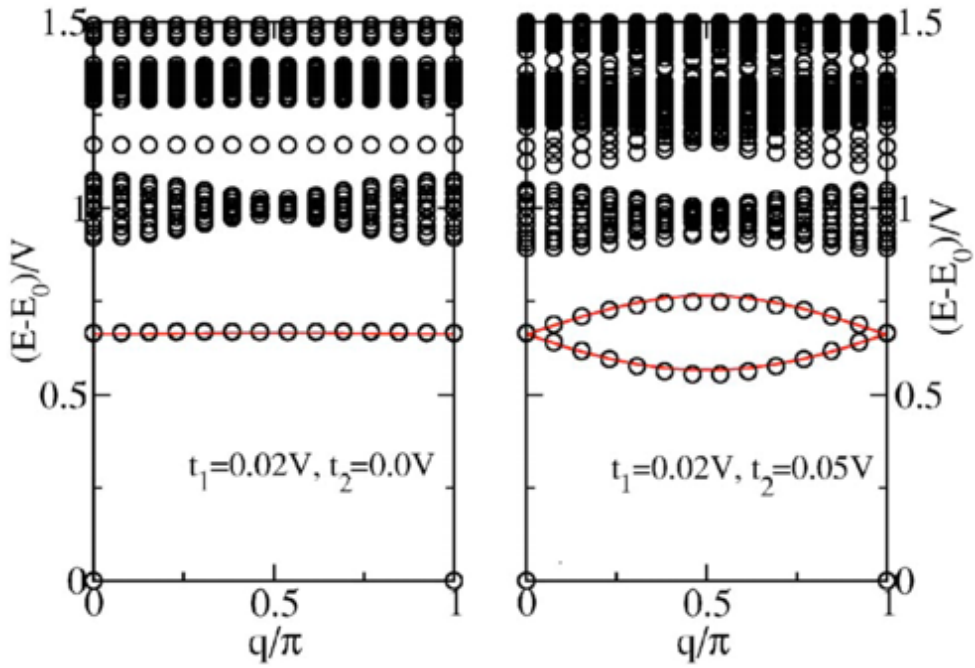

Figure 2.10: Excitation spectrum at the quarter-filling and truncated Coulomb interaction. Circles represent the numerical results for different second-neighbour-hopping matrix elements: $t_2 = 0$ and $t_2 > t_1$. After Mayr and Horsch (53).

domain-wall continuum and is an excitonic state due to Coulomb attraction between domain-wall pairs. This state is well separated from the bottom of the continuum and disperses upwards from $q = 0$, shaping the domain wall continua.

The incorporation of NNN hopping motion t_2 to the model changes the situation qualitatively compared to the t_1 case, as shown in Figure 2.9 (b). The numerical results show that the two-domain-wall continuum is almost unaffected by the large value NNN hopping t_2, with the exception of a small downward shift due to broadening of the higher-energy continuum. However, the bound excitonic state, in contrast to the pure t_1 case, disperses downward from $q = 0$, independently of the sign of t_2. Therefore, the strong effect of the t_2 process is expressed as a shift of the minimum of the exciton dispersion to $q = \frac{\pi}{2}$.

Figure 2.10 shows the excitation spectrum for a 26 sites chain at quarter-filling and Coulomb interaction truncated at the third site (l_{max}=3) for the NNN hopping motion $t_2 = 0$ and $t_2 = 0.05V$, $t_2 > t_1$. In this case the domain-wall continuum is centered around V. Compared to the case with long-range Coulomb interaction [Figure 2.9 (a)], the excitonic state for the $t_2 = 0$ case, when interactions are truncated, is dispersionless. This is explained by the larger splitting between the exciton and continuum. For the case $t_1 = 0.02V$, $t_2 = 0.05V$, when the degeneracy of the exciton is lifted, two exciton branches are clearly seen. While the lower exciton branch disperses downwards, the higher one goes upwards. Thus, the formation of an exciton doublet is possible in the edge-sharing chain cuprates with competing hoppings.

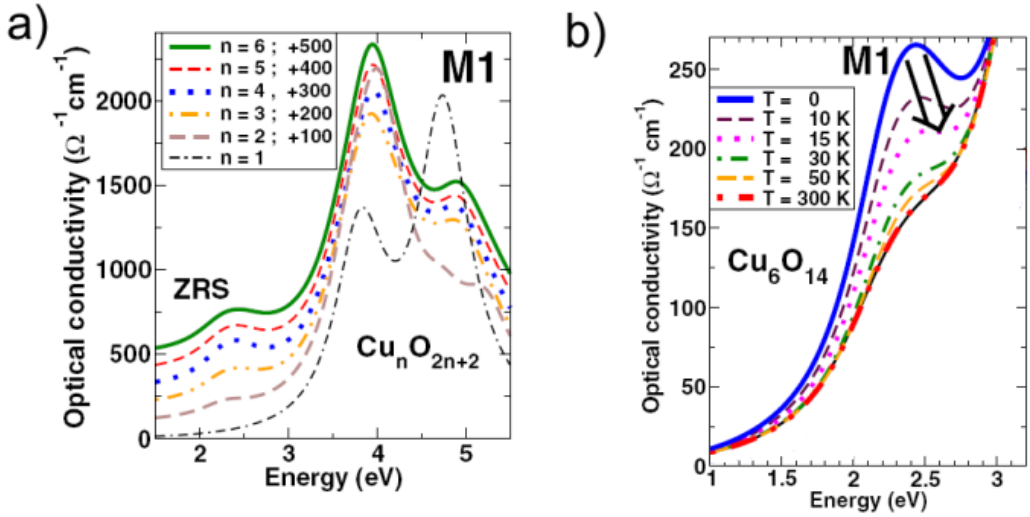

Figure 2.11: (a) Calculated optical conductivity $\sigma(\omega)$ for various clusters within a low-spin ground state. Curves are shifted for clarity. (b) Temperature dependent optical conductivity $\sigma(\omega)$ within the region of ZRS transition for clusters within a low-spin ground state. After Malek *et al.* (62).

Recently, calculations of the optical conductivity of edge-sharing Cu_nO_{2n+2} chain clusters within a *pd*-Hubbard model including the on-site Coulomb repulsion have assigned the lowest-energy transition along the chains to ZRS excitations (62). The approach has been applied to the Li_2CuO_2 compound, where single-crystal optical data are available at room temperature (29). The model includes kinetic, Coulomb and exchange contributions and is highly parameterized. Figure 2.11 (a) shows the exact diagonalization results of this model for different cluster sizes. The calculated optical conductivity $\sigma(\omega)$ for the large clusters number reveals a multiple peak structure. The most interesting here is the weak peak at 2.4 eV, denoted as a ZRS excitation. For this excitation, a strong temperature dependence of the spectral weight due to spin-correlation effects is also predicted, see Figure 2.11 (b). At room temperature, the 2.4 eV peak is largely suppressed, and only below 50 K a remarkable growth of its spectral weight is seen.

The latter model does not include the long-range Coulomb interactions. Excitations associated with the ZRS form a continuum, which is in contrast to the approach of Mayr and Horsch, where features associated with ZRS have an excitonic nature. To test both models, low temperature optical data are required.

2.5 Spectroscopic optical data. Literature overview

Features associated with ZRS excitations were evident in optical conductivity spectra of corner-sharing Pr_2CuO_4 and Sr_2CuO_3 compounds (11, 63). Even at room temperature these features are intensive and well discerned from the continuum

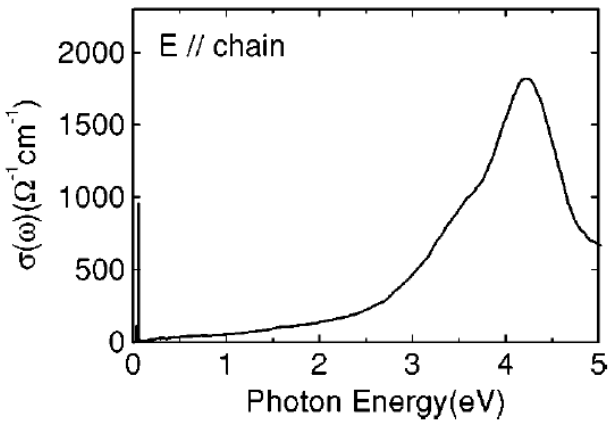

Figure 2.12: The optical conductivity spectrum $\sigma(\omega)$ along the edge-sharing chains at room temperature for a single-crystalline sample of Li_2CuO_2 (29).

associated with *p-d* transitions at higher energies.

However, there is a big difference between the optical response of edge- and corner-sharing compounds due to different linkage of CuO_4 units. In corner-sharing cuprates, the Cu-O-Cu angle is close to 180° and the nonlocal excitation involving neighboring units is strong. In contrast, the nonlocal excitations between neighboring CuO_4 units in edge-sharing chain compounds are suppressed due to the 90° angle of the Cu-O-Cu bond, which results in a smaller spectral weight of features associated with ZRS excitations. As a result of electron exchange (64), an intrinsic broadening of the linewidth of the exciton formed by ZRS-d^{10} pairs is expected. It has therefore been difficult to separate the intrinsically broad and weak features due to ZRS excitons from the strong absorption continuum due to incoherent *p-d* transitions .

Despite a large number of edge-sharing chain compounds, available as single crystals, only a small number of linear optical spectroscopy studies has been reported. In 1998, Mizuno *et al.* reported on optical conductivity spectra $\sigma(\omega)$ for Li_2CuO_2 for polarization of incident light along the edge-sharing chains at room temperature (Figure 2.12) (29). The data were obtained by a Kramers-Kronig transformation of the reflectivity spectrum. In these data, the peak with a large spectral weight at 4.2 eV was assigned to the *p-d* excitation from oxygen non-bonding states to the upper Hubbard band. The intensity of the spectrum falls off monotonously toward low energies, while there is a tiny bump on the left shoulder of the 4.2 eV peak. No evidence of features associated with the ZRS excitations was observed, while the theoretical calculations for this compound (62) propose the development of the ZRS peak at 2.4 eV at low temperatures.

Reflectivity data of an edge-sharing $LiCu_2O_2$ single crystal are available in the literature (65). Authors of the cited paper assigned strong absorptions observed at 3.1 eV (along *a* and *b* axis) to the ZRS excitations. However, this assignment seems not to be correct, since the anomalous absorption band is evidenced in polarizations along and perpendicular to the edge-sharing chains, while features associated with ZRS should be visible only along the chains, because of the one-dimensional geome-

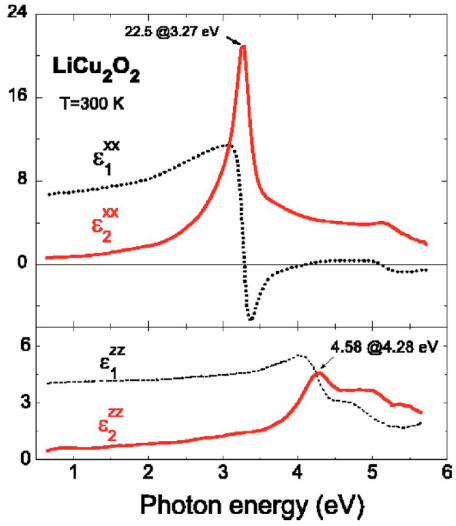

Figure 2.13: (a) Room temperature spectra of the real ε_1 and imaginary ε_2 parts of the dielectric functions for the light polarized perpendicular and parallel to the O^{2-}-Cu^{1+}-O^{2-} dumbbell axis z. From Ref. (66).

try of the CuO net. In the later work by Pisarev *et al.*, ellipsometric data are shown for the same compound (66), see Figure 2.13. While the reflectivity and ellipsometric in-plane data are in agreement, Pisarev assigned the anomalous absorption to an exciton-like transition in the O^{2-}-Cu^{1+}-O^{2-} dumbbell complexes of $LiCu_2O_2$, rather than to the ZRS. Such contradictions in the data interpretation can be caused by twinning of the crystals and by defects caused by Li-Cu substitution. A discussion of details of this work is carried out in the next chapter.

The largest amount of optical data is available for the edge-sharing $CuGeO_3$ compound, famous as the first inorganic compound undergoing the spin-Peierls transition (31). The measured polarization-dependent optical absorption and transmission data, their temperature and doping dependencies have been intensively discussed in the literature (67, 68, 69, 70, 71). Figure 2.14 (a) shows room temperature absorption spectra of $CuGeO_3$ measured along and perpendicular to the chains. The energy gap is observed to be anisotropic and temperature dependent (67). The ellipsometrically measured loss spectra $\mathrm{Im}[-\frac{1}{\varepsilon(\omega)}]$ obtained for polarization along the CuO chains ($E \parallel c$) at room temperature (72) revealed a well developed single band at 3.7 eV, see Figure 2.14 (b), however no conclusions were drawn about the origin of the observed excitation. No data measured for other polarizations or temperature dependencies have been reported.

Recently, Kim *et al.* reported reflectivity data of the corner-sharing chain compound Sr_2CuO_3 (51). In the reflectivity spectrum (see Figure 2.15) at 10 K on top of the charge transfer excitation, which forms a clear gap edge along the 180° bonded Cu-O-Cu chains, two weakly resolved peaks are identified. The authors attributed these sharp peaks to excitons, which come to existence due to the long-range Coulomb interaction. Although peak structures arising from excitons have

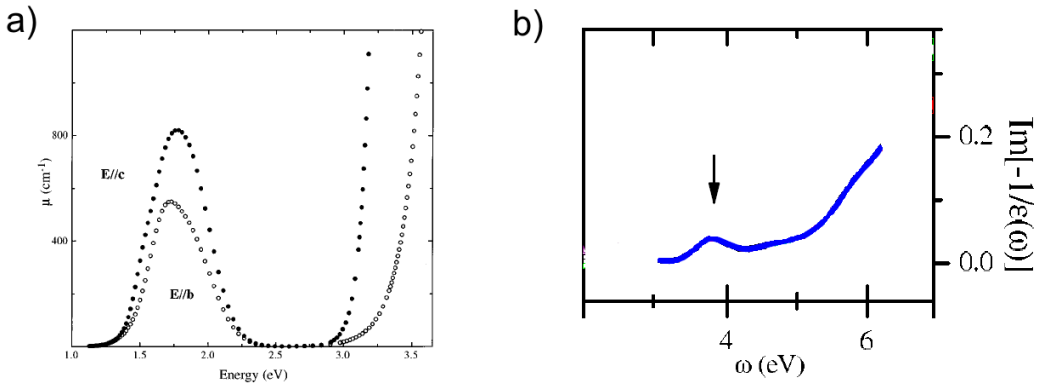

Figure 2.14: (a) Room temperature absorption spectra of $CuGeO_3$. The polarization angle changes from $E \parallel c$ to $E \parallel b$. From Ref. (67). (b) The energy loss spectra measured by ellipsometry, $\mathrm{Im}[-\frac{1}{\varepsilon(\omega)}]$, obtained for polarization along the CuO chains ($E \parallel c$) at room temperature. From Ref. (72).

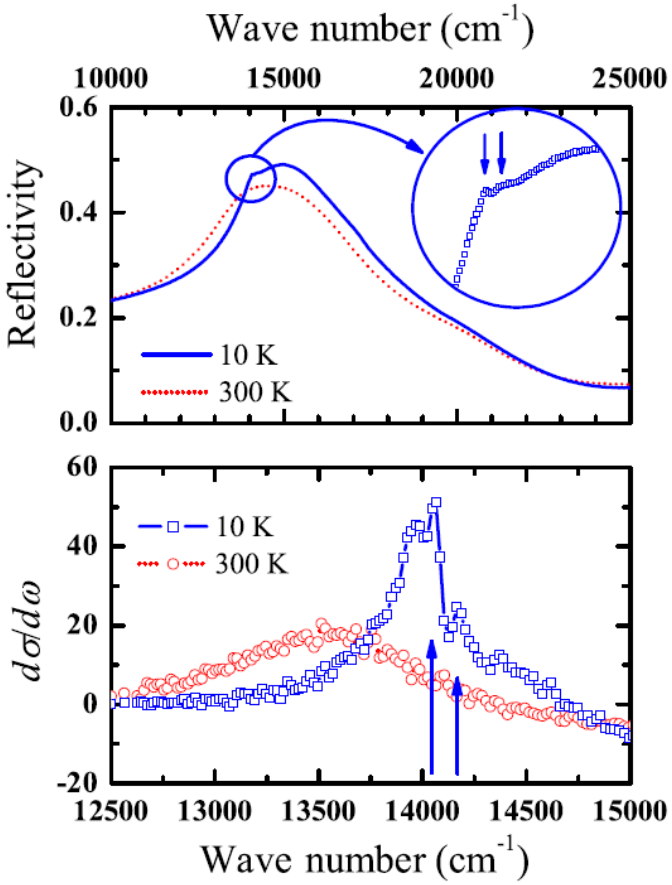

Figure 2.15: Reflectivity and derivative spectra of $\sigma(\omega)$Þ along the edge-sharing chain direction of Sr_2CuO_3. Peaks at 10 K are marked with arrows. (51).

been identified in frequency-derivative reflectivity spectra, an accurate determination of the exciton's spectral weight (SW) has not been reported.

In conclusion of the review, features associated with the ZRS excitations have not been unambiguously identified in optical experiments for the edge-sharing chain compounds, and a quantitative comparison with model calculations has thus far not been reported.

3 Experimental results. Edge-Sharing CuO Chain Compounds

Introduction

The elementary charge excitations observed by optical spectroscopy are a key source of information on electronic correlations in transition metal oxides. Because of their particularly simple electronic structure (with a single hole in the *d*-electron shell) and their importance for high-temperature superconductivity and other electronic ordering phenomena, compounds containing insulating copper-oxide planes or chains have long been recognized as model systems for charge excitations in the strong-correlation limit.

In this chapter of the thesis, a comprehensive ellipsometric study of charge excitations in the edge-sharing chain cuprates $LiCuVO_4$, $NaCu_2O_2$, Li_2CuO_2, $CuGeO_3$ and CuV_2O_6 is reported. In the optical experiments described here, weak but well-resolved two-peak structures were observed for photon polarization along the chains, along with the *p*-*d* transitions reported previously. Using ellipsometry complemented by transmission measurements, we accurately determine their temperature-dependent spectral weights and show that they are controlled by the thermal variation of the NN and NNN spin correlation functions. The peaks can thus be identified as an exciton doublet arising from the long-range Coulomb interaction along the chains. By virtue of their exceptionally narrow electronic bandwidth, compounds with edge-sharing copper-oxide chains thus provide a highly favorable platform for the investigation of exciton formation and the interplay between spin and charge correlations in the cuprates.

3.1 $LiCuVO_4$

Structure. Magnetic properties. Experimental details

$LiCuVO_4$ crystallizes in the orthorhombic space group *Imma*, with edge-sharing CuO chains running along the *b*-axis separated by non-magnetic LiO_6 octahedra and V^{5+} ions, see Figure 3.1 (a). The orthorhombic cell parameters at room temperature are $a = 5.662$ Å, $b = 5.809$ Å, $c = 8.758$ Å (73). There are 4 Cu^{2+} ions per unit cell, therefore the density of Cu^{2+} ions is $N_{Cu^{2+}} = 1.4 \cdot 10^{22}$ cm^{-3}. Within a single chain, the Cu^{2+}-Cu^{2+} distance is 2.899 Å, and the Cu-O-Cu bond angle is 96°. Single crystals of $LiCuVO_4$ were grown from $LiVO_3$-based flux, as described by Prokofiev *et al.* (74).

The temperature dependence of the magnetic susceptibility $\chi(T)$ along the principal axes is shown in Figure 3.1 (b). It exhibits two characteristic maxima: a broad maximum at $T = 28$ K, due to the establishment of magnetic correlations within the Cu-O chains, and a sharp one at $T_N = 2.4$ K, due to the formation of three-dimensional long-range order (44, 75, 76, 77). The magnetic susceptibility data obeys the Curie-Weiss law for paramagnetic media above 80 K, with parameters $C = 0.480$ cm^{3}K/mol, $-\Theta = 22$ K. The Curie-Weiss fit of data along the chains (along *b* axis) is shown by the thin solid red line in Figure 3.1 (b). Prokofiev *et al.* showed that the magnetic susceptibility data can be excellently fitted within the $S = 1/2$ Heisenberg antiferromagnetic chain model by summing paramagnetic impurity and Bonner-Fisher (58) terms (77).

The magnetic structure of $LiCuVO_4$ has been intensively studied by different

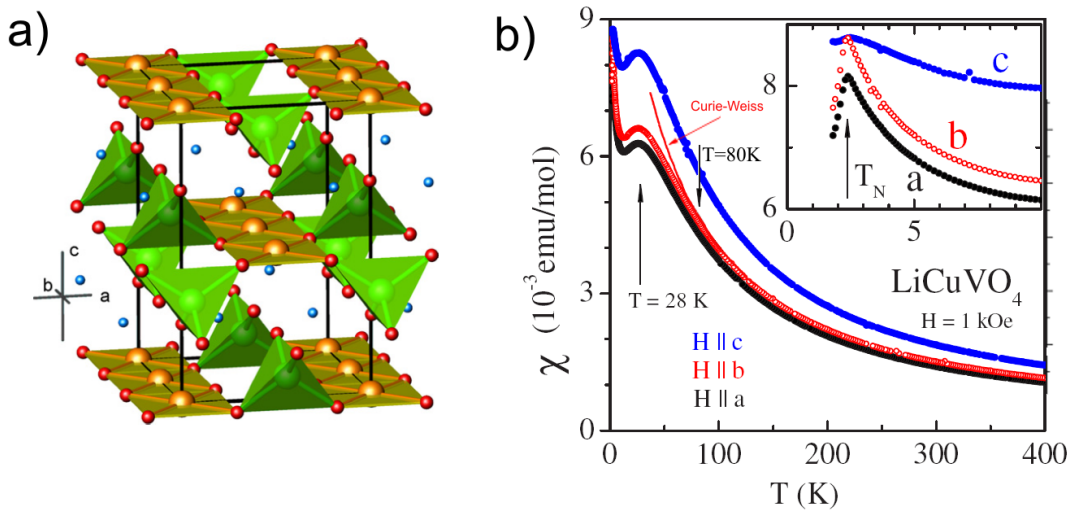

Figure 3.1: (a) Schematic structure of $LiCuVO_4$. CuO chains shown by orange and red colors, vanadium octahedra – green, Li ions – blue. (b) Temperature dependence of the magnetic susceptibility $\chi(T)$ of $LiCuVO_4$ single-crystal along the principal *a*, *b* and *c* axes; the applied magnetic field is 1 kOe. After Büttgen *et al.* (76).

techniques (44, 75, 76, 78). Recently, Gibson *et al.* observed long-range incommensurate magnetic order with a propagation vector $k = (0, 0.532, 0)$ below 2.1 K by studying elastic neutron diffraction data on the single crystals (75). Enderle *et al.* established that the magnetic excitations are described by the frustrated quantum spin chain model with $S = 1/2$ (44). Within this model the nearest neighbor spins are coupled ferromagnetically ($J_1 < 0$) and next-nearest neighbors antiferromagnetically ($J_2 > 0$), with $\mid J_1 \mid < J_2$. Inelastic neutron scattering data indicate exchange integrals $J_1 = -18$ K, $J_2 = 49$ K. Small interchain interactions lead to 3D ordering below T_N.

For the optical measurements, samples with size 7 mm × 3 mm × 1.5 mm were used. The samples were oriented for these experiments by X-ray diffraction measurements. The rocking-curve measurements confirmed the high quality of the crystals, the half-width-at-half-maximum is less than 1.5°. The *ab* surface was freshly cleaved just prior to the measurements. The *ac* surface was polished to optical grade, using a 0.25 μm diamond suspension.

Experimental data

The room temperature raw ellipsometric data represented by ellipsometric angles Ψ and Δ are shown in Figure 3.2. The data were measured at 70° angle of incidence for photon polarizations E ∥ *a*-, E ∥ *b*- and E ∥ *c*-axis, ((0°,0°,0°), (90°,0°,0°) and (90°,90°,0°) in Euler-angle representation). The inherent anisotropy of the response to the electric field manifests itself in changes of the spectra with alternation of principal optical axes with respect to the incident light. Therefore, ellipsometry yields the anisotropic frequency dependent complex dielectric tensor, $\varepsilon(\omega) = \varepsilon_1(\omega) + \mathrm{i}\varepsilon_2(\omega) = 1 + \mathrm{i}\ 4\pi\sigma(\omega)/\omega$.

A numerical regression procedure (4), as described in the Chapter 1 of this thesis, was applied to derive the principal components of the dielectric tensor from the ellipsometric data at different Euler angles. Fits of the measured data for all orientations are shown in Figure 3.2 by thin solid cyan lines.

Figures 3.3 (a, b, c) show the real and imaginary parts of the dielectric function of $LiCuVO_4$ at representative temperatures 300, 100, and 7 K. Clearly, the optical response is highly anisotropic. While the spectrum along the *c*-axis shows no significant temperature dependence, temperature-dependent features are apparent along both *a*- and *b*-axis. The main temperature dependent features [marked by arrows in Figures 3.3 (a, b)] are centered at 4.2 eV for polarization along the *a*- and at 2.95 eV along the *b*-axis.

In order to separate contributions from the different bands to the optical response of $LiCuVO_4$, and to explore the origin of the temperature dependence, we performed a classical dispersion analysis by simultaneous fitting to $\varepsilon_1(\omega)$ and $\varepsilon_2(\omega)$. The decomposition of the optical response in terms of a sum of Lorentzians is a phenomenological fitting procedure to quantitatively parameterize the observed temperature-driven optical anomalies and spectral weight transfer. Moreover, the agreement between the simulated and measured spectra shown in Figure 3.2 confirms that our data for $\varepsilon_1(\omega)$ and $\varepsilon_2(\omega)$ (or $\sigma_1(\omega)$) determined independently by spectroscopic ellipsometry are Kramers-Kronig consistent.

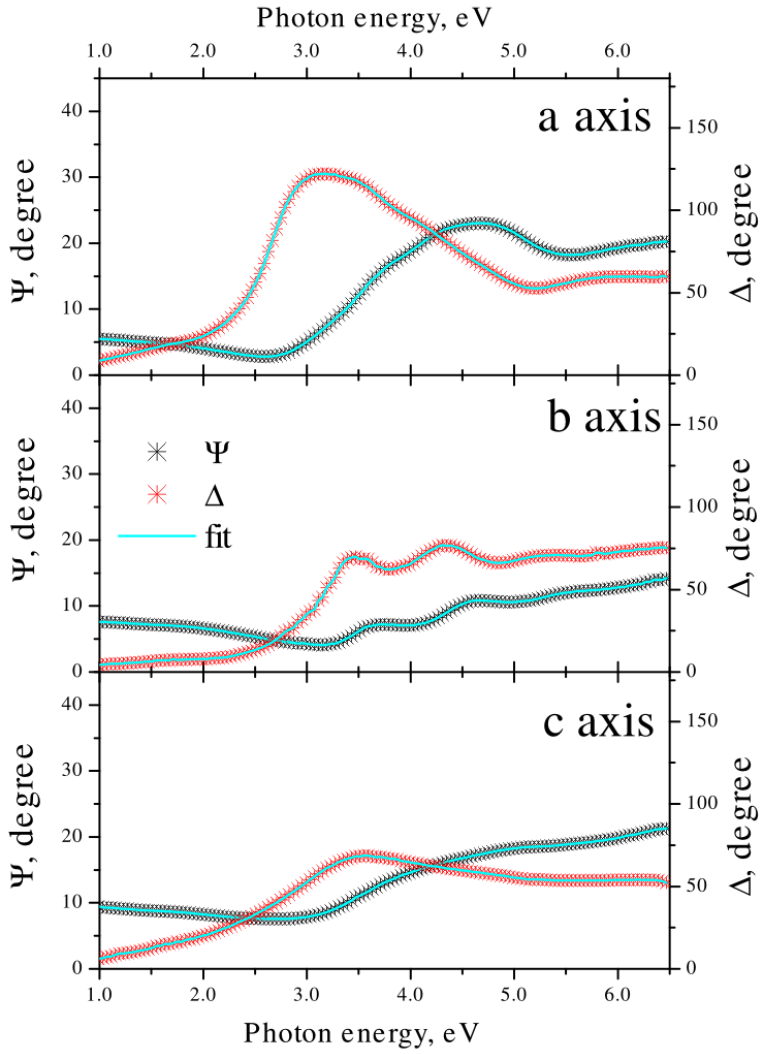

Figure 3.2: Ellipsometric angles Ψ and Δ for photon polarizations E ∥ *a*-, E ∥ *b*- and E ∥ *c*-axis for 70° angle of incidence measured at room temperature. By solid cyan lines a numerical regression procedure fit is shown (79).

A minimum set of Lorentzian oscillators, with one high-energy oscillator beyond the investigated spectral range, was introduced to represent a dielectric function in the form $\varepsilon(\omega) = \varepsilon_\infty + \sum_j \frac{S_j}{\omega_j^2 - \omega^2 - \mathrm{i}\omega\Gamma_j}$, where ω_j, Γ_j, and S_j are the peak energy, width, and oscillator strength of the jth oscillator, and ε_∞ is the core contribution from the dielectric function, as described in Chapter 1 of this thesis. The parameters determined by simultaneous fitting to $\varepsilon_1(\omega)$ and $\varepsilon_2(\omega)$ measured at 7 K are listed in Table 3.1. The respective spectra and Lorentzians are shown in Figure 3.4.

Since the spectrum along the *c*-axis shows no anomalies and no significant temperature dependence, only the optical response within the *ab* plane (along *a*-axis, or perpendicular to the CuO chains, and along *b*-axis, or along the CuO chains) is considered. A detailed analysis of the spectra, shown in Figures 3.3 (a,b), reveals that the origin of the temperature dependence for both polarizations is qualitatively

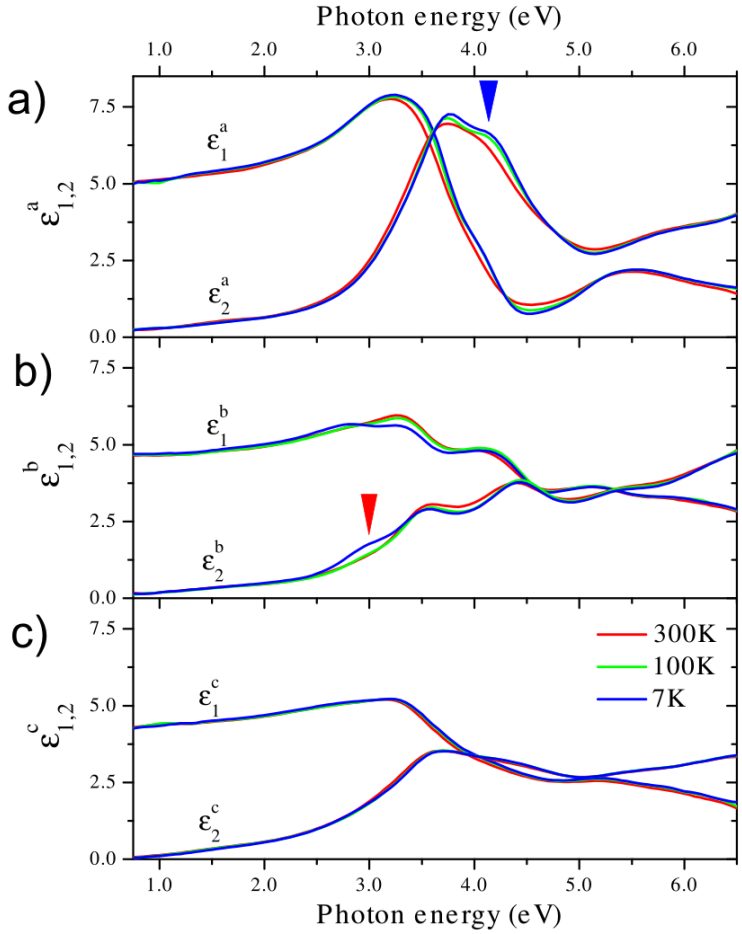

Figure 3.3: Real $\varepsilon_1(\omega)$ and imaginary $\varepsilon_2(\omega)$ parts of the dielectric function of $LiCuVO_4$ at 7, 100, and 300 K for photon polarizations (a) E $\parallel$ a-, (b) E $\parallel$ b- and (c) E $\parallel$ c-axis. Blue and red arrows mark the temperature dependent features discussed in the text (79).

different.

At first, we focus on the data with polarization along the a-axis, perpendicular to the chains. The temperature-difference spectra $\Delta\sigma_1^a(\omega, T)$ and $\Delta\varepsilon_1^a(\omega, T)$ (with con-

Table 3.1: Parameters of Lorentz oscillators resulting from a dispersion analysis of complex dielectric response in a-axis (b-axis) [c-axis] polarization in $LiCuVO_4$ measured at $T = 7$ K. ε_∞=1.75 (ε_∞=1.69) [ε_∞=1.55] (79).

ω_j(eV)	S_j (eV^2)	Γ_j(eV)
3.31 (2.93)	1.86 (0.52)	0.62 (0.47)
3.70 (3.55) [3.59]	9.30 (5.92) [6.83]	0.67 (0.93) [1.11]
4.20 (4.41) [4.38]	20.6 (7.19) [15.7]	1.07 (0.81) [2.03]
5.94 (5.47) [5.58]	21.5 (16.8) [2.80]	1.62 (1.76) [1.11]
6.86 (7.00) [7.00]	24.0 (66.2) [59.3]	1.00 (1.90) [2.79]

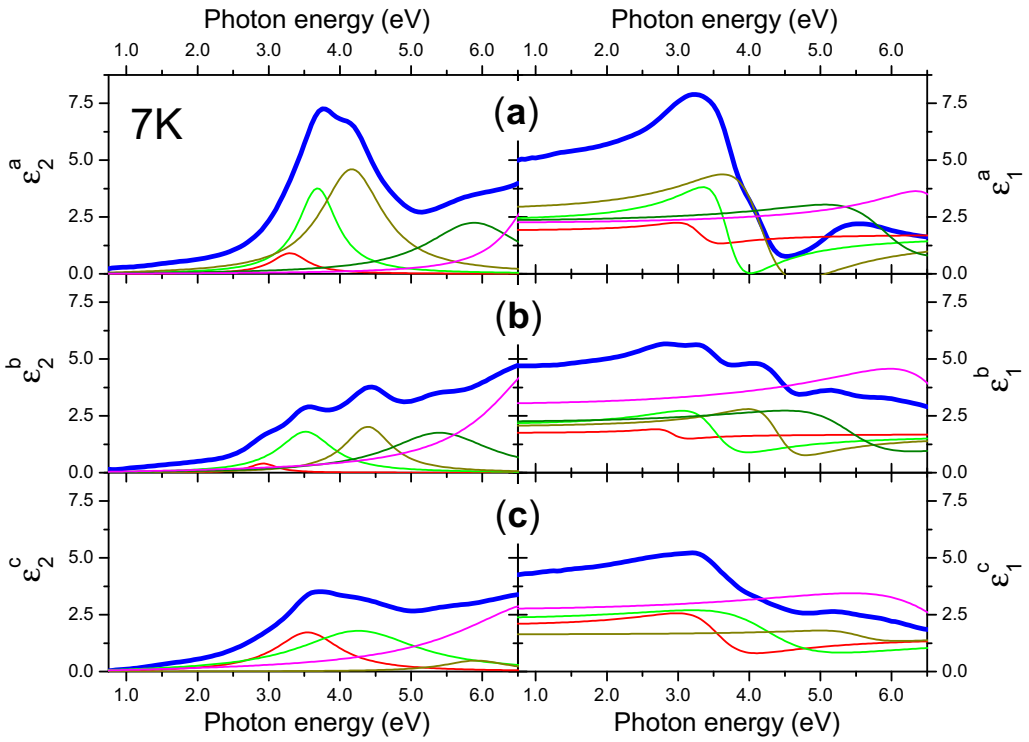

Figure 3.4: Real $\varepsilon_1(\omega)$ and imaginary $\varepsilon_2(\omega)$ parts of the dielectric function of $LiCuVO_4$ measured at 7K for photon polarizations (a) E $\parallel$ a, (b) E $\parallel$ b and (c) E $\parallel$ c and represented by the individual contributions of separate Lorentzian bands. The parameters are listed in Table 3.1 (79).

secutive intervals $\Delta T = 50$ K) displayed in Figure 3.5 (a) can be described mainly as a gradual narrowing and shift of the optical band at 4.2 eV with decreasing temperature, without any discernible change in its intensity. This behavior is typical for interband transitions and can be attributed to lattice anharmonicity. This conclusion is supported by the smooth temperature evolution of the σ_1^a amplitude at 4.2 eV and the changes in ε_1^a at 3.8 and 4.45 eV [upper and lower panels in Figure 3.5 (b), respectively].

A noticeable kink in the temperature dependence of σ_1^a and ε_1^a is revealed at about 30 K. A maximum in the magnetic susceptibility of $LiCuVO_4$ was also observed at almost the same temperature ($\sim$ 28 K). This close agreement suggests that the additional narrowing of the inter-chain charge transfer excitation below 30 K may occur as the result of the in-plane magnetic correlations established within the Cu-O chains.

In contrast, the $\Delta\sigma_1^b(\omega)$ difference spectra along the chains [see Figure 3.6 (a)] show the emergence of a well-defined absorption peak at 2.95 eV at low temperatures, which is accompanied by an antiresonance feature with zero-crossing at the same energy in $\Delta\varepsilon_1^b(\omega)$. Figure 3.6 (b) shows the temperature dependence of the σ_1^b amplitude near the center of this peak (upper trace) and the corresponding changes

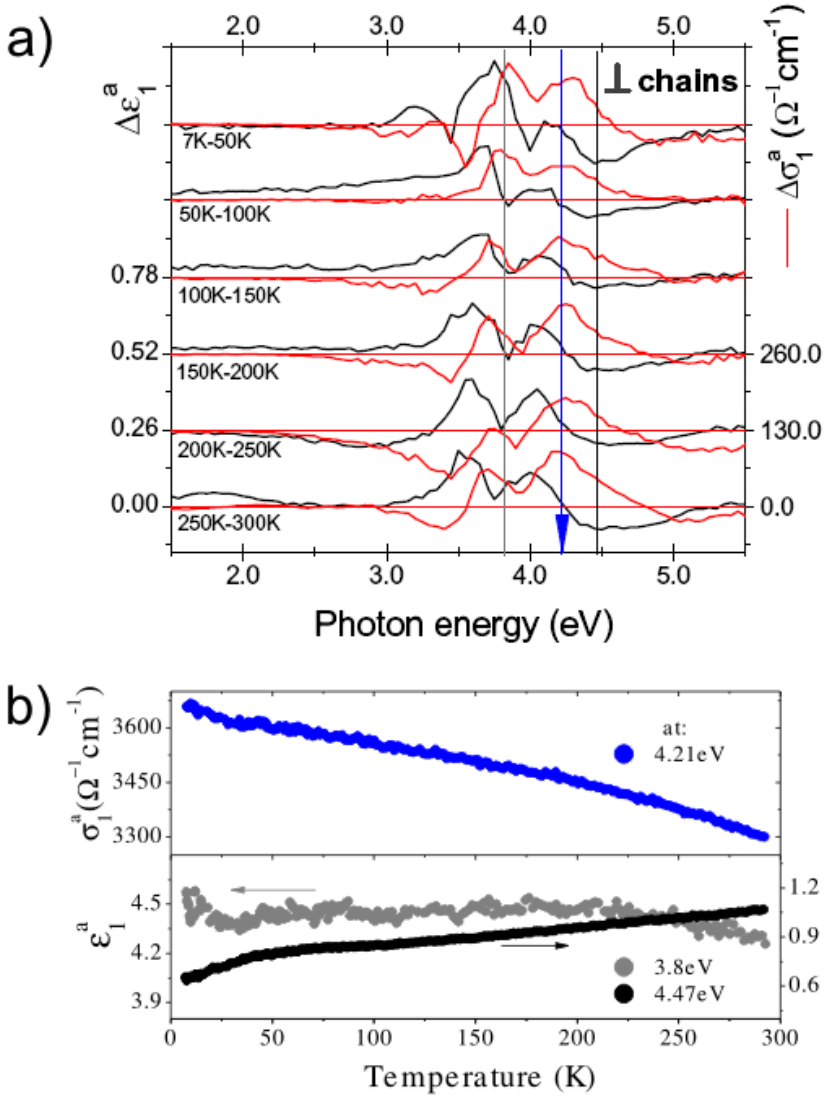

Figure 3.5: (a) Temperature-difference spectra $\Delta\sigma_1^a(T,\omega) = \sigma_1^a(T_1,\omega) - \sigma_1^a(T_2,\omega)$ (red) and $\Delta\varepsilon_1^a(T,\omega) = \varepsilon_1^a(T_1,\omega) - \varepsilon_1^a(T_2,\omega)$ (black) of $LiCuVO_4$ for polarizations perpendicular to the chains. Successive $\Delta\sigma_1^a(T,\omega)$ and $\Delta\varepsilon_1^a(T,\omega)$ spectra are shifted by 130 Ω^{-1}cm^{-1} and 0.26 for clarity. The arrow marks the same energy as in Figure 3.3 (a). (b) Temperature dependence of σ_1^a and ε_1^a measured at 3.8, 4.21 and 4.47 eV for polarization perpendicular to the chains, as marked by vertical lines in (a). Cooling-down and warming-up curves are consistent and were averaged (79).

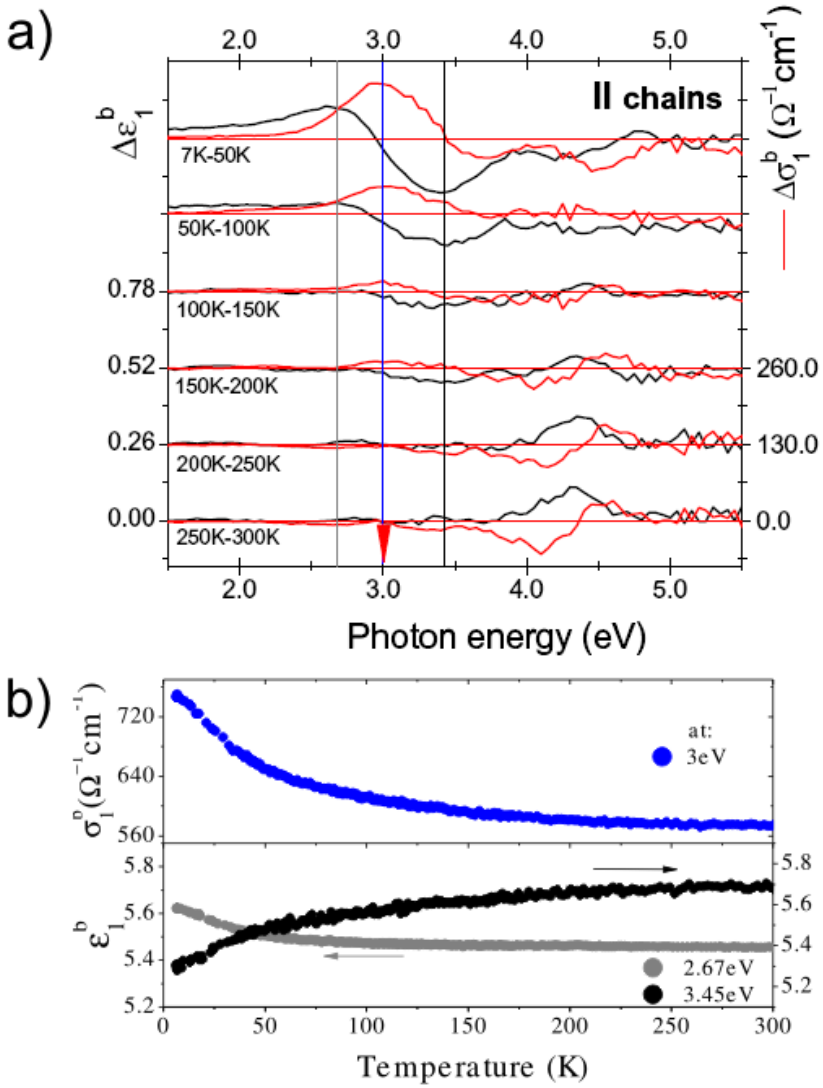

Figure 3.6: (a) Temperature-difference spectra $\Delta\sigma_1^b(T,\omega) = \sigma_1^b(T_1,\omega) - \sigma_1^b(T_2,\omega)$ (red) and $\Delta\varepsilon_1^b(T,\omega) = \varepsilon_1^b(T_1,\omega) - \varepsilon_1^b(T_2,\omega)$ (black) of $LiCuVO_4$ for polarizations along the chains. Successive $\Delta\sigma_1^b(T,\omega)$ and $\Delta\varepsilon_1^b(T,\omega)$ spectra are shifted by 130 Ω^{-1}cm^{-1} and 0.26 for clarity. The arrow marks the same energy as in Figure 3.3 (b). (b) Temperature dependence of σ_1^b and ε_1^b measured at 2.67, 3.0 and 3.45 eV for polarization along the chains, as marked by vertical lines in (a). Cooling-down and warming-up curves are consistent and were averaged (79).

in ε_1^b measured at the off-resonant photon energies 2.65 and 3.45 eV (lower traces). These changes are Kramers-Kronig consistent and indicate a pronounced intensity enhancement of the band at 2.95 eV below 80 K, the temperature below which the magnetic susceptibility begins to deviate from the mean-field Curie-Weiss behavior due to the appearance of short-range spin correlations along the copper-oxide chains (77), as shown in Figure 3.1 (b).

The existence of positive and negative regions in the $\Delta\sigma_1^{a,b}(\omega)$ spectra [Figures 3.5 (a) and 3.6 (a)] indicates a redistribution of optical spectral weight between single bands. This can be quantified by integrating the optical conductivity in terms of the effective charge density

$$\Delta N_{eff}(\omega, T) = \frac{2m}{\pi e^2 N_{\mathrm{Cu}}} \int_0^{\omega} \Delta\sigma_1(\omega', T) d\omega', \tag{3.1}$$

where m is the free electron mass and $N_{\mathrm{Cu}} = 1.4 \times 10^{22}$ cm^{-3} is the density of Cu atoms. Figure 3.7 (a) summarizes the low-temperature changes in spectral weight. For polarization along the chains, the integral increases at low ω because of the band at 2.95 eV, but this gain is compensated by a spectral weight loss within the spectral range of the higher energy bands at 3.5 and 4.4 eV, such that the optical sum rule is satisfied. For polarization perpendicular to the chains, the integral of $\Delta\sigma_1^a(\omega)$ is consistent with a narrowing of the band at 4.2 eV upon cooling, and no spectral weight redistribution between the 3.7 and 4.2 eV bands is indicated.

Discussion

Now, we will compare the salient observations to the results of model calculations (by P. Horsch, Max Planck Institute for Solid State Research, Stuttgart, Gemany), beginning with the overall anisotropy of the optical spectrum [Figure 3.3 (a,b)]. Since the main transitions are expected to be due to Op^6 Cu$d^9 \rightarrow$ Op^5 Cud^{10} excitations, the optical spectrum of the previously proposed (80) *pd*-Hamiltonian, with on-site energies $\epsilon_p - \epsilon_d = 3.5$ eV and hopping parameters $t_{pd} = 1.4$, $t_{pp}^a = 0.55, t_{pp}^b = 0.5, t_{pp}^{2b} = 0.4$ eV, was computed [Figure 3.7 (b)]. While the overall agreement with the experimental data is reasonable, the mode at 2.95 eV is not described by the single-electron *pd* model, and the strong temperature dependence of its spectral weight suggests that it is generated by many-body effects. Recent calculations of the optical conductivity of edge-sharing copper-oxide chains within a *pd* model including the on-site Coulomb repulsion (62) have assigned the lowest-energy transition along the chains to ZRS excitations. A strong temperature dependence of the spectral weight due to spin-correlation effects was also predicted, in qualitative agreement with our data.

However, close inspection of the ellipsometric data indicates a more complex behavior that cannot be understood in terms of incoherent ZRS excitations.

In Figure 3.8 (a) an enlarged view of the complex dielectric function is shown within the spectral region of the 2.95 eV band. From this picture, the emergence of the satellite absorption peak at 2.15 eV at low T is evident from the changes in both the imaginary, $\varepsilon_2^b(\omega)$, and real, $\varepsilon_1^b(\omega)$, parts of the complex dielectric function presented in Figure 3.3(b). The arrow in the lower panel of Figure 3.8 (a) marks, in

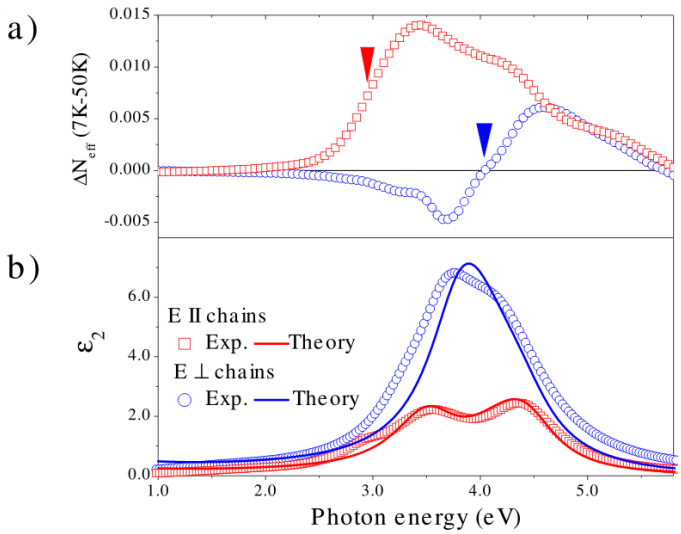

Figure 3.7: (a) Spectral weight changes $\Delta N_{eff}(\omega) = N_{eff}(\omega, 50\ \mathrm{K}) - N_{eff}(\omega, 7\ \mathrm{K})$ in $LiCuVO_4$ for polarizations along (open squares) and perpendicular (open circles) to the chains. The arrows mark the same energies as in Figs. 3.3 (a,b). (b) ε_2 spectrum for polarizations along and perpendicular to the chains derived from experiment at 7 K and calculated from the *pd*-Hamiltonian as described in text. The optical bands above 5 eV listed in Table 3.1 were subtracted (79).

particular, the photon energy at which the positive changes in $\varepsilon_2^b(\omega)$ coincide with a crossing in $\varepsilon_1^b(\omega)$, as the temperature decreases from 300 K to 100 K. These features are clearly resolved in the temperature-difference spectra shown in Figure 3.8 (b), as a "bump" in $\Delta\varepsilon_2^b(\omega)$ and a "wiggle" in $\Delta\varepsilon_1^b(\omega)$. Therefore, Figure 3.8 (b) shows that the 2.95 eV band exhibits a double-peak structure with a satellite peak at 2.15 eV that is not visible in Figures 3.3 – 3.7 because of its low intensity.

Figure 3.9 (b) shows the temperature differences spectra of $\varepsilon_2^b(\omega)$ near 2.9 eV corrected for a background arising from the temperature variation of the high-energy optical bands. The gradual changes of the electronic background with temperature are well controlled by the dispersion analysis of the whole $\varepsilon_1^b(\omega)$ and $\varepsilon_2^b(\omega)$ spectra performed at every temperature.

The features shown in Figure 3.8 and can be quantitatively parameterized by the Lorentzian fit. From this fit, the temperature dependence of each individual band spectral weight is determined by its oscillator strength, $\Delta SW^{(l)}(T) = S_l(T)[\mathrm{eV}^2]$. Alternatively, one can integrate the real part of the optical conductivity within the individual band, $\Delta SW^{(l)}(T) = 1/4\pi \int^{(l)} \omega \Delta\varepsilon_2^b(\omega) d\omega$, after subtraction of the electronic background. Both the above procedures give the same temperature dependence of the individual band spectral weight, the uncertainty is within the symbol size in Figure 3.9 (c).

The temperature dependence of the individual band spectral weight was parameterized as $\Delta N_{eff}^{(l)}(T) = \frac{2m}{N_{\mathrm{Cu}}\pi e^2} \Delta SW^{(l)}(T)$ in Figure 3.9 (c), where $\Delta SW^{(l)}(T)$ is determined by the oscillator strength of the individual band. The spectral weight of both bands increases upon cooling down to ~ 80 K in a parallel manner. For lower

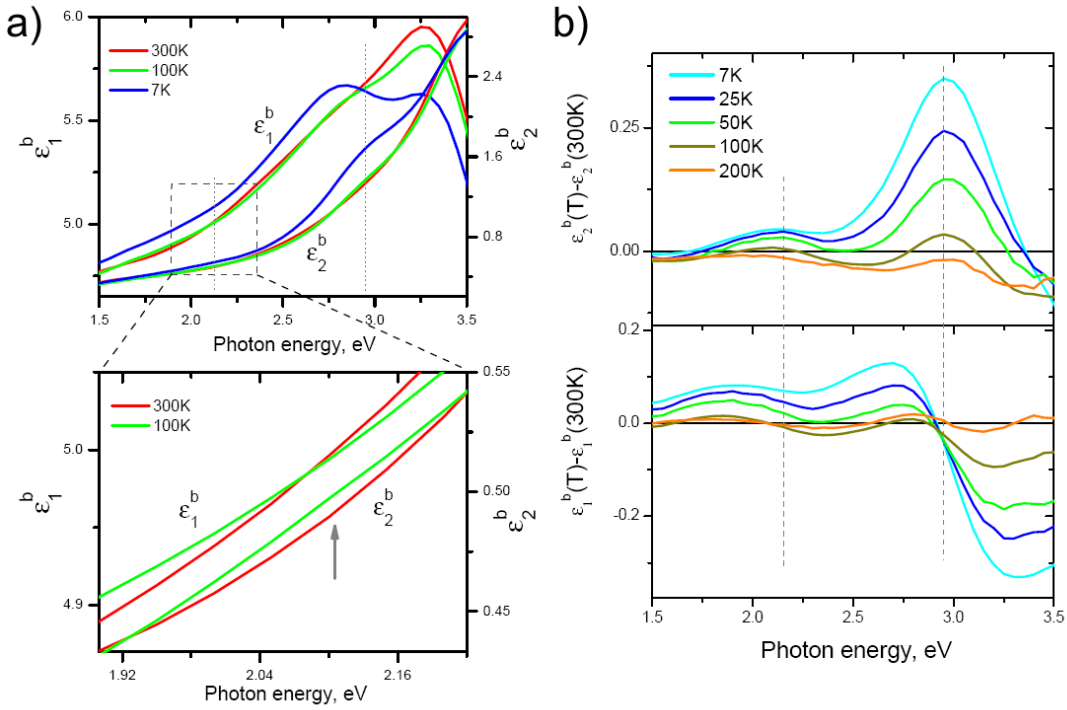

Figure 3.8: (a) The enlarged view of complex dielectric function: real $\varepsilon_1^b(\omega)$ and imaginary $\varepsilon_2^b(\omega)$ parts of the dielectric function of $LiCuVO_4$ measured at 7, 100, and 300 K in $b-$axis polarization. (b) Temperature-difference spectra of imaginary $\varepsilon_2^b(\omega)$ (upper panel) and real $\varepsilon_1^b(\omega)$ (lower panel) parts of the dielectric function of $LiCuVO_4$ for polarization along the chains. Vertical dashed lines mark photon energies 2.15 eV and 2.95 eV at which resonant behavior in $\Delta\varepsilon_2^b(\omega)$ coincides with zero crossing in $\Delta\varepsilon_1^b(\omega)$. (79).

temperatures, however, the intensity of the lower-energy band saturates, while that of the higher-energy band keeps increasing.

The two bands can be quantitatively described as an exciton doublet in a model incorporating long-range Coulomb interactions, if the one-band Hubbard model obtained by downfolding from the *pd*-Hamiltonian (81) is considered. In the case of edge-sharing chains, it is important to consider both NN (t_1) and NNN (t_2) hopping [Figure 3.9 (a)]. Besides the kinetic energy terms

$$K_{i,l} = -\sum_{\sigma} t_l (c^+_{i+l,\sigma} c_{i,\sigma} + c^+_{i,\sigma} c_{i+l,\sigma}), \tag{3.2}$$

the local Hubbard interaction U and the long-range Coulomb interaction V_l are included. The model thus reads (82):

$$H = \sum_{l=1}^{2} \sum_{i} K_{i,l} + U \sum_{i} n_{i,\uparrow} n_{i,\downarrow} + \sum_{i,l\geq 1} V_l n_i n_{i+l}. \tag{3.3}$$

Here $V_l = V/l$ is parameterized by the *nn* Coulomb interaction V. An optical excitation induced by the current operators $j_l = -ie \sum_{i,\sigma} d_l t_l (c^+_{i+l,\sigma} c_{i,\sigma} - \text{h.c.})$

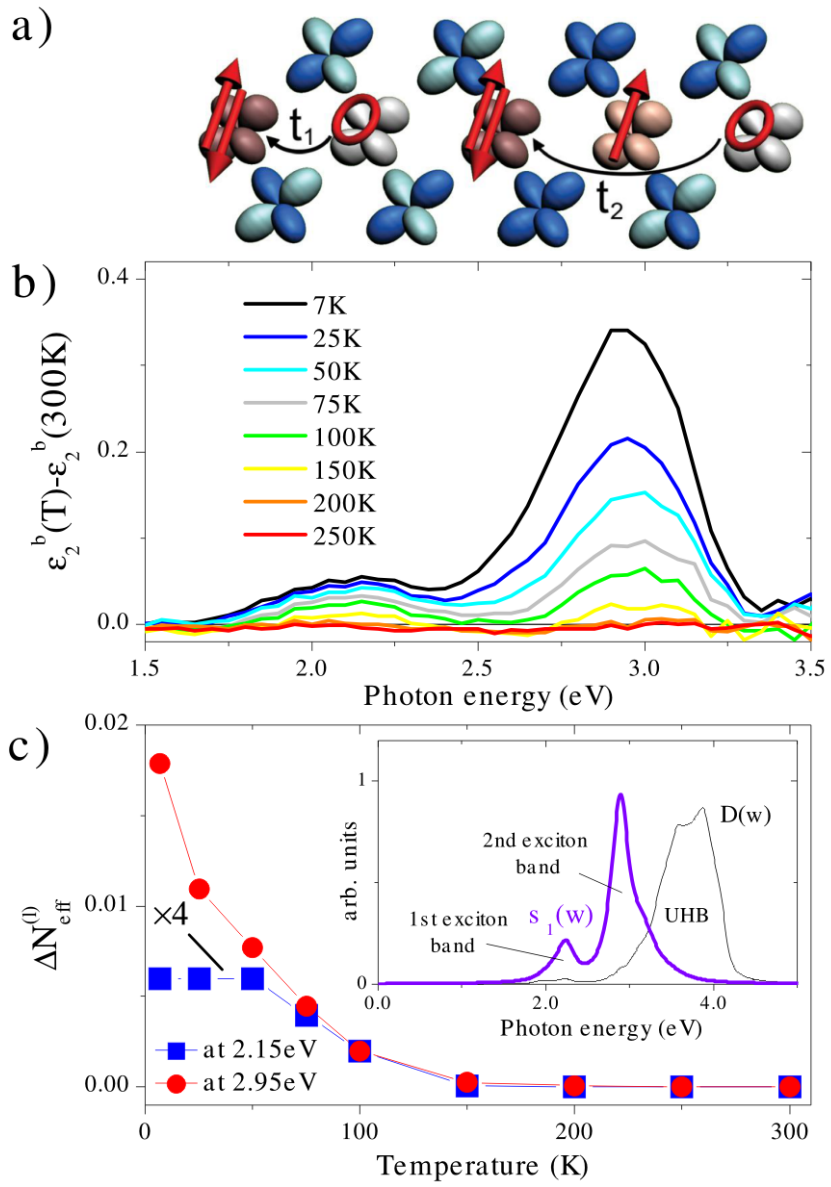

Figure 3.9: (a) Mott-Hubbard exciton formed by d^9L_h and d^{10} states generated by NN (t_1) or NNN (t_2) hopping. (b) Temperature-difference spectra of ε_2 near 2.9 eV for polarization along the chains. (c) Temperature dependence of spectral weight of exciton bands at 2.15 and 2.95 eV. Inset: $\sigma_1(\omega)$ and density of states $D(\omega)$ of the UHB calculated with Equation 3.3 at $T = 0$ and parameters $U = 3.75$, $V = 1.6$, $t_1 = 0.08$ and $t_2 = 0.1$ eV (broadening $\delta = 0.1$) (79).

generates an empty site (ZRS) and a doubly occupied site (doublon in the upper Hubbard band, UHB) one ($d_1 = b$) or two ($d_2 = 2b$) Cu sites apart [Figure 3.9 (a)] (47). As a result of the Coulomb attraction between the positive hole and the negative doublon, exciton states emerge below the UHB. For NN hopping only, the lowest-energy exciton dispersion is small, $\sim -(2t_1 \cos(k/2))^2/V$ (46, 48, 49). In our case, however, the dispersion is large and given by $E_1(k) = U - V \pm 2t_2 \cos(k)$ due to the t_2 process, and the twofold degeneracy is lifted. The second exciton is centered at $U - V/2$. As seen in the inset of Fig. 3.9(c), the SW is concentrated in the exciton states, and only little optical weight is found in the UHB, despite its large density of states. While this representation gives a correct description of the energy scales, one would expect sharp excitons if one considered the charge sector only. It is argued in Ref. (79), however, that the coupling of the spin degrees of freedom (mainly due to t_2-processes) implies a momentum average over the exciton band. This leads to a band with a width of $\sim 4t_2 \sim 0.4$ eV for the lowest exciton, consistent with our experimental data.

The spectral weight for the individual exciton transitions can be expressed in terms of the kinetic energy per bond and the hopping length d_l as $\Delta N_{eff}^{(l)} = -\frac{m}{\hbar^2} d_l^2 \langle K_{i,l} \rangle$. The kinetic energy of the model given in Equation (3.3) is equivalent to the superexchange energy of the corresponding Heisenberg model $H_s = \sum_l J_l \sum_i (\vec{S}_i \cdot \vec{S}_{i+l} - 1/4) - J_1^F \sum_i \vec{S}_i \cdot \vec{S}_{i+l}$ where $J_l \simeq 4t_l^2/(U - V_l)$. The ferromagnetic coupling J_1^F originates from a two hole state on O that is not included in Equation 3.3, but must be considered for the magnetism. Thus, the weights of the first and second excitons are directly related to the corresponding spin correlations:

$$\Delta N_{eff}^{(l)} = -\frac{m}{\hbar^2} d_l^2 J_l \langle \vec{S}_i \cdot \vec{S}_{i+l} - 1/4 \rangle. \tag{3.4}$$

This relation explains why the second exciton is much stronger: (i) $d_2 = 2d_1$ and (ii) the NN spin-correlation function ($l = 1$) is frustrated and small, because $J_1 - J_1^F$ is ferromagnetic and small compared to the antiferromagnetic coupling constant J_2. For $l = 2$, the correlation function is large and negative, leading to large variation in $\Delta N_{eff}^{(2)}$ as a function of temperature. These arguments also explain why the first exciton band experimentally observed at 2.15 eV is suppressed below 80 K, whereas the second band at 2.95 eV shows a steep increase, see Figure 3.9 (c), following the spin-correlation effects. A numerical computation of Equation 3.4 using exchange parameters determined by neutron scattering (44) agrees within a factor of two with the experimentally determined $\Delta N_{eff}^{(2)}(75\text{ K} - 7\text{ K}) \simeq 0.013$. Within the model the exciton mode draws its spectral weight from the UHB, which may be superimposed on the charge-transfer excitations at 3.5 and 4.4 eV.

In summary, our optical measurements have yielded clear evidence for exciton formation and interesting insights into the relationship between the charge dynamics and frustrated magnetism in a Mott-Hubbard insulator with edge-sharing copper-oxide chains. The results and methodology established here are a good starting point for further investigations of compounds with doped copper-oxide chains and planes.

3.2 $NaCu_2O_2$

Structure. Magnetic properties. Experimental details

The crystal structure of $NaCu_2O_2$ belongs to the *Pnma* space group with an orthorhombic crystal structure, $a = 6.2087$Å, $b = 2.9343$Å, $c = 13.0648$Å (83). The unit cell is composed of two pairs of edge-sharing CuO chains, running along the b axis and shifted relative to each other by $b/2$. They are separated by non-magnetic Na^+ ions along the a axis and interconnected by diamagnetic Cu^{1+} ions in O-Cu^{1+}-O dumbbell complexes along the c axis, see Figure 3.10 (a). There are 4 Cu^{2+} ions per unit cell, therefore the density of Cu^{2+} ions is $N_{Cu^{2+}} = 1.68 \cdot 10^{22}$ cm^{-3}. Within the single chain, the Cu^{2+}-Cu^{2+} distance is 2.934 Å, and the Cu-O-Cu bond angle is 92.9°.

The magnetic properties and magnetic structure of $NaCu_2O_2$ have been intensively studied by single-crystal neutron diffraction (84), powder neutron diffraction (43), nuclear magnetic resonance (NMR) (85), and resonant X-ray diffraction (86). Magnetic susceptibility data for a single crystal of $NaCu_2O_2$ along the principal axes are shown in Figure 3.10 (b). The data obey the Curie-Weiss law for paramagnetic media above 150 K, with the Curie temperature $\Theta_C = -62$ K (43). A broad maximum, typical for low-dimensional spin magnets, is observed at $T = 52$ K, associated with short-range antiferromagnetic correlations within the chains. The low-temperature susceptibility and specific heat data indicate a magnetic phase transition at $T_N = 11.5$ K (86). Because of the 92.9° Cu-O-Cu bond angle within the chains, the NN exchange integral is small ($J_1 = -16.4$ K) and dominated by that between the next-nearest neighbours ($J_2 = 90$ K). Based on powder neutron diffraction and NMR data, a circular *bc*-polarized helix structure was proposed as the magnetic ground state (43, 85). Recently, single-crystal neutron diffraction data revealed a

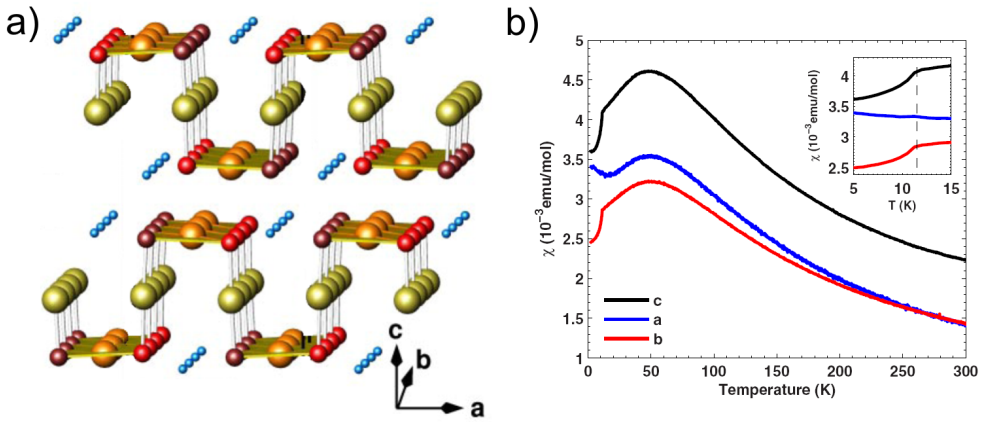

Figure 3.10: (a) Schematic structure of $NaCu_2O_2$. The CuO chains shown by orange and red colors, Na ions – green, Cu^{1+} ions – yellow. (b) Temperature dependence of the magnetic susceptibility $\chi(T)$ of $NaCu_2O_2$ single-crystal along the principal a, b and c axes; the applied magnetic field is 1 kOe (86).

more complex elliptical helix structure with alternating polarization planes with the propagation vector $k = (0.5, \xi, 0)$, $\xi = 0.228 \pm 0.002$ (84).

Single crystals of $NaCu_2O_2$ were grown by the self-flux technique, as described in Ref. (83). X-ray diffraction and inductively coupled plasma atomic spectroscopy measurements showed no impurity phases and chemical composition consistent with ideal stoichiometry (43). For our optical measurements a single crystal of $NaCu_2O_2$ with dimensions 5×5×0.2 mm and a freshly cleaved *ab* surface was used.

Experimental data

Room temperature ellipsometric data represented by the angles Ψ and Δ are shown in Figure 3.11. The data were measured at 65° and 72.5° angles of incidence for orientations of the sample with the *a* or *b* axis in plane of incidence, denoted as ⊥ and ∥, respectively, corresponding to the orientation of the electric field with respect to the CuO edge-sharing chains. In the Euler angle representation, these orientations are read as (0°,0°,0°) and (90°,0°,0°).

Changes of ellipsometric spectra with alternation of the sample orientation (Figure 3.11) point to an intrinsic anisotropy of $NaCu_2O_2$. To derive the in-plane principal components of the dielectric tensor from the measured ellipsometric data, a numerical regression procedure was employed (4), as described in Chapter 1. Since

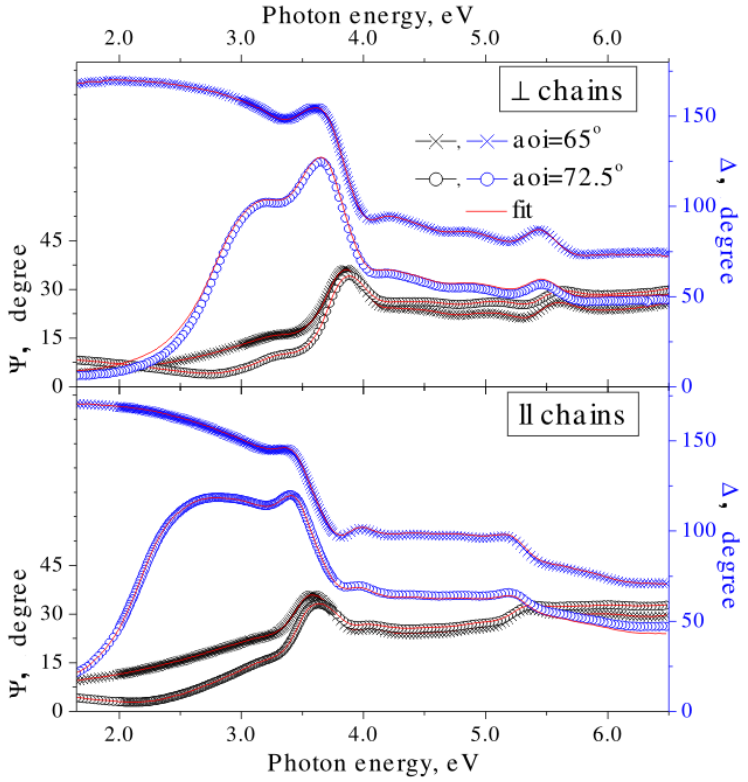

Figure 3.11: The room temperature ellipsometric angles Ψ and Δ measured for polarizations along and perpendicular to the CuO chains of $NaCu_2O_2$.

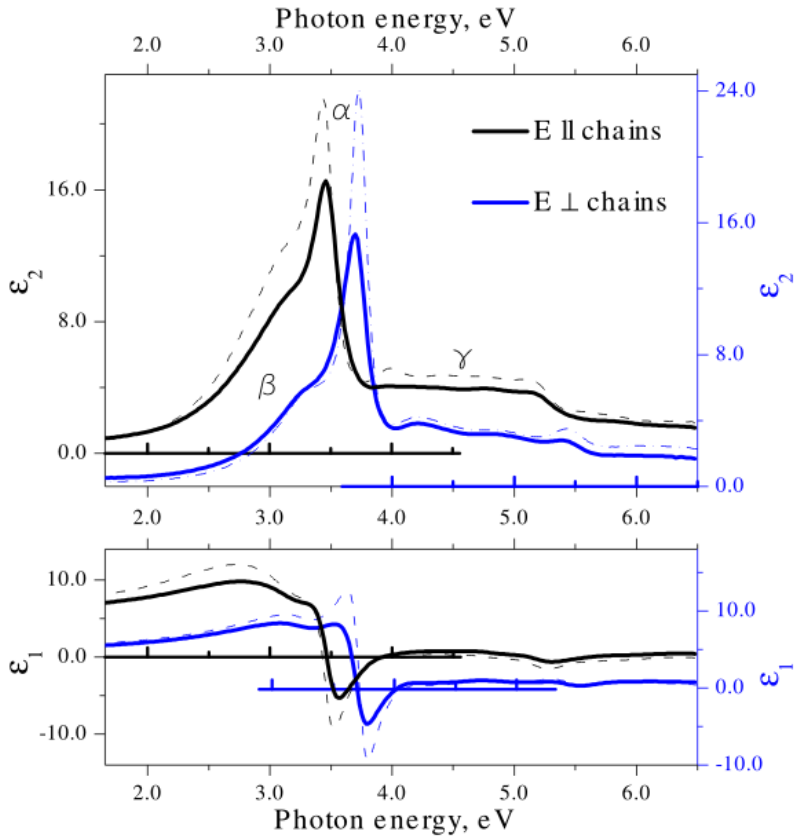

Figure 3.12: Room temperature spectra of the real ε_1 and imaginary ε_2 parts of the dielectric function for polarizations along and perpendicular to the chains of $NaCu_2O_2$. For polarization along the chains spectra are shifted by 2 for ε_2 and 4 for ε_1 for clarity. Dotted lines depict the pseudo-dielectric functions.

measurements of the optical response along the c axis could not be obtained due to the thinness of the sample, the spectra measured at two angles of incidence for each polarization were used in the fitting procedure. The fit of data is shown by thin red lines in Figure 3.11. Resulting from the fit, the real and imaginary parts of the dielectric function for both polarizations are drawn in Figure 3.12. In this figure, the pseudo-dielectric function measured at 65° angle of incidence is also shown by dotted lines. The effect of anisotropy mainly appears in the pronounced peaks in the spectral range 2.5 – 4 eV. From this point we will discuss only the corrected dielectric function.

The optical spectra for both polarizations can be broken up into α, β and γ zones, as shown in Figure 3.12. The α zone comprises the spectral range of the strong and narrow absorption peaks located at 3.45 (along the chains) and 3.7 eV (perpendicular to the chains) that are dominating the spectra. The anomalous strength of these excitations leads to the negative values of ε_2. The left shoulders of these peaks near the insulating gap are marked as the β zone. The γ zone includes the broad and weak features above 4 eV, that give rise to a rather flat and featureless optical

Table 3.2: Parameters of Lorentz oscillators resulting from a dispersion analysis in polarizations perpendicular and (along) the chains in $NaCu_2O_2$ measured at $T = 7$ K. ε_∞=2.00, (ε_∞=1.77).

	ω_j(eV)	$\Delta\varepsilon$	γ_j(eV)
	(2.65)	(0.56)	(0.60)
β	3.37 (3.08)	0.91 (0.78)	0.57 (0.52)
	(3.26)	(0.47)	(0.33)
α	3.63 (3.40)	0.42 (0.32)	0.19 (0.19)
	3.71 (3.46)	0.38 (0.50)	0.12 (0.14)
	4.30 (4.01)	0.17 (0.22)	0.39 (0.51)
	4.85 (4.41)	0.42 (0.23)	0.87 (0.58)
γ	(4.75)	(0.19)	(0.52)
	5.40 (5.16)	0.11 (0.22)	0.43 (0.52)
	6.14 (5.96)	0.16 (0.12)	0.87 (0.89)
	7.07 (7.73)	0.26 (0.59)	0.88 (3.02)

response.

To separate the contributions from different optical bands to the dielectric function spectra for both polarizations, a classical dispersion analysis was performed, as described in Chapter 1. The parameters of a single complex Lorentzian oscillator were derived with high accuracy and reliability by simultaneously fitting to $\varepsilon_1(\omega)$ and $\varepsilon_2(\omega)$. They are listed in Table 3.2. Figure 3.13 represents the principal bands composing the dielectric response at 7 K for polarizations along and perpendicular to the chains.

According to the dispersion analysis, for polarization perpendicular to (along) the chains, the α zone of the spectra is composed of two narrow bands at 3.63 (3.40) and 3.71 (3.46) eV, giving in sum the extremely strong assymetric absorption band at 3.7 (3.45) eV. The γ zone of the spectra is composed of a series of excitation bands. Along the chains, four nearly equally spaced optical bands (4.01, 4.41, 4.75 and 5.16 eV) are resolved. Perpendicular to the chains, the dispersion analysis gives a broad band at 4.85 eV. However, this band can be split into two subbands which, being surrounded by excitations at 4.30 and 5.40 eV, form a series of excitations similar to that for polarization along the chains. The γ regions for both polarizations end in a broad weak band near 6 eV and one optical band beyond the investigated spectral range. Only one band located at 3.37 eV is lying in the β zone for polarization perpendicular to the chains. Along the chains this band is resolved into two subbands at 3.08 and 3.26 eV. In addition, there is an extra band at 2.68 eV, being the lowest-energy excitation along the chains.

The temperature dependencies of the real parts of the optical conductivity σ_1 and the real parts of the dielectric function ε_1 for both polarizations are plotted in Figure 3.14. The strongest temperature effect on the optical spectra observed is a growth of the 3.45 (3.7) eV sharp peak for polarization along (perpendicular to) the chains with decreasing temperature. Against a background of this growth, some

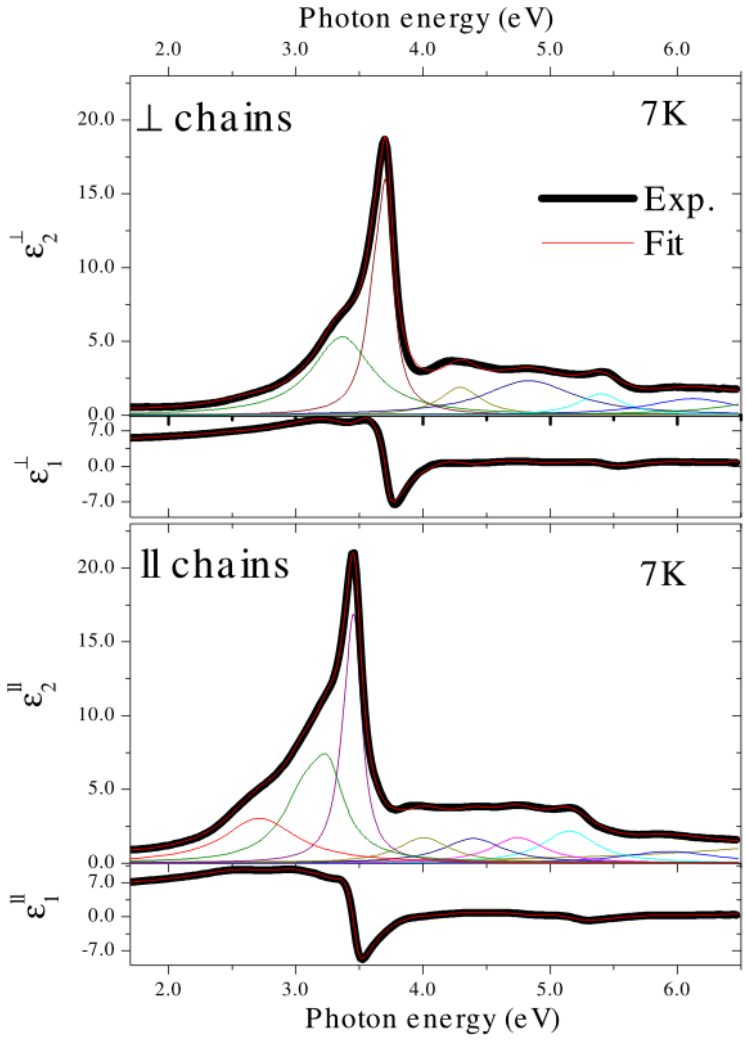

Figure 3.13: The real ε_1 and imaginary ε_2 parts of the dielectric function of $NaCu_2O_2$ measured at 7K (dark thick line) and dispersion analysis fit to the data (light thin line) for photon polarizations (a) perpendicular to and (b) along the chains of $NaCu_2O_2$. Thin colored lines draw the principal bands composing the optical response (see Table 3.2), as derived from dispersion analysis.

changes are apparent on the left shoulders of the strong peaks. Among them the temperature-driven feature centered near 2.65 eV for polarization along the chains is the most intriguing (see inset of Figure 3.14).

To study the temperature-driven changes in detail, temperature-difference spectra $\Delta\sigma_1(\omega, T)$ and $\Delta\varepsilon_1(\omega, T)$ with respect to 150 K are plotted in Figure 3.15. Perpendicular to the chains, ostensible collective changes in $\Delta\varepsilon_1^\perp$ and $\Delta\sigma_1^\perp$ are seen in the α and β zones between 2.5 and 4.5 eV. Alternating areas of positive and negative regions in the $\Delta\sigma_1^\perp(\omega)$ spectra within this spectral range are mutually compensated. This observation points to no spectral weight redistribution between individual bands and to conservation of optical-band intensities within this spectral

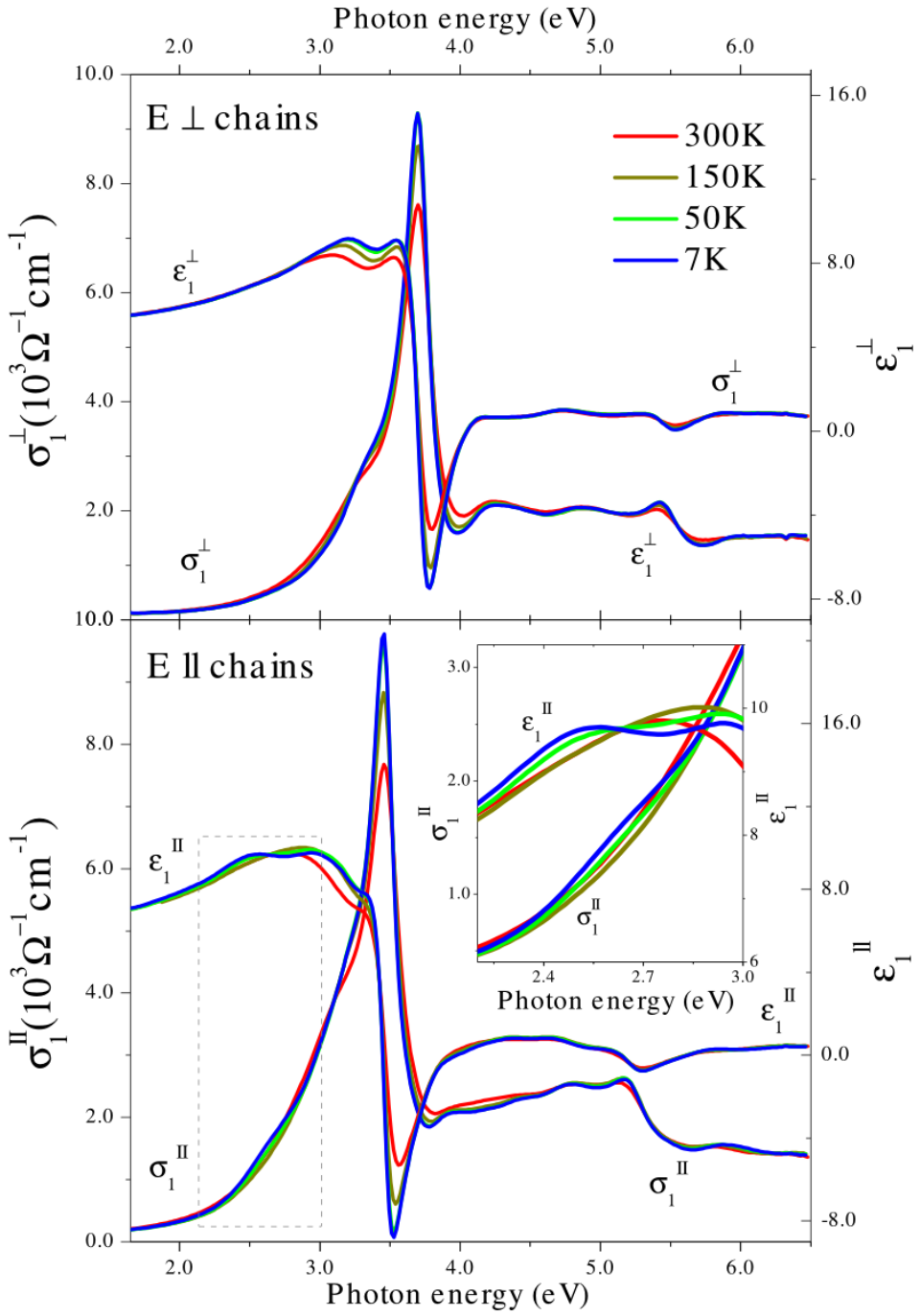

Figure 3.14: The real part ε_1 of the dielectric function and the real part σ_1 of the optical conductivity for polarizations along and perpendicular to the chains of $NaCu_2O_2$ measured at different temperatures. Inset: magnified view of σ_1 and ε_1 for polarization along the chains.

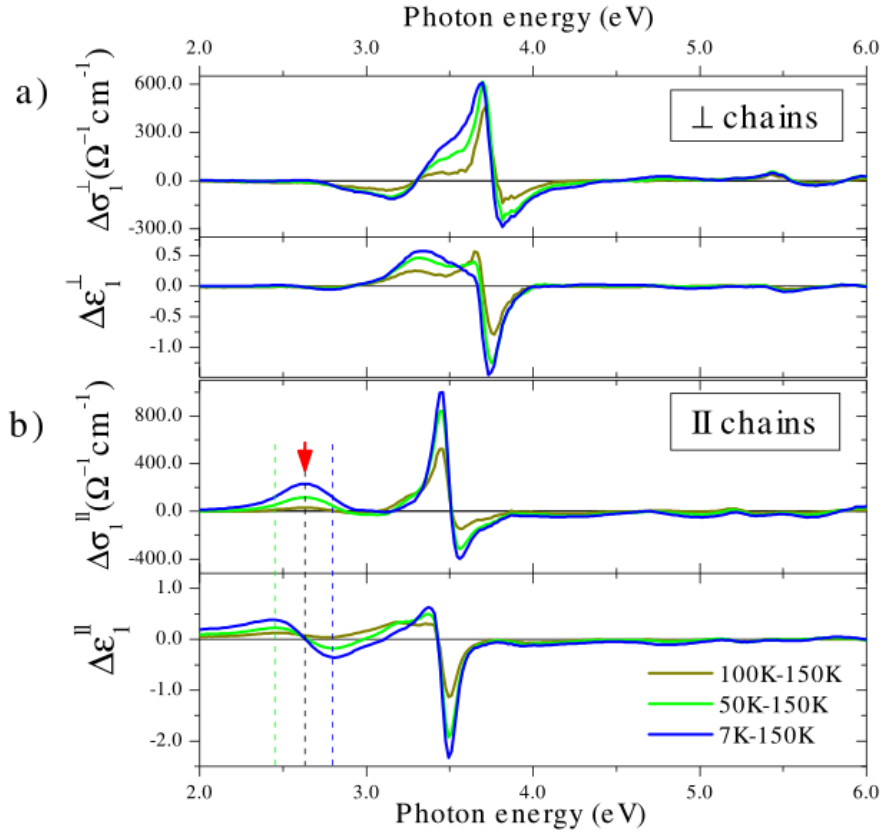

Figure 3.15: Temperature-difference spectra $\Delta\sigma_1(\omega,T) = \sigma_1(\omega,T) - \sigma_1(\omega, 150\text{ K})$ and $\Delta\varepsilon_1(\omega,T) = \varepsilon_1(\omega,T) - \varepsilon_1(\omega, 150\text{ K})$ of $NaCu_2O_2$ for polarizations (a) perpendicular to and (b) along the chains.

range. Therefore, these changes are induced by concurrent narrowing of the pronounced band at 3.7 eV and optical band located on its left shoulder at 3.37 eV. Above 4.5 eV there are no other changes, except tiny alterations near 5.5 eV, which can be attributed to the weak narrowing of the 5.4 eV band.

Along the chains, the appearance of the feature marked with red arrow in Figure 3.15 (b) makes the temperature-difference spectra $\Delta\varepsilon_1^{\parallel}$ and $\Delta\sigma_1^{\parallel}$ qualitatively different from those for polarization perpendicular to the chains. The resonance in $\Delta\sigma_1^{\parallel}$ at 2.65 eV and antiresonance with zero-crossing at the same energy in $\Delta\varepsilon_1^{\parallel}$, developing below 150 K, indicate a temperature-driven uprise of the optical band. The changes of the $\Delta\sigma_1^{\parallel}$ amplitude with temperature at the resonance frequency for this band and $\Delta\varepsilon_1^{\parallel}$ right below and above, as marked with vertical lines [see Figure 3.14 (b)], were, in particular, studied by dynamic scans shown in Figure 3.16. Being Kramers-Kronig consistent, an enhancement of $\sigma_1^{\parallel}$ at 2.62 eV below 150 K together with an upturn and a downturn in $\varepsilon_1^{\parallel}$ at 2.45 and 2.74 eV, respectively, confirms the pronounced intensity increase of the 2.65 eV band with decreasing temperature.

The transfer of spectral weight can be quantified by integrating the optical conductivity in terms of the effective charge density $\Delta N_{eff}(\omega,T) = \frac{2m}{\pi e^2 N_{\mathrm{Cu}}} \int_0^{\omega} \Delta\sigma_1^{\parallel}(\omega', T)d\omega'$,

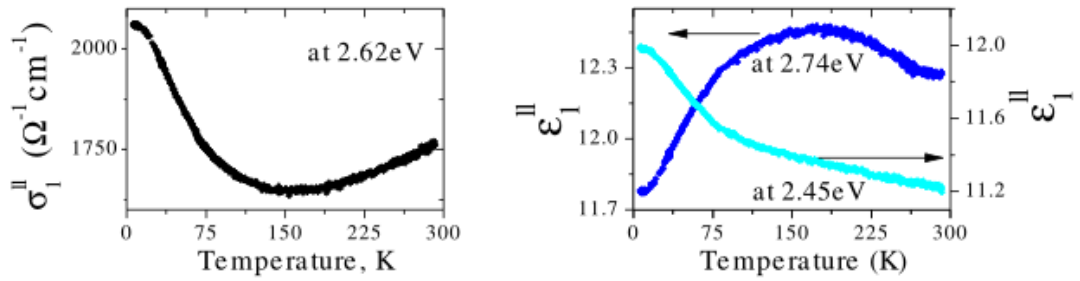

Figure 3.16: Temperature dependence of $\sigma_1^{\parallel}$ measured at 2.62 eV and $\varepsilon_1^{\parallel}$ measured at 2.45 and 2.74 eV for polarization along the chains of $NaCu_2O_2$, as marked by vertical lines in Figure 3.13 (b).

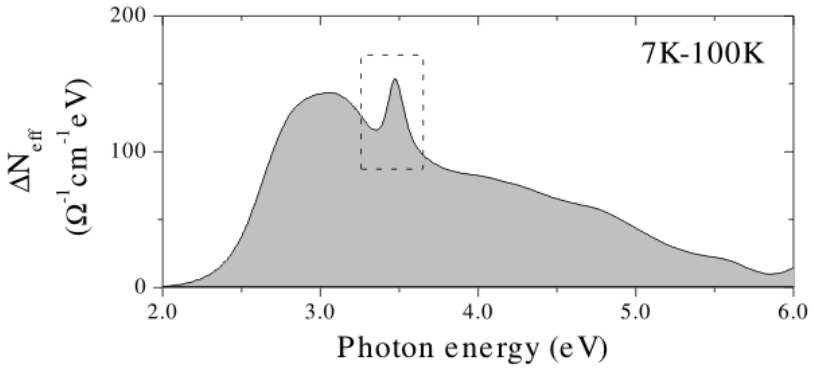

Figure 3.17: Spectral weight changes $\Delta N_{eff}(\omega) = N_{eff}(\omega, 7\text{ K}) - N_{eff}(\omega, 100\text{ K})$ for polarization along the chains of $NaCu_2O_2$.

where m is the free electron mass and $N_{Cu^{2+}} = 1.68 \times 10^{22}\text{cm}^{-3}$ is the density of Cu^{2+} ions. Figure 3.17 shows the changes in the spectral weight below 100 K along the chains. The rise of the spectral weight at low energies is due to the band at 2.65 eV. Above 3 eV this growth is compensated by a loss in the spectral weight of the higher-energy bands, following the optical sum rule. The feature marked with a rectangle in Figure 3.17 is originating from the narrowing of the strong optical band at 3.45 eV with temperature and signals of the spectral weight retaining within this band.

The temperature evolution of the bands at 3.7 eV (perpendicular to the chains) and at 2.65 and 3.45 eV (along the chains) can be also studied by a dispersion analysis. The oscillator strength of the 3.7 (3.45) eV band is 10.75 (9.93) eV^2. While the spectral weights located within these bands are conserved and independent of temperature, their bandwidths decrease gradually with temperature, as shown in Figure 3.18, left panel. The dispersion analysis demonstrates a prominent strengthening of the optical band at 2.65 eV along the chains with temperature decreasing below 150 K, see Figure 3.18, right panel, which is in full agreement with the measured dynamical scans, shown in Figure 3.16.

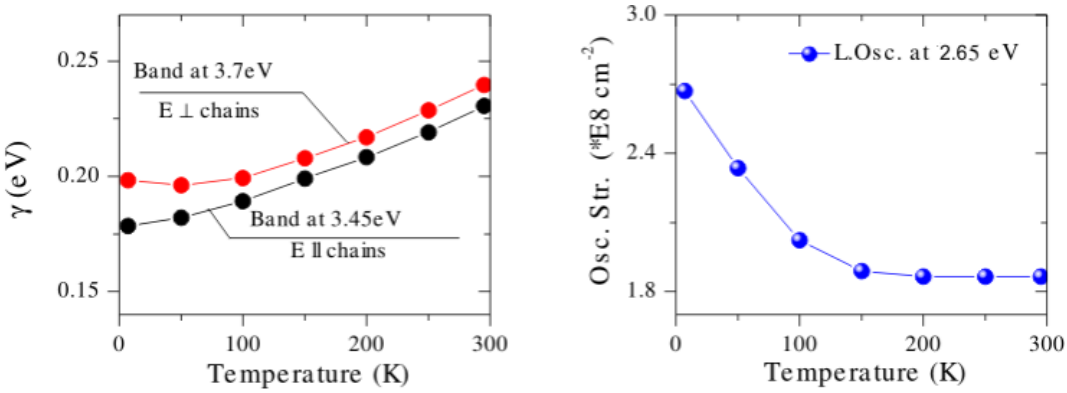

Figure 3.18: On the left: temperature dependence of the bandwidths of the Lorentz oscillators at 3.45 (black) and 3.7 eV (red) for polarizations along and perpendicular to the chains, respectively, of $NaCu_2O_2$. On the right: temperature dependence of the oscillator strengths of the 2.65 eV band for polarization along the chains.

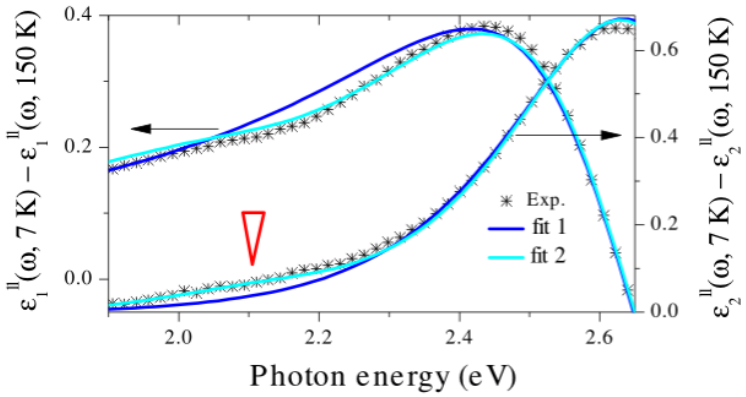

Figure 3.19: Temperature-difference spectra $\Delta\varepsilon_1(\omega) = \varepsilon_1(\omega, 7\text{ K}) - \varepsilon_1(\omega, 150\text{ K})$ and $\Delta\varepsilon_2(\omega) = \varepsilon_2(\omega, 7\text{ K}) - \varepsilon_2(\omega, 150\text{ K})$ for polarizations along the chains of $NaCu_2O_2$ and fit1 and fit2, as described in text.

The close inspection of the temperature-difference spectra $\Delta\varepsilon_1^{\parallel}$ and $\Delta\varepsilon_2^{\parallel}$ in the spectral region below 2.5 eV reveals a deviation of the fit, incorporating the bands listed in Table 3.2, from the experimental data, as shown in Figure 3.19 by blue solid lines. The deviation in both $\Delta\varepsilon_1^{\parallel}$ and $\Delta\varepsilon_2^{\parallel}$ spectra can be removed by introducing the extra weak band at 2.1 eV [cyan solid lines in Figure 3.19]. However, its weakness did not allow us to study its temperature dependence.

Discussion. Optical response of CuO chains

The optical responses for two polarizations are composed of the similar sets of oscillators, as revealed by the dispersion analysis. The only qualitative difference is the temperature-dependent band at 2.65 eV observed along the chains. The comparison

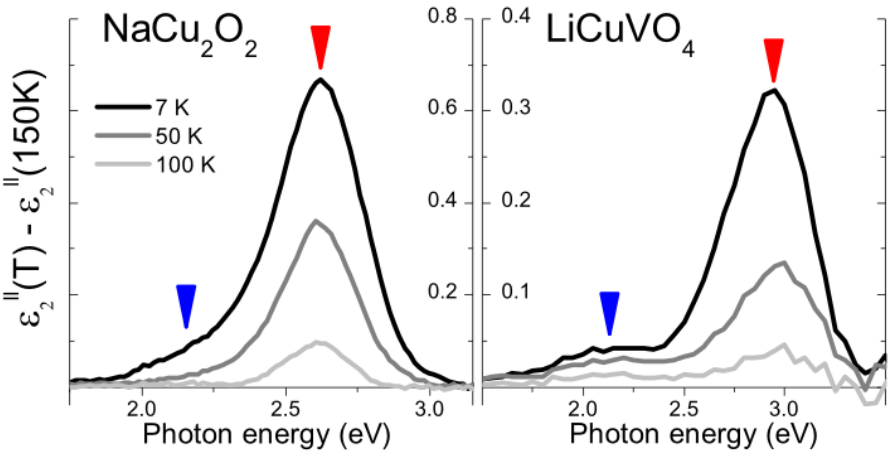

Figure 3.20: Temperature-difference spectra $\Delta\varepsilon_2(\omega) = \varepsilon_2(\omega, T) - \varepsilon_2(\omega, 150\text{ K})$ along the chains in $NaCu_2O_2$ and $LiCuVO_4$ at low energies. The red and blue arrows mark the positions of bands composing doublets.

of its temperature evolution, Figures 3.16 and 3.18, with the magnetic susceptibility data, Figure 3.10 (b), points to the spin-controlled behavior of this band. When below 150 K spin-correlations appear within the CuO chains, the magnetic susceptibility data deviate from the Curie-Weiss behaviour (83). Concurrently with establishing of the spin correlations, the intensity of the 2.65 eV band is enhanced, while it is constant above 150 K.

The dispersion analysis picked out the low-energy side band at 2.1 eV, see Figure 3.19, apparent at 7 K. Therefore, the lowest-energy excitation along the CuO chains has a doublet structure, as shown in Figure 3.20, left panel. Its characteristics, as the energy positions, the spectral weights for the individual bands, their evolution with temperature, are similar to those of the two-peak structure centered at 2.15 and 2.95 eV in $LiCuVO_4$ (79), as was observed along the chains in this compound, see Chapter 3.1. The manifest analogy evidences the same origin of excitations. It ascribes the double-peak structure observed in $NaCu_2O_2$ to the Mott-Hubbard excitons generated by the NN- and NNN-site hopping of electrons along the chains in a model incorporating the long-range Coulomb repulsion (79, 81, 82). The energy parameters dictated by centering of the bands are the local Hubbard interaction $U = 3.2$ eV and the long range Coulomb repulsion $V = 1.1$ eV.

However, one can find a noticeable difference between two compounds in the effective charge density of the individual bands $N_{eff}^{(l)} = \frac{2m}{N_{\mathrm{Cu}}\pi e^2}\mathrm{SW}$, where SW is determined by the oscillator strength of the single bands:

$$\frac{\Delta N_{eff}^{(2.95eV)}(7\mathrm{K}-150\mathrm{K})}{\Delta N_{eff}^{(2.15eV)}(7\mathrm{K}-150\mathrm{K})}\Big|_{\mathrm{LiCuVO_4}} \approx 11.5,$$

$$\frac{\Delta N_{eff}^{(2.65eV)}(7\mathrm{K}-150\mathrm{K})}{\Delta N_{eff}^{(2.1eV)}(7\mathrm{K}-150\mathrm{K})}\Big|_{\mathrm{NaCu_2O_2}} \approx 24.$$

In $NaCu_2O_2$ the ratio between the NN and NNN exchange integrals is $\alpha_{\mathrm{NaCu_2O_2}} = -\frac{J_2}{J_1} \approx 5.6$. $LiCuVO_4$, on the other hand, is characterized by the smaller NNN exchange, leading to the reduced ratio, $\alpha_{\mathrm{LiCuVO_4}} = -\frac{J_2}{J_1} \approx 2.7$ (44). This factor of

2 explains the difference in the *SW* for the exciton transitions between two compounds. These observation validate Equation 3.4 for the weights of the exciton bands, represented in terms of hopping lengths and spin correlation functions.

Discussion. In-plane anisotropy and anomalous absorptions

The measured in-plane dielectric function for $NaCu_2O_2$ revealed anomalously strong temperature dependent absorptions at 3.45 and 3.7 eV perpendicular and parallel to the chains, respectively, which are unusual for strongly correlated electron systems. The energy difference of 0.25 eV between the positions of these bands is a basic tendency also for other bands marked out by the dispersion analysis, giving the anisotropy observed. The unique exception is the 2.65 eV band, apparent only along the chains and discussed in detail above. Since compounds with mixed-valent Cu atoms are scarce, the obtained experimental data are of special interest for studying the low-energy electronic excitations in insulating cuprates.

One of the mixed-valence compounds is the parent compound of a well known family of superconductors $YBa_2Cu_3O_6$, which shares some of its structural units with $NaCu_2O_2$: Cu^{2+} ions are centered in the CuO_4 plaquettes forming the CuO_2 conducting planes and Cu^{1+} ions construct the O-Cu^{1+}-O dumbbells, see inset in Figure 3.21 (a). Ellipsometric measurements with light polarized within the *ab* plane along the *a*-axis showed that the dielectric function for $YBa_2Cu_3O_6$ exhibits a relatively sharp and very intense peak at 4.1 eV (87) [Figure 3.21 (a)], which disappears with increasing oxygen content (88). Local density approximation (LDA) calculations attributed this strong feature to intraionic transitions within Cu^{1+} ions of the O-Cu^{1+}-O complexes (87). The initial states were assigned to Cu^{1+} $3d_{3z^2-1}$ orbitals, the final states to a band comprised of Cu^{1+} $4p_x$ orbitals and Ba $5d, 4f$ orbitals. Transitions into the latter states give a minor contribution because of small matrix elements. The calculated band structure and transitions are shown in

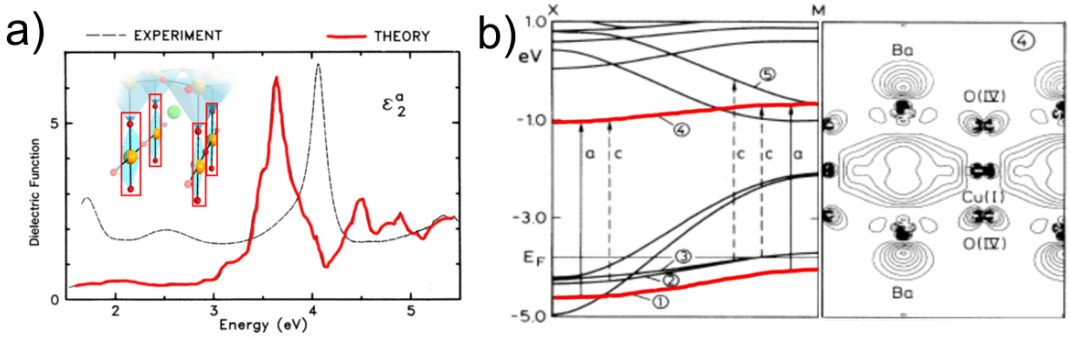

Figure 3.21: (a) Room temperature imaginary part ε_2 of the dielectric function for $YBa_2Cu_3O_6$ for photon polarization along the *a* axis, as obtained by ellipsometry measurements and by LDA calculations (87). Inset shows part of the $YBa_2Cu_3O_6$ structure, where the O-Cu^{1+}-O dumbbells are bounded by red. (b) Calculated LDA energy bands from X [100] to M [110] in the tetragonal Brillouin zone (left panel). The contour plot in the [110] plane passing through Ba, O and Cu^{1+} (right panel).

Figure 3.21 (b).

Among transition-metal oxides, the highest value of $\varepsilon_2(\omega)$ was observed in Li_2CuO_2 compound, isostructural to $NaCu_2O_2$, where the measured dielectric function exhibited an extremely strong and narrow absorption peak at 3.27 eV (66), see Figure 2.13. As a whole, the in-plane response is resembling our measured data and is composed of a similar set of Lorentz oscillators. However, Li-Cu chemical substitution, a 10% nonmagnetic LiCuO impurity phase and the twinned nature of Li_2CuO_2 crystals (89, 90) obliterate the dielectric anisotropy in the *ab* plane. Reviewing the optical data of cuprates with O-Cu^{1+}-O complexes, Pisarev (66) has pointed to the relationship between the Cu^{1+}-Cu^{1+} and Cu^{1+}-O^{2-} bond lengths and the sharp peaks' positions and intensities, which implies that observed anomaly is originated from the dumbbells. Arguing on the basis of the peculiar intensity of the 3.27 eV band, these authors proposed an exciton-type model and attributed the observed anomaly to an intra-atomic interaction between correlated Cu^{1+} $4p$ electrons and $3d$ holes.

Discussion. LDA and LSDA+U calculations

In order to interpret the observed anisotropy and clarify the origin of the strong absorptions, calculations were performed using a linear-muffin-tin orbital method in the atomic sphere approximation (91) within the LDA starting from the known crystal structure of $NaCu_2O_2$ (by A. Yaresko, Max Planck Institute for Solid State Research, Stuttgart, Gemany).

The results of band-structure calculations and the partial electronic density of states (DOSs) are shown in Figure 3.22. The Cu^{1+} p and Cu^{2+} d DOS are shown only, as they are the main contributions to the total DOS. As the LDA results in a metallic solution, narrow partially filled bands corresponding to Cu^{2+} d orbitals with *xy, xz* symmetry cross the Fermi level and give a DOS peak at E_F. The valence band between –4 and –1 eV below the Fermi energy E_F is a mixture of Cu^{1+} and Cu^{2+} d states of different symmetries strongly hybridized with O $2p$ states. The modest band at near 2 eV above the Fermi energy is mainly formed by empty p and d_{3z^2-1} states of Cu^{1+}.

The calculated optical conductivity spectra $\sigma_1^{\perp}$ and $\sigma_1^{\parallel}$ obtained from the band structure are shown in Figure 3.23. The sums of all the interband transition contributions to the optical conductivity (the total optical conductivity) are shown by black solid curves. Blue dashed and red dash-dotted curves indicate the spectral weights connected with transitions to the unoccupied Cu^{1+} and Cu^{2+} states, respectively. The calculated optical response below 2.4 eV is entirely originating from transitions involving Cu^{2+} final states and discussed in details below.

The calculated spectra above 2.4 eV, contributed mostly by the transitions to the Cu^{1+} states, conform to the experimentally observed response in the γ region and background of the dominating bands at 3.45 and 3.7 eV in the β regions, see Figure 3.12. While the dispersion analysis of the experimental data separates the γ zone into bands with halfwidths ∼0.5 eV, the LDA gives sharper structures. However, within this spectral range, the average calculated optical conductivity $\sim 25 \cdot 10^2\ \Omega^{-1}\mathrm{cm}^{-1}$ is in agreement with the measured data. The intensities of both calculated and

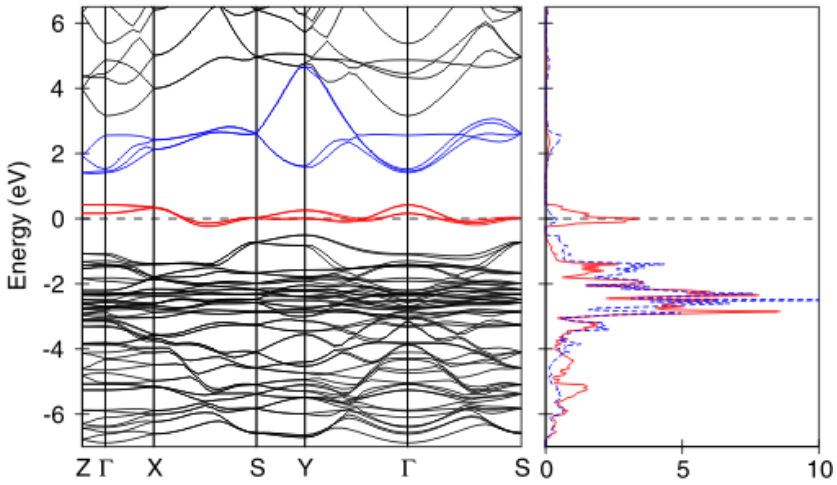

Figure 3.22: The energy band dispersion and DOS projected on the Cu^{2+} $3d$ (red solid curve) and Cu^{1+} $3d$ (blue dashed curve) atomic states of $NaCu_2O_2$ calculated by the LDA approximation for $NaCu_2O_2$. The Fermi level is at zero energy.

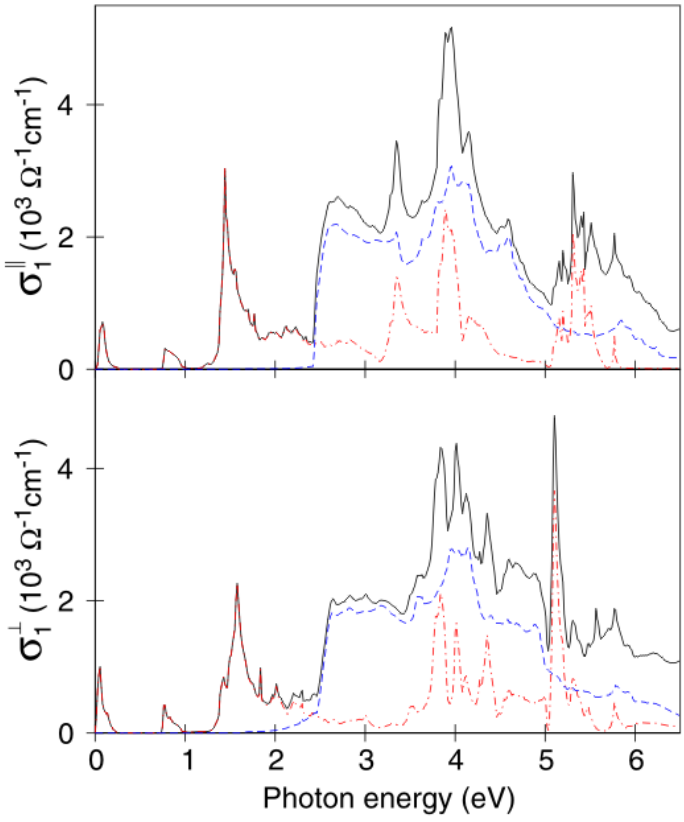

Figure 3.23: Calculated diagonal elements of the optical conductivity $\sigma_1^{\perp}$ and $\sigma_1^{\parallel}$ (black solid curves) and its decomposition into transitions to the Cu^{2+} (red dash-dotted curve) and the Cu^{1+} (blue dashed curve) final states for $NaCu_2O_2$.

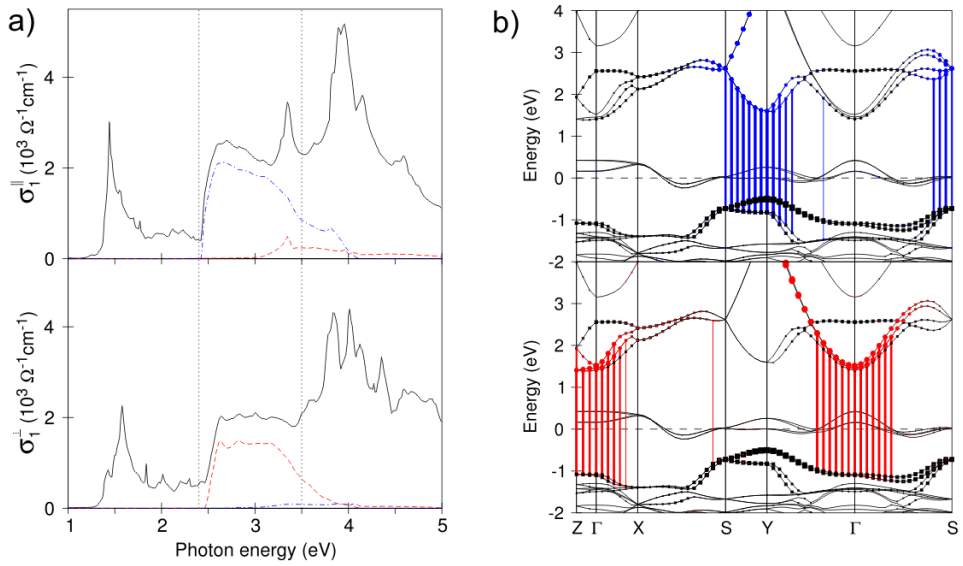

Figure 3.24: (a): The partial contribution of transitions from the occupied Cu^{1+} $3d_{z^2}$ to the unoccupied $4p_x$ (blue dash-dotted curve) and $4p_y$ (red dashed curve) states to $\sigma_1^{\perp}$ and $\sigma_1^{\parallel}$ within spectral range 2.35 – 3.5 eV. (b) The belts of transitions from Cu^{1+} $3d_{z^2}$ to $4p_x$ (blue) and to $4p_y$ (red) states, partially contributing to $\sigma_1^{\perp}$ and $\sigma_1^{\parallel}$ as shown on (a), and the energy band dispersion in fat-band representation. The size of black squares, blue and red circles is proportional to the partial weights of the Cu^{1+} $3d_{z^2}$, $4p_x$ and $4p_y$ states in the Bloch wave function, respectively.

experimental spectra are reduced above 5 eV.

To find out the origin of the observed in-plane anisotropy, appearing as a shift of the spectra by 0.25 eV, we analysed the interband transitions contributing to the optical conductivity above 2.4 eV. The decomposition of the calculated $\sigma_1^{\perp}$ and $\sigma_1^{\parallel}$ spectra into separate transitions revealed that the Cu^{1+} $3d_{z^2}$ orbitals serve as *initial* states for transitions within the spectral range 2.4 – 3.5 eV [Figure 3.24 (a)]. The *final* states involved are of Cu^{1+} $4p$ character with x and y symmetries. The respective transitions and dispersions of bands in a fat-band representation are illustrated in Figures 3.24 (b). As shown in Figure 3.24 (a), the $\sigma_1^{\parallel}$ spectrum around 3 eV is, mainly, formed by transitions into the Cu^{1+} $4p_x$ states (blue dash-dotted curve), while transitions into the $4p_y$ states (red dashed curve) dominantly form the $\sigma_1^{\perp}$ spectra. Because of the large dispersion of these states, the transitions give a rather flat shape of the optical conductivity in this spectral range and spread out up to 5 eV (not shown here). Above 3.2 eV the calculated spectra are formed by the Cu^{1+} $3d \rightarrow$ "free" states and O $2p \rightarrow$ Cu^{2+} $3d$ interband transitions, contributing equally to both $\sigma_1^{\perp}$ and $\sigma_1^{\parallel}$.

Let us turn now to the interband transitions associated with the Cu^{2+} $3d$ *final* states, giving, in particular, the isolated peaks near 1.5 eV, as seen in Figure 3.23. The decomposition into partial contributions reveals that the named peaks are formed by transitions from the occupied Cu^{1+} $3d_{xz,yz}$ bands to Cu^{2+} $3d$ states with xy symmetry, see Figure 3.25 (a). The high intensity and sharpness of the

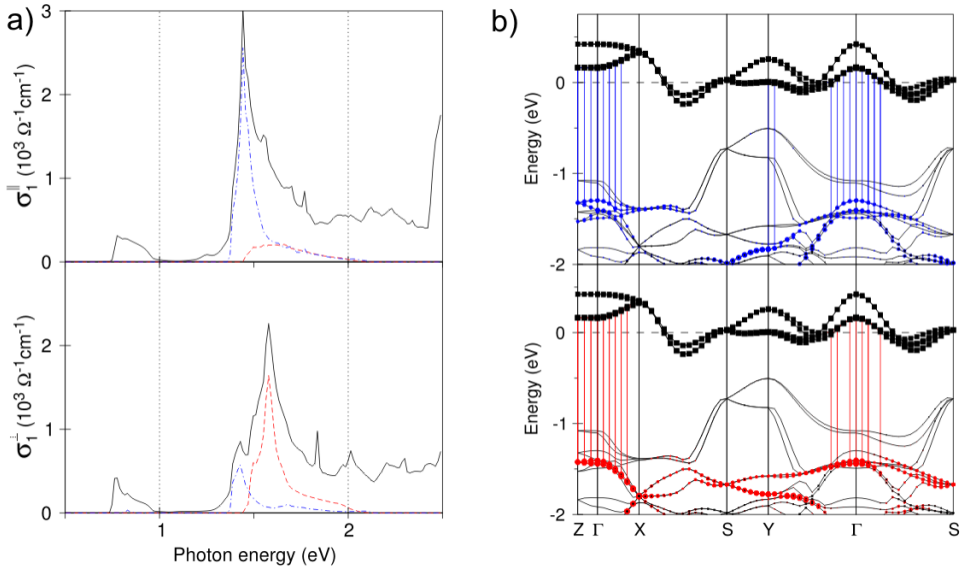

Figure 3.25: (a): The partial contribution of transitions from the occupied Cu^{1+} $3d_{xz}$ (blue dashed curve) and $3d_{yz}$ (red dashed curve) to the unoccupied Cu^{2+} $3d_{xy}$ states to $\sigma_1^{\perp}$ and $\sigma_1^{\parallel}$ within spectral range 1 – 2 eV. (b) The belts of transitions from Cu^{1+} $3d_{xz}$ (blue) and Cu^{1+} $3d_{yz}$ (red) to Cu^{2+} $3d_{xy}$ states, partially contributing to $\sigma_1^{\perp}$ and $\sigma_1^{\parallel}$, as shown on (a), and the energy band dispersion in a fat-band representation. The size of black squares, blue and red circles is proportional to the partial weights of the Cu^{2+} $3d_{xy}$, Cu^{1+} $3d_{xz}$ and Cu^{1+} $3d_{yz}$ states in the Bloch wave function, respectively.

peaks are explained by the low dispersion of the Cu^{2+} $3d_{xy}$ states, lying at the Fermi level in the LDA calculations, and the Cu^{1+} $3d_{xz,yz}$ bands near the Γ points of the Brillouin-zone, Figure 3.25 (b). The *initial* states with different symmetries, *xz* and *yz*, contribute differently to the optical conductivities $\sigma_1^{\perp}$ and $\sigma_1^{\parallel}$, as indicated in Figure 3.25. While these transitions have predominantly *d* character, the contribution of *p* states to the Cu^{1+} $3d_{xz,yz}$ bands is sufficient to provide a significant transition probability through optical dipole matrix elements.

The above analysis of the interband transitions potentially responsible for the strong anisotropy of the optical properties of $NaCu_2O_2$ is based on the spin-restricted LDA calculation which gives a metallic solution with four Cu^{2+} d_{xy}derived bands crossing the Fermi level (Figure 3.22). Although a tiny gap of less than 0.1 eV opens in LSDA calculations for spin-spirals, it is still much smaller than the experimental gap of 2 eV. The reason for the discrepancy is that the strength of electronic correlations in the Cu^{2+} $3d$ shell is strongly underestimated within the L(S)DA. When properly accounted for, the on-site Coulomb repulsion U would split the half-filled Cu^{2+} d_{xy} bands into occupied lower and unoccupied upper Hubbard bands and open an insulating gap. Then, the sharp peaks of the calculated optical conductivity, which appear at ∼1.5 eV due to the interband transitions involving Cu^{2+} d_{xy} *final* states (see Figure 3.22), would shift to higher photon energies improving the agreement with the measured spectra. In order to illustrate the effect of the electronic correlations on the optical conductivity of $NaCu_2O_2$ we recalculated its

band structure and optical spectra using the LSDA+U method (92). The LSDA+U calculations were performed assuming ferromagnetic order of the Cu^{2+} moments. The value of the exchange integral J was fixed to the LSDA value of 1 eV and the on-site Coulomb repulsion U was varied from 2 to 8 eV.

Before presenting the results of the LSDA+U calculations its is worth recalling that when the so-called atomic limit is used for the double counting term (93) and non-spherical contributions to U and J are neglected, the expression for the orbital dependent LSDA+U potential $V_{\sigma i}$, which is to be added to the LSDA potential, becomes particularly simple:

$$V_{\sigma i} = (U - J)\left(\frac{1}{2} - n_{\sigma i}\right), \tag{3.5}$$

where $n_{\sigma i}$ is the occupation of i-th localized orbital with the spin σ. One immediately notices that the main effect of LSDA+U is to split occupied ($n_{\sigma i} \approx 1$) and unoccupied ($n_{\sigma i} \approx 0$) states by shifting the former by $(U - J)/2$ downwards and the latter by the same amount upwards with respect to their LSDA energy position.

Since all the Cu^{2+} d states, except for d_{xy} ones, are completely filled already in LDA, they shift by $(U - J)/2$ to lower energies when U is applied. The half-filled d_{xy} states contribute substantially to bonding O p–Cu d states near the bottom of the valence band because of strong σ-type hybridization with O $(p_x \pm p_y)/\sqrt{2}$ states. In LSDA+U calculations the majority spin d_{xy} state becomes fully occupied and moves by $(U - J)/2$ downwards. The occupation of the minority spin d_{xy} state, however, does not go to zero, as one would expect for a formally unoccupied state, but instead remains close to 0.5 due to the strong d_{xy} contribution to the occupied O p–Cu d bonding states. According to Equation 3.5, the LSDA+U potential acting on the minority spin Cu^{2+} d_{xy} state is much less than $(U - J)/2$ and the energy of the bands formed by these states remains close to the LSDA value. In order to avoid such assymetric splitting of the d_{xy} bands, we performed the LSDA+U calculations with the occupation numbers of the majority and minority spin Cu^{2+} d_{xy} states fixed to 1 and 0, respectively. In this way the corresponding majority and minority spin bands are shifted by $\pm(U - J)/2$ with respect to their LDA position.

The optical conductivities $\sigma_1^{\perp}$ and $\sigma_1^{\parallel}$ calculated with U=6 eV acting on the Cu^{2+} d states are plotted in the lower panel of Figure 3.26. With this value of U, the unoccupied bands formed by the minority spin Cu^{2+} d_{xy} states lie ∼2 eV above the Fermi level and, in contrast to the LDA result, the LSDA+U band structure is insulating with a gap of about 1.8 eV. The sharp absorption peaks, which are caused by inter-band transitions to the final states of the Cu^{2+} d_{xy} character and appear at ∼1.5 eV in the LDA spectra (Figure 3.23), shift to 3 eV in much better agreement with the experiment. The peaks show strong polarization dependence, with the $\sigma_1^{\parallel}$ peak being 0.3 eV lower than the $\sigma_1^{\parallel}$ one. When U of 6 eV is applied also to the d states of Cu^{1+} ions, the bands formed by Cu^{1+} d_{yz} and d_{zx} states, which are the initial states for the interband transitions responsible for the sharp peaks, shift to lower energies. In this case all $n_{\sigma i} \approx 1$, and LSDA+U mimics to some extent the effect of the so-called self-interaction corrections (94) by shifting all the Cu^{1+} d states downwards. This brings the conductivity peaks even closer to their experimental positions. Nevertheless, the magnitude of the calculated optical con-

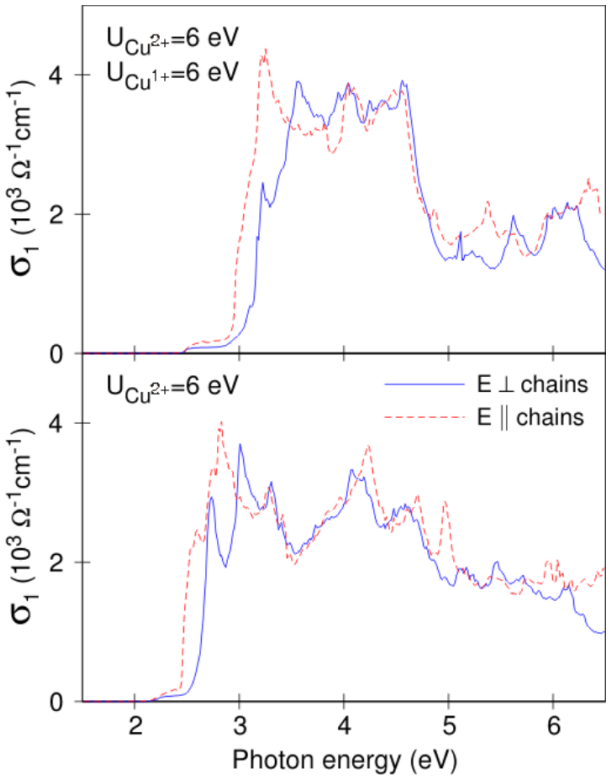

Figure 3.26: Optical conductivities $\sigma_1^{\perp}$ and $\sigma_1^{\parallel}$ calculated with U=6 eV acting on the Cu^{2+} and Cu^{1+} d states (upper panel) and on the Cu^{2+} d states (lower panel).

ductivity remains lower than in the experiment. One would expect some narrowing of the unoccupied Cu^{2+} d_{xy} bands if the LSDA+U calculation were performed for the incommensurate magnetic structure observed experimentally. This could result in sharpening of the peaks and an increase of the calculated conductivity. However, the most probable explanation for the discrepancies between the theory and the experiment is that LSDA+U is too crude an approximation to the electronic structure and optical properties of complex Cu oxides.

Our calculations suggest that the origin of the anomalously strong absorption peaks observed at 3.45 and 3.7 eV can be ascribed to the interband Cu^{1+} $3d \rightarrow Cu^{2+}$ $3d$ transitions. The observed shift in the peak positions between two polarizations arises from different contributions of transitions from the *initial* d_{zx} and d_{yz} states to the optical conductivity, as shown in Figure 3.25. The experimentally observed anisotropy of the background, assigned to the Cu^{1+} $3d \rightarrow 4p$ transitions, is due to the different contributions of transitions to the *final* states with p_x and p_y characters to optical conductivities $\sigma_1^{\perp}$ and $\sigma_1^{\parallel}$, as shown in Figure 3.24.

3.3 Li_2CuO_2

Structure. Magnetic properties. Experimental details

Li_2CuO_2 crystallizes in the body-centered orthorhombic space group *Immm*, with the edge-sharing CuO chains running along the *b*-axis separated by non-magnetic LiO_4 tetrahedra, Figure 3.27 (a). The orthorhombic cell parameters at room temperature are $a = 3.661$ Å, $b = 2.863$ Å, $c = 9.393$ Å (95). Within the single chain, the Cu^{2+}-Cu^{2+} distance is 2.863 Å, the Cu-O-Cu bond angle is 93.96°. Single crystals of Li_2CuO_2 were grown by the travelling-solvent floating-zone method under high pressure (96).

The temperature dependence of the magnetic susceptibility $\chi(T)$ along the principal axes is shown in Figure 3.27 (b). It shows a clear drop below 9.2 K, which is the transition temperature to the 3D ordered state or the Neel temperature (97). In contrast to $LiCuVO_4$ or $NaCu_2O_2$ magnetic susceptibility data, here is no broad maximum specific for low-dimensional magnates. The high-temperature data can be fitted with the Curie-Weiss law down to 20 K with $-\Theta = 40$ K, indicating a predominantly antiferromagnetic character of the magnetic interaction (98). At 2.4 K Li_2CuO_2 undergoes a phase transition to a spin-canted state (97, 99).

The magnetic structure of the ground state of Li_2CuO_2 was observed to be collinear (95) in disagreement with recent LDA calculations (100). Lorenz *et al.* have detected magnetic excitations with a large dispersion along the CuO chains. The dispersion is caused by the large ferromagnetic NN exchange integral $J_1 = -228$ K and relatively weak antiferromagnetic NNN exchange $J_2 = 76$ K (101). The pitch angle, then, $\alpha = -J_2/J_1 = 0.332$. Thus, the condition for the spin-spiral structure $\alpha > 0.25$ is satisfied. The weak interchain exchange integrals, governing the 3D magnetic order at low temperature, apparently suppress the spiral state (101).

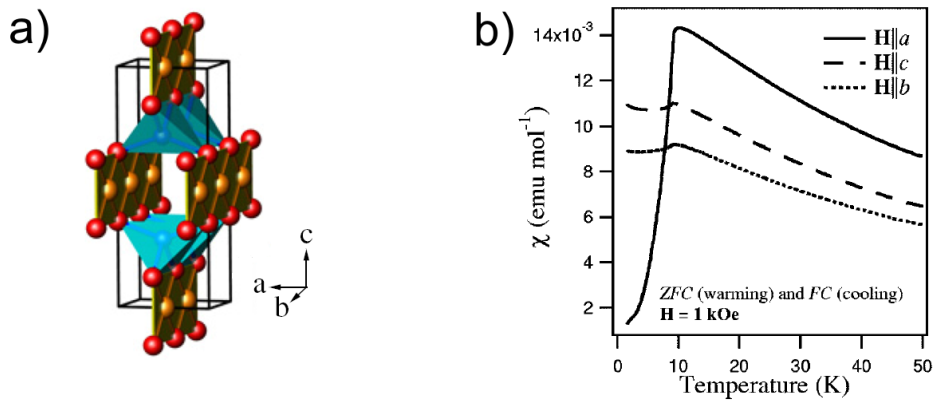

Figure 3.27: (a) Schematic structure of Li_2CuO_2. CuO chains shown by orange and red colors, lithium octahedra are blue. (b) Temperature dependence of the magnetic susceptibility $\chi(T)$ of single crystal Li_2CuO_2 along the principle *a*, *b* and *c* axes; the applied magnetic field is 1 kOe (97).

For our optical measurements, samples with size 5 mm × 5 mm × 3 mm were used. The samples were cleaved along the natural cleaving plane [101] just prior to the measurements. To prevent from oxidation, the sample depositing, surface preparation procedure and transportation of the cleaved sample to the cryostat had been held in argon atmosphere.

Experimental data

Room-temperature raw ellipsometric data represented by the ellipsometric angles Ψ and Δ are shown in Figure 3.28. The data were measured at 68.5° angle of incidence for photon polarizations along the chains (E ∥ b-axis) and perpendicular to the chains (E ⊥ b-axis).

Figure 3.29 shows the real ε_1^* and imaginary ε_2^* parts of the pseudo-dielectric function of Li_2CuO_2 for both polarizations at representative temperatures 300, 150, 12 and 7 K. The optical spectra are highly anisotropic. Along the chains, no temperature effect is seen down to 12 K. However, when temperature passes trough $T_N = 9$ K, a peak at 3.7 eV becomes apparent on the left shoulder of the pronounced band at 3.9 eV. The band at 3.9 eV, on the other hand, is suppressed upon cooling below 12 K. For the polarization perpendicular to the chains no temperature-driven effects are seen, except for the minor narrowing of the bands peaked between 2 – 5 eV upon cooling to 150 K. Thus we focus on the optical response along the CuO chains.

In order to separate contributions from the different bands to the optical response

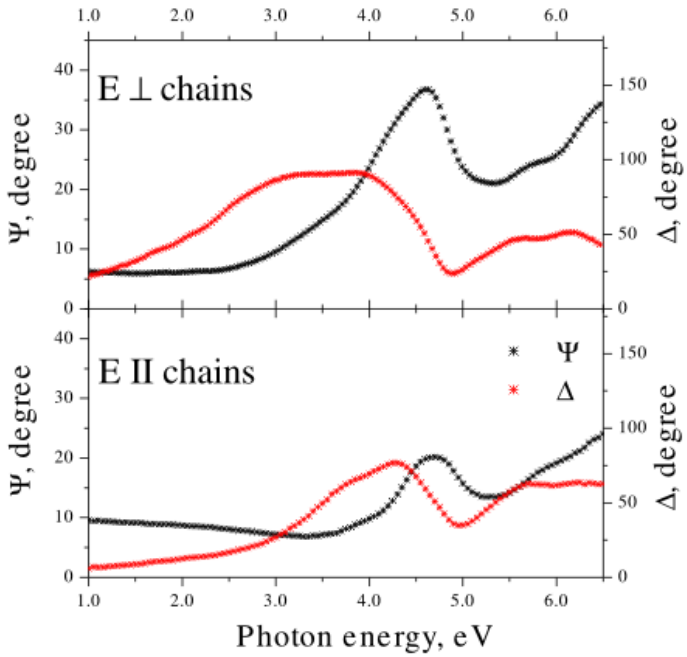

Figure 3.28: Ellipsometric angles Ψ and Δ for photon polarizations along and perpendicular to the CuO chains for Li_2CuO_2 measured at 68.5° angle of incidence at room temperature.

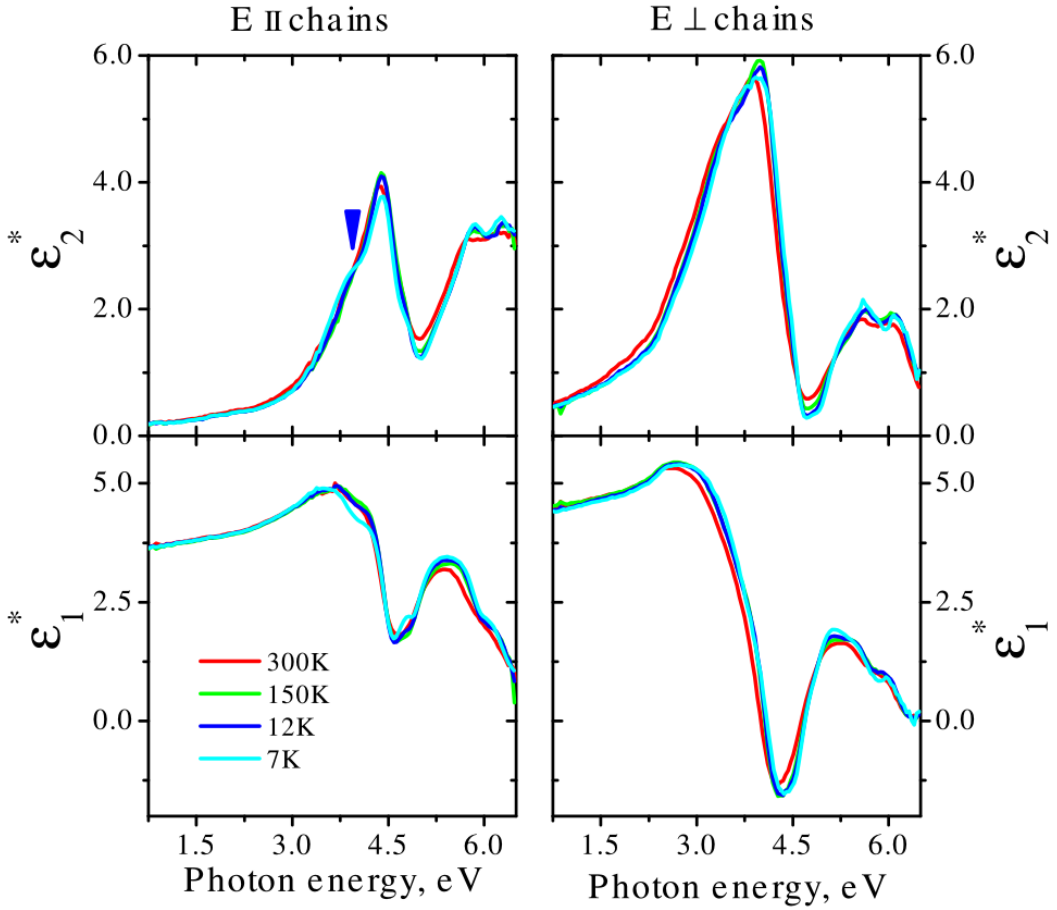

Figure 3.29: Real $\varepsilon_1^*(\omega)$ and imaginary $\varepsilon_2^*(\omega)$ parts of the pseudo dielectric function of Li_2CuO_2 at 7, 12, 150, and 300 K for photon polarizations along the chains (left side) and perpendicular to the chains (right side). Blue arrow marks the temperature dependent features discussed in the text.

of Li_2CuO_2 along the chains, and to explore the origin of the optical anomaly at the magnetic transition temperature, a classical dispersion analysis was performed by simultaneous fitting to $\varepsilon_1^*(\omega)$ and $\varepsilon_2^*(\omega)$, as described in Chapter 1. The parameters determined by simultaneous fitting to $\varepsilon_1^*(\omega)$ and $\varepsilon_2^*(\omega)$ measured at 7 K are listed in Table 3.3. The respective spectra, fit to data and principal bands composing the optical response are shown in Figure 3.30. The bands at 4.42 and 5.79 eV are composed of two and three simple Lorentzians, respectively, which results in the asymmetrical shape of these bands.

Since the temperature effect is seen only below 12 K, spectroscopic scans were performed around the Neel temperature $T_N = 9.2$ K at 6.9, 7.2, 8, 8.5, 8.7, 9.1, 9.5, 10, 11, 12 K along the chains. The temperature difference spectra $\Delta\varepsilon_1^*(\omega, 7.2\text{ K}-T)$ and $\Delta\varepsilon_2^*(\omega, 7.2\text{ K}-T)$ are shown in Figure 3.31. The $\Delta\varepsilon_2^*(\omega)$ spectra show the emergence of the well-defined absorption peak at 3.7 eV below T_N, which is accompanied by an antiresonance feature with zero-crossing at the same energy in $\Delta\varepsilon_1^*(\omega)$. It is also evident from both $\Delta\varepsilon_2^*(\omega)$ and $\Delta\varepsilon_1^*(\omega)$ spectra, that the growth

Table 3.3: Parameters of Lorentz oscillators resulting from a dispersion analysis of the complex pseudo-dielectric function for polarization along the chains of Li_2CuO_2 measured at $T = 7$ K, ε_∞=2.21.

ω_j(eV)	S_j (eV^2)	Γ_j(eV)
3.72	9.89	0.50
4.40	11.80	0.24
4.8	0.432	0.09
5.79	14.48	0.42
6.23	6.35	0.26
6.60	19.8	0.30

of the band at 3.7 eV is concomitant with a suppression of the band at 4.4 eV.

To clarify the details of temperature dependence for the peaks at 3.7 and 4.4 eV, dynamic scans were performed at 3.68, 4.38 and 4.75 eV, shown in Figure 3.32. In this figure the read-off values from the spectroscopic scans in Figure 3.31 are shown for the same energies and for 4 eV. Abrupt changes in ε_2^* at 3.68 eV are clearly seen at the Néel temperature (top left panel in Figure 3.32). Below 8 K the rate of changes in ε_2^* decreases, however, because of the small temperature interval,

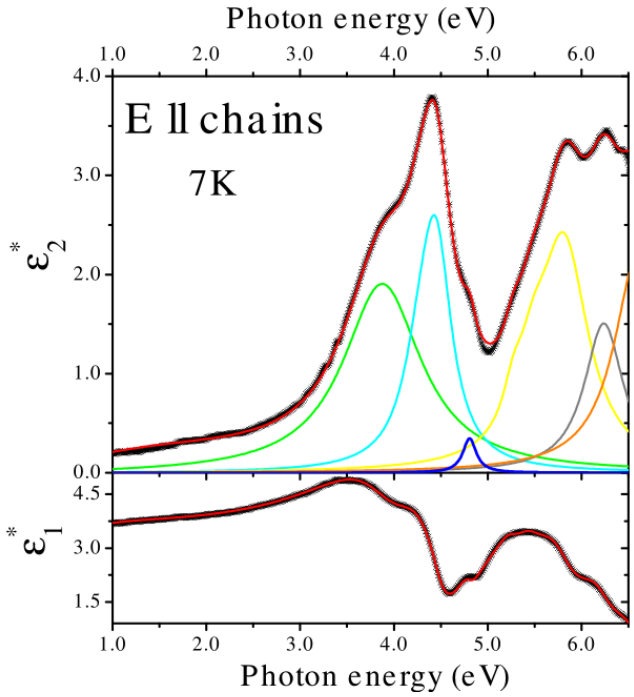

Figure 3.30: Real $\varepsilon_1^*(\omega)$ and imaginary $\varepsilon_2^*(\omega)$ parts of the pseudo dielectric function of Li_2CuO_2 measured at 7K for photon polarization along the chains (stared black lines) and dispersion analysis fit to the data (thin red lines). Thin colored lines draw the principal bands composing optical response with parameters listed in Table 3.3.

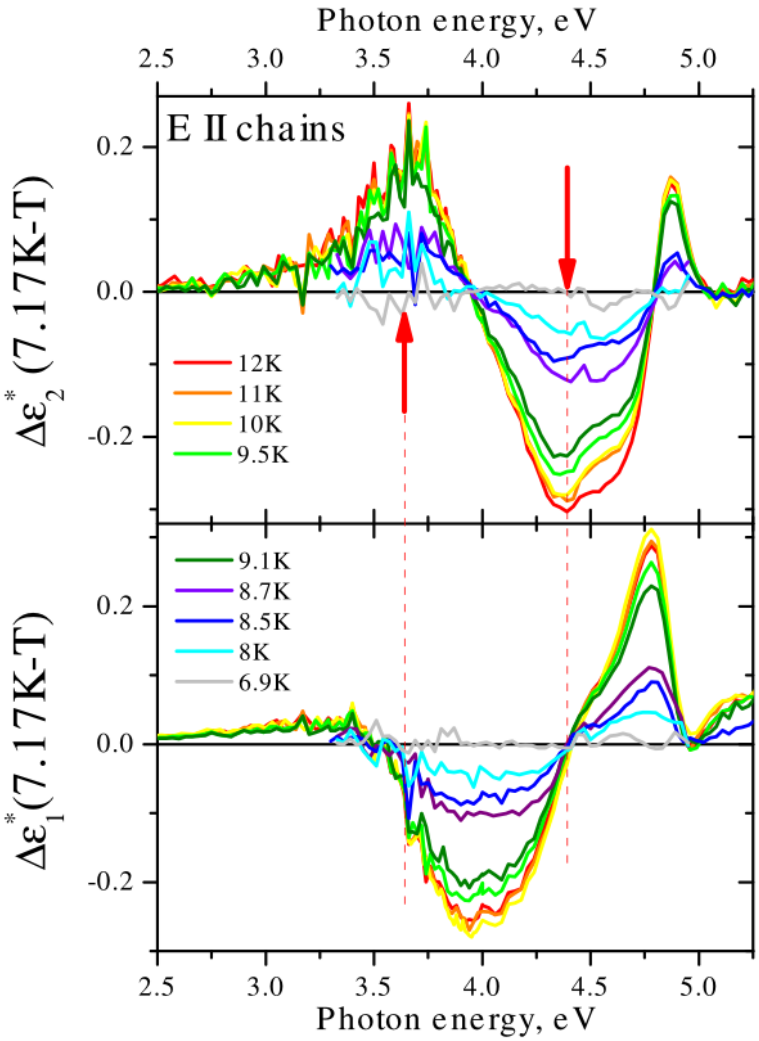

Figure 3.31: Temperature-difference spectra $\Delta\varepsilon_2^*(\omega, 7.17\text{K}-T)$ and $\Delta\varepsilon_1^*(\omega, 7.17\text{K}-T)$ of Li_2CuO_2 for polarization along the chains. The arrows mark the same energy as in Figure 3.29 and 4.38 eV.

one can not conclude whether ε_2^* at 3.68 eV saturates at the lowest temperature. The substantial growth of the optical band at 3.7 eV at the Néel temperature is consistent with the temperature dependence of ε_1^* at 4.0 eV shown in Figure 3.32, top-right panel.

The optical band at 4.40 eV behaves in the opposite manner. The imaginary part of the pseudo-dielectric function ε_2^* suddenly drops at the Néel temperature (bottom-left panel in Figure 3.32), while the real part ε_1^* increases at 4.75 eV (bottom-right panel in Figure 3.32) and decreases at 4.0 eV below T_N. These changes are Kramer-Kronig consistent and point to the suppression of the band at 4.4 eV.

It is interesting to consider the spectral weight redistribution between single optical bands. This can be quantified by integrating the optical conductivity in terms of the effective charge density

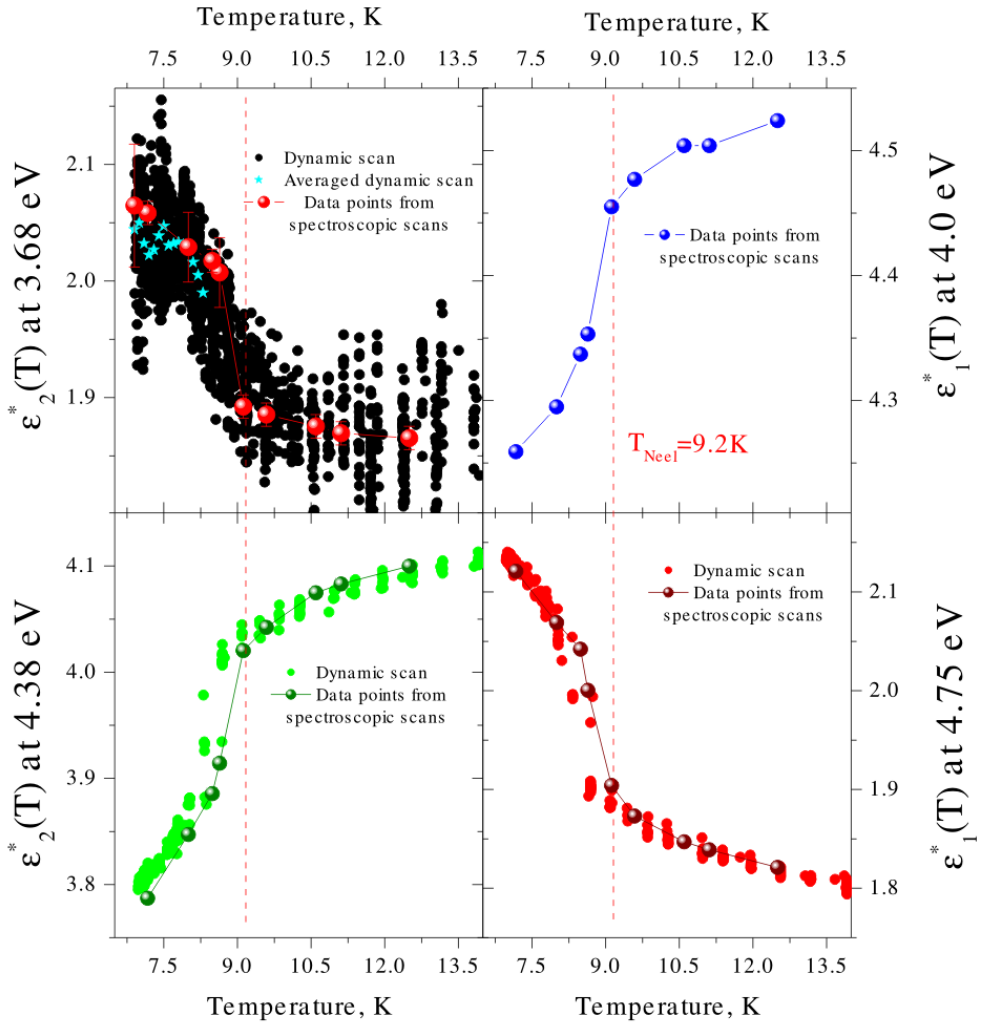

Figure 3.32: Temperature dependencies of $\Delta\varepsilon_1^*$ and $\Delta\varepsilon_2^*$ measured at 3.68, 4.38 and 4.75 eV for polarization along the chains. Cooling-down and warming-up curves are averaged. Red dashed vertical lines mark the Neel temperature $T_N = 9.2$ K.

$$\Delta N_{eff}(\omega, T) = \frac{2m}{\pi e^2 N_{\mathrm{Cu}}} \int_0^{\omega} \Delta\sigma_1(\omega', T) d\omega', \tag{3.6}$$

where m is the free electron mass and $N_{\mathrm{Cu}} = 2.02 \times 10^{22}\mathrm{cm}^{-3}$ is the density of Cu atoms in Li_2CuO_2. Figure 3.33 shows the low-temperature spectral weight changes for the polarization along the chains. Below 4.0 eV the integral increases because of the growth of the band at 3.7 eV. Above 4.0 eV the integral drops to negative values because of the suppression of the band at 4.4 eV. Above 4.7 eV the losses in spectral weight are compensated by the gain within the spectral range of the higher energy bands at 5.8 and 6.23 eV, but not fully. To satisfy the optical sum rule, the compensation is, perhaps, completed at 6.5 eV, as seen from the dynamics of spectral weight changes with energy. Thus, the spectral weight, lost by the optical

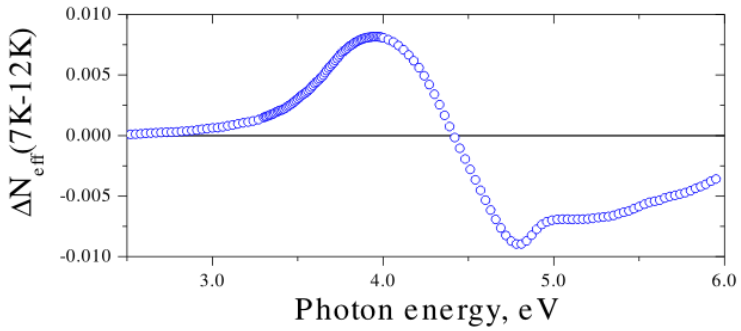

Figure 3.33: Spectral weight changes $\Delta N_{eff}(\omega, 7\text{ K}-12\text{ K})$ in Li_2CuO_2 for polarization along the chains.

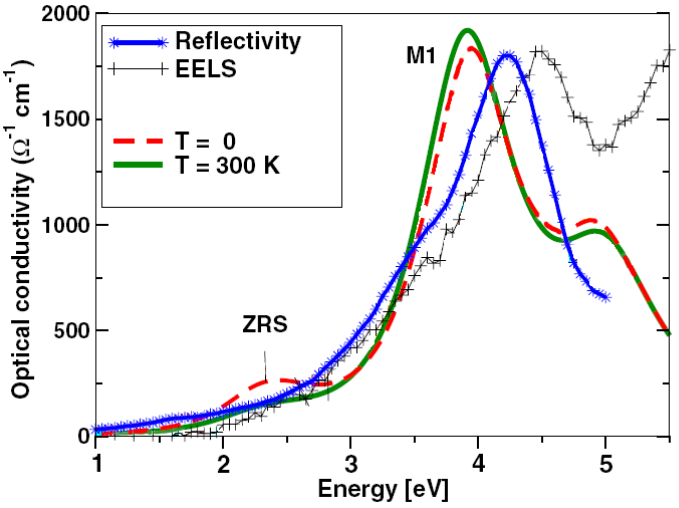

Figure 3.34: Experimental (29, 102) and theoretical optical in-chain conductivities for $T = 0$ and $T = 300$ K (62).

band at 4.4 eV, is redistributed between the band at 3.7 eV and higher energy bands.

Discussion

Two sets of optical data for Li_2CuO_2 are available in the literature to date. The optical conductivity data reported by Mizuno *et al.* in 1998 (29) (Figure 2.12 and blue stared curve in Figure 3.34) are derived from the reflectivity by Kramer-Kronig transformation. The optical conductivity data reported by Atzkern *et al.* (102) are derived from electron energy-loss spectroscopy measurements in transmission mode (gray crossed curve in Figure 3.34). Both spectra were measured at room temperature and dominated by the peak at near 4.3 eV. They reveal no excitations associated with the ZRS state.

The optical conductivity $\sigma(\omega)$ was calculated for CuO chain clusters within the *pd*-Hubbard model (62). The model many-body Hamiltonian with parameters lead-

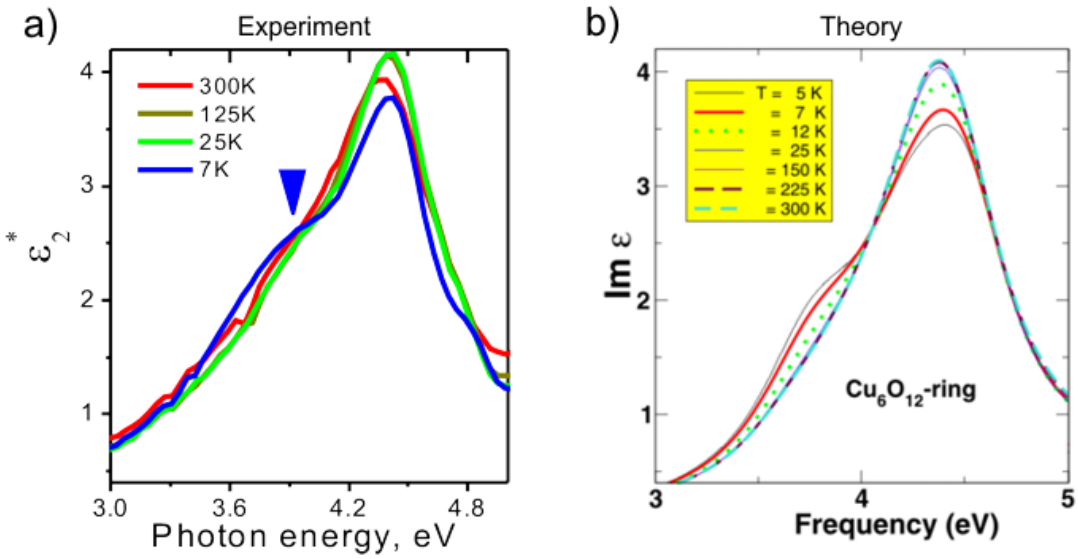

Figure 3.35: (a) The enlarged view of imaginary part of pseudodielectric function $\varepsilon_2^*(\omega)$ measured along the chains of Li_2CuO_2 at representative temperatures. (b) The calculated imaginary part of dielectric function of Cu_6O_{12}-ring as described in Ref. (62) with corrected energy parameters and incorporated long-range Coulomb interactions (by J. Malek, S. Nishimoto, S.-L. Drechsler, Leibniz-Institute für Festkörper- und Werkstoffforschung, Dresden, Germany).

ing to the low-spin (spiral) ground state was able to adequately reproduce the experimental data at room temperature, as seen in Figure 3.34. The Hamiltonian parameters used were taken the same as discussed in Ref. (29), *i.e.* $U_d = 8.5$ eV, $U_p = 4.1$ eV, $V_{pp} = 2.9$ eV. The zero temperature calculations yield the ZRS peak at near 2.5 eV. The spectral weight of this excitation is strongly dependent on the temperature. The predicted suppression of it with warming up to 30 K is clearly seen in Figure 2.11 (b).

In our ellipsometry data, the low temperature feature is arising not at 2.5 eV, but at 3.7 eV on the shoulder of the main transition. Nevertheless, when comparing the spectra calculated for the low temperatures with the actual optical data, the observed temperature behaviour of the peak at 3.7 eV is well reproduced by the modeled ZRS excitation, despite its shift to a lower energy. The substantial discrepancy of the low temperature anomaly's position between calculation and experiment can be illuminated by correction of the model parameters, based on the experience of the data analysis for $LiCuVO_4$ and $NaCu_2O_2$ compounds. A five band Cu3d-O2p extended Hubbard model (62), with included long-range Coulomb interaction between NN copper sites $V_{NN} = 0.7$ eV, gives the conductivity spectra in good agreement with experimental data within the discussed spectral range, as shown in Figure 3.35 (by J. Malek, S. Nishimoto, S.-L. Drechsler, Leibniz-Institute für Festkörper- und Werkstoffforschung, Dresden, Germany). The recalculated spectra well reproduce the ZRS excitation and its temperature dependence. Moreover, the peak at 4.4 eV in the calculated spectra loses its spectral weight upon cooling down to 5K in the

similar manner to the experimentally observed behaviour.

In contrast to $LiCuVO_4$ and $NaCu_2O_2$, only one spin-controlled band at 3.7 eV is observed in Li_2CuO_2. Following the same line of arguments as in the $LiCuVO_4$ and $NaCu_2O_2$ cases, one would expect an additional exciton band at lower energy. Based on the relation $E_l = U - V/l$, $l = 1, 2$ and energies $E_2 = 3.7$ eV and $U = 4.1$ eV, taken from experimental data, the position of the "missed" band is calculated as 3 eV for $V = 1.3$ eV. While there is no evidence of the weak 3 eV band in the measured spectra in Figures 3.29 – 3.31, the imperfection of sample crystallinity or possible surface oxidation might cause the full smearing of the weak excitation, making it impossible to be observed.

3.4 $CuGeO_3$

Structure. Magnetic properties. Experimental details

$CuGeO_3$ belongs to the orthorhombic space group *Pbmm* at room temperature. The edge-sharing CuO chains run along the *c*-axis and are separated by non-magnetic GeO_4 tetrahedra, Figure 3.36 (a). The orthorhombic cell parameters at room temperature are $a = 4.81$ Å, $b = 8.47$ Å, $c = 2.94$ Å (103). Within the single chain, the Cu^{2+}-Cu^{2+} distance is 2.9346 Å, the Cu-O-Cu bond angle is 97.654°.

The temperature dependence of the magnetic susceptibility $\chi(T)$ along the principal axes is shown in Figure 3.36 (b). The maximum of the magnetic susceptibility is around 60 K, pointing to the low-dimensional nature of magnetism in the system. The abrupt drop at 14 K for magnetic field applied along all crystallographic directions indicates a three-dimensional structural phase transition to the spin-Peierls, or dimerized, state. In this state, a doubling of the primitive cell along the *c* axis and a symmetry change occur (31). The inelastic neutron scattering data gave the intrachain exchange integrals $J_1 = 10$ meV= 130 K (104, 105) and $J_2 = 58$ K (106). The interchain exchange integrals are rather weak: $J_a = -0.01J_1$ (108), $J_b = 0.06J_1$ (105).

For spectroscopic ellipsometry measurements, $CuGeO_3$ samples were cleaved along the *a* axis. The optical surfaces used were about 3 mm×6 mm. For transmission measurements, a freshly cleaved 150 μm-thick sample was mounted to the sample holder as shown in Figure 1.5.

Ellipsometry data

Room temperature raw ellipsometric data represented by ellipsometric angles Ψ and Δ are shown in Figure 3.37. The data were measured at 70° angle of incidence for photon polarizations along the chains (E $\parallel$ *c*-axis) and perpendicular to the chains (E $\perp$ *c*-axis). In the thin insulating samples, a Fabry-Pérot resonance effect occurs

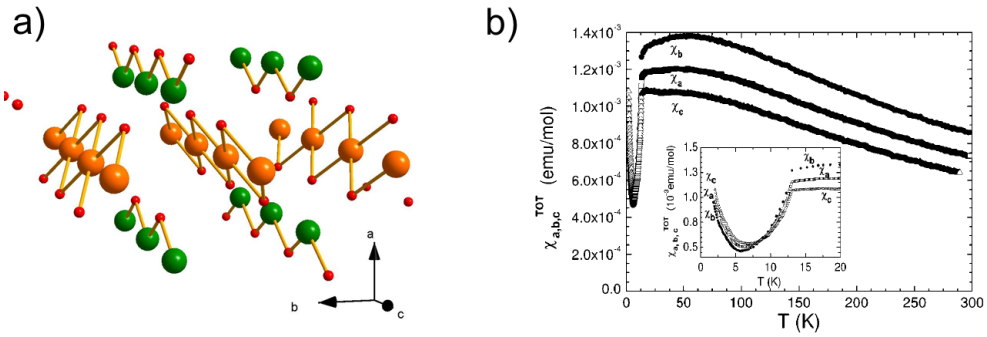

Figure 3.36: (a) Schematic structure of $CuGeO_3$. CuO chains are shown by orange and red colors, germanium ions - green. (b) Temperature dependence of the magnetic susceptibility $\chi(T)$ of single crystal $CuGeO_3$ along the principal *a*, *b* and *c* axes (107).

within the transparency region (4, 107). It reveals itself as inconsistent "jumps" in the ellipsometric angles Ψ and Δ. For this reason the low-energy ellipsometric spectra were limited to 3.2 (3.45) eV for polarization along (perpendicular to) the chains.

Figure 3.38 shows the real ε_1^* and imaginary ε_2^* parts of the pseudo dielectric function of $CuGeO_3$ for both polarizations at representative temperatures 300, 150, 50 and 7 K. The optical response is highly anisotropic. The main difference between the two polarizations is the well developed band at 3.7 eV along the chains. For the other polarization, the first absorption band is centered near 5.2 eV, see Figure 3.39 and Table 3.4. The temperature effect is pronounced, mostly, on the 3.7 eV band along the chains. With cooling down to 7 K, the intensity of this band is almost doubled. Some minor temperature effect is seen at high energies for both polarizations, representing the weak thermal shift and narrowing of optical bands.

Figure 3.40 (a) shows the temperature difference spectra $\Delta\varepsilon_2^*(T - 300\text{ K})$ and $\Delta\varepsilon_1^*(T - 300\text{ K})$ for polarization along the chains (a). The difference spectra show a gradual development of the absorption peak at 3.7 eV with resonance features in $\Delta\varepsilon_2^*(\omega)$ and antiresonance features with zero crossings at the same energy in $\Delta\varepsilon_1^*(\omega)$. The evolution of the peak with temperature was studied by dynamic scans at the peak position, 3.7 eV, and at the off-resonance energy, 3.85 eV, as shown in Figure 3.40 (b). The increase in ε_2^* and recession in ε_1^* upon cooling are Kramers-Kronig consistent and indicate an intensity enhancement of the band at 3.7 eV. The evolution of the band changes rate below 100 K, where the noticeable kink is seen in the dynamic scans.

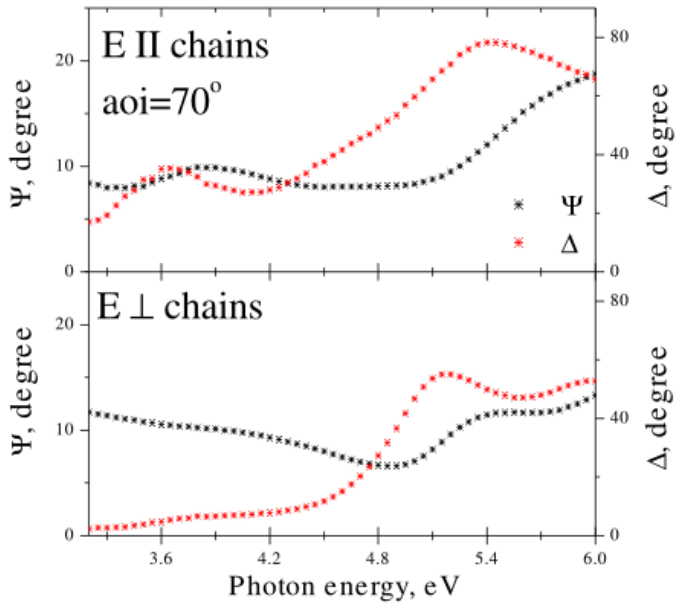

Figure 3.37: Ellipsometric angles Ψ and Δ for photon polarizations along and perpendicular to the CuO chains for $CuGeO_3$ measured at 65° and 70° angle of incidencies, respectively, at room temperature.

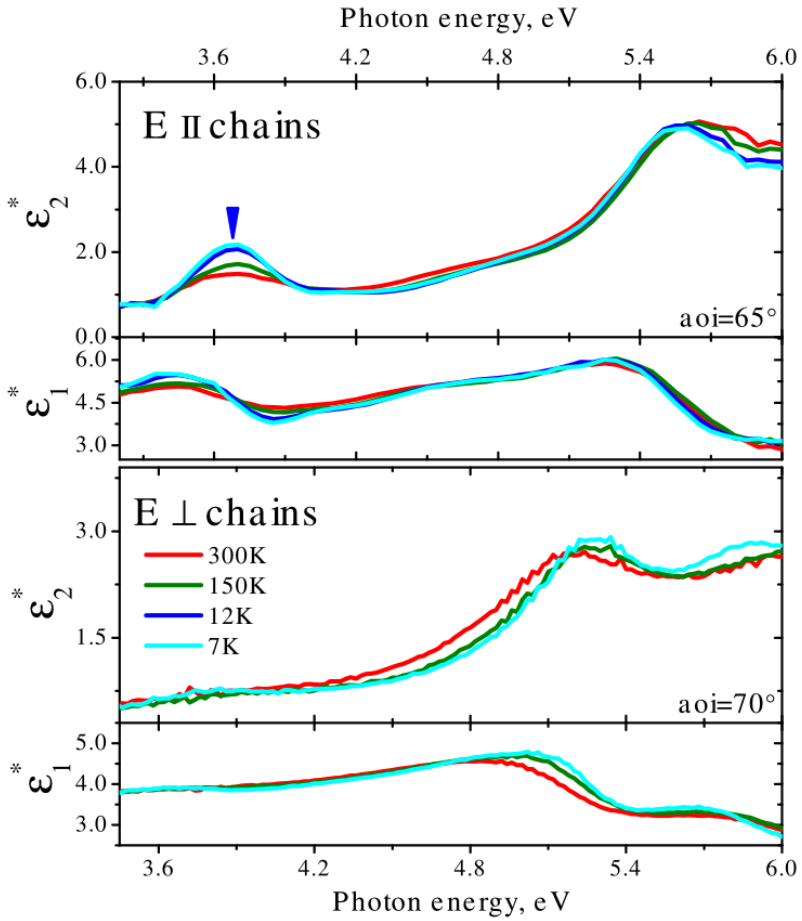

Figure 3.38: Real $\varepsilon_1^*(\omega)$ and imaginary $\varepsilon_2^*(\omega)$ parts of the pseudo dielectric function of $CuGeO_3$ at 7, 50, 150, and 300 K for photon polarizations along and perpendicular to the chains. Blue arrow marks the temperature dependent feature at 3.7 eV discussed in the text.

Table 3.4: Parameters of Lorentz oscillators resulting from a dispersion analysis of complex pseudo-dielectric response in polarizations along (perpendicular to) the chains in $CuGeO_3$ measured at $T = 7$ K. ε_∞=2.21 (ε_∞=2.40).

ω_j(eV)	S_j (eV^2)	Γ_j(eV)
3.70	3.29	0.45
4.18	0.12	0.21
4.82 (5.24)	3.25 (4.39)	0.90 (0.53)
5.53	12.2	0.66
6.14 (6.80)	18.8 (18.3)	1.08 (1.93)

The room temperature spectrum along the chains is in agreement with ellipsometric data from Ref. (72) shown in Figure 2.14 (b). An earlier study of $CuGeO_3$ with electron energy loss spectroscopy by Atzkern (110) has revealed a strong anisotropy

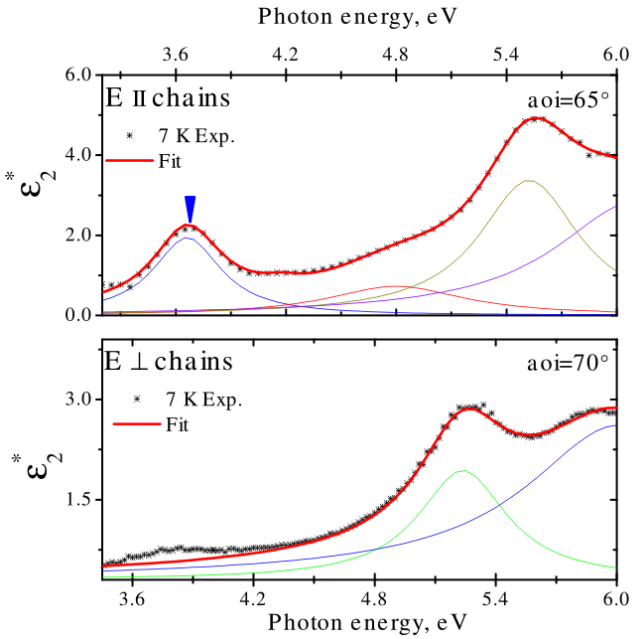

Figure 3.39: Real $\varepsilon_1^*(\omega)$ and imaginary $\varepsilon_2^*(\omega)$ parts of the pseudo-dielectric function of $CuGeO_3$ measured at 7K and dispersion analysis fit to the data for photon polarizations along and perpendicular to the chains. Thin colored lines draw the principal bands composing optical response (see Table 3.2), as derived from dispersion analysis.

in loss functions with $q \parallel c$ and $q \parallel b$. In particular, the peak at 3.5 eV was identified along the c-axis, in agreement with our optical data, which was attributed to the Zhang-Rice singlet state. In the later work of Qian *et al.* the dispersion relation of the 3.8 eV excitations was studied by resonant X-ray scattering (109). The authors have shown that energy dispersion of this excitation is rather weak, suggesting a localized excitonic character of the transition.

In our study, the peak at 3.7 eV is apparent only along the CuO chains ($E \parallel c$-axis), has a strong temperature dependence and follows the temperature evaluation of the peaks observed at 2.95 eV, 2.65 and 3.7 eV in $LiCuVO_4$, $NaCu_2O_2$ and Li_2CuO_2, respectively. Such similarities, supported by independent experimental studies (72, 109, 110), undoubtedly allow us to assign the ZRS character to this peak.

On the other hand, by analogy with the exciton doublet observed in the $LiCuVO_4$ and $NaCu_2O_2$ compounds, one would expect a second excitation at energy lower than 3.7 eV. Since the ellipsometry spectra are limited to 3.2 eV due to Fabry-Pérot resonances, the optical study was performed in a transmission mode within the spectral range 0.75 – 3.6 eV.

Transmission data

Transmission and absorption data for $CuGeO_3$ within the range 1.0 – 3.8 eV are abundantly available in the literature (67, 68, 69, 70, 71). The main features common

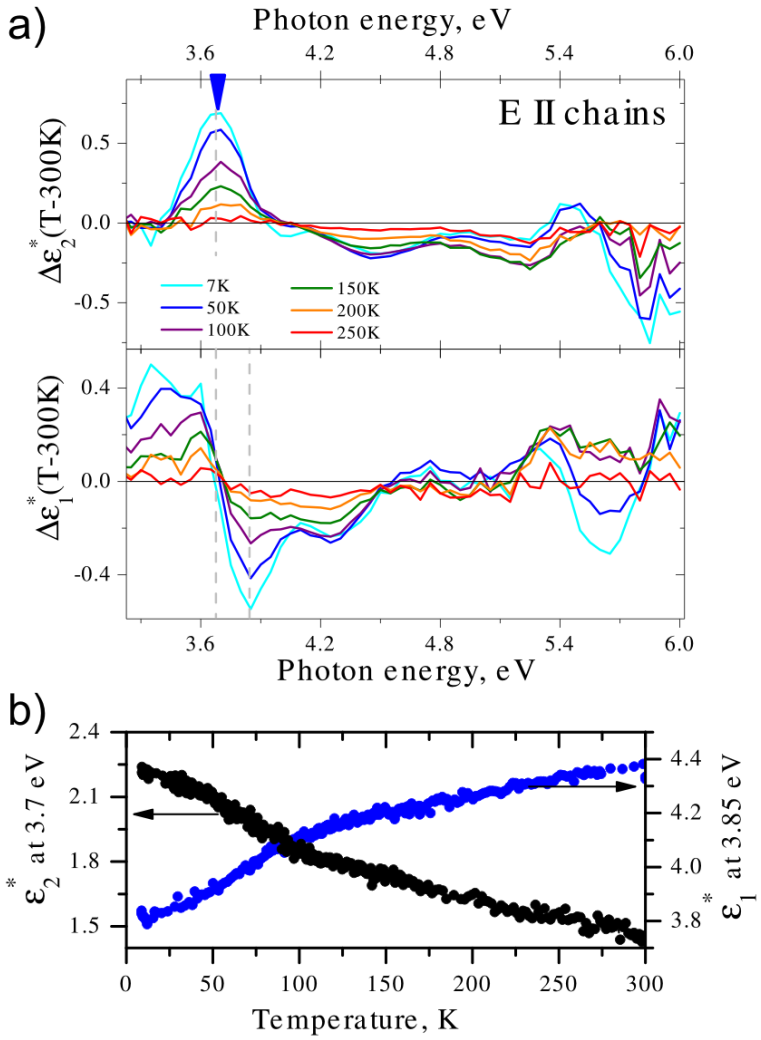

Figure 3.40: (a) Temperature-difference spectra $\Delta\varepsilon_2^*(T - 300\ \mathrm{K})$ and $\Delta\varepsilon_1^*(T - 300\ \mathrm{K})$ of $CuGeO_3$ for polarization along the chains. The arrows mark the same energy as in Figure 3.12. (b) Temperature dependence of ε_1^* and ε_2^* measured at 3.7 and 3.85 eV for polarization along the chains, as marked by vertical lines in (a). Cooling-down and warming-up curves are consistent and were averaged.

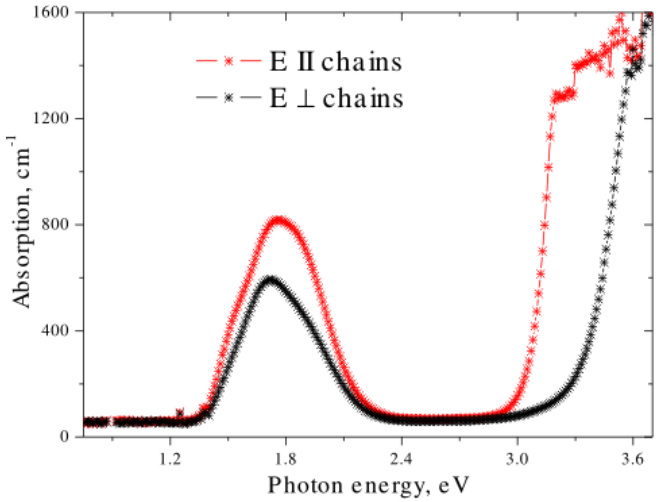

Figure 3.41: Absorption spectra of a single crystal $CuGeO_3$ at room temperature in polarizations along the chains ($E \parallel c$-axis) and perpendicular to the chains ($E \parallel b$-axis).

for all studies are an anisotropic absorption edge (∼3.1 eV along the chains and ∼3.5 eV perpendicular to the chains) and a broad absorption feature at around 1.7 eV, assigned to the phonon-assisted d-d transitions and responsible for the light blue color of the samples. The absorption spectra exhibit a red shift of the absorption edge and sharpening of the bands composing the feature at 1.7 eV with decreasing temperature. The wide absorption bands at 1.7 eV are discussed in the literature in detail (69, 71) and are not of interest of this thesis. Only the spectral region around the absorption edge is discussed below.

In our study, the measured transmission was converted to the absorption using Equation 1.9. The absorption spectra for polarizations along and perpendicular to the chains are shown in Figure 3.41. The data are in agreement with published spectra. The absorption edge appears anisotropic with a difference of about 0.32 eV between two polarizations.

Figure 3.42 (a) shows the temperature dependence of the absorption edge. For both polarizations, the absorption edge has a similar red-shift. In Figure 3.42 (b) the absorption coefficient squared is shown as a function of photon energy at 20 K. Showing the linear behavior with frequency, the absorption edge is, therefore, formed by a direct energy gap (111). A linear extrapolation of the function to the zero absorption level gives energy gaps 3.22 and 3.52 eV for polarizations along and perpendicular to the chains, respectively.

When considering the absorption spectra for polarization along the chains at different temperatures, the tails of absorption coincide at the intercept coordinate $E_0 = 3.51$ eV, $\mu_0 = 116400$ cm^{-1}, as shown in Figure 3.43. The point of interception can be found for polarization perpendicular to the chains at $E_0 = 3.71$ eV, $\mu_0 = 4976$ cm^{-1}. Therefore, the absorption near the fundamental absorption edge exponentially depends on photon energy, or obeys Urbach's rule (112):

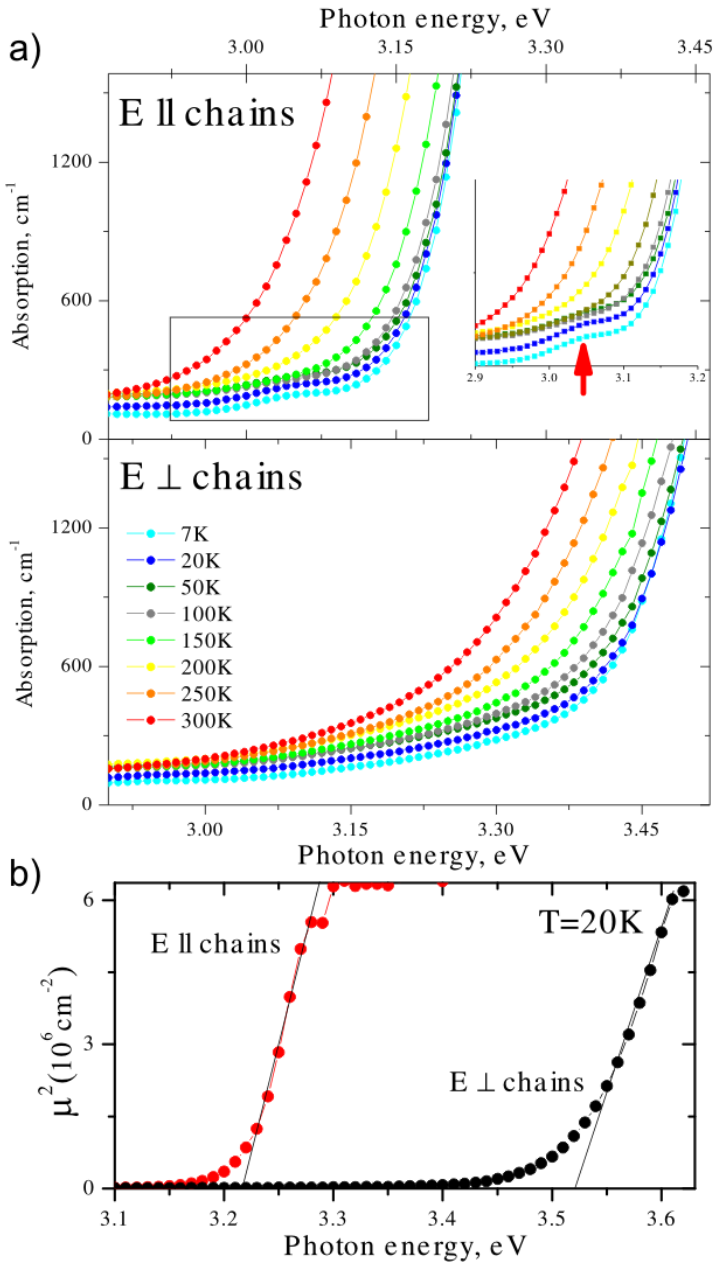

Figure 3.42: (a) Temperature dependence of absorption spectra of a single crystal $CuGeO_3$ for polarizations along the chains and perpendicular to the chains within spectral interval of absorption edge. The inset shows magnified view of experimental data as marked by rectangle. (b) Squared absorption coefficient of $CuGeO_3$ at 20 K for both polarizations.

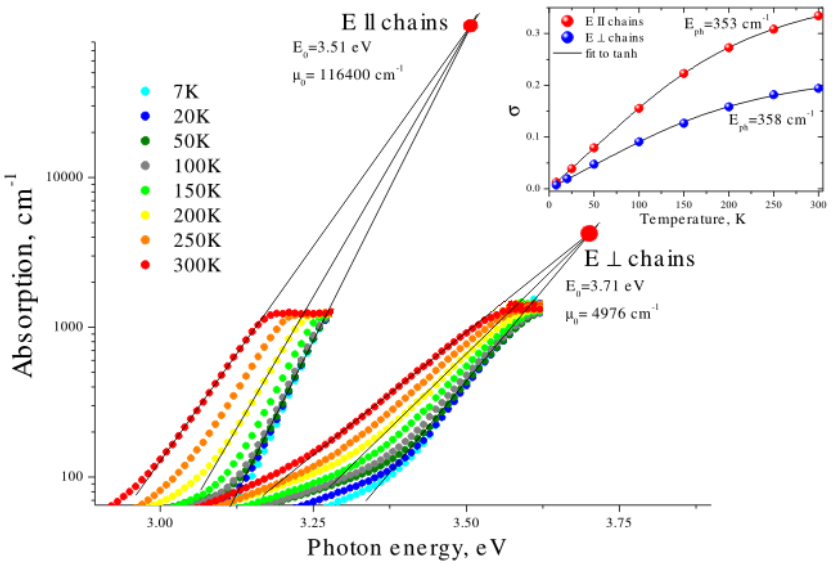

Figure 3.43: Absorption spectra of a single crystal $CuGeO_3$ at different temperatures for polarizations along and perpendicular to the chains. The linear lines coincide with data over decade and are extrapolated to a focal points 3.51 and 3.71 eV. The inset shows the temperature dependence of steepness σ of absorption tails for two polarizations.

$$\mu = \mu_0 \cdot e^{\frac{\sigma(T)(h\nu - E_0)}{k_B T}}, \tag{3.7}$$

where E_0, μ_0 are temperature independent characteristic constants of the material, $h\nu$ is photon energy, k_B is Boltzmann constant, $\sigma(T)$ is the temperature dependent steepness of the absorption edge. The dependence of σ on temperature has a hyperbolic tangent character:

$$\sigma(T) = \sigma_0 \frac{2k_B T}{\hbar\omega_p} \tanh \frac{\hbar\omega_p}{2k_B T}, \tag{3.8}$$

where σ_0 is temperature independent constant and ω_p is the energy of phonons involved in the formation of the absorption edge. The best fit of steepness σ to the Equation (3.7) is shown in the inset of Figure 3.43. The phonon energies determined from this fit are 353 and 358 cm^{-1} for polarizations along and perpendicular to the chains, respectively. Obtained phonon modes are close to the cenergy of the phonon mode $A_{1g} = 332$ Å as measured by Raman scattering (113).

Discussion

The formation of the absorption edge was assigned by different authors to the charge transfer transitions (110, 114). By combining the analysis of the experimental transmission data with density of states calculations and group theory considerations, the observed anisotropy was explained by different initial states of the charge transfer transitions forming the edge. Along the c axis the edge is assigned to the

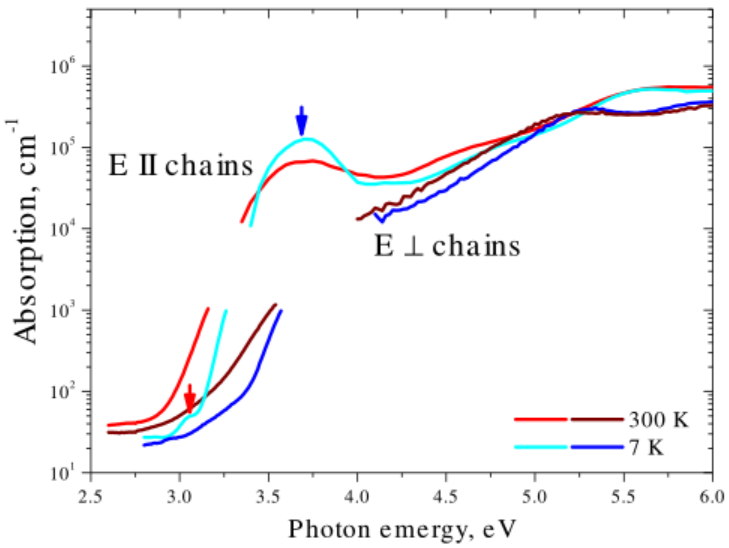

Figure 3.44: Absorption spectra of a single crystal $CuGeO_3$ at 300 K and 7 K for polarizations along and perpendicular to the chains. Absorption spectra above 3.5 eV (3.6 eV) for polarization along (perpendicular to) the chains are derived from ellipsometry data corrected to background, as described in Chapter 1. The arrows mark 3.05 and 3.7 eV peak positions, as in Figures 3.38, 3.39, 3.41 and as discussed in the text.

transitions from O $2p_{x,y}$ orbitals to singly filled Cu $3d$ states. Perpendicular to the chains, along the b axis, the edge is ascribed to the transitions from O $2p_z$ states to singly filled Cu $3d$ states (70). The O $2p_z$ states are at lower energy than the O $2p_{x,y}$ explaining the higher energy absorption onset. However, the combination of the low-energy transmission and high-energy ellipsometric data shows that the absorption edge along the c axis is formed not by the charge-transfer transitions, but by the transition incorporating the ZRS state.

Figure 3.44 shows the absorption coefficient, as calculated from ellipsometry data above 3.2 eV using Equation 1.11 and united to the measured transmission data. Perpendicular to the chains, the first pronounced absorption peak is seen only at 5.2 eV, as confirmed by the dispersion analysis (Table 3.4). This excitation has the charge-transfer character. The band is broad, with damping of about 1 eV, and its absorption tail extends down to the 3 eV, forming the absorption edge observed perpendicular to the chains in transmission measurements. In contrast, for polarization along the chains the strong optical band at 3.7 eV, marked by blue arrow in Figure 3.44 and assigned to the ZRS excitation, stands out against the background of higher energy transitions. Being well developed, this excitation shifts the absorption edge to the lower energy.

The quantitative difference in the absorption edge behavior between two polarizations becomes even more evident, when the absorption tails are inspected for details. While along b axis ($E \perp$ chains) no anomalies are seen in Figure 3.42 (a), there is a weak bump at 3.05 eV on the absorption tail at low temperatures along the c axis ($E \parallel$ chains), see inset in Figure 3.42 (a). Despite the large number of

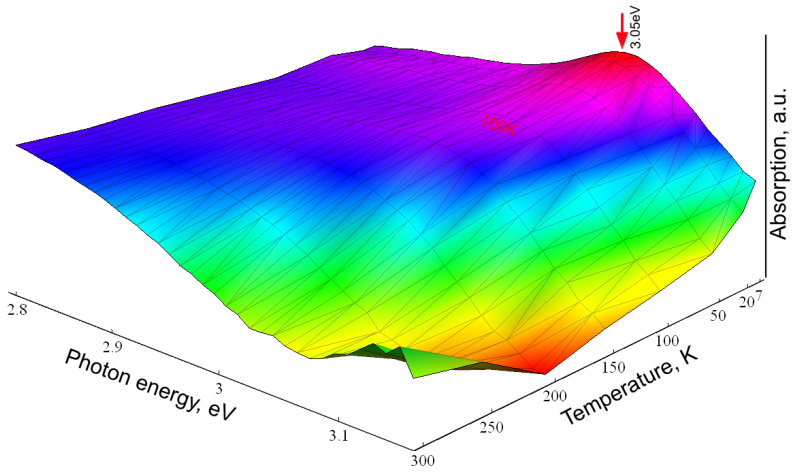

Figure 3.45: The surface formed by absorption spectra, background and Urbach's tails corrected as described in the text, of a single crystal $CuGeO_3$ at different temperature in polarizations along the chains ($E \parallel c$-axis). The arrow marks the same energy as in Figure 3.17.

published optical data, this feature is observed for the first time.

Figure 3.45 shows the temperature behavior of the observed anomaly at 3.05 eV. The Urbach tails of absorption edge were subtracted from the spectra in accordance to the fit to Equation 3.6. The resulting background-corrected spectra at different temperatures form the skeleton for the surface stretched on it. From this 3D plot the development of the anomaly is seen in details: at 7 K the peak is apparent at 3.05 eV. With warming up the peak loses its intensity and completely disappears above 100 K.

In summary, in $CuGeO_3$ for polarization along the chains, the two peak structure, marked by blue and red arrows in Figure 3.44, is observed. The weak band at 3.05 eV is seen on the absorption spectra, whereas the band at 3.7 eV is apparent in ellipsometric data. The peaks form the absorption edge of $CuGeO_3$ along the chains and are strongly temperature dependent. The evolution of both peaks undergoes the changes at 100 K, where the growth of the 3.05 eV band starts (Figure 3.45), and the growth of the 3.7 eV is enhanced [Figure 3.40 (b)]. This temperature is close to the temperature of maximum in magnetic susceptibility data in Figure 3.36 (b), pointing to the low-dimensional character of the magnetic order. In analogy with $LiCuVO_4$ and $NaCu_2O_2$ compounds, two peaks found in $CuGeO_3$ along the chains can be also assigned as an exciton doublet. The positions of the exciton bands, in accordance with the model described in Chapter 3.1, give $U = 4.3$ eV and $V = 1.2$ eV.

3.5 α-CuV_2O_6

Structure. Magnetic properties. Experimental details

The α-phase of CuV_2O_6 crystallizes in the triclinic structure of space group $P\bar{1}$. The cell parameters at room temperature are $a = 9.168$ Å, $b = 3.543$ Å, $c = 6.478$ Å, $\alpha = 92.25°$, $\beta = 110.34°$, $\gamma = 91.88°$ (115). Within the single chain, the Cu^{2+}-Cu^{2+} distance is 3.543 Å, the Cu-O-Cu bond angle is 97.9°. The edge-sharing CuO chains run along the b-axis, Figure 3.46 (a).

The temperature dependence of the magnetic susceptibility $\chi(T)$ exhibits a broad maximum around 48 K, Figure 3.46 (b), indicating a low-dimensional character of the spin system (116). The magnetic properties are well described by a model based on $S = 1/2$ Heisenberg antiferromagnetic linear chains. Below T_N=22.6 K the commensurate antiferromagnetic ordering along [110] direction was proposed based on powder neutron diffraction and nuclear magnetic resonance measurements (56). The estimated intra- and interchain exchanges are $J_1 = 34$ K and $J_{\text{inter}} = -14$ K, respectively. The frustration ratio α is unknown, however, and it was also pointed out that the exchange coupling J_2 between NNN Cu^{2+} ions is stronger than J_1.

For the spectroscopic ellipsometry measurements, a single crystal of α-CuV_2O_6 cleaved along the ab plane was used. The orientation of the sample was checked by X-ray diffraction. The optical surface used was about 1 mm×1 mm.

Results and discussion

The α-CuV_2O_6 compound is less studied than the other edge-sharing systems discussed in the thesis. There are no spectroscopic data available in the literature to date and the electronic band structure near the Fermi energy has not been reported.

Figure 3.47 shows the ellipsometric angles, Ψ and Δ, measured for photon polarizations along the chains (E $\parallel$ b-axis) and perpendicular to the chains (E $\perp$ a-axis)

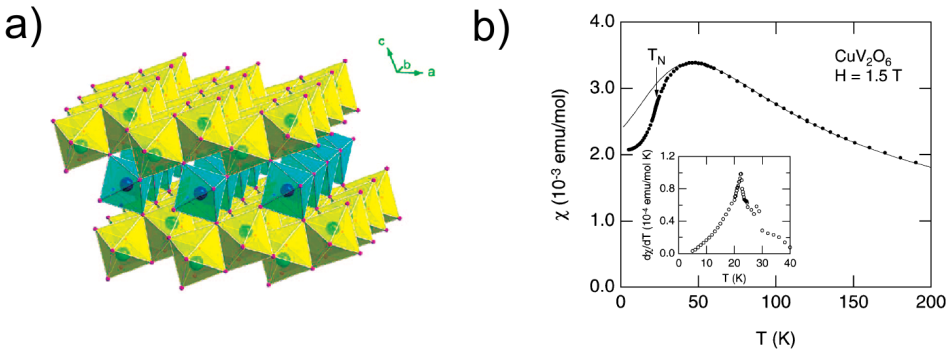

Figure 3.46: (a) Schematic structure of α-CuV_2O_6. Vanadium-oxygen octahedra are shown by yellow, copper-oxygen octahedra are shown by blue. (b) Temperature dependence of the magnetic susceptibility $\chi(T)$ of α-CuV_2O_6 polycrystalline sample (56).

at room temperature. Figure 3.48 (a, b) shows the real ε_1^* and imaginary ε_2^* parts of the pseudo-dielectric function of α-CuV_2O_6 for polarizations along and perpendicular to the chains, respectively, measured at representative temperatures 300, 200, 100, 60 and 7 K.

In polarization perpendicular to the chains, the optical response is dominated by the strong absorption band near 3.7 eV. Its temperature dependence is weak and appears as narrowing with decreasing temperature.

Along the chains, the spectrum is mainly composed of the strong broad optical band at 3.6 eV and the two weaker bands at 2.15 and 2.7 eV, revealed from the dispersion analysis. Figure 3.49 shows the individual bands composing the optical response of α-CuV_2O_6 along the chains at 7 K derived by simultaneous fit of a sum of Lorentz oscillators to $\varepsilon_1^*(\omega)$ and $\varepsilon_2^*(\omega)$, see Chapter 1.

The bands at 2.15 and 3.6 eV considerably increase their spectral weight with decreasing temperature, see Figure 3.48 (a). To illuminate the difference in the temperature evolutions of these bands, the temperature-difference spectra $\Delta\varepsilon_2^*(T - 330\text{ K}, \omega)$ and $\Delta\varepsilon_1^*(T - 330\text{ K}, \omega)$ are plotted in Figure 3.50. No suppression of any single band is observed. It implies that the optical spectral weight is accumulated within the whole studied spectral region from the higher-energy bands.

The changes in both $\Delta\varepsilon_2^*(\omega)$ and $\Delta\varepsilon_1^*(\omega)$ between 3 and 5 eV in Figure 3.50 are evidence of the growth of the peak at 3.6 eV with decreasing temperature. The read-

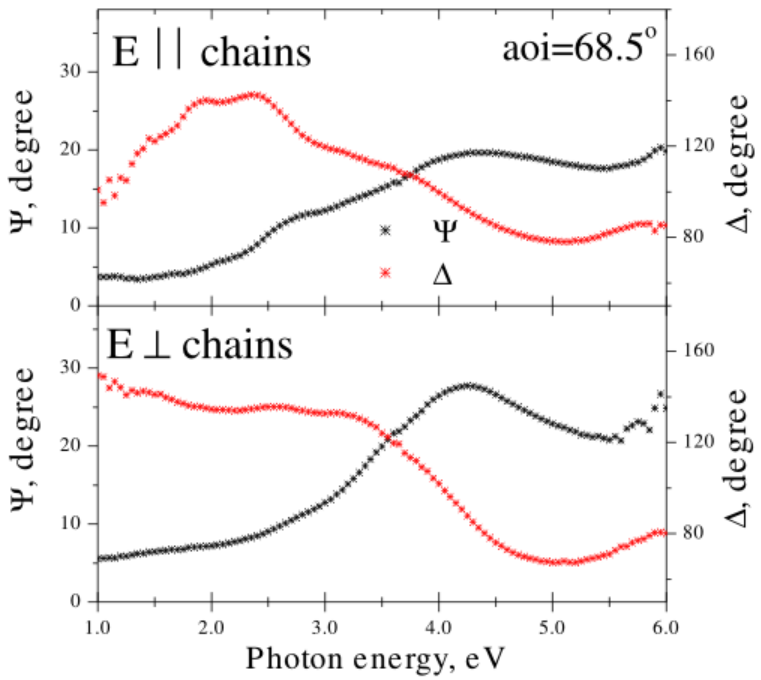

Figure 3.47: (a) The ellipsometric angles Ψ and Δ for photon polarizations along and perpendicular to the CuO chains for α-CuV_2O_6 as measured at room temperature at 68.5° angle of incidence.

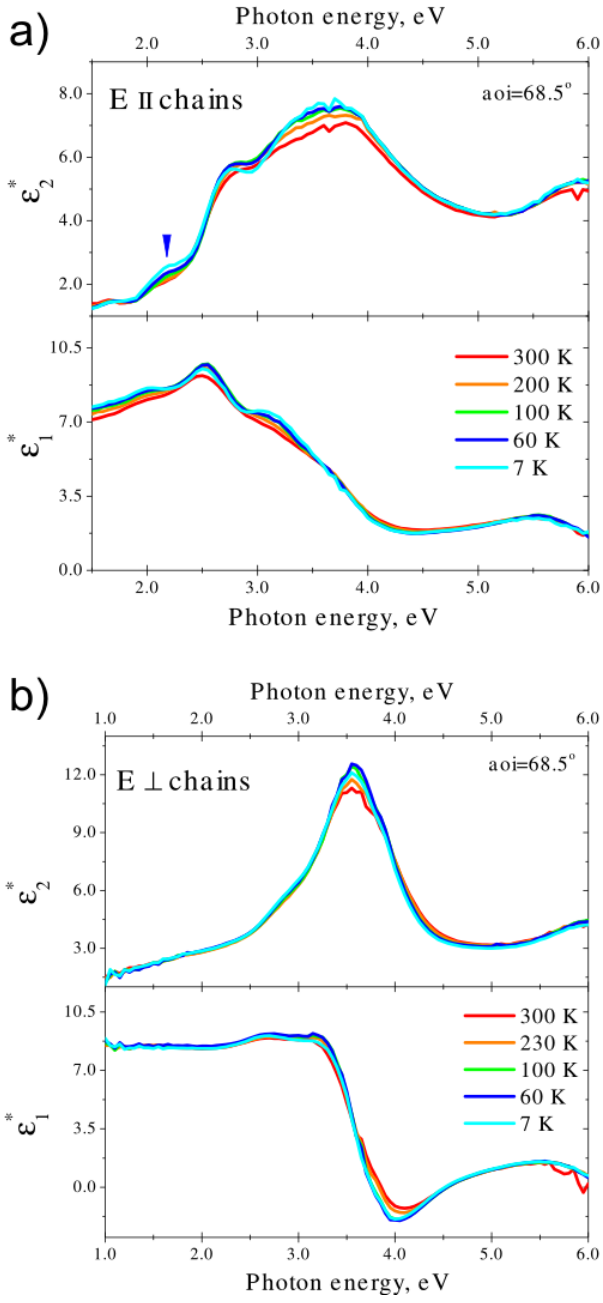

Figure 3.48: (a) Real $\varepsilon_1^*(\omega)$ and imaginary $\varepsilon_2^*(\omega)$ parts of the pseudo-dielectric function of α-CuV_2O_6 at representative temperatures for photon polarizations (a) along and (b) perpendicular to the chains. Blue arrow marks the temperature dependent feature at 2.15 eV discussed in the text.

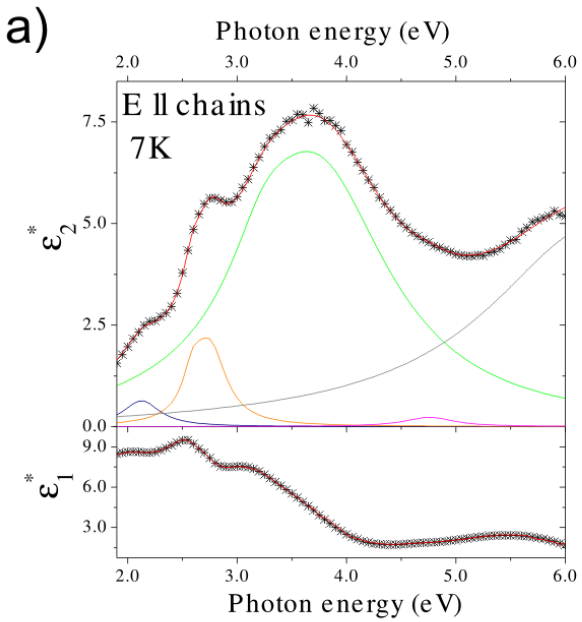

b)

ω_j(eV)	S_j (eV^2)	Γ_j(eV)
2.14	0.56	0.41
2.70	2.30	0.45
3.60	41.0	1.97
4.77	0.68	0.55
6.41	75.7	2.41

Figure 3.49: (a) Real $\varepsilon_1^*(\omega)$ and imaginary $\varepsilon_2^*(\omega)$ parts of the pseudo dielectric function of α-CuV_2O_6 measured at 7K for photon polarization along the chains (stared black lines) and dispersion analysis fit to the data (thin red lines). Thin colored lines draw the principal bands composing optical response with parameters listed in table on the right. (b) Parameters of Lorentz oscillators resulting from a dispersion analysis of the complex pseudo-dielectric response for polarization along the chains of α-CuV_2O_6 measured at $T = 7$ K. ε_∞=1.81.

off $\Delta\varepsilon_2^*$ data from the difference spectra at 3.55 eV are shown in the inset in Figure 3.50. The inset shows that $\Delta\varepsilon_2^*(\omega)$ at 3.55 eV exhibits nearly linear dependence with temperature.

The upgrowth of the 2.15 eV band is studied by read-off data from spectroscopic ε_2^* spectra, as shown in Figure 3.51 (a). In contrast to the band at 3.6 eV, the noticeable enhancement of the band at 2.15 eV starts only below 150 K. To underline the correlation of the observed anomaly at 2.15 eV with magnetism, the magnetic susceptibility data from Ref. (117) and fit to the paramagnetic Curie-Weiss law of it are shown on the same panel. The deviation from the Curie-Weiss behaviour appears below 150 K, where the marked growth of the band at 2.15 eV starts. This behavior reiterates the evolution of the band at 2.95 eV in $LiCuVO_4$.

At lower energies on $\Delta\varepsilon_2^*(\omega)$ spectra a weak feature is seen at about 1.75 eV, as marked by the red arrow in Figure 3.50. The magnified view of $\Delta\varepsilon_2^*(\omega)$ and $\Delta\varepsilon_1^*(\omega)$ spectra around this energy are shown in Figure 3.51 (b). $\Delta\varepsilon_2^*(\omega)$ spectra reveal a clear bump at 1.75 eV accounting for the drop in the real part of the pseudo-dielectric function, $\Delta\varepsilon_1^* = 0.2$. Thus, both resonance and antiresonance features are observed at 1.75 eV. They are evidence of a weak excitation at this energy. The details of temperature evolution of this excitation are unresolved.

The bands at 1.75 and 2.14 eV can be considered as excitations associated with

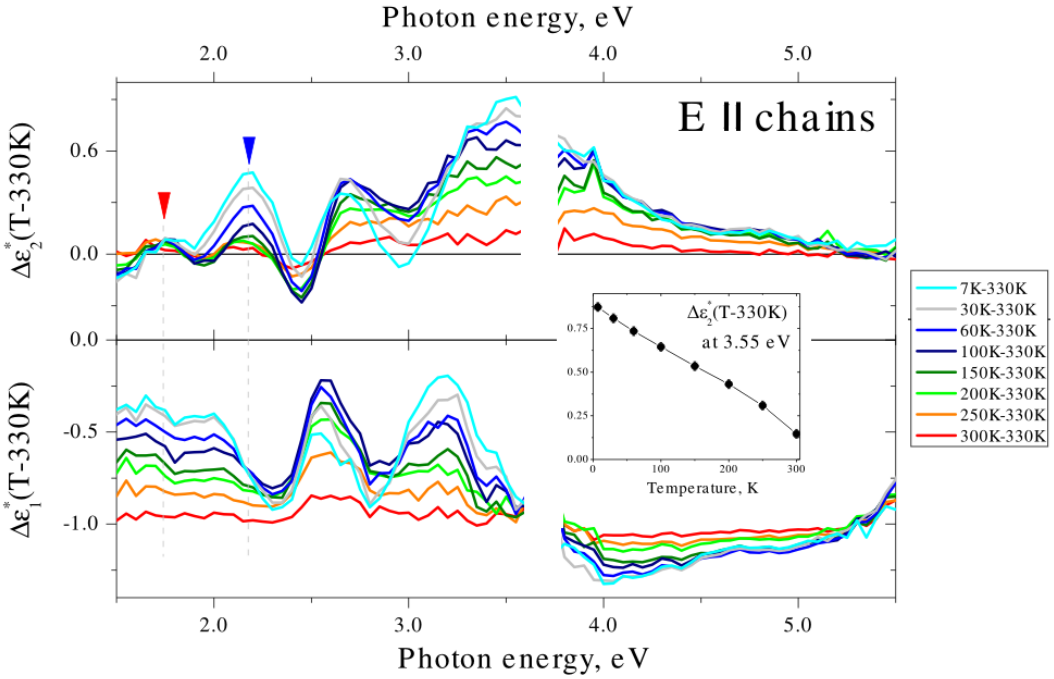

Figure 3.50: (a) Temperature-difference spectra $\Delta\varepsilon_2^*(T - 330\ \mathrm{K})$ and $\Delta\varepsilon_1^*(T - 330\ \mathrm{K})$ of α-CuV_2O_6 for polarization along the chains. The blue arrow mark the same energy as in Figure 3.47 (a). For better representation, the data in spectral range 3.55 – 3.75 eV are cut because of noise. The inset shows the read-off values from the difference spectra at 3.55 eV. The error-bar is within symbol size.

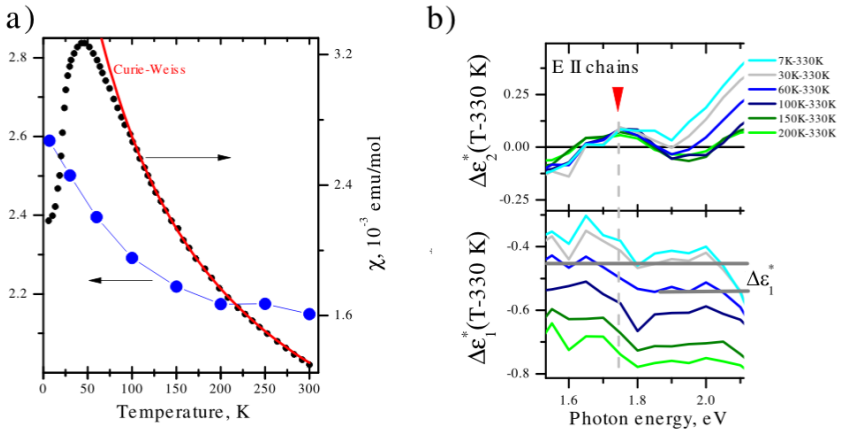

Figure 3.51: (a) The read-off data from spectroscopic scans of ε_2^* at 2.15 eV for polarization along the chains, as marked by blue arrow in Figure 3.47 (a). Magnetic susceptibility data from Ref. (117) and fit to paramagnetic Curie-Weiss law. (b) Temperature-difference spectra $\Delta\varepsilon_2^*(T$ - 330 K) and $\Delta\varepsilon_1^*(T$ - 330 K) of α-CuV_2O_6 for polarization along the chains, as in Figure 3.49. The red arrow mark the same energy as in Figure 3.47.

ZRS, or an exciton doublet in analogy to the lowest-energy excitations in the edge-sharing compounds discussed in previous subchapters. Summing up the energy parameters of the observed excitations, one can estimate the Coulomb repulsion and interaction energies: $U = 2.55$ and $V = 0.8$ eV.

3.6 Conclusions

A comprehensive optical study was performed on a set of the spin-chain compounds $LiCuVO_4$, $NaCu_2O_2$, Li_2CuO_2, $CuGeO_3$ and α-CuV_2O_6. The electronically active units of this compounds, determining the band structure near the Fermi level, are edge-sharing chains of CuO_4 plaquettes.

The optical response of compounds studied here consists of (i) the local excitations within CuO_4 unit, namely the *p-d* charge-transfer transitions, and (ii) the non-local excitations incorporating neighboring CuO_4 plaquettes, namely the temperature-dependent peak structures at low energies apparent along the chains only.

(i) Within the investigated spectral range, the optical response of the studied systems is composed, mainly, of the *p-d* charge-transfer transitions from oxygen to copper. These excitations are present for photon polarizations both parallel and perpendicular to the chains, but reveal a strong anisotropy. Figure 3.52 shows the optical data for $LiCuVO_4$, Li_2CuO_2, $NaCu_2O_2$, $CuGeO_3$ and α-CuV_2O_6 obtained along the chains. The spectra are composed of the *p-d* character, superimposed optical bands. In this Figure, the interesting change in the position of the energy of the charge-transfer gap peak, Δ_{pd}, is seen between different compounds, as marked by heavy dots above the spectra.

Figure 3.53 (a) shows energies of the charge-transfer gap peaks Δ_{pd} versus $Cu^{2+}-O$ distance for all studied compounds. From this Figure, the change of Δ_{pd} indicates its sensitivity to the geometry of CuO_4 plaquette. In Ref. (29), the charge-transfer energy Δ_{pd} was expressed, within the ionic model, as

$$\Delta_{pd} = \frac{\Delta V_m}{\varepsilon_\infty} + \Delta_0, \tag{3.9}$$

where ΔV_m ($\sim \frac{1}{d_{Cu^{2+}-O}}$) is the difference in the Madelung site potentials for a hole between copper and in-plane oxygen ions, Δ_0 represents contributions to Δ_{pd} that are independent of $d_{Cu^{2+}-O}$ (electron ionization and affinity energies). Thus, the charge transfer gap is dominantly determined by the geometry dependent Madelung potentials and the polarization effect represented by the dielectric constant ε_∞.

The correlations between the electronic structure and the Madelung potentials (or $Cu^{2+}-O$ distance) were studied earlier in insulating cuprates [M_2CuO_4 (M=Pr, Nd, Sm, Eu, Gd, La), (Ca-Sr)CuO_2, $Bi_2Sr_2YCu_2O_8$, $YBa_2Cu_3O_6$] with planar CuO nets (118). In that study, the calculated and experimental charge transfer gap energy data showed the decrease with increasing Cu-O distance, see Figure 3.53 (c). In our study, the experimentally observed qualitative correlations of Δ_{pd} and $d_{Cu^{2+}-O}$ are in agreement with that in Ref. (118). The charge-transfer gap energies obtained in our study of the edge-sharing cuprates are higher those that of planar cuprates, because of the larger Madelung potentials ΔV_m (29) and the smaller dielectric constants ε_∞ ($\lesssim 2$) compared to 3.5 for the CuO_2 planes of high-T_c cuprates.

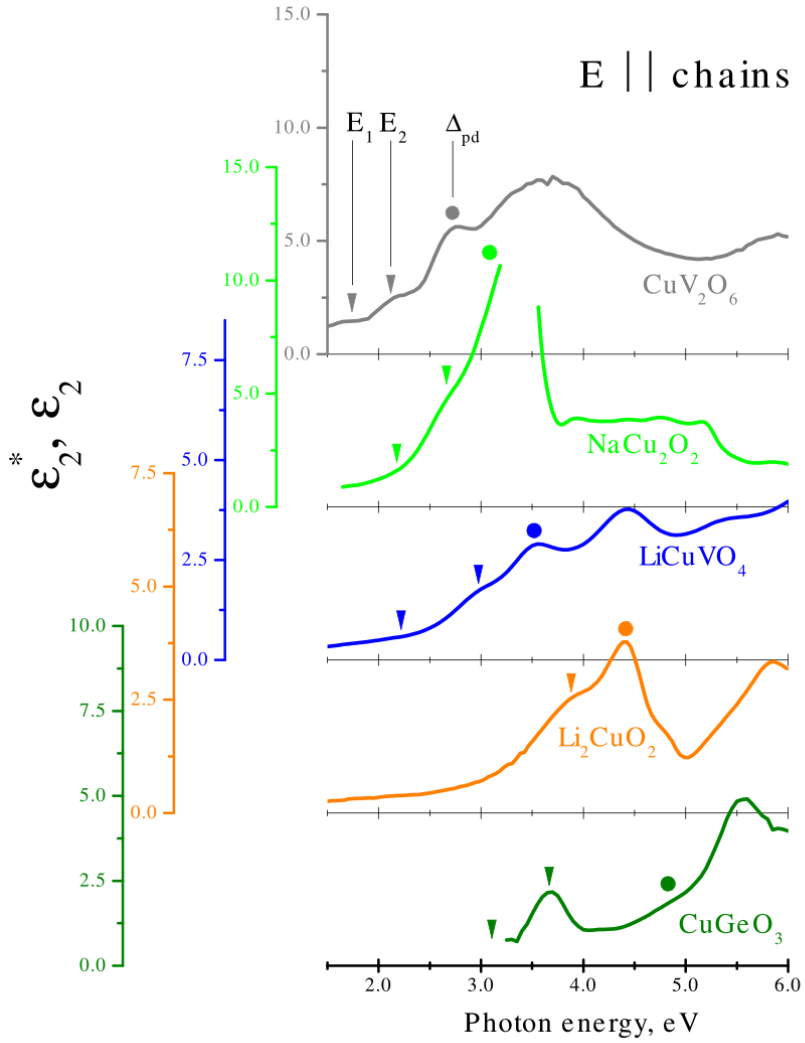

Figure 3.52: Imaginary $\varepsilon_2(\omega)$ part of the dielectric functions of $LiCuVO_4$ $NaCu_2O_2$ and imaginary $\varepsilon_2^*(\omega)$ parts of the pseudo-dielectric functions of Li_2CuO_2, $CuGeO_3$ and α-CuV_2O_6 measured for photon polarizations along the chains at 7 K. The spectra are shifted vertically for clarity. Dots mark the charge-transfer gap peaks, as described in the text. Arrows mark the centering of the exciton doublet.

(ii) All the measured compounds revealed low-energy anomalies apparent only for polarization along the chains. Weak structures centered at 2.15 and 2.95 eV ($LiCuVO_4$), 2.15 and 2.65 eV ($NaCu_2O_2$), 3.05 and 3.7 eV ($CuGeO_3$), 1.75 and 2.15 eV (CuV_2O_6) were observed for polarization of photons along the CuO edge-sharing chains. A single peak with similar temperature dependence was identified at 3.7 eV in Li_2CuO_2. These double-peak bands were identified as an exciton doublet, originating from the long-range Coulomb interaction V between holons and doublons within the CuO chains. The temperature dependence of observed excitonic bands follows spin correlations within the chains, which make them apparent at low temperatures only.

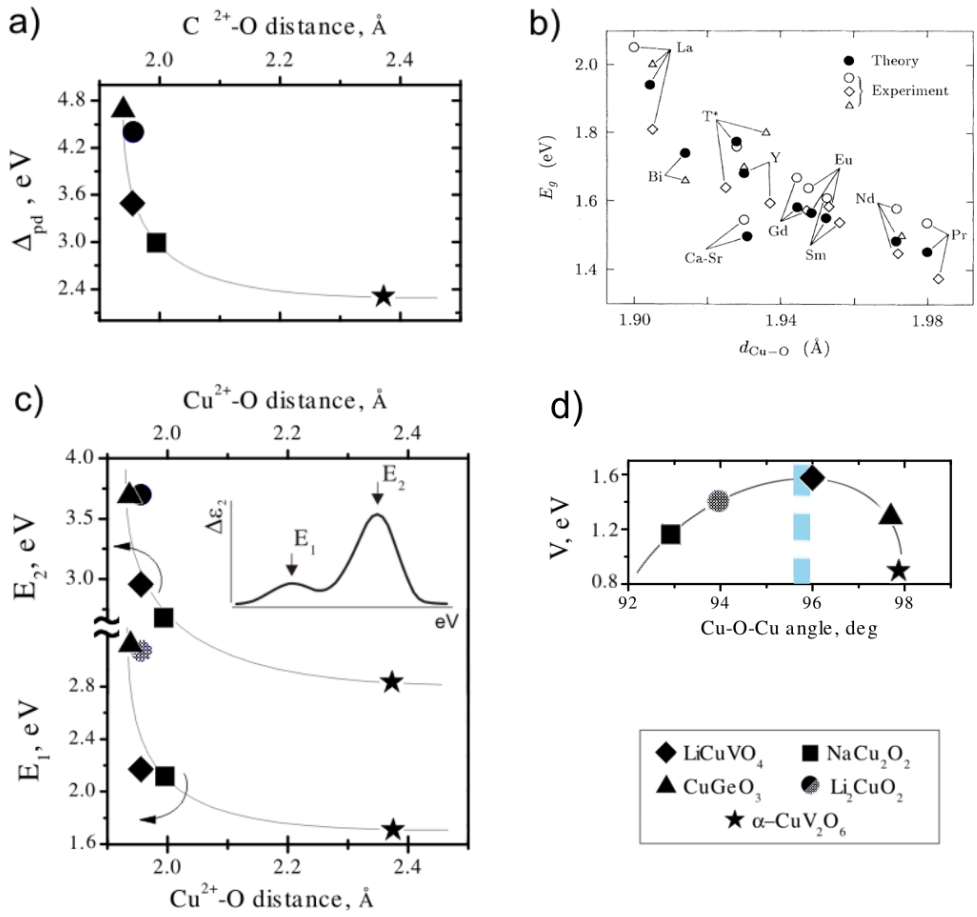

Figure 3.53: (a) The dependence of the charge-transfer peak energy, Δ_{pd}, defined along the chains as described in the text, on the Cu^{2+}-O distance. The thin solid line is a guide to the eyes. (b) The calculated charge-transfer gap energy compared with the data of the optical conductivity measurements of insulating cuprates M_2CuO_4. From Ref. (118). (c) The experimental dependencies of excitons centering on the Cu^{2+}-O distance. Thin solid lines are guides to the eyes (d) The experimental dependence of Coulomb interaction V (thin line is guide for the eyes) on the Cu^{2+}-O-Cu^{2+} bond angle.

The centering of double-peak anomalies (E_1 and E_2) is plotted in Figures 3.53 (c) as a function of $d_{Cu^{2+}-O}$ distance . To be mentioned, E_1 and V values for Li_2CuO_2 are taken as described in Chapter 3.4. The centering of the exciton bands reveals the dependence on the $d_{Cu^{2+}-O}$ distance, similar to that of the charge transfer peak energy, E_{pd}, shown in Figure 3.53 (a). It is expected naturally since the energy of the ZRS band, originating the observed excitons, is determined by the O $2p$ non-bonding state, originating the local charge-transfer energy (see Chapter 2.2).

Figure 3.53 (d) shows the long range Coulomb interaction V, determined from the experimentally measured exciton peak positions as $V = 2(E_2 - E_1)$, versus the Cu^{2+}-O-Cu^{2+} bond angle. One should notice that the V value reaches its maximum at the bond angle of about 96° ($LiCuVO_4$), where the exchange interaction J_1 changes its character from antiferromagnetic to ferromagnetic, as calculated by Mizuno *et al.* for edge-sharing cuprates (29). This empirical interrelation does not allow for a simple explanation and requires an additional study.

Our results have not only persuasively demonstrated the formation of the Mott-Hubbard excitons associated with the ZRS state in the edge-sharing compounds for the first time, but also quantified the characteristic energy scales, such as the local Hubbard U ($2.55 - 4.3$ eV) and long-range Coulomb V ($0.8 - 1.6$ eV) interactions.

4 Charge dynamics in Ni-based heterostructures

4.1 Introduction

Since the discovery of superconductivity, the layered cuprates remain the only materials which exhibit a transition to a superconducting phase above the temperature of liquid nitrogen. From a theoretical point of view, an orbitally nondegenerate spin one-half electronic structure resembling that of cuprate superconductors may be expected in the heterostructured Cu-neighboring nickelates, opening new perspectives for high-Tc superconductivity (119). The proposed superlattices, in which metallic $LaNiO_3$ layers are alternated with band-insulating $LaAlO_3$ layers, imitate layered cuprates with similar low-energy electronic and spin excitations (120). Our motivation to study the $LaNiO_3$-based superlattices derives mainly from these predictions.

The extensive body of knowledge that has been accumulated on bulk nickelate perovskites is another reason why we have chosen this system for our study, which is aimed at controlling the collective phase behaviour systematically – an essential step beyond prior work that was focused on understanding rather than control. A route towards control of correlated-electron systems is indicated by recent advances in the synthesis of transition-metal oxide (TMO) heterostructures and superlattices with atomically sharp interfaces. In principle, the carrier concentration in a heterostructure can be tuned by a gate voltage in a field-effect arrangement, without introducing substitutional disorder, and the dimensionality can be modified by means of the deposition sequence of electronically active and inactive TMO layers. In practice, however, attempts to implement this approach have faced many of the same difficulties encountered in the chemical synthesis of bulk materials. For instance, defects created by interdiffusion or strain relaxation can influence the transport properties of the interfacial electron system in an uncontrolled manner.

Motivated by the desire to overcome these difficulties and to realize the potential of TMO heterostructures in controlling collective quantum phases, we have used wide-band spectroscopic ellipsometry to accurately determine the dynamical electrical conductivity and dielectric permetivity, which (in contrast to the dc conductivity) are not influenced by extended defects. The dimensionality of the $LaNiO_3$ electron system was used as a control parameter. In order to discriminate between the influence of dimensionality and epitaxial strain, we have grown SLs on both $SrTiO_3$ and and $LaSrAlO_4$ substrates, which induces tensile and compressive strain in the overlayer, respectively. Low-energy muons, which are stopped in the SL before

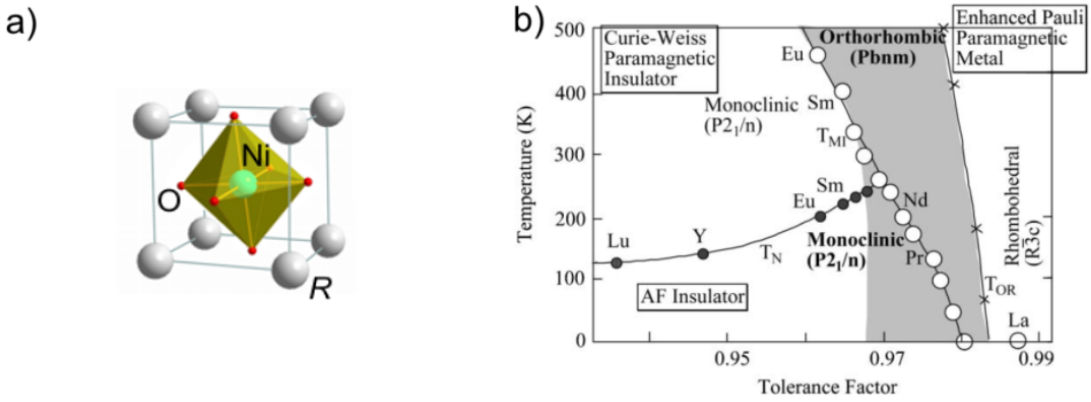

Figure 4.1: (a) The unit cell of $R\mathrm{NiO_3}$ consists of a central Ni-ion, which is octahedrally coordinated by 6 $\mathrm{O^{2-}}$-ions. At the corners of the cube R-ions are located. (b) Temperature-tolerance factor phase diagram for $R\mathrm{NiO_3}$ (122).

they reach the substrate, served as a sensitive probe of the internal magnetic field distribution. Two consecutive sharp phase transitions in the charge and spin sector revealed by this experimental approach demonstrate that the electronic properties of our SLs are determined by electron correlations, and not by interfacial disorder. By changing the $\mathrm{LaNiO_3}$ layer thickness, we demonstrate full dimensionality control over the collective phase behavior.

Bulk nickelates

The nickelates $R\mathrm{NiO_3}$ belong to the perovskite family. The unit cell of $R\mathrm{NiO_3}$ consists of a central Ni-ion, which is octahedrally coordinated by 6 $\mathrm{O^{2-}}$-ions, see Figure 4.1 (a). At the corners of the cube R-ions are situated. The increase in size of rare-earth elements (from Lu to Pr) causes changes in bond lengths, (R-O) and (Ni-O), forming the geometric tolerance factor

$$t = \frac{(R\text{-O})}{\sqrt{2}(\text{Ni-O})}. \tag{4.1}$$

The compressive stress of the (Ni-O) bond and tensile stress of the (R-O) bond is accommodated by tilting and rotation of $\mathrm{NiO_6}$ octahedra and shift of the$R$ position (or orthorhombic distortion). Because of the orthorhombic distortion, the (Ni-O-Ni) bond angle deviates from 180° , the more the smaller is the size of rare-earth element R. With further increase of rear-earth element size (to R=La) an orthorhombic-rhombohedral transition occurs. The rhombohedral $\mathrm{LaNiO_3}$ has the biggest tolerance factor (0.986) and Ni-O-Ni bond angle (165.2°) among other nickelate oxides (121), see Figure 4.1 (b).

The structural, transport and magnetic properties of bulk $R\mathrm{NiO_3}$ (R - rare-earth element) nickel oxides have been studied extensively (121). The intermediate character between an itinerant metal and a localized Mott-Hubbard insulator makes the physics of bulk rear-earth $\mathrm{RNiO_3}$ nickel perovskites nontrivial but fascinating, with a broad spectrum of intrinsic competing ground states, such as charge and

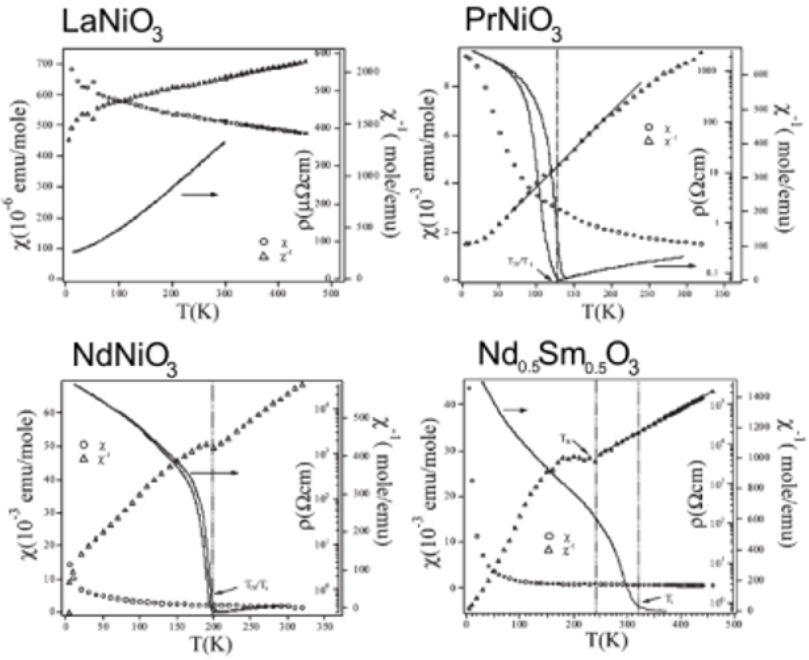

Figure 4.2: Temperature dependence of resistivity ρ, molar magnetic susceptibility χ, and its reciprocal χ^{-1} for $LaNiO_3$, $PrNiO_3$, $NdNiO_3$ and $Nd_{0.5}Sm_{0.5}NiO_3$ (123).

magnetic ordering (126, 163) and possible superconductivity (119, 120). The orthorhombic part of this family (R=Pr, Nd, Sm, Eu) exhibits a thermally induced transition from itinerant to localized $3d$ e_g^1 electrons at T_{MI}. The dependence of resistivity ρ on temperature for $PrNiO_3$, $NdNiO_3$ and $Nd_{0.5}Sm_{0.5}NiO_3$ is shown in Figure 4.2 (123). For these compounds the sharp first-order metal to insulator transition is observed with transition temperature T_{MI} decreasing with increasing size of the rare-earth element. Furthermore, the hysteretic behaviour of the resistivity is evident in Figure 4.2 for $NdNiO_3$ and $PrNiO_3$. However, because of the unusual charge and magnetic ordering pattern, unprecedented in other correlated $3d$ oxides, the ground state cannot be classified as a Mott-Hubbard insulator but as an intermediate phase with charge disproportionation, $2Ni^{3+} \rightarrow Ni^{3+\delta} + Ni^{3-\delta}$, alternative to the orbital ordering. The charge transfer between Ni sites may occur at low temperatures, where the Hund's exchange J_H overcomes the Coulomb repulsion U competing with the e_g^1 electron kinetic energy, $U/W \sim 1$. The proximity of the competing characteristic energies can be easily rebalanced with temperature, pressure and variation of chemical composition (123, 124, 125, 127) . With increasing R-ion radius the electronic bands W widen and the metal-insulator transition temperature T_{MI} decreases. High-resolution X-ray powder diffraction measurements found that strongly distorted perovskite nickelates have a charge ordered ground state (129, 130). Resonant X-ray diffraction and x-ray absorption studies indicated that the charge ordered state occurs also in R = Pr and Nd nickelates (131, 132).

In the nickelate series with small R ions, from Lu to Sm, the magnetic ordering temperature T_N is well below and almost independent of the metal-insulator transi-

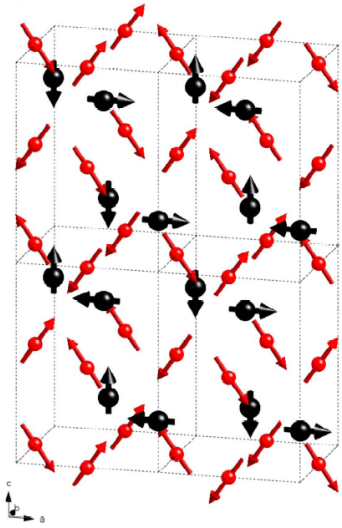

Figure 4.3: The noncollinear magnetic structure of $NdNiO_3$. Nd and Ni ions are indicated by black and red spheres, respectively. Magnetic moment directions are indicated with arrows. Form Ref. (136).

tion. In $NdNiO_3$ and $PrNiO_3$ the metal-insulator and antiferromagnetic transitions occur simultaneously. $LaNiO_3$ is the only member of the series that remains a paramagnetic metal (3D Fermi liquid with correlated $3d$ electrons in a 1/4-filled e_g band) down to the lowest temperatures (123, 133).

The magnetic properties of the nickelates are also dependent on the rare-earth ion size. For nickelates with R = Lu to Sm, three phases are observed [Figure 4.1 (b)]. At high temperatures the Ni sublattice is enhanced-Pauli paramagnetic. With cooling below T_{MI} and with decreasing rare-earth ion size the contribution of Curie-Weiss paramagnetic component increases. Paramagnetism is lost at $T_N (< T_{MI})$, where transition to antiferromagntic phase occurs. In $NdNiO_3$ and $PrNiO_3$ the metal-insulator and antifferomagnetic transitions occur simultaneously. Contrary to all other members of $RNiO_3$ family, $LaNiO_3$ remains paramagnetic.

The magnetic ground state for the perovskite nickelates is discussed within different models (129, 134, 135). Recent resonant soft x-ray diffraction measurements on $NdNiO_3$ indicate that the Ni magnetic structure is noncollinear with propagation vector $(\frac{1}{2}\ 0\ \frac{1}{2})$, consistent with the charge ordering (136), see Fig. 4.3. This scenario is supported by by neutron powder diffraction on $HoNiO_3$ (135).

Optical spectroscopy of perovskite nickelates

A quantitative analysis of the temperature driven changes in electronic structure across the metal to charge ordered transition for $NdNiO_3$ was reported by Katsufuji *et al.* on the basis of a comprehensive optical study in a wide spectral range (0.06 – 15 eV) (138).

The optical conductivity $\sigma(\omega)$ and the real part of the dielectric function $\varepsilon_1(\omega)$ spectra for $NdNiO_3$ at different temperatures, obtained by the Kramer-Kronig analysis of the reflectivity spectra, are shown in Figure 4.4 (a). At room temperature

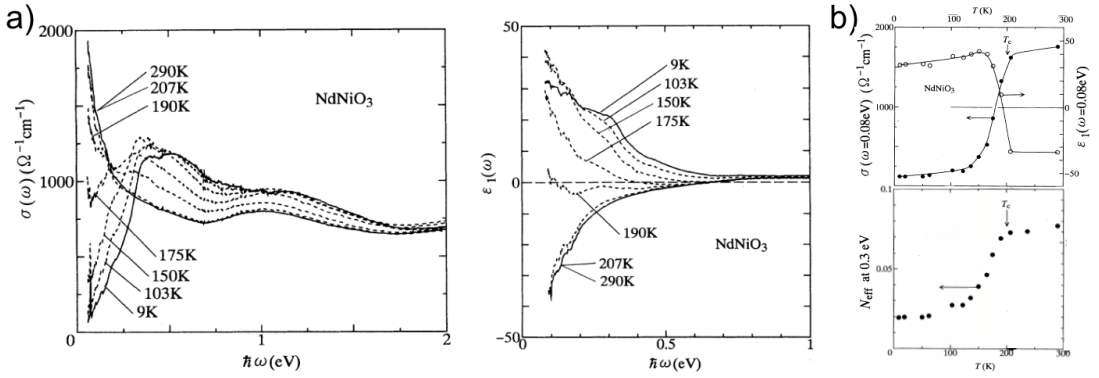

Figure 4.4: (a) Optical conductivity $\sigma(\omega)$ and real part of dielectric function $\varepsilon_1(\omega)$ spectra for $NdNiO_3$ at different temperatures. (b) Upper panel: temperature dependence of σ and ε_1 at 0.08 eV. Lower panel: Effective number of carriers N_{eff} at 0.3 eV (138).

below 0.5 eV the increase in optical conductivity and falling of the real part of dielectric function below zero with approaching zero energy, or Drude-like response, are evidence of typical metal behavior. With temperature decreasing down to 190 K, the Drude-like component is suppressed. At low temperatures ε_2 becomes positive, while the optical conductivity σ drastically drops. The temperature driven changes in σ and ε_1 at 0.08 eV are shown in Figure 4.4 (b) in the upper panel. From this figure one can see that $T_{MI} = 200$ K. The temperature dependence of effective number of free carriers, calculated as the integrated optical conductivity in the spectral range up to the cutoff frequency $\omega_c = 0.3$ eV, is shown on the lower panel in Figure 4.4 (b). From there, the number of electrons, localized at the metal-insulator transition, is 0.058.

The spectroscopic optical reflectivity data are available in the literature for $LaNiO_3$ thin films grown on $LaAlO_3$, $(LaAlO_3)_{0.3}(Sr_2AlTaO_6)_{0.7}$ and $DyScO_3$ substrates (144). The optical conductivity data of bare nickelate oxide films were obtained from the Kramers-Kronig transformation and solution of the vacuum-film-substrate problem. The resulting $\sigma_1(\omega)$ spectra exhibit Drude response below 0.5 eV independent of the substrate, see Figure 4.5. However, the cumulative spectral weight within the Drude part for films grown on $DyScO_3$ substrates is distinctly smaller compared to other substrates. The conductivity spectra extrapolated to zero frequency well coincide with measured dc transport. However, these data are limited only to room temperature and no data are available for low temperatures, where possible effects of strain or thickness of films may cause a transition to the localized state.

$LaNiO_3$ ultrathin films

Recently, several reports have appeared in the literature on the electrical resistivity of $LaNiO_3$ thin films (139, 140, 141, 142, 143) where, contrary to the bulk $LaNiO_3$, evidence of a metal to localized state transition has been observed. The observed electron localization at low temperatures is discussed to be driven by the thickness of the $LaNiO_3$ film, strain, oxygen content or disorder.

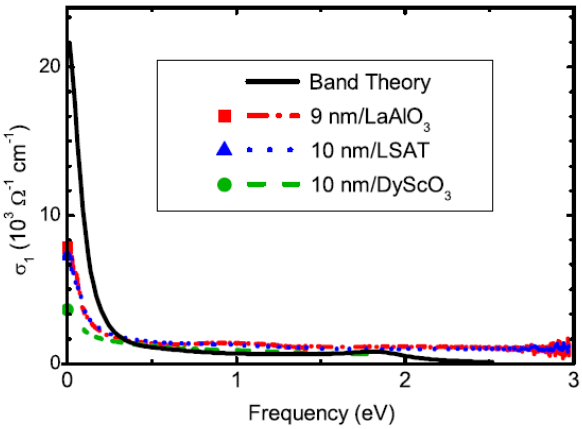

Figure 4.5: Calculated and measured optical conductivity spectra of the 10 nm films grown on $LaAlO_3$, LSAT and $DyScO_3$ substrates obtained from reflectivity. The data points at zero show dc electrical measurements (144).

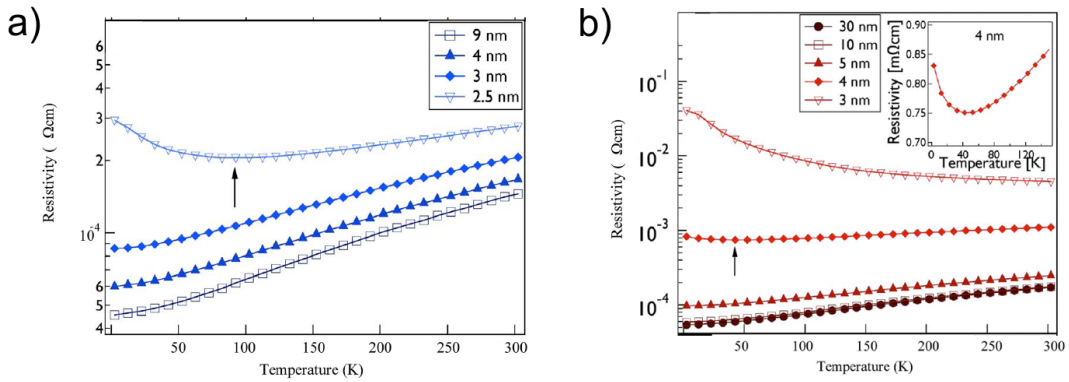

Figure 4.6: Temperature dependence of the resistivity of $LaNiO_3$ films with different thickness grown on (a) $LaAlO_3$ and (b) $(LaAlO_3)_{0.3}(Sr_2AlTaO_6)_{0.7}$ substrates (142).

Figure 4.6 shows the temperature dependencies of the resistivity of $LaNiO_3$ films with different thicknesses grown on $LaAlO_3$ and LSAT substrates, inducing compressive and tensile strain, respectively (142). Thinning of films causes an upturn in resistivity upon cooling below 80 K (40 K) for films grown on $LaAlO_3$ (LSAT) substrates, indicating the electron localization.

The oxygen content of $LaNiO_{3-\delta}$ can be easily changed ($0 \leq \delta \leq 1$) causing an adjustment of the Ni valence state. The deficiency δ=0.5 leads to the divalent oxidation state of Ni ion and drastically changes the conductive properties (140). The δ=0.5 deficiency changes not only the room temperature resistivity up to three orders of magnitude, but causes the 80 nm thick $LaNiO_{3-0.5}$ film to be semiconducting, see Figure 4.7.

Also, the localization of electrons can be caused by the shortening of the electron mean free path, which can be achieved by introducing disorder in the material.

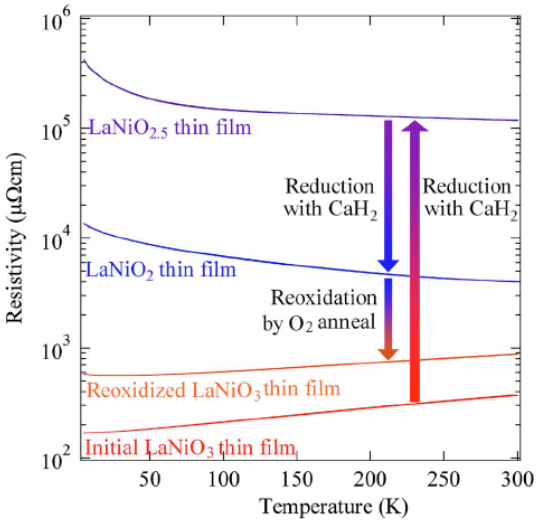

Figure 4.7: Temperature dependence of resistivity ρ of 80 nm thick $LaNiO_3$ film, $LaNiO_{2.5}$ and $LaNiO_2$ films prepared by low-temperature reduction with CaH_2 and reoxidized $LaNO_3$ film, grown on $SrTiO_3$ substrate (140).

Kumar *et al.* (143) showed that a 200 nm $LaNiO_3$ film grown on $LaAlO_3$ substrate and highly irradiated by 200 MeV Ag^{15+} beam exhibits semiconducting behavior.

In the last years, enormous attention was focused on transition-metal oxides superlattices with atomically sharp interfaces due to possibility of developing interface- and dimensionality-controlled devices (145, 146, 147, 148). Recently, May *et al.* reported on the growth and properties of $(LaNiO_3)_n/(SrMnO_3)_2$ superlattices (149). The epitaxially grown superlattices were under tensile stress when deposited on $SrTiO_3$ substrates. The resistivity measurements revealed a transition to an insulating to insulating phase as the thickness of the $LaNiO_3$ layers decreases from 4 to 1 unit cells, resembling the behavior of a bare thin $LaNiO_3$ film deposited on a tensile substrate as shown above.

4.2 Sample growth. Sample quality

For our study, high-quality superlattices (SLs) composed of N u.c. consecutive layers of $LaNiO_3$ and $LaAlO_3$ were grown by pulsed-laser deposition from stoichiometric targets using a KrF Excimer laser with 2 Hz pulse rate and 1.6 J/cm^2 energy density. Both compounds were deposited in 0.5 mbar oxygen atmosphere at 730°C and subsequently annealed in 1 bar oxygen atmosphere at 690°C for 30 min.

SLs were grown on two kinds of single-crystalline substrates: $SrTiO_3$, which induces tensile strain in the overlayer, and $LaSrAlO_4$, which induces compressive strain, see Figure 4.10. All substrates were $(10\times10\times0.5)\,mm^3$ or $(5\times5\times0.5)\,mm^3$ (001)-oriented plates with a miscut angle $< 0.1°$. The growth rate for the individual layers were controlled by counting laser pulses in combination with feedback from high-resolution X-ray diffraction measurements.

The crystallinity, superlattice structure and sharpness of the interfaces (with roughness ≤ 1 u.c.) were verified by x-ray reflectivity and high-resolution hard x-ray diffraction scans which revealed, besides the perovskite Bragg reflections, satellite peaks due to the long-range multilayer superstructure and Kiessig fringes caused by total-thickness interference.

Representative scans along the specular truncation rod are shown in Figure 4.8 for samples grown on the different substrates. Symmetrically around the (001) layer Bragg peak one can see superlattice satellites. The position of the satellites corresponds to a ($LaNiO_3$ | $LaAlO_3$) bilayer thickness of 15.5 ± 0.5 Å for $N = 2$ in good agreement with the $2Nc$ value, where c is the average epilayer lattice constant,

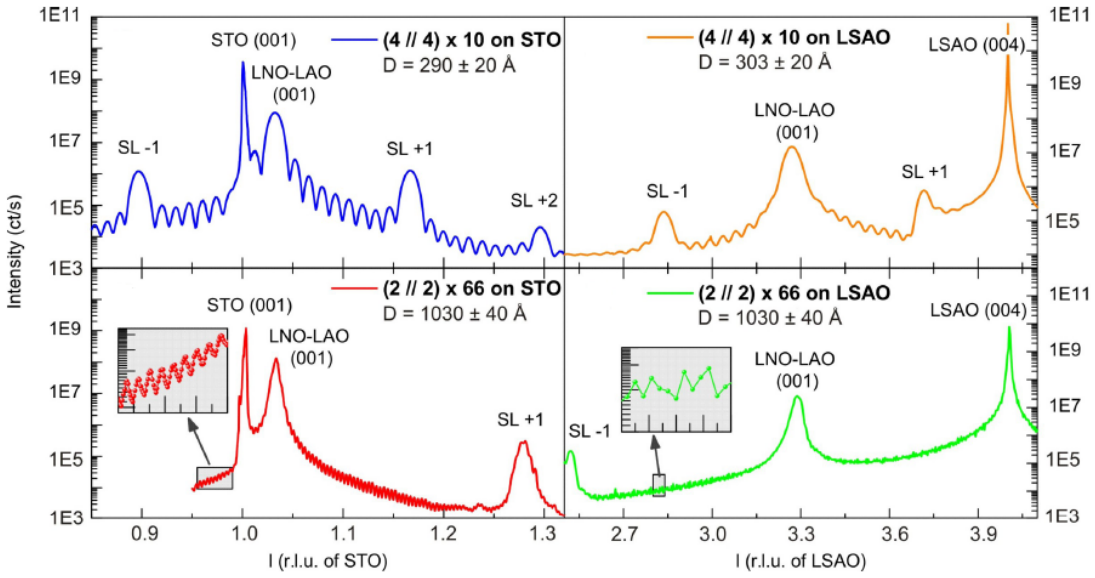

Figure 4.8: High-resolution X-ray diffraction measured with 10 keV synchrotron radiation at the MPI-MF beamline of the ANKA facility at the Karlsruhe Institute of Technology for the 100 nm thick $N = 2$ and 30 nm thick $N = 4$ superlattices on $SrTiO_3$ and $LaSrAlO_4$ substrates (150) (by E. Benckiser and A. Frano).

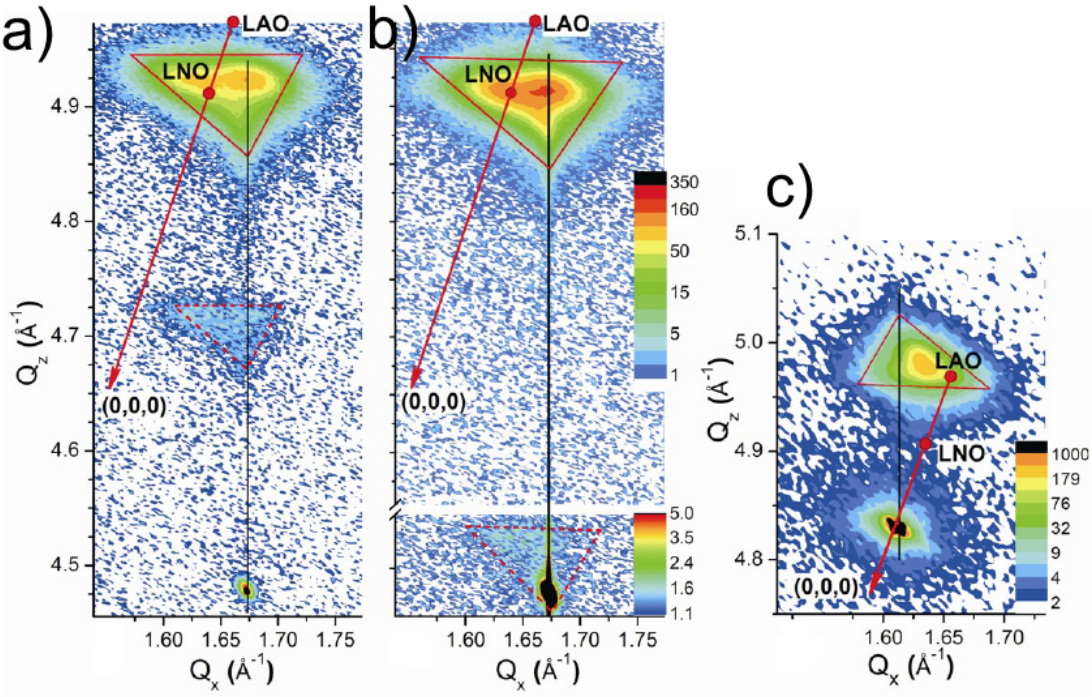

Figure 4.9: Reciprocal-space maps of 100-nm-thick superlattices grown under compressive strain on $LaSrAlO_4$ with (a) $N = 4$ and (b) $N = 2$ and (c) under tensile strain on $SrTiO_3$ with $N = 2$. The black vertical lines indicate the in-plane (Q_x) position of the $LaSrAlO_4$ (109) and $SrTiO_3$ (103) reflections. The strain state of the perovskite epilayers is identified by the intensity distribution in the vicinity of the (103) layer Bragg peak and its superlattice satellite, which are delineated by solid- and dashed-line triangles, respectively. The reciprocal spacings of 103 strain-free pseudo-cubic $LaNiO_3$ and $LaAlO_3$ are indicated by the red circles. The red arrows point towards the origin (150) (by E. Benckiser and A. Frano).

	a,b (Å)	c (Å)
SL on $LaSrAlO_4$	3.769	3.853
SL on $SrTiO_3$	3.845	3.790
$LaNiO_3$	3.837	3.837
$LaAlO_3$	3.789	3.789
$LaSrAlO_4$	3.756	12.636
$SrTiO_3$	3.905	3.905

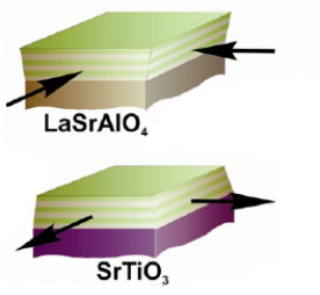

Figure 4.10: The average lattice constants of 100 nm thick $N = 2$ SLs grown on (001)-oriented $SrTiO_3$ and $LaSrAlO_4$ substrates (determined from the main (103) layer Bragg peak positions) in comparison with the lattice constants of strain-free pseudo-cubic $LaNiO_3$ and $LaAlO_3$ and those of the substrates (150).

Figure 4.10. Accordingly, the Kiessig fringes in Figure 4.8 correspond to the total thickness $M \times 2Nc$, with M being the number of bilayer repetitions. X-ray reflectivity was also used to characterize the superlattice structure and sharpness of the interfaces.

In general, the physical properties of thin films are strongly influenced by substrate-induced strain and relaxation effects. It has thus far proven difficult to separate the influence of the dimensionality from that of other parameters such as the strain-induced local structural distortions and interfacial defects. In order to discriminate between these effects we chose to work on SLs grown on both $SrTiO_3$, which induces tensile strain in the overlayer, and $LaSrAlO_4$, which induces compressive strain.

The comprehensive reciprocal-space mapping measurements (151) supplemented by high-resolution transmission electron microscopy micrographs verified that strain and relaxation effects are strongly affected by inversion of the type of substrate-induced strain, but remain essentially unchanged by varying the individual layer thicknesses.

Figure 4.9 shows contour maps of the diffracted X-ray intensity distribution in the vicinity of the (103) perovskite Bragg peak for $N = 4$ and $N = 2$ SLs samples grown on $LaSrAlO_4$ and for with $N = 2$ sample grown on $SrTiO_3$. Apparently, the position and the shape of the layer reflection are strongly affected by inversion of the type of substrate-induced strain, from compressive to tensile [Figures 4.9 (a) and (c)], but remain essentially unchanged by varying the individual layer thicknesses N [Figure 4.9 (a) and (b)]. Compressive strain reduces the in-plane lattice parameter by $\Delta a/a \approx 1.8$ % relative to the bulk $LaNiO_3$ lattice, whereas tensile strain results in a reduction of the out-of-plane lattice constant by $\Delta c/c \approx 1.2$ %. The compressive and tensile types of local distortions in the perovskite structure are accommodated by rotations of the NiO_6 octahedra about different Cartesian axes (152), which, in turn, exert an inequivalent influence on the $LaNiO_3$ electronic structure. A distribution of the diffracted intensity near the epilayer reflection for SLs grown on $LaSrAlO_4$ has a characteristic triangular shape with dispersion along the in-plane Q_x direction towards the (103) Bragg reflection of strain-free bulk $LaNiO_3$. This double-peak intensity pattern suggests the formation of twinning domains after a certain layer thickness (150). This is in contrast to the tensile-strained SLs grown on $SrTiO_3$ where the strain relaxation is characterized by nearly elliptical contour lines close to the (103) Bragg reflection of cubic $LaAlO_3$. This suggests that other types of interfacial defects, presumably oxygen vacancies (155), are mostly responsible for the misfit relief in the tensile case. For details on the contour maps see supplementary materials to Ref. (150) and Ref. (151).

Figure 4.11 shows high-resolution TEM micrographs (recorded at a JEOL JEM4000FX microscope) of the $LaNiO_3$ | $LaAlO_3$ layer system grown on $LaSrAlO_4$ substrate (by E. Detemple). Visible planar defects (marked by arrows) are oriented perpendicular to the substrate plane and extend through the entire SL. As shown in the magnified inset image, the stacking sequence changes at these faults (yellow broken line). The size of the defect-free blocks varies between 15 and 50 nm. The microstructure of the layer system on the $SrTiO_3$ substrate (not shown here, see (150)) only very occasionally shows planar defects. Instead, localized defects are found close to the substrate. These defects may be associated with the creation of oxygen vacancies

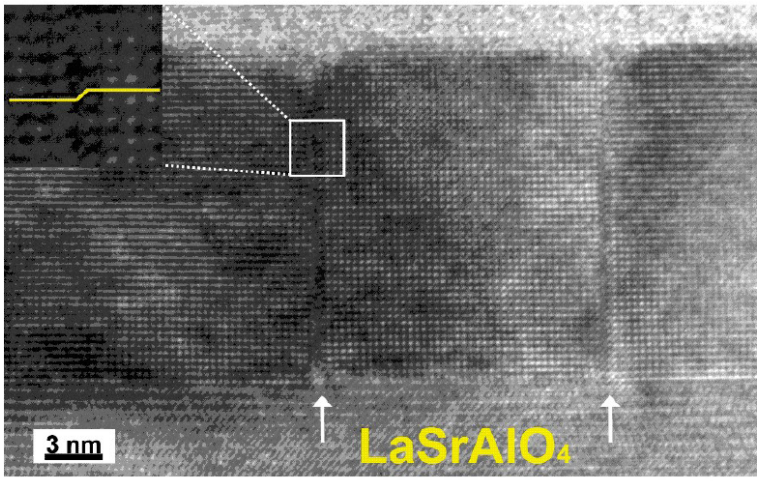

Figure 4.11: High-resolution TEM micrographs of $LaNiO_3$ | $LaAlO_3$ SLs on $LaSrAlO_4$ substrate. Defects are marked by arrows. The inset in shows a magnified area close to a planar defect (150) (by E. Detemple).

and changes in the oxygen coordination of Ni ions at the substrate interface.

Recent hard X-ray photoelectron spectroscopy (HAXPES) measurements on some of samples have confirmed that the initial growth on the $SrTiO_3$ surface leads to the Ni^{2+} valence state. The oxygen vacancy formation energy gradually decreases with increasing the in-plane perovskite lattice spacing (159), which can explain the marked difference in the oxygen vacancy concentration in thin films grown under tensile or compressive strain (155). Nevertheless, in our study, the temperature-induced phase transitions occur in the $N = 2$ (but not in $N = 4$) SLs irrespective of whether the substrate-induced strain is compressive or tensile, which clearly distinguishes these transitions from those in highly oxygen deficient $LaNiO_{3-\delta}$ ($\delta \geq 0.25$) (160, 140). Moreover, the reduced insulating phases require more than 1/3 of divalent Ni^{2+} in square planar (vs. perovskite octahedral) sites. Based on the detailed characterization of our samples by means of XRD, XAS, RSM, HAXPES, and TEM we can definitively rule out such a scenario.

In conclusion, detailed analysis confirm the high quality of the synthesized SLs, which exhibit abrupt interfaces and excellent crystallinity. The defect-free atomically precise 15-50 nm blocks are separated by $\sim$ 1 u.c. stacking faults. These planar defects are inevitably caused by atomic step on the substrate in combination with strain relaxation effects, and can block the current flow through the atomically thin layers. Because of it, the local probe measurements, such as ellipsometry, have a big advantage for studying the charge dynamics in SLs.

4.3 Charge transport properties. Spectroscopic ellipsometry measurements and data analysis

We have used wide-band spectroscopic ellipsometry to accurately determine the dynamical electrical conductivity and permittivity of the SLs. In contrast to *dc* transport experiments, this method exposes the intrinsic electrodynamic response of SLs, which is not influenced by the substrate, contacts and extended defects. As a low-energy spectroscopic tool, it serves to determine critical parameters of the metal-insulator transition such as the energy gap and the density of carriers localized below T_{MI}. Variable angle ellipsometry is very sensitive to thin-film properties due to the oblique incidence of light, and it is generally used to derive optical constants of thin films and complex heterostructures (4), as discussed in Chapter 1 of this thesis.

Figure 4.12 shows the representative infrared spectra of $\Psi(\omega)$ and $\Delta(\omega)$ for the $N = 4$ and 2 SLs and for the bare $LaSrAlO_4$ and $SrTiO_3$ substrates. For the frequencies studied here, the penetration depth of the incident light is larger than the thickness of the Sls, which implies that the substrate affects the measured ellip-

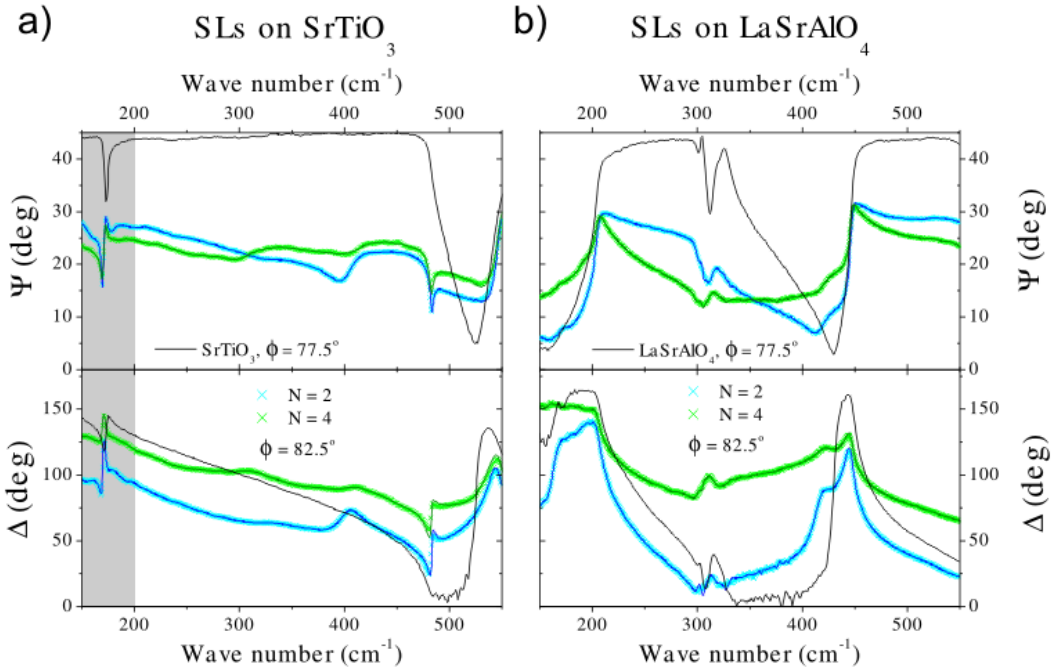

Figure 4.12: Experimental (thick colored lines) and best-fit calculated (thin gray lines) ellipsometry spectra of the N = 2 and N = 4 SLs on (a) $SrTiO_3$ at $T = 100$ K and (b) $LaSrAlO_4$ at $T = 175$ K. The angle of incidence of the polarized light was $\phi = 82.5°$. Ellipsometry spectra of the bare substrates measured at $\phi = 77.5°$ are shown for comparison (black solid lines). The gray shaded area in (a) indicates the region where the data analysis is affected by dielectric microwave dispersion of the ferroelectric soft mode of $SrTiO_3$ (150).

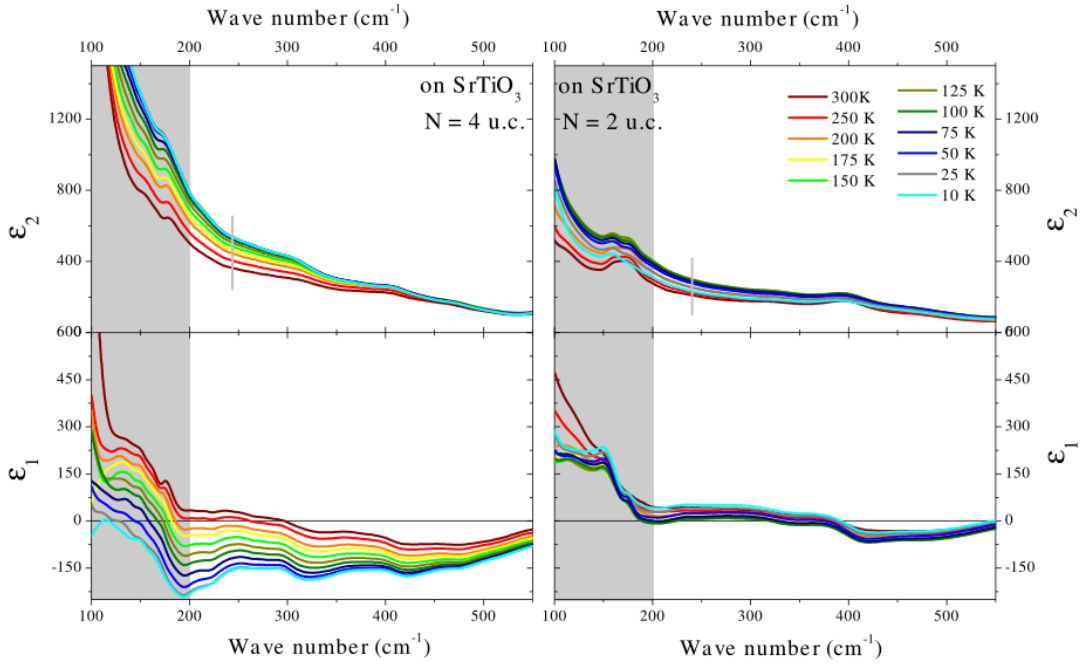

Figure 4.13: Real $\varepsilon_1(\omega)$ and imaginary $\varepsilon_2(\omega)$ spectra of the $N = 2$ and $N = 4$ SLs on $SrTiO_3$ substrate measured at representative temperatures. The gray shaded area indicates the region where the data analysis is affected by dielectric microwave dispersion of the ferroelectric soft mode of $SrTiO_3$ (161).

sometric spectra. This is clearly seen in spectra shown in Figure 4.12, where the strong optical phonon features of the substrate influence the optical response of the thin-SLs samples. The SLs were treated as single-layer films according to an effective-medium approximation with a mixture of the nickelate and aluminate layers. A wavelength-by-wavelength regression procedure has been employed to extract the real and imaginary parts of the dielectric function, see Chapter 1 for details.

Figures 4.13 and 4.14 show the infrared spectra of the real $\varepsilon_1(\omega)$ and imaginary $\varepsilon_2(\omega)$ parts of the dielectric function of $N = 4$ and 2 SLs grown on $SrTiO_3$ and $LaSrAlO_4$, respectively, measured at different temperatures. Although the SLs were treated as single-layer films according to an effective-medium approximation, the dielectric spectra in Figures 4.13 and 4.14 are representative of the in-plane dielectric response of the metallic $LaNiO_3$ layer.

The temperature dependencies of ε_2 at 250 cm^{-1}, as marked by gray lines in Figures 4.13 – 14, for $N = 2$ and 4 SLs grown on $LaSrAlO_4$ and $SrTiO_3$ substrates are shown in Figure 4.15 (a, b). The gradual evolution of ε_2 with temperature over the far-infrared range confirms that the $N = 4$ SLs remain metallic at all temperatures. In contrast, the $N = 2$ SLs show clear evidence of a metal-insulator transition upon cooling. The transition temperature T_{MI} varies from 150 K to 100 K for the SLs grown on the $LaSrAlO_4$ and $SrTiO_3$ substrates, respectively.

The infrared spectra are well described by a broad Drude response

$$\varepsilon(\omega) = \varepsilon_\infty - \omega_{pl}^2/(\omega^2 + i\omega\gamma), \tag{4.2}$$

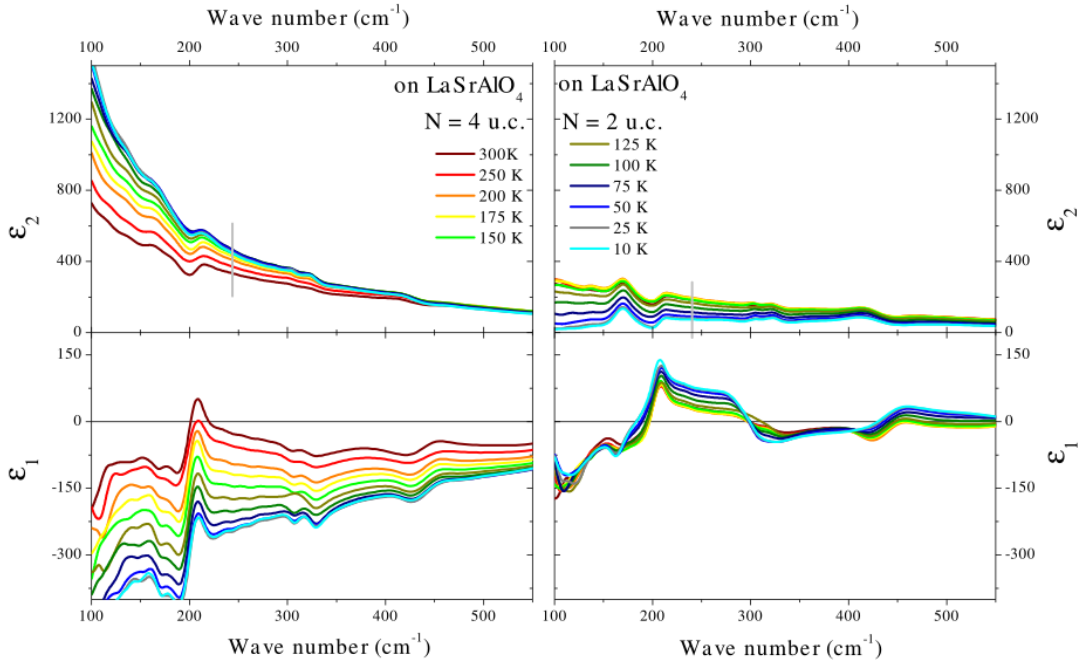

Figure 4.14: Real $\varepsilon_1(\omega)$ and imaginary $\varepsilon_2(\omega)$ spectra of the $N = 2$ and $N = 4$ SLs on $LaSrAlO_4$ substrate measured at representative temperatures.

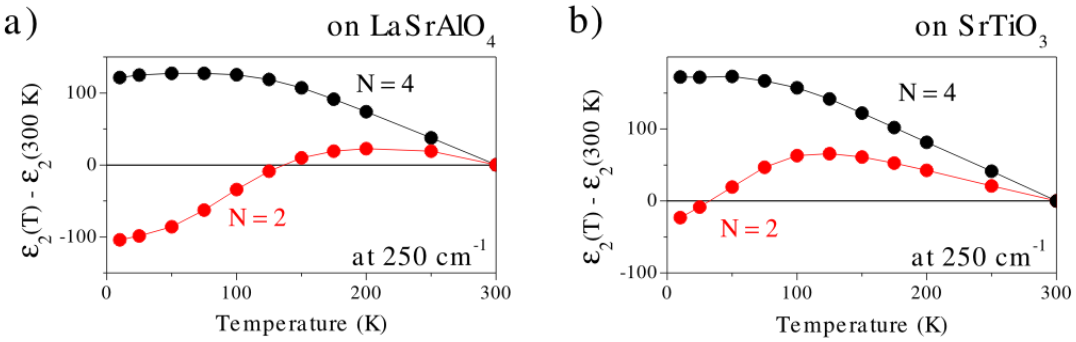

Figure 4.15: Temperature dependencies of ε_2 at 250 cm^{-1} for the $N = 2$ and $N = 4$ SLs grown on (a) $LaSrAlO_4$ and (b) $SrTiO_3$ substrates (150).

with a ratio of scattering rate and plasma frequency $\gamma/\omega_{pl} \approx 0.1 - 0.2$ that is typical for bulk complex oxides. The parameters in the Drude fit (Table 4.1) are well constrained, because both $\varepsilon_1(\omega)$ and $\varepsilon_2(\omega)$ are available. The deviation of the Drude fit from the measured $\varepsilon_1(\omega)$ and $\varepsilon_2(\omega)$ below 200 cm^{-1}(25 meV) in Figure 4.16 (gray shadow area) can reflect the uncertainty in the inversion procedure for SLs on $SrTiO_3$ due to the microwave dispersion of the ferroelectric soft mode of $SrTiO_3$ (161) and/or due to the presence of a dead layer with reduced conductivity at the substrate interface.

This low-energy uncertainty does not, however, affect the relative spectral weight

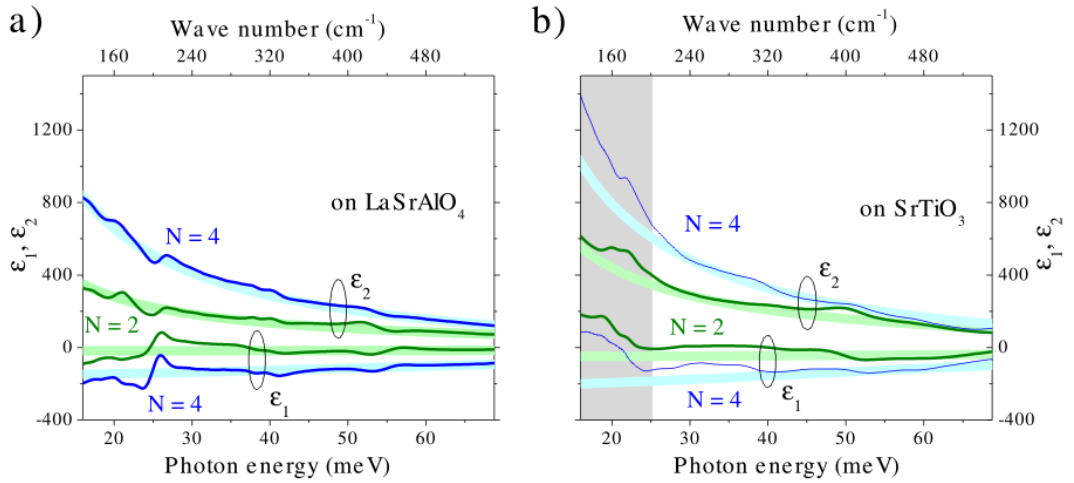

Figure 4.16: Real $\varepsilon_1(\omega)$ and imaginary $\varepsilon_2(\omega)$ parts of dielectric function for the $N = 2$ and $N = 4$ SLs on (a) $LaSrAlO_4$ at $T = 175$ K and (b) $SrTiO_3$ at $T = 100$ K. The shaded lines represent the Drude model simultaneous fit to both $\varepsilon_1(\omega)$ and $\varepsilon_2(\omega)$ with parameters ω_{pl} and γ described in the Table 4.1. The gray shaded area in (b) indicates the region where the model fitting curves deviate significantly from the data (150).

Table 4.1: The parameters ω_{pl} and γ of the Drude model fit to both $\varepsilon_1(\omega)$ and $\varepsilon_2(\omega)$ for $N = 4$ and $N = 2$ SLs grown on the $LaSrAlO_4$ and $SrTiO_3$ substrates measured at 175 K and 100K, respectively, as shown in Figure 4.15 (150).

	$N = 4$ SL on $LaSrAlO_4$	$N = 2$ SL on $LaSrAlO_4$
ω_{pl}, eV	1.1	1.05
γ, meV	87	196
	$N = 4$ SL on $SrTiO_3$	$N = 2$ SL on $SrTiO_3$
ω_{pl}, eV	1.1	1.1
γ, meV	72	136

reduction, $\Delta SW \approx 0.03$ ($\pm 10\%$) per Ni atom, within the gap energy range below $\Omega_G \approx 0.43$ eV at the metal insulator transition in the $N = 2$ SL on $SrTiO_3$.

The effective mass enhancement m^*/m is estimated from the plasma frequency as

$$m^*/m = \frac{4\pi e^2 n}{m\omega_{pl}^2} \approx \frac{11.7}{(\omega_{pl}, [eV])^2}, \tag{4.3}$$

where $n = \frac{1}{2} \times 1.7 \times 10^{22}$ cm^{-3}, by assuming one electron per Ni atom. With $\omega_{pl} \approx 1.1$ eV, as derived from the Drude model fits in Figure 4.15 and Table 4.1, we obtain $m^*/m \approx 10$ which is in good agreement with the value for bulk $LaNiO_3$ from the specific heat measurements (162). Using the Fermi energy $E_F = 0.5$ eV derived from the thermopower of $LaNiO_3$ (162), the Fermi velocity can be estimated as

$$v_F = c\sqrt{\frac{2E_F}{mc^2}\frac{m}{m^*}} \approx 1.33 \times 10^7 \text{cm/s}. \tag{4.4}$$

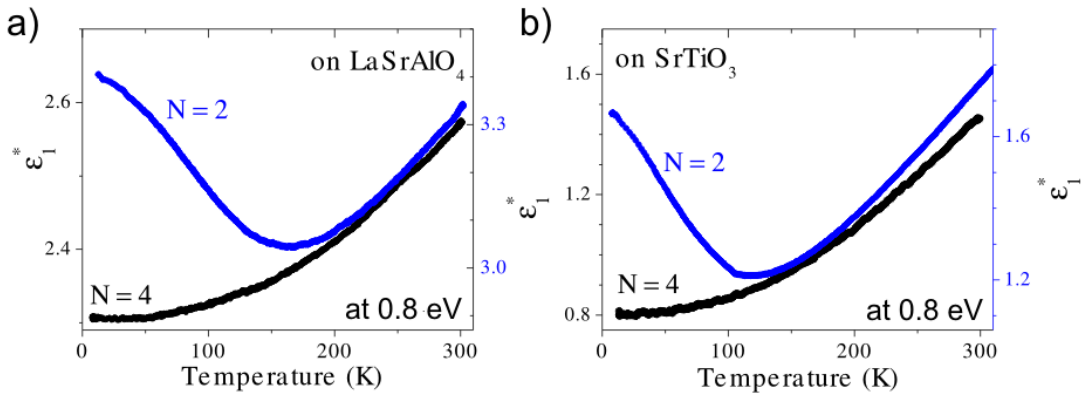

Figure 4.17: Temperature dependence of the as-measured pseudo-dielectric permittivity ε_1^* at $\hbar\omega = 0.8$ eV in the $N = 2$ (blue) and $N = 4$ (black) SLs on (a) $LaSrAlO_4$ and (b) $SrTiO_3$ (150).

The mean free path, l, can be estimated from

$$l\ [\text{Å}] = v_F\tau = \frac{v_F}{2\pi c\gamma} = 6.57 \times 10^{-5}\frac{v_F\ [\text{cm/s}]}{\gamma\ [\text{meV}]} \approx \frac{874}{\gamma\ [\text{meV}]}. \tag{4.5}$$

With $\gamma \approx$200 meV [Figure 4.16 (a), Table 4.1], obtained mean free path is $l = 4.4$ Å for the $N = 2$ SL on $LaSrAlO_4$. For the $N = 2$ SL on $SrTiO_3$ the estimated mean free path is $l = 6.4$ Å. With $\gamma \approx 90$ meV [Figure 4.16 (b), Table 4.1], obtained mean free path is $l = 9.7$ Å for the $N = 4$ SL on $LaSrAlO_4$. For the $N = 4$ SL on $SrTiO_3$, the estimated mean free path is $l = 12$ Å. Remarkably, the mean free path correlates with the individual $LaNiO_3$ layer thickness.

The charge-carrier localization at lower temperature can be readily identified through a rapid drop in $\varepsilon_2(T)$ and progressive deviation of $\varepsilon_2(\omega)$ from the Drude function due to the formation of a charge gap. The temperature evolution of the real part of the dielectric function, $\varepsilon_1(T)$, provides complementary information about the optical spectral weight redistribution.

Figures 4.17 (a,b) show the temperature dependencies of the as-measured permittivity, ε_1^*, at energy 0.8 eV, which is above the gap energy. In the metallic phase ε_1^* decreases with decreasing temperature, following the temperature dependence of the scattering rate, $\gamma(T)$. This is characteristic of a narrowing of the Drude peak where the spectral weight is removed from from the high-energy tail and transferred to the far-infrared range near the origin. The charge gap formation below T_{MI} in $N = 2$ SLs leads to the reverse spectral weight transfer from the inner-gap region to excitations across the gap, and as consequence, to an increase in ε_1^*. [1]

The consistent temperature evolution of ε_1 and ε_2 over a broad range of photon energies demonstrates the intrinsic nature of the charge-localization transition

[1] T_{MI} is identified as the temperature at which the temperature derivative of both $\varepsilon_2(T)$ (Figure 4.15) and $\varepsilon_1(T)$ (Figure 4.17) change sign. In the $\omega \to 0$ limit this criterion is analogous to a sign change of the temperature derivative of the *dc* resistivity, $d\rho/dT$, observed at T_{MI} in bulk $R\text{NiO}_3$.

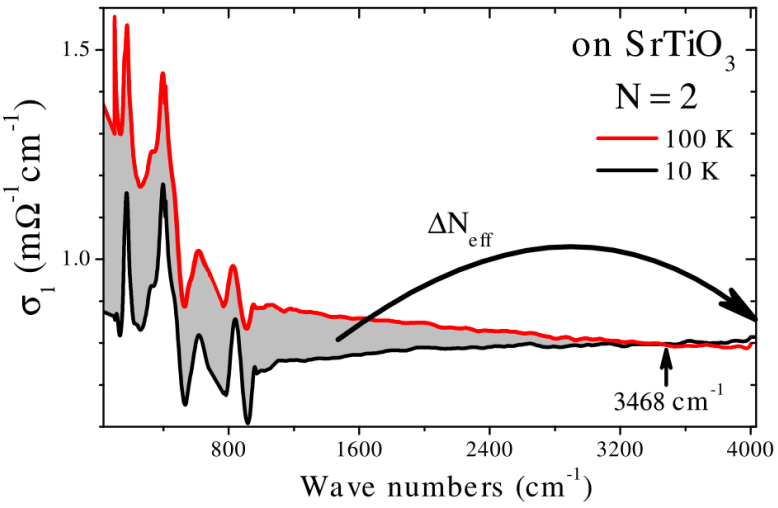

Figure 4.18: The difference between the optical conductivity spectra $\sigma_1(100\ \mathrm{K}, \omega)$ and $\sigma_1(10\ \mathrm{K}, \omega)$ (shaded area) quantifies the reduction of the effective charge density, $\Delta SW \approx 0.03$ per Ni atom, within the gap energy range below 3468 cm^{-1} at the charge ordering transition in the $N = 2$ superlattice on $SrTiO_3$ **a**.

observed in SLs with $N = 2$ and provides clues to its origin. This is in contrast to results of recent dc electrical resistivity measurements where the insulating behavior of 2 u.c. thick $LaNiO_3$ is observed over the entire temperature range and attributed to variable range hopping transport (148) or film-substrate interface effects (141, 142). The spectral weight reduction within the gap can be quantified in terms of the effective number of charge carriers per Ni atom and extracted from a sum-rule analysis as

$$\Delta N_{eff} = \frac{2m}{\pi e^2 N_{\mathrm{Ni}}} \int_0^{\Omega_G} [\sigma_1(T \approx T_{MI}, \omega) - \sigma_1(T << T_{MI}, \omega)] d\omega, \qquad (4.6)$$

where m is the free-electron mass and N_{Ni} the density of Ni atoms. The upper integration limit, $\Omega_G \approx 0.43$ eV $= 3468\ \mathrm{cm}^{-1}$, is a measure of the charge gap and can be identified with the equal-absorption (or isosbestic) point, where $\sigma_1(\omega)$ curves at different temperatures intersect (Figure 4.18). The charge-gap formation on this energy scale can be attributed to a charge-ordering instability, as in the case of bulk lanthanide nickelates $RNiO_3$ with smaller R-ion radius (136, 163, 164). The spectral weight $\Delta N_{eff} = 0.03$ below $\Omega_G \approx 0.43$ eV determined for the $N = 2$ SL (Figure 4.18) is of the same order as, albeit somewhat lower than, the corresponding quantity $\Delta N_{eff} = 0.058$ below $\Omega_G \approx 0.3$ eV reported at the metal-insulator transition in bulk which is known to be due to charge order (138).

To highlight the analogy to the behavior in bulk nickelates, Figure 4.19 shows reference measurements on single 100 nm thick films of $NdNiO_3$ and $LaNiO_3$, measured under the same conditions as in Figure 4.16. Since ε_1^* at 0.8 eV for the single $NdNiO_3$ film displays closely similar temperature dependence as found for $N = 2$ SLs, we conclude that the gap formation in the latter case also reflects charge ordering. In $NdNiO_3$ the metal-insulator transition occurs as a first order transition

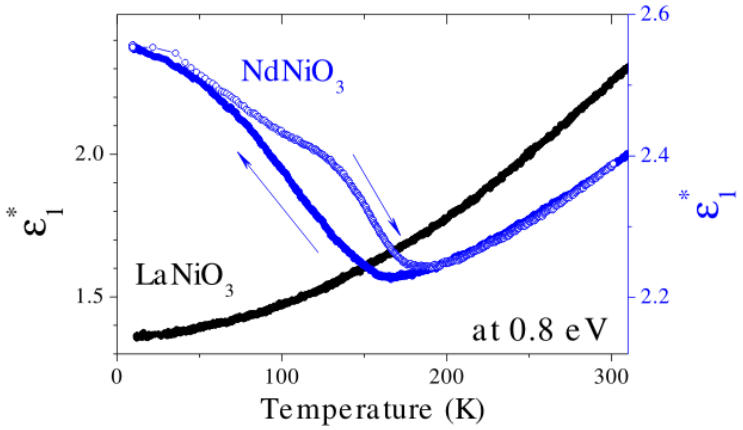

Figure 4.19: Temperature dependence of ε_1^* at 0.8 eV of reference 100 nm films of $LaNiO_3$ (black) and $NdNiO_3$ (blue) (150).

with a concomitant noncollinear antiferromagnetic ordering, $T_N = T_{MI}$ (136, 164).

The thermal hysteresis in the $\varepsilon_1^*(T)$ curve for $NdNiO_3$ in Figure 4.18 is consistent with the first-order character of the transition, with uniform and charge ordered phases coexisting over a broad temperature range. In contrast, there is no discernible hysteresis observed in $\varepsilon_1^*(T)$ of $N = 2$ SLs (Figure 4.17). Continuing the analogy with bulk nickelate series $R\mathrm{NiO}_3$, one would then expect another second-order transition due to the onset of antiferromagnetic ordering at $T_N < T_{MI}$ in the $N = 2$ SLs, as in $R\mathrm{NiO}_3$ with small R, from Lu to Sm.

Ellipsomtery results indicate that, even in the $N = 2$ samples at $T \gtrsim T_{MI}$, the conductivity of the $LaNiO_3$ layers exhibits a clearly metallic temperature and frequency dependence. This is at variance with previously reported results of electrical resistivity measurements on $(LaNiO_3)_N/(SrMnO_3)_2$ SLs (148) and ultrathin

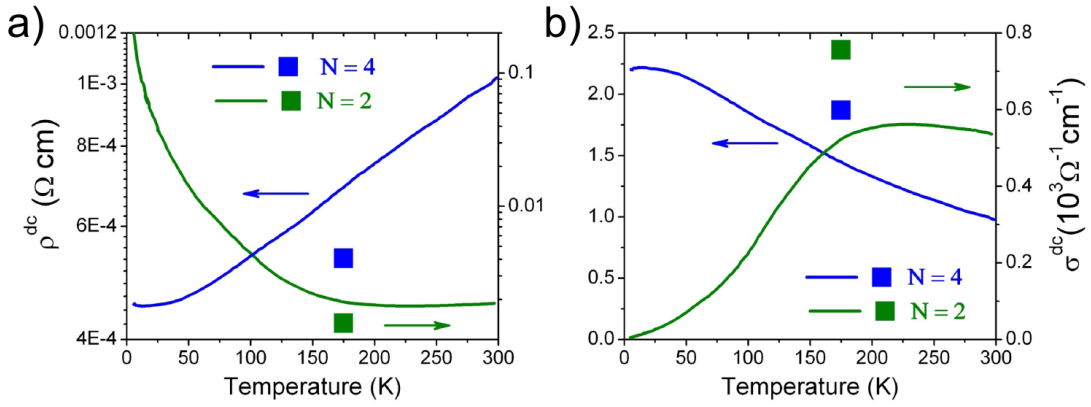

Figure 4.20: Temperature dependence of the *dc* (a) resistivity and (b) conductivity of the N = 2 (green) and N = 4 (blue) SLs on $LaSrAlO_4$. Solid squares represent the conductivity obtained from the Drude model parameters, see Table 4.1, which exceeds the corresponding σ^{dc} ($T = 175$ K) values by less than 20 % (150).

films of $LaNiO_3$ (141, 142). For a thickness of $N = 2$ u.c. the behaviour of $(LaNiO_3)_N/(SrMnO_3)_2$ SLs is insulating over the entire temperature range, whereas the $N = 4$ u.c. SL is metallic with an upturn in resistivity below 50 K. Even in the $N = 4$ u.c. metallic sample, the mean free path is estimated to be less than a single unit cell (148). This suggests that Anderson localization induced by disorder is responsible for the insulating behavior in these systems, in contrast to the sharp temperature dependence observed in our SLs that indicates a metal-insulator transition driven by collective interactions. Ultrathin single films of $LaNiO_3$ show a crossover from metallic to insulating behaviour at a larger thickness, which varies from 6 u.c. to 13 u.c. depending on the substrate. We argue that the presence of planar stacking fault defects and a dead layer with reduced conductivity at the substrate interface, as discussed above (Figure 4.11), makes the analysis of the temperature-dependent resistivity measurements challenging and inconclusive about the conduction mechanism of ultrathin $LaNiO_3$ films.

In order to directly compare results obtained here with those reported in Refs. (141, 142, 148) (and shown above in the introduction to this Chapter), *dc* resistivity measurements were performed on the $N = 2$ and $N = 4$ SLs on $LaSrAlO_4$. Figure 4.19 shows that *dc* and optical conductivity data [Figures 4.13 and 4.15 (a)] are in close agreement. This resemblance once more indicates a low density of stacking faults in our samples, testifying to the high quality of the interfaces.

4.4 Magnetic properties

In this section the brief overview of magnetic properties of Ni-based SLs studied by low-energy muon spin rotation (LE-μSR) measurements using the μE4 beamline at the Paul Scherrer Institute (168, 169) is reported. Details of the experiment and data analysis can be found in Ref. (150) and supplemenatry materials to it available on-line.

The left panel of Figure 4.21 shows muon decay asymmetry data from a SL with $N = 2$ at selected temperatures with no external field. At $T > 50$ K, the asymmetry is described by a Gaussian with relatively slow relaxation, σ, given by $A(0)\times\exp(-\sigma^2 t^2/2)$ (solid lines in Figure 4.21)[2], typical of dipolar magnetic fields generated by nuclear moments of La and Al. As the temperature decreases, there is a gradual increase in σ from 0.17 μs^{-1} at 250 K to 0.27 μs^{-1} at 20 K. Below 50 K the asymmetry drops sharply, and the μSR spectra can be fitted well by introducing an additional exponential relaxation $\exp(-\Lambda t)$. The fast depolarization rate Λ reaches a value of $\approx 17 \mu s^{-1}$ at 5 K, implying a resulting Lorentzian distribution of local fields with half-width-at-half-maximum $\Delta B = 0.75\Lambda/\gamma_\mu \approx 150$ G (150). The fast increase in Λ with decreasing temperature below 50 K is similar to the behavior in bulk $NdNiO_3$ (165) and $(Y, Lu)NiO_3$ (166) below T_N, caused by static internal fields from ordered Ni magnetic moments. The wide field distribution ΔB and

[2]The initial asymmetry, $A(0) \approx 0.18$, is smaller than the asymmetry of the LE-μSR setup of ≈ 0.27, because only 2/3 of the muon beam with a diameter of about 2 cm hit the sample with an area of 1×2 cm^2. The sample was surrounded by a Ni-coated sample holder, which causes a very fast depolarization (< 0.06 μs) of muons missing the sample.

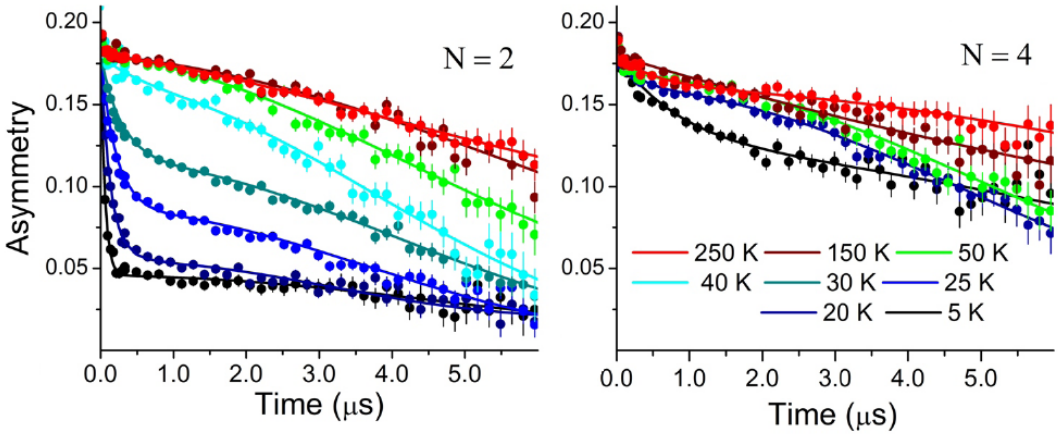

Figure 4.21: The time evolution of the zero-field muon spin polarization at various temperatures for the $N = 2$ (left panel) and $N = 4$ (right panel) superlattices on $LaSrAlO_4$ (150).

the absence of a unique muon precession frequency reflects the SL structure with several inequivalent muon stopping sites in the alternating magnetic ($LaNiO_3$) and nonmagnetic ($LaAlO_3$) layers, probably compounded by a complex non-collinear spin structure as in the bulk nickelates (165, 166).

To determine the fraction of muons, f_m, experiencing static local magnetic fields $B_{loc} > B_{TF}$ (i.e. showing no detectable precession with $\omega = \gamma_\mu B_{TF}$), 100 G transverse field measurements were used (150). Figure 4.22 (a) indicates that the $N = 2$ SL shows a transition from an entirely paramagnetic muon environment ($f_m = 0$) to a nearly full volume of static internal fields, with a sharp onset at $T_N \sim 50$ K. The magnetic state at 5 K is robust against externally applied transverse fields up to 3 kG, that is the limit of time resolution of the setup. The continuous temperature dependence of f_m and the absence of thermal hysteresis indicate that the magnetic transition for the $N = 2$ SLs is second-order.

At the same time, Figures 4.21 and 4.22 (b) show that SLs with thicker $LaNiO_3$ layers remain paramagnetic down to the lowest temperatures, as in bulk $LaNiO_3$. An additional slow exponential relaxation with $\Lambda = 0.9\ \mu s^{-1}$ is seen only at $T = 5$ K. It results in a relatively small increase in relaxation rate, but no loss in asymmetry of the transverse field μSR signal [Figure 4.22 (b)]. The effect is likely due to weak dynamical spin correlations that are quenched already in a field of 100 G, in clear contrast to the long-range static magnetic order observed in the $N = 2$ samples.

As a local probe, μSR does not allow definite conclusions about the magnetic ordering pattern in the $N = 2$ SLs. However, ferromagnetism and a spin-glass state were ruled out (150), implying an antiferromagnetic origin of the phase transition in the $N = 2$ SLs.

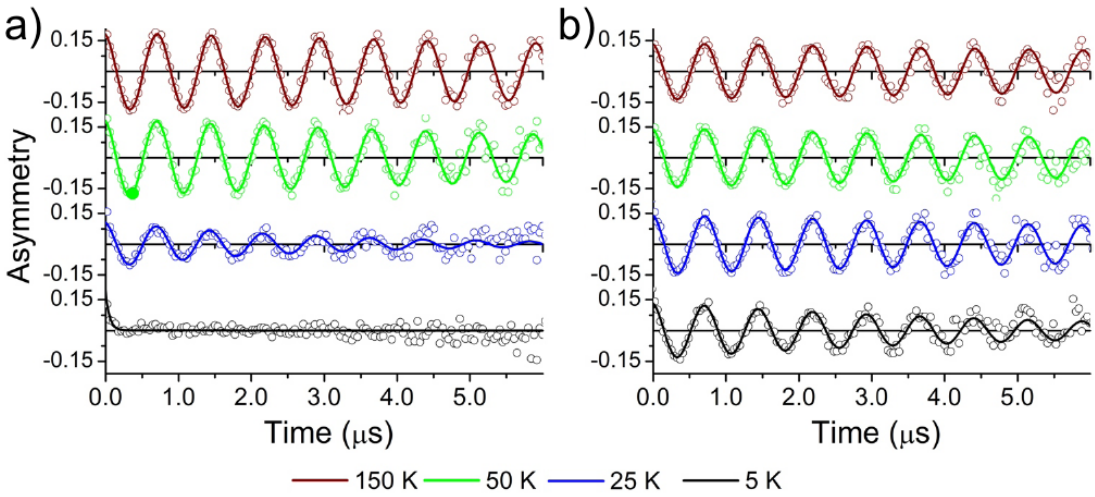

Figure 4.22: Muon spin relaxation spectra in a weak transverse magnetic field of 100 G in the (a) $N = 2$ and (b) $N = 4$ superlattices on $LaSrAlO_4$ (150).

4.5 Conclusions

Wide-band spectroscopic ellipsometry was used to accurately determine the dynamical electrical conductivity and permittivity of nickel-oxide superlattices, which (in contrast to the *dc* conductivity) are not influenced by misfit dislocations. Using optical ellipsometry and low-energy muon spin rotation, as a sensitive probe of the internal magnetic field distribution, it was shown that superlattices with $LaNiO_3$ as thin as two unit cells undergo a sequence of collective charge- and spin-ordering transitions as a function of decreasing temperature, whereas samples with thicker $LaNiO_3$ layers remain paramagnetic and metallic at all temperatures, see Figure 4.23.

Figure 4.24 summarizes the phase behavior of the $N = 2$ SLs, which undergo a sequence of two sharp charge- and spin-ordering transitions upon cooling, while the $N = 4$ counterparts remain uniformly metallic and paramagnetic at all temperatures. Thus, full dimensionality control of these collective instabilities is demonstrated. The higher propensity towards charge and spin order in the two-dimensional systems probably reflects enhanced nesting of the $LaNiO_3$ Fermi surface. The phase behavior is qualitatively similar to the one observed in bulk $RNiO_3$ with small radius of the R anions, which results from bandwidth narrowing due to rotation of NiO_6 octahedra, but the transition temperatures and the order parameters are substantially lower, probably because of the reduced dimensionality.

Since the transitions occur in the $N = 2$ SLs irrespective of whether the substrate-induced strain is compressive ($LaSrAlO_4$ substrate) or tensile ($SrTiO_3$ substrate), structural parameters such as rotation and elongation of the NiO_6 octahedra can be ruled out as primary driving forces. However, the infrared conductivity is higher (Figures 4.12 and 4.13) and the transition temperatures are lower (Figure 4.22) in the $N = 2$ SL grown under tensile strain. The more metallic response of these SLs, compared to those grown under compressive strain, may reflect a widening of the

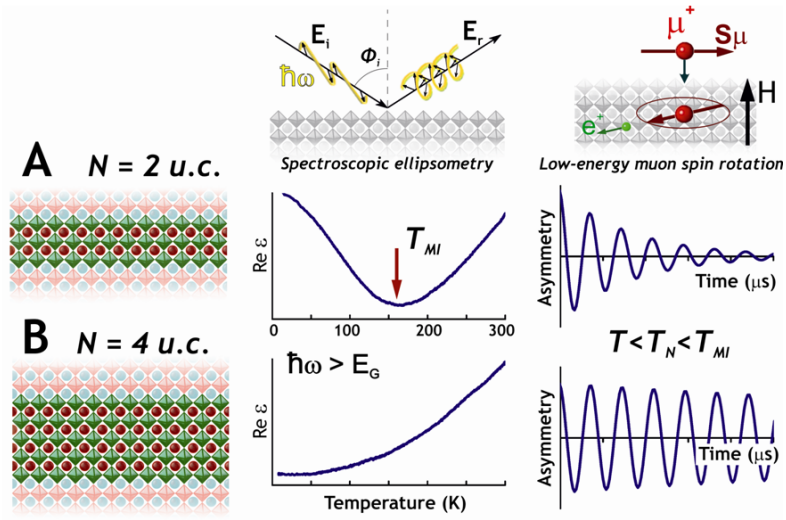

Figure 4.23: Schematic representation of the main experimental results: Dielectric response and transverse field muon spin rotation measurements show that A. superlattices with $LaNiO_3$ as thin as two unit cells undergo a sequence of collective metal-insulator and antiferromagnetic transitions upon cooling, whereas B. superlattices with thicker $LaNiO_3$ layers remain metallic and paramagnetic at all temperatures.

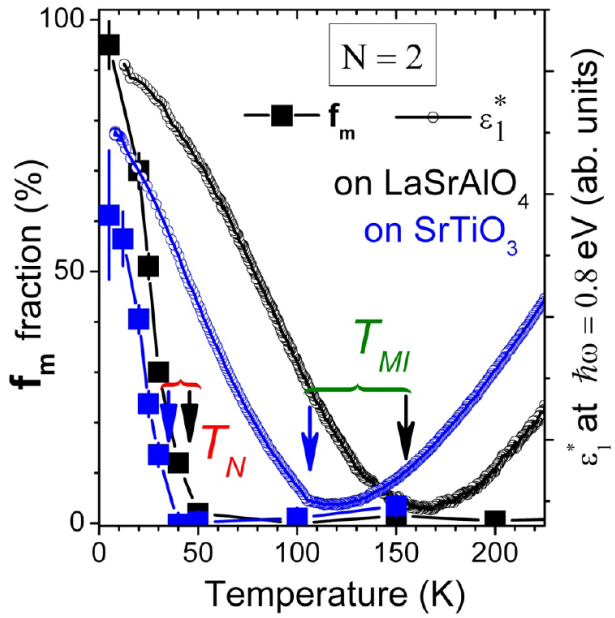

Figure 4.24: Temperature dependencies of the fraction of muons experiencing static local magnetic fields, f_m, and the normalized permittivity ε_1^* at 0.8 eV in the $N = 2$ superlattices. The black and blue arrows mark the magnetic (T_N) and metal-insulator (T_{MI}) transition temperatures for the superlattices on $LaSrAlO_4$ and $SrTiO_3$, respectively (150).

Ni *3d* bandwidth and/or an enhanced occupation of the Ni $d_{x^2-y^2}$ orbital polarized parallel to the $LaNiO_3$ layers. This indicates further opportunities for orbital control of the collective phase behavior of the nickelates.

Bibliography

[1] P. Drude. Ann. der Physik **36**, 532 (1889).

[2] P. Drude. Ann. der Physik **36**, 865 (1889).

[3] R. M. A. Azzam and N. M. Bashara, *Ellipsometry and Polarized Light*, Elsevier Science Pub Co (1987).

[4] H. G. Tompkins and E. A. Irene, *Handbook of Ellipsometry*, William Andrews Publications, Norwich, NY (2005).

[5] WVASE manual, *Guide to Using WVASE 32^{TM}*, J. A. Woollam Co., Inc. (1999).

[6] F. Stern, *Elementary Optical Properties of Solids*, Academic Press New York (1963).

[7] J. Kircher, R. Henn, M. Cardona, P.L. Richards and G.P. Williams. J. Opt. Soc. Am. B **14**, 705 (1997).

[8] R. Henn, C. Bernhard, A. Wittlin, M. Cardona and S. Uchida. Thin Solid Films **313-314**, 643 (1998).

[9] C. Bernhard, J. Humlíček, and B. Keimer, Thin Solid Films **455-456**, 143 (2004).

[10] R. Kubo, J. Phys. Soc. Japan **12**, 579 (1957).

[11] M. Imada, A. Fujimori, Y. Tokura, Rev. Mod. Phys **70**, 1039 (1998).

[12] G. H. Jonker and J. H. Van Santen, Physica **16**, 377 (1950).

[13] E. Dagotto, *Nanoscale Phase Separation and Colossal Magnetoresistance: The Physics of Manganites and Related Compounds*, Springer-Verlag, New York (2002).

[14] C. N. R. Rao and A. K. Cheetham, Science **276**, 911 (1997).

[15] J.G. Bednorz and K.A. Mueller. Z. Phys. B **64**, 189 (1986).

[16] J. Zaanen, G. A. Sawatzky, and J. W. Allen, Phys. Rev. Lett. **55**, 418 (1985).

[17] J. L. Garcia-Munoz, J. Rodriguez-Carvajal, F. Sapina, M. J. Sanchis, R. Ibanez, and D. Beltrn-Porter, J. Phys.: Condens. Matter **2**, 2205 (1990).

[18] C. L. Teske and H. Muller-Buschbaum, Z. Anorg. Allg. Chem. **371**, 325 (1969).

[19] M. Hidaka, M. Hatae, I. Yamada, M. Nishi, and J. Akimitsu, J. Phys.: Condens. Matter **9**, 809 (1997).

[20] Y. Matsushita, Y. Oyama, M. Hasegawa, and H. Takei, J. Solid State Chem. **114**, 289 (1994).

[21] E. Dagotto and T. M. Rice, Science **271**, 618 (1996).

[22] W. E. Pickett, Rev. Mod. Phys. **61**, 433 (1989).

[23] A. Dubroka, L. Yu, D. Munzar, K. W. Kim , M. Rössle, V. K. Malik, C. T. Lin, B. Keimer, Th. Wolf, and C. Bernhard, Eur. Phys. J. Special Topics **188**, 73 (2010).

[24] O. Fischer, M. Kugler, I. Maggio-Aprile, C. Berthod, and C. Renner, Rev. Mod. Phys. **79**, 353 (2007).

[25] J. Meng, G. Liu, W. Zhang, L. Zhao, H. Liu, X. Jia, D. Mu, S. Liu, X. Dong, J. Zhang, W. Lu, G. Wang, Y. Zhou, Y. Zhu, X. Wang, Z. Xu, C. Chen, and X. J. Zhou, Nature **462**, 335 (2009).

[26] A. Damascelli, Z. Hussain, and Z.-X. Shen, Rev. Mod. Phys. **75**, 473 (2003).

[27] Suchitra E. Sebastian, N. Harrison, P. A. Goddard, M. M. Altarawneh, C. H. Mielke, Ruixing Liang, D. A. Bonn, W. N. Hardy, O. K. Andersen and G. G. Lonzarich, Phys. Rev. B **81**, 214524 (2010).

[28] S. Maekawa and T. Tohyama, Rep. Prog. Phys. **64** 383 (2001).

[29] Y. Mizuno, T. Tohyama, S. Maekawa, T. Osafune, N. Motoyama, H. Eisaki, and S. Uchida, Phys. Rev. B **57**, 5326 (1998).

[30] Motoyama, H. Eisaki, and S. Uchida, Phys. Rev. Lett. **76**, 3212 (1996).

[31] M. Hase, I. Terasaki, and K. Uchinokura, Phys. Rev. Lett. **70**, 3651 (1993).

[32] S. Park, Y. J. Choi, C. L. Zhang, and S.-W. Cheong, Phys. Rev. Lett. **98**, 057601 (2007).

[33] Y. Naito, K. Sato, Y. Yasui, Y. Kobayashi, Y. Kobayaashi, and M. Sato, J. Phys. Soc. Jpn. **76**, 023708 (2007).

[34] T. Giamarchi, *Quantum Physics in One Dimension Oxford Science Publications*, New York (2004).

[35] C. Kim, A. Y. Matsuura, Z.-X. Shen, N. Motoyama, H. Eisaki, S. Uchida, T. Tohyama, and S. Maekawa, Phys. Rev. Lett. **77**, 4054 (1996).

[36] A. V. Sologubenko, T. Lorenz, H. R. Ott, and A. Freimuth, J. Low Temp. Phys. **147**, 387 (2007).

[37] F. Heidrich-Meisner, A. Honecker, and W. Brenig, Phys. Rev. B **71**, 184415 (2005).

[38] A. V. Savin, G. P. Tsironis, and X. Zotos, Phys. Rev. B **75**, 214305 (2007).

[39] J. B. Goodenough, Phys. Rev. **100**, 564 (1955).

[40] J. Kanamori, J. Phys. Chem. Solids **10**, 87 (1959).

[41] P. W. Anderson, Solid State Phys. **14**, 99 (1963).

[42] U. Schollwöck, J. Richter, D. J. J. Farnell, and R. F. Bishop, *Quantum Magnetism*, Lect. Notes Phys. **645**, Springer, Berlin (2004).

[43] L. Capogna, M. Mayr, P. Horsch, M. Raichle, R. K. Kremer, M. Sofin, A. Maljuk, M. Jansen, and B. Keimer, Phys. Rev. B **71**, 140402(R) (2005).

[44] M. Enderle, C. Mukherjee, B. Fak, R. K. Kremer, J.-M. Broto, H. Rosner, S.-L. Drechsler, J. Richter, J. Malek, A. Prokofiev, W. Assmus, S. Pujol, J.-L. Raggazzoni, H. Rakoto, M. Rheinstaedter, and H. M. Ronnow, Europhys. Lett. **70**, 237 (2005).

[45] H. F. Fong, B. Keimer, J. W. Lynn, A. Hayashi, and R. J. Cava, Phys. Rev. B **59**, 6873 (1999).

[46] W. Barford, Phys. Rev. B **65**, 205118 (2002).

[47] E. Jeckelmann, Phys. Rev. B **67**, 075106 (2003).

[48] F. Gebhard, K. Bott, M. Scheidler, P. Thomas, and S. W. Koch, Philos. Mag. B **75**, 47 (1997).

[49] F.B. Gallagher and S. Mazumdar, Phys. Rev. B **56**, 15025 (1997).

[50] K. A. Al-Hassanieh, F. A. Reboredo, A. E. Feiguin, I. González, and E. Dagotto, Phys. Rev. Lett. **100**, 166403 (2008).

[51] K. W. Kim, G. D. Gu, C. C. Homes, and T. W. Noh, Phys. Rev. Lett. **101**, 177404 (2008).

[52] F. C. Zhang and T. M. Rice, Phys. Rev. B **37**, 3759 (1988).

[53] M. Mayr, and P. Horsch, Phys. Rev. B **73**, 195103 (2006).

[54] V. J. Emery, Phys. Rev. Lett. **58**, 2794 (1987).

[55] J. Hubbard, Phys. Rev. B **17**, 494 (1978).

[56] J. Kikuchi, K. Ishiguchi, K. Motoya, M. Itoh, K. Inari, N. Eguchi, and J. Akimitsu, J. Phys. Soc. Jpn. **69**, 2660 (2000).

[57] S.-L. Drechsler, J. Richter, R. Kuzian, J. Málek, N. Tristan, B. Büchner, A. S. Moskvin, A. A. Gippius, A. Vasiliev, O. Volkova, A. Prokofiev, H. Rakotoh, J.-M. Broto, W. Schnelle, M. Schmitt, A. Ormeci, C. Loison, and H. Rosner, J. Magn. Magn. Mater. **316**, 306 (2007).

[58] J. C. Bonner and M. E. Fisher, Phys. Rev. **135**, A640 (1964).

[59] M. E. Simòn, A. A. Aligia, C. D. Batista, E. R. Gagliano, and F. Lema, Phys. Rev. B **54**, 3780(R) (1996).

[60] F. C. Zhang and K. K. Ng, Phys. Rev. B **58**, 13520 (1998).

[61] E. Wigner, Phys. Rev. **46**, 1002 (1934).

[62] J. Malek, S.-L. Drechsler, U. Nitzsche, H. Rosner, and H. Eschrig, Phys. Rev. B **78**, 060508(R) (2008).

[63] T. Arima, T. Kikuchi, M. Kasuya, S. Koshihara, Y. Tokura, T. Ido, and S. Uchida, Phys. Rev. B **44**, 917 (1991).

[64] S. Doniach, B. J. Roulet, and M. E. Fisher, Phys. Rev. Lett. **27**, 262 (1971).

[65] M. Papagno, D. Pacilé, G. Caimi, H. Berger, L. Degiorgi, and M.Grioni, Phys. Rev. B **73**, 115120 (2006).

[66] R. V. Pisarev, A. S. Moskvin, A. M. Kalashnikova, A. A. Bush, and Th. Rasing, Phys. Rev. B **74**, 132509 (2006).

[67] M. Bassi, P. Camagni, R. Rolli, G. Samoggia, F. Parmigiani, G. Dhalenne, and A. Revcolevschi, Phys. Rev. B **54**, 11030(R) (1996).

[68] A. Damascelli, D. van der Marel, G. Dhalenne, and A. Revcolevschi, Phys. Rev. B **61**, 12063 (2000).

[69] S. D. Dević, Z. V. Popović, A. Breitschwerdt, G. Dhalenne, and A. Revcolevchi, Phys. Status Solidi B **203**, 579 (1997).

[70] G. Y. Rudko, V. C. Long, J. L. Musfeldt, H. J. Koo, M. H. Whangbo, A. Revcolevschi, G. Dhalenne, and D. E. Bernholdt, Chem. Mater. **13**, 939 (2001).

[71] V. C. Long, J. L. Musfeldt, T. Schmiedel, A. Revcolevschi, and G. Dhalenne, Phys. Rev. B **56**, 14263 (1997)

[72] J. Kim, D. S. Ellis, H. Zhang, Y.-J. Kim, J.P. Hill, F.C. Chou, T. Gog, and D. Casa, Phys. Rev. B **79**, 094525 (2009).

[73] M.A. Lafontaine, M. Leblanc and G. Ferey, Acta Crystallogr. C **45**, 1205 (1989).

[74] A.V. Prokofiev, D. Wichert and W. Assmus, J. Crystal Growth **220**, 345 (2000).

[75] B. J. Gibson, R. K. Kremer, A. V. Prokofiev, W. Assmus, G. J. McIntyre, Physica B **350**, 253 (2004).

[76] N. Büttgen, H.-A. Krug von Nidda, L. E. Svistov, L. A. Prozorova, A. Prokofiev, and W. Assmus, Phys. Rev. B **76**, 014440 (2007).

[77] A. V. Prokofiev, I. G. Vasilyeva, V. N. Ikorskii, V. V. Malakhov, I. P. Asanov, and W. Assmus, J. Solid State Chem. **177**, 3131 (2004).

[78] M. Enderle, B. Fåk, H.-J. Mikeska, R. K. Kremer, A. Prokofiev, and W. Assmus, Phys. Rev. Lett. **104**, 237207 (2010).

[79] Y. Matiks, P. Horsch, R. K. Kremer, B. Keimer, and A. V. Boris, Phys. Rev. Lett. **103**, 187401 (2009).

[80] F. Vernay, B. Moritz, I. S. Elfimov, J. Geck, D. Hawthorn, T. P. Devereaux, and G. A. Sawatzky, Phys. Rev. B **77**, 104519 (2008).

[81] M. Ogata and H. Fukuyama, Rep. Prog. Phys. **71**, 036501 (2008).

[82] P. Horsch, M. Sofin, M. Mayr, and M. Jansen, Phys. Rev. Lett. **94**, 076403 (2005).

[83] A. Maljuk, A. B. Kulakov, M. Sofin, L. Capogna, J. Strempfer, C. T. Lina, M. Jansen, and B. Keimer, J. Cryst. Growth **263**, 338 (2004).

[84] L. Capogna, M. Reehuis, A. Maljuk, R. K. Kremer, B. Ouladdiaf, M. Jansen, and B. Keimer, Phys. Rev. B **82**, 014407 (2010).

[85] A. A. Gippius, A. S. Moskvin, and S.-L. Drechsler, Phys. Rev. B **77**, 180403(R) (2008).

[86] Ph. Leininger, M. Rahlenbeck, M. Raichle, B. Bohnenbuck, A. Maljuk, C. T. Lin, B. Keimer, E. Weschke, E. Schierle, S. Seki, Y. Tokura, and J. W. Freeland, Phys. Rev. B **81**, 085111 (2010).

[87] J. Kircher, M. Alouani, M. Garriga, P. Murugaraj, J. Maier, C. Thomsen, M. Cardona, O. K. Andersen, and O. Jepsen, Phys. Rev. B **40**, 7368 (1989).

[88] M. K. Kelly, P. Barboux, J.-M. Tarascon, and D. E. Aspnes, Phys. Rev. B **40**, 6797 (1989).

[89] T. Masuda, A. Zheludev, B. Roessli, A. Bush, M. Markina and A. Vasiliev, Phys. Rev. Lett. **92**, 177201 (2004).

[90] S. Zvyagin, Phys. Rev. Lett. **66**, 064424 (2002).

[91] O. K. Andersen, Phys. Rev. B **12**, 3060 (1975).

[92] V.I. Anisimov, J. Zaanen, and O. K. Andersen, Phys. Rev. B **44**, 943 (1991).

[93] M. T. Czyżyk and G. A. Sawatzky, Phys. Rev. B **49**, 14211 (1994).

[94] J.P. Perdew and A. Zunger, Phys. Rev. B **23**, 5048 (1981).

[95] F. Sapiña, J. Rodríguez-Carvajal, M. J. Sanchis, R. Ibá?z, A. Beltrán, and D. Beltrán, Solid State Commun. **74**, 779 (1990).

[96] G. Behr, W. Löser and D. Souptel et al., J. Cryst. Growth **310**, 2268 (2008).

[97] E. M. L. Chung, G. J. McIntyre, D. M. Paul, G. Balakrishnan, and M. R. Lees, Phys. Rev. B **68**, 144410 (2003).

[98] M. Boehm, S. Coad, B. Roessli, A. Zheludev, M. Zolliker, P. Boni, D. McK. Paul, H. Eisaki, N. Motoyama, and S. Uchida, Europhys. Lett. **43**, 77 (1998).

[99] U. Staub, B. Roessli, and A. Amato, Physica B **289-290**, 299 (2000).

[100] H. J. Xiang, C. Lee, and M.-H. Whangbo, Phys. Rev. B **76**, 220411(R) (2007).

[101] W.E.A Lorenz, R.O. Kuzian, S.-L. Drechsler, W.-D. Stein, N. Wizent, G. Behr, J. Mlek, U. Nitzsche, H. Rosner, A. Hiess, W. Schmidt, R. Klingeler, M. Loewenhaupt, B. Büchner, Europhys. Lett. **88**, 37002 (2009).

[102] S. Atzkern, M. Knupfer, M. S. Golden, J. Fink, C. Waidacher, J. Richter, K. W. Becker, N. Motoyama, H. Eisaki, and S. Uchida, Phys. Rev. B **62**, 7845 (2000).

[103] M. Hidaka, M. Hatae, I. Yamada, M. Nishi, and J. Akimitsu, J. Phys.: Condens. Matter **9**, 809 (1997).

[104] W. Geertsma and D. Khomskii. Phys. Rev. B **54**, 3011 (1996).

[105] D. Khomskii, W. Geertsma and M. Mostovoy. Czech. J. Phys. **46**, 3239 (1996).

[106] T. Lorenz. PhD thesis, Universitäat zu Käoln (1998).

[107] M. Miljak, M. Herak, A. Revcolevschi, and G. Dhalenne, Europhys. Lett. **70**, (3) 369 (2005).

[108] M. Nishi, O. Fujita and J. Akimitsu. Phys. Rev. B **50**, 6508 (1994).

[109] D. Qian, Y. Li, M. Z. Hasan, D. M. Casa, T. Gog, Y.-D. Chuang, K. Tsutsui, T. Tohyama, S. Maekawa, H. Eisaki, and S. Uchida, J. Phys. Chem. Solids **66**, 2212 (2005).

[110] S. Atzkern, M. Knupfer, M. S. Golden, J. Fink, A. Hübsch, C. Waidacher, K. W. Becker, W. von der Linden, M. Weiden, and C. Geibel, Phys. Rev. B **64**, 075112 (2001).

[111] P. Yu and M. Cardona, *Fundamentals of Semiconductors*, Springer (2010).

[112] F. Urbach Phys. Rev. **92**, 1324 (1953).

[113] Z. V. Popovíc, S. D. Devíc, V. N. Popov, G. Dhalenne, and A. Revcolevschi, Phys. Rev. B **52**, 4185 (1995).

[114] C. Giannetti, G. Zgrablic, C. Consani, A. Crepaldi, D. Nardi, G. Ferrini, G. Dhalenne, A. Revcolevschi, and F. Parmigiani, Phys. Rev. B **80**, 235129 (2009).

[115] C. Calvo and D. Manolescu, Acta Crystallogr., Sect. B: Struct. Crystallogr. Cryst. Chem. **29**, 1743 (1973).

[116] A. N. Vasil'ev, L. A. Ponomarenko, A. L. Smirnov, E. V. Antipov, Yu. A. Velikodny, M. Isobe and Y. Ueda. Phys. Rev. B **60**, 3021 (1999).

[117] A. N. Vasil'ev, L. A. Ponomarenko, E. V. Antipov, Yu. A. Velikodny, A. I. Smirnov, M. Isobe and Y. Ueda, Physica B **284**, 1615 (2000).

[118] Y. Ohta, T. Tohyama, and S. Maekawa. Phys. Rev. B **66**, 1228 (1991).

[119] J. Chaloupka and G. Khaliullin, Phys. Rev. Lett. **100**, 016404 (2008).

[120] P. Hansmann, X. Yang, A. Toschi, G. Khaliullin, O. K. Andersen, and K. Held, Phys. Rev. Lett. **103**, 016401 (2009).

[121] M.L. Medarde, J. Phys.: Condens. Matter **9**, 1679 (1997).

[122] J.B. Goodenough and J.-S. Zhou, J. Mater. Chem. **17**, 2394 (2007).

[123] J.-S. Zhou, J.B. Goodenough, and B. Dabrowski, Phys. Rev. B **67**, 020404(R) (2003).

[124] X. Obradors, L. M. Paulius, M. B. Maple, J. B. Torrance, A. I. Nazzal, J. Fontcuberta, and X. Granados, Phys. Rev. B **47**, 12353 (1993).

[125] P. C. Canfield, J. D. Thompson, S.-W. Choeng, and L. W. Rupp, Phys. Rev. B **47**, 12357 (1993).

[126] U. Staub, G. I. Meijer, F. Fauth, R. Allenspach, J. G. Bednorz, J. Karpinski, S. M. Kazakov, L. Paolasini, and F. dŠAcapito, Phys. Rev. Lett. **88**, 126402 (2002).

[127] J.-G. Cheng, J.-S. Zhou, J. B. Goodenough, J. A. Alonso, and M. J. Martinez-Lope, Phys. Rev. B **82**, 085107 (2010).

[128] J.-S. Zhou, J.B. Goodenough, and B. Dabrowski, Phys. Rev. Lett. **94**, 226602 (2005).

[129] J.A. Alonso, J.L. García-Muñoz, M.T. Fernandez-Diaz, M.A.G. Aranda, M.J. Martinez-Lope, and M.T. Casais, Phys. Rev. Lett. **82**, 3871 (1999).

[130] J.A. Alonso, M.J. Martinez-Lope, M.T. Casais, J.L. García-Muñoz, M.T. Fernandez-Diaz, and M.A.G. Aranda, Phys. Rev. B **64**, 094102 (2001).

[131] M. Medarde, M. T. Fernandez-Diaz, and Ph. Lacorre, Phys. Rev. B **78**, 212101 (2008).

[132] M. Acosta-Alejandro, J. M. de Leon, M. Medarde, P. Lacorre, K. Konder, and P. A. Montano, Phys. Rev. B **77**, 085107 (2008).

[133] R. Eguchi, A. Chainani, M. Taguchi, M. Matsunami, Y. Ishida, K. Horiba, Y. Senba, H. Ohashi, and S. Shin, Phys. Rev. B **79**, 115122 (2009).

[134] J.L. García-Muñoz, J. Rodriguez-Carvajal and P. Lacorre, Europhys. Lett. **20**, 241 (1992).

[135] M. T. Fernandez-Diaz, J. A. Alonso, M. J. Martinez-Lope, M. T. Casais, and J.L. García-Muñoz, Phys. Rev. B **64**, 144417 (2001).

[136] V. Scagnoli, U. Staub, Y. Bodenthin, M. García-Fernández, G. I. Meijer, and G. Hammerl, Phys. Rev. B **77**, 115138 (2008).

[137] J. B. Torrance, P. Lacorre, A. I. Nazzal, E. D. Ansaldo, and Ch. Niedermayer, Phys. Rev. B **45**, 8209 (1992).

[138] T. Katsufuji, Y. Okimoto, T. Arima, Y. Tokura, and J. B. Torrance, Phys. Rev. B **51**, 4830 (1995).

[139] G. Herranz, F. Sanchez, J. Fontcuberta, V. Laukhin, J. Galibert, M. V. Garcia-Cuenca, C. Ferrater, and M. Varela, Phys. Rev. B **72**, 014457 (2005).

[140] M. Kawai, S. Inoue, M. Mizumaki, N. Kawamura, N. Ichikawa, and Y. Shimakawa, Appl. Phys. Lett. **94**, 082102 (2009).

[141] R. Scherwitzl, P. Zubko, C. Lichtensteiger, and J. -M. Triscone, Appl. Phys. Lett. **95**, 222114 (2009).

[142] J. Son, P. Moetakef, J. M. LeBeau, D. Ouellette, L. Balents, S. J. Allen, and S. Stemmer, Appl. Phys. Lett. **96**, 062114 (2010).

[143] Y. Kumar, R.J. Choudhary, A.P. Singh, G. Anjum, and R. Kumar, J. Appl. Phys. **108**, 083706 (2010).

[144] D.G. Ouellette, S.B. Lee, J. Son, S. Stemmer, L. Balents, A.J. Millis, and S.J. Allen, Phys. Rev. B **82**, 165112 (2010).

[145] A. Ohtomo, and H.Y. Hwang, Nature **427**, 423 (2004).

[146] E. Bousquet, M. Dawber, N. Stucki, C. Lichtensteiger, P. Hermet, S. Gariglio, J.-M. Triscone, and P. Ghosez, Nature **452**, (7188), 732 (2008).

[147] J. Chakhalian J., J. W. Freeland, H.-U. Habermeier, G. Cristiani, G. Khaliullin, M. van Veenendaal, B. Keimer. Science **318**, 1115 (2007).

[148] S.J. May, P.J. Ryan, J.L. Robertson, J.-W. Kim, T.S. Santos, E. Karapetrova, J.L. Zarestky, X. Zhai, S.G.E. te Velthuis, J.N. Eckstein, S.D. Bader and A. Bhattacharya, Nature Mat. **8**, 892 (2009).

[149] S. J. May, T. S. Santos, and A. Bhattacharya, Phys. Rev. B **79**, 115127 (2009).

[150] A. V. Boris, Y. Matiks, E. Benckiser, A. Frano, P. Popovich, V. Hinkov, P. Wochner, E. Detemple, V. K. Malik, C. Bernhard, T. Prokscha, A. Suter, Z. Salman, E. Morenzoni, G. Cristiani, H.-U. Habermeier, and B. Keimer, submitted to Science.

[151] A. Frano, MSc Thesis, University of Stuttgart (2010).

[152] S. J. May, J.-W. Kim, J. M. Rondinelli, E. Karapetrova, N. A. Spaldin, A. Bhattacharya, and P. J. Ryan, Phys. Rev. B **82**, 014110 (2010).

[153] H. Heinke, S. Einfeldt, B. Kuhn-Heinrich, G. Plahl, M.O. Möller, and G. Landwehr, J. Phys. D **28**, A104 (1995).

[154] H. Heinke, M.O. Möller, D. Hommel, and G. Landwehr, J. Cryst. Growth **135**, 41 (1994).

[155] F. Conchon, A. Boulle, R. Guinebretière, C. Girardot, S. Pignard, J. Kreisel, F. Weiss, E. Dooryhée, and J.-L. Hodeau, Appl. Phys. Lett. **91**, 192110 (2007).

[156] J. Liu, M. Kareev, S. Prosandeev, B. Gray, P. Ryan, J. W. Freeland, and J. Chakhalian, Appl. Phys. Lett. **96**, 133111 (2010).

[157] U. Gebhardt, N. V. Kasper, A. Vigliante, P. Wochner, H. Dosch, F. S. Razavi, and H. U. Habermeier, Phys. Rev. Lett. **98**, 096101 (2007).

[158] U. Gebhardt, Ph.D. Thesis, University of Stuttgart (2006).

[159] Y. F. Zhukovskii, E. A. Kotomin, S. Piskunov, and D. E. Ellis, Solid State Commun. **149**, 1359 (2009).

[160] R. D. Sánchez, M. T. Causa, A. Caneiro, A. Butera, M. Vallet-Regí, M. J. Sayagués, J. González-Calbet, F. García-Sanz, and J. Rivas, Phys. Rev. B **54**, 16574 (1996).

[161] A.A. Sirenko, C. Bernhard, A. Golnik, A.M. Clark,J. Hao, W. Si, and X.X. Xi, Nature **404**, 373 (2000).

[162] X. Q. Xu, J. L. Peng, Z. Y. Li, H. L. Ju, and R. L. Greene, Phys. Rev. B **48**, 1112 (1993).

[163] I. I. Mazin, D. I. Khomskii, R. Lengsdorf, J. A. Alonso, W. G. Marshall, R. M. Ibberson, A. Podlesnyak, M. J. Martinez-Lope, and M. M. Abd-Elmeguid, Phys. Rev. Lett. **98**, 176406 (2007).

[164] J. L. García-Muñoz, M. A. G. Aranda, J. A. Alonso, and M. J. Martinez-Lope, Phys. Rev. B **79**, 134432 (2009).

[165] J. L. García-Muñoz, P. Lacorre, and R. Cywinski, Phys. Rev. B **51**, 15197 (1995).

[166] J.L. García-Muñoz, R. Mortimer, A. LLobet, J. Alonso, M. Martínez-Lope, and S. Cottrell, Physica B (Amsterdam) **374-375**, 87 (2006).

[167] I. A. Campbell, A. Amato, F. N. Gygax, D. Herlach, A. Schenck, R. Cywinski, and S. H. Kilcoyne, Phys. Rev. Lett. **72**, 1291 (1994).

[168] T. Prokscha, E. Morenzoni, K. Deiters, F. Foroughi, D. George, R. Kobler, A. Suter, and V. Vrankovic, Nucl. Instr. Meth. A **595**, 317 (2008).

[169] For conventional μSR methods see, for example, J. E. Sonier, μSR brochure (http://musr.org/intro/musr/muSRBrochure.pdf).

Publications

- Y. Matiks, P. Horsch, R. K. Kremer, B. Keimer, and A. V. Boris: Exciton Doublet in the Mott-Hubbard Insulator $LiCuVO_4$ Identified by Spectral Ellipsometry;

  Phys. Rev. Lett. 103 (2009), 187401.

- A. V. Boris, N. N. Kovaleva, S. S. A. Seo, J. S. Kim, P. Popovich, Y. Matiks, R. K. Kremer, and B. Keimer: Signatures of Electronic Correlations in Optical Properties of $LaFeAsO_{1-x}F_x$;

  Phys. Rev. Lett. 102 (2009), 027001.

- A. V. Boris, Y. Matiks, E. Benckiser, A. Frano, P. Popovich, V. Hinkov, P. Wochner, M. Castro Colin, E. Detemple, V. K. Malik, C. Bernhard, T. Prokscha, A. Suter, Z. Salman, E. Morenzoni, G. Cristiani, H.-U. Habermeier, and B. Keimer: Dimensionality Control of Electronic Phase Transitions in Nickel-Oxide Superlattices;

  Science, 332 (2011), 937.

- A. Charnukha, P. Popovich, Y. Matiks, D. L. Sun, C. T. Lin, A. N. Yaresko, B. Keimer, and A. V. Boris: Superconductivity-Induced Optical Anomaly in an Iron Arsenide;

  Nature Communications 2 (2011), 219.

- A. Charnukha, O. V. Dolgov, A. A. Golubov, Y. Matiks, D. L. Sun, C. T. Lin, B. Keimer, and A. V. Boris: Eliashberg approach to superconductivity-induced infrared anomalies in $Ba_{0.68}K_{0.32}Fe_2As_2$;

  submitted to Phys. Rev. Lett..

- Y. Matiks, A.Yaresko, M.-W. Kim, P. Horsch, A. Maljuk, B. Keimer, and A. V. Boris: Anisotropy of the Optical Response of the Mixed-Valent Insulator $NaCu_2O_2$;

  submitted to Phys. Rev. B.

Acknowledgements

I would like to express my deep and sincere gratitude to the people without whom this thesis would not have been possible.

Thanks to...

...Prof. Dr. Bernhard Keimer for accepting me as a PhD student in his group and giving me the opportunity to carry out this work.

...Alexander Boris for his kind supervision through these years and constant support.

...our optical spectroscopy group for their support in the labs and during synchrotron experiments and for being great colleagues; and especially to Paul Popovich and Vekaran Khana for nice beamtimes at ANKA and for being more than colleagues.

....Peter Horsch, Alexander Yaresko and Stefan-Ludwig Drechsler for collaboration, support, theoretical calculations and intensive discussions on the cuprates from which I have learned a lot.

...Eva Benckiser and Alex Frano for the excellent collaboration in the investigation of Ni-based superlattices.

...Reinhard K. Kremer, Georg Cristiani and Andrej Maljuk for providing with the high quality samples, without which this work would have not been realized.

...Yves-Laurent Mathis for support at the infrared IR1 beamline at ANKA and Thomas Prokscha for support at the LEM beamline at PSI.

...the International Max Planck Research School for Advanced Materials; Hans-George Libuda for the administrative help and support during my first months in Germany; to IMPRS student members for great time we spent together and a lot of fun during the status seminars, free time and, especially, the three winter days in Tieringen.

...my room mates, Britta Bohnenbuck and Junghwa Kim, for cordial atmosphere in our office.

...Benjamin Bruha and Heiko Uhlig for their continuous technical support in the optical labs, and, also, Michael Schutz and Manfred Ohl.

...all former and present members of Prof. Keimer's group for the collaboration and the good work atmosphere.

...Claudia Hagemann for help.

...Daniel Pröpper for the german translation of the abstract.

...Dmytro and Katja Inosov for being friends, for cycling together, for learning how to make great photos and for inspiration, and, also, for the careful reading of my thesis.

... my good friends, Isabella Gierz, Georgijs Bakradze, Adarsh Sagar and Ludwig Klam for their encouragement, for all those days, evenings, dinners, cakes, talks, jokes, for understanding, for keeping me smiling and optimistic.

... my lovely friends in Russia for their encouragement and for the nice time we spent together.

Finally, I am deeply indebted to my beloved parents, my sister Anna and her husband Dmitry for their endless love, invaluable support and encouragement from long distance.